



**Università
degli Studi
di Ferrara**



**DOCTORAL COURSE IN
"Earth and Marine Science-EMAS"**

CYCLE XXXVI

COORDINATOR Prof. PAOLO CIAVOLA

**"COMBINED TECHNIQUES STUDY FOR THE IDENTIFICATION OF MAIN DRIVES IN COASTAL
CLIFF PROCESSES BETWEEN PORTONOVO AND TRAVE (ANCONA, ITALY)"**

Scientific/Disciplinary Sector (SDS) Geo/05

Candidate

Dott. FULLIN NICOLA

Supervisors

Prof. GHIROTTI MONICA, Prof. PAOLO CIAVOLA

(signature)

(signature)

Year 2020/2023

Abstract

Factors governing slope stability include lithology, geological structures, hydrogeological conditions, and landform evolution. Given the intricate interplay among these factors, a comprehensive analysis is required to identify the mechanisms and processes leading to slope instability. The introduction and advancement of remote sensing techniques have significantly increased the quantity and quality of geological data that can be gathered. These techniques, including satellite imagery, aerial photography, and ground-based measurements, play a crucial role in improving our comprehension of geological phenomena, especially in areas that are challenging to access. Coastal regions present a particular challenge due to the inaccessibility of coastal slopes and the multitude of drivers influencing coastal processes, including subaerial, marine, and endogenic factors.

Moreover, the erosion of coastal cliffs poses a significant risk to human safety and infrastructure, necessitating active monitoring for informed management decisions.

In the current study, we have identified morphodynamic changes over time through repeated change detection analyses, particularly with the application of Unmanned Aerial Vehicle (UAV) digital photogrammetry. The findings underscore the significance of actively monitoring these regions and the availability of highly accurate and detailed three-dimensional (3D) geospatial data.

Rocky coastlines, characterized by steep cliffs, undergo diverse natural processes such as rainfall, ice and water run-off, and marine action. The integration of high temporal and spatial resolution data through remote sensing and geomatics techniques enables the exploration of otherwise inaccessible areas. Integrating these datasets with fieldwork surveys enables analysis using Machine Learning (ML) algorithms to identify the primary influencing factors causing erosion. This identification is further supported through numerical modeling for assessing slope stability.

In this comprehensive study, we explore the cliffs within the Conero Regional Park, located in Northern Adriatic Sea, Ancona province, Italy. The specific focus is on evaluating the cliff-top retreat occurring between the beaches of Portonovo and Trave.

The study spans several decades, utilizing aerial orthophotos acquired between 1978 and 2021, UAV photographs surveyed in September 2021, and 2012 Light Detection and Ranging (LiDAR) data. The United States Geological Survey's (USGS) Digital Shoreline Analysis System (DSAS) was employed to analyze the aerial orthophotos, identifying and estimating top-cliff erosion. The results were cross-verified with wave data and rainfall from the corresponding period.

Over this forty-year period in the northernmost sector (Trave), erosion of up to 40 meters was detected. Additionally, a Digital Elevation Model (DEM) of Difference (DoD) was implemented to validate the DSAS results revealing a consistent agreement between the retreat areas identified by DSAS and the sections of the coast characterized by high values of DoD.

Subsequently, in the Portonovo-Trave cliffs, two UAV surveys conducted in September 2021 and October 2022 successfully provided dense point clouds, making it possible the application of the Multiscale-Model-to-Model Cloud-Comparison algorithm (M3C2) for change detection analysis. Volume estimation performed using the 2.5D Volume tool implemented in CloudCompare processing software, revealed erosion exceeding 500 m³ in one segment of Trave sector, interpreted and attributed both to notch erosion at the base and landslide processes along the slope. Mezzavalle sector differently from first DSAS analysis, showed erosion, even due to notch erosion, and differential accretion was noted along a section of this sector on the berm. Eventually, in the Portonovo-Trave cliffs a 2022 UAV survey of the Portonovo-Trave cliffs was complemented with geomechanical data collected during fieldwork.

The determination of cliff top retreat was carried out within a GIS environment comparing orthophotos taken in 1978 and a new UAV survey in 2022 using the DSAS tool.

Furthermore, two Machine Learning (ML) algorithms, Random Forest (RF) and eXtreme Gradient Boosting (XGB), were employed to analyze the data. The Mean Decrease in Impurity (MDI) methodology assessed the significance of each factor, with both algorithms consistently highlighting slope height as a primary influencer of cliff-top erosion rates.

To validate the results of the ML algorithms, a 2D Limit Equilibrium Method (LEM) was employed. The ten sections exhibiting the most substantial cliff top retreat, as identified by DSAS, were analyzed through 2D LEM analysis. Factor of Safety (FS) values were compared with the cliff height of each profile, and the outcomes from the 2D LEM analyses were consistent with the results obtained from the ML algorithms.

In conclusion, the integration of various remote sensing techniques, as well as machine learning (ML) and limit equilibrium method (LEM) analyses, has proven to be an effective methodology for studying slope and erosion processes in a coastal area.

This study reinforces the importance of utilizing high-resolution datasets to detect diverse processes and emphasizes the adaptability of UAV devices in complex environments. The findings also underscore how continuous monitoring and the use of advanced technologies are crucial for effectively assessing and managing coastal erosion.

The findings contribute to the broader understanding of coastal processes, emphasizing the need for a holistic approach that integrates fieldwork, remote sensing, machine learning, and numerical modeling for comprehensive and accurate assessments.

A novel methodology, accompanied by open-source code, is proposed to investigate site-specific cliff erosion. The results obtained from this approach identify the crucial factors that determine the erosion process.

Riassunto

La stabilità dei versanti è governata da svariati fattori che includono la litologia, le strutture geologiche, ovvero assetto geologico e/o presenza di disturbi tettonici, le condizioni idrogeologiche e l'evoluzione del rilievo nel tempo, condizionata a sua volta da fattori esterni al versante.

L'identificazione dei processi e dei meccanismi che possono portare a condizioni di instabilità, è un'operazione complessa anche in virtù della variabilità spaziale e temporale delle condizioni predisponenti ed innescanti.

Le coste alte, in particolare, rappresentano un caso particolare nell'ambito della stabilità dei versanti a causa dell'interazione tra fattori subaerei, marini ed endogeni. In particolare, i processi erosivi che affliggono le coste alte costituiscono un ulteriore fattore di pericolosità per la sicurezza umana nel caso di un loro utilizzo ad uso balneare e per le eventuali infrastrutture presenti a monte o alla base della costa.

Lo sviluppo e l'avanzamento delle tecniche di telerilevamento nel campo della stabilità dei versanti hanno aumentato notevolmente la possibilità di avere a disposizione una grande mole di dati geologici, idrogeologici e topografici nel tempo, anche in aree inaccessibili, grazie alla ripetibilità delle campagne di acquisizione.

Diversi autori hanno evidenziato una lacuna nella ricerca riguardante l'erosione e l'evoluzione delle falesie. Nel corso del XX secolo, questa ricerca è stata condotta da pochi ricercatori, con limitato interesse da parte degli operatori nei campi affini, come l'ingegneria costiera, nell'unione dei dati per la ricostruzione di un modello multidisciplinare. Questa limitazione è stata accentuata dal fatto che le indagini venivano condotte da piccoli gruppi di ricercatori sparsi senza cooperazione nei diversi ambiti di ricerca.

Nonostante questa mancanza, finora non è stato sviluppato un modello completo che integri i molteplici fattori che influenzano l'erosione delle scogliere, come la dinamica delle onde, le caratteristiche della spiaggia, i materiali delle scogliere e i meccanismi di cedimento. L'obiettivo di questo lavoro è colmare almeno in parte questa lacuna.

Pertanto, il lavoro si è focalizzato nel determinare l'importanza di vari fattori che contribuiscono all'erosione delle falesie, con l'obiettivo di comprendere meglio i legami tra questi ed il processo erosivo.

La tesi presenta tre studi condotti nell'area tra Portonovo ed il Trave, esaminando in prima battuta l'evoluzione geomorfologica dei versanti nel lasso temporale 1978-2021 e poi nell'evoluzione annuale 2021-2022. I dati ricavati sull'erosione decennale sono stati poi riutilizzati unitamente ai dati geologici, topografici e marini per ricavare l'importanza di ciascun fattore rispetto all'erosione, mediante l'utilizzo di algoritmi di apprendimento automatico (ML).

Nel primo studio, viene analizzato e quantificato l'arretramento della falesia ubicata tra la spiaggia di Portonovo e il Trave, all'interno del Parco Regionale del Conero (Ancona, Italia). I cambiamenti morfodinamici sono stati valutati in un arco temporale complessivo di oltre 40 anni e in intervalli temporali minori (10 anni) utilizzando analisi di ortofoto aeree acquisite tra il 1978 e il 2021, dati da fotogrammetria digitale UAV (Unmanned Aerial Vehicle) e da Light Detection and Ranging (LiDAR). La combinazione di questi dati, integrata con rilevamenti sul campo, ha consentito mediante algoritmi di ML di identificare i principali fattori che causano l'erosione. Analisi di stabilità all'equilibrio limite 2D (LEM), condotte lungo sezioni rappresentative delle aree che mostravano i maggiori valori di arretramento del ciglio della falesia, hanno ulteriormente validato i risultati del ML.

In questo periodo di quarant'anni nel settore più settentrionale (Trave), è stata identificata un'erosione di oltre 40 metri. Inoltre, è stato calcolato un Modello Digitale di Elevazione (DEM) delle Differenze (DoD) per convalidare i risultati DSAS, rivelando un buon accordo tra le aree di ritiro identificate da DSAS e le sezioni della costa caratterizzate da valori elevati di DoD.

Nel secondo studio sulle Falesie di Portonovo-Trave, due rilevamenti UAV condotti nel settembre 2021 e nell'ottobre 2022 hanno fornito con successo nuvole di punti dense, consentendo l'applicazione dell'algoritmo di confronto tra nuvole di punti Multiscale-Model-to-Model Cloud-Comparison (M3C2) per l'analisi dei cambiamenti. La stima del volume, effettuata utilizzando lo strumento di Volume 2.5D implementato nel software di elaborazione CloudCompare, ha rivelato un'erosione superiore a 500 m³ in un segmento del settore del Trave, interpretata ed attribuita sia all'erosione alla base (solco di battigia) che ai processi di frana lungo il pendio. Il settore di Mezzavalle ha mostrato un'attività, anche con la formazione del solco di battigia, non registrata dalle analisi precedenti per le differenti modalità di analisi del dato e sono state osservate accrescimenti differenziali lungo una sezione della spiaggia di Mezzavalle.

Nel terzo studio, al rilevamento UAV del 2022 è stato accompagnato da dati geomeccanici raccolti durante il lavoro sul campo. La determinazione del ritiro della cima della falesia in un ambiente GIS ha coinvolto il confronto tra le ortofoto scattate nel 1978 e un nuovo rilevamento UAV nel 2022 utilizzando lo strumento DSAS. Inoltre, sono stati impiegati due algoritmi di apprendimento automatico (ML), Random Forest (RF) ed eXtreme Gradient Boosting (XGB), per analizzare i dati. La metodologia Mean Decrease in Impurity (MDI) ha valutato la significatività di ciascun fattore, con entrambi gli algoritmi evidenziando in modo coerente l'altezza del pendio come principale influenzatore dei tassi di erosione della cima della falesia.

Per convalidare i risultati degli algoritmi di apprendimento automatico, è stato applicato un Metodo di Equilibrio Limite (LEM) bidimensionale (2D). Le dieci sezioni che mostravano il ritiro più importante della cima della falesia, come identificato da DSAS, sono state analizzate attraverso l'analisi LEM 2D. I valori del Fattore di Sicurezza (FS) sono stati confrontati con l'altezza della falesia di ciascun profilo, e i risultati delle analisi LEM 2D sono stati coerenti con i risultati ottenuti dagli algoritmi di apprendimento automatico.

In conclusione, l'integrazione di varie tecniche di telerilevamento, nonché di analisi di apprendimento automatico (ML) e metodo di equilibrio limite (LEM), si è dimostrata essere una metodologia efficace per lo studio dei processi di pendio ed erosione in un'area costiera. Questo studio sottolinea l'importanza dell'utilizzo di set di dati ad alta risoluzione per rilevare processi diversificati e enfatizza l'adattabilità dei dispositivi UAV in ambienti complessi. I risultati sottolineano anche come il monitoraggio continuo e l'uso di tecnologie avanzate siano cruciali per valutare e gestire in modo efficace l'erosione costiera. Le conclusioni contribuiscono alla comprensione più ampia dei processi costieri, sottolineando la necessità di un approccio olistico che integri il lavoro sul campo, il telerilevamento, l'apprendimento automatico e la modellizzazione numerica per valutazioni complete e accurate. Una nuova metodologia, accompagnata da codice open source, è proposta per studiare l'erosione specifica del sito e ottenere come risultato i fattori che sono importanti nel determinare il processo.

ACKNOWLEDGMENTS

It seems impossible that three years have already passed since I first sat in my office in Ferrara, and it is time to reflect on all that has happened during this time. Writing in English is a challenge as I consider which language to use to acknowledge all the people who have helped me on this journey. If I think of my Italian friends and colleagues, Italian would be more suitable; for my family, "pagot" would be better (though not understandable by all); for my friends from Cadiz, Spanish would be a better compromise. However, in the end, as in science, English is the best compromise.

Firstly, I want to start where this journey began. It was a sunny day in April 2020 in Vancouver when Monica called me about my Master's thesis and unexpectedly offered to continue working together on a PhD, focusing on landslides in coastal environments. It was a significant moment. I was taken aback by this proposal, as I had planned to start working immediately upon my return to Italy. I discussed it with my friends, particularly Davide, who was more of a big brother than a supervisor, and my colleagues in Italy. Twenty-four hours were not enough to make such a decision! However, everyone I spoke to agree on one point: "Nicola, you are 24; you have time to work even after. If you feel you want to take this opportunity, don't hesitate." I felt the desire to try this experience, but I feared falling behind in my professional life. Emre, a man who had escaped from Erdogan's regime and had essentially built the SFU lab computers, offered wise words: "I don't know what's best for you, Nicola, but choose the hardest option, because there will come a time when you won't choose what you want, but what you have to do." After all these discussions, I called Monica and gave her my first important YES.

Thus began an incredible adventure. Monica showed her belief in me through actions, always opening new possibilities, introducing me to new people, investing heavily in my preparation, supporting my ideas, and offering encouragement during tough times, like a second mother. This adventure took me abroad again, to Cadiz; It will always hold a special place in my heart. It's more than a city; it's a state of the soul. There, I met amazing people: Marine, Thet, Angel, Francesca, and the Carmens, who shared their thoughts and time with me. I am grateful to Giorgio, both Irene, and others for our shared lunches and their help in improving my Spanish.

Although I didn't achieve all the results I aimed for, that's part of the PhD journey. For the first time, I understood that life experience and work experience go hand in hand.

My site case became an open laboratory where many people worked simultaneously with different perspectives. Here, I was fortunate to find Davide Torre, a scientific brother, with whom a strong bond formed, leading to ongoing fruitful discussions on various scientific (and non-scientific) topics. If I can submit this work to reviewers today, it's thanks to a great professor, but above all, a great man, Mirko Francioni. I'm still amazed that while I was in Spain, he conducted a UAV survey on my behalf. This act was truly rare, unexpected, and taught me a lot about the essence of science, passion, and friendship.

I'm grateful to Satish and Nandini, my lab mates in 212. Publishing my first paper was a significant achievement, but the joy of reuniting them after years apart surpassed it all.

It's impossible to list everyone who contributed to my life in these three years. I want to highlight the role of my best friends, Bruno and his girlfriend Adele, who were always ready to relax tough situations. Also, all the PhD students who shared parties, soccer games, and advices on how not to give up on duties.

I want to thank Clara; we shared an intense period of our lives. It was crucial for our personal and emotional growth. Even though we realized our paths were not aligned, our connection remains strong because we share the same love for life and the desire to donate ourselves to other people.

Lastly, my family. I don't know if God exists; it's unknowable. However, if He does, I want to acknowledge Him for blessing me with such an incredible family. All my achievements are the result of their sacrifices and teachings, from grandparents to parents.

I know this work will be improved upon in the future and likely forgotten. That's the nature of science, Kronos will always eat his sons. But I'm proud to have shared this part of my life with others. I hope it can be helpful to someone, and if it is, then I've achieved my goal. We only leave behind in this world what we give to others.

Table of contents

1. INTRODUCTION	9
1.1 Scope and problem definition	9
1.2 Project history	10
1.3 Thesis outline	10
1.4 List of figures	12
1.5 List of tables	16
2. PART I: BACKGROUND AND SETTING	17
2.1 Rocky Coasts	17
2.2 Remote sensing	28
2.3 Rock-mass and Stability of rock slopes	38
2.4 Digital Shoreline Analysis System (DSAS)	53
2.5 Machine learning	56
3. PART II: STUDIES PERFORMED AT THE TEST SITE	62
3.1 Quantitative characterization of coastal cliff retreat and landslide processes at Portonovo-Trave cliffs (Conero, Ancona, Italy) using multi-source remote sensing data.	63
3.2 Comparing Multiple High Accuracy UAV-SfM Derived Point Clouds for Geomorphological Change Detection at Portonovo-Trave cliffs (Conero, Ancona, Italy).	84
3.3 Detection of cliff top erosion drives through machine learning algorithms between Portonovo and Trave cliffs (Ancona, Italy).	99
4. PART III: DISCUSSION AND CONCLUSIONS	123
4.1 General discussion	123
4.2 Final conclusions and future developments	126
REFERENCES	129
APPENDIX	157
APPENDIX 1: PARAMETERS EXTRACTED (Data starts from transect 1 to 310)	157
APPENDIX 2: MACHINE LEARNING CODE	165
APPENDIX 3: LEM RESULTS	170

1. INTRODUCTION

1.1 Scope and problem definition

Coastal environments are fundamental places where human activities and settlements are widely present (Martínez et al., 2007). The majority of the world's coastlines consist of high cliffs, exhibiting a high level of complexity due to numerous variables as wave action, rainfall, tidal fluctuation, etc. simultaneously influencing them. This complexity makes it challenging to determine how they have changed over time (Williams and Pranzini, 2018).

Enhancing our understanding of these phenomena is imperative to comprehend the inherent hazards within cliff environments and anticipate associated risks.

Several authors have highlighted the scarcity of studies focusing on cliff erosion and evolution. They noted that in the 20th century, research on rock coasts was limited to a relatively small group of scientists, with little attention from practitioners in related fields like coastal engineering. Small teams of widely scattered researchers often conducted research (Naylor et al., 2010).

Despite this, there hasn't been a model that comprehensively integrates many drives to investigate the links between wave dynamics, beach characteristics, cliff materials, failure mechanisms, and episodic coastal recession (Castedo et al., 2012).

This work aims to address a portion of the gap highlighted by the writers, focusing particularly on one crucial objective: determining the significance of various factors contributing to cliff erosion.

A cliff may recede in response to either externally acting or slope-independent processes. The stability of the slope can be altered by waves cutting its foot, leading to a rapid collapse of the cliff. Additionally, heavy precipitation, in combination with an unfavourable slope attitude and specific geological characteristics, can independently cause the cliff to become unstable (Sunamura T., 1992; Trenhaile, 2012).

How is it possible to determine when one action is more important significant than another? There is a categorization that considers the morphologies of cliffs to identify recurring processes currently affecting the slope (Emery and Kuhn, 1982; Trenhaile, 2012). However, this classification relies on qualitative estimates of the cliff's form in relation to limit instances, rather than numerical values.

In this work, the predominance of a certain element in the retreat process and its impact on other factors will be determined using numerical data rather than qualitative descriptions.

Machine Learning (ML) approaches will be employed to identify potential relationships between topographical characteristics, maritime data, and geological measurements and erosion.

To date, there have been no academic studies of cliffs using ML from this perspective. Only one study (Dickson and Perry, 2016) has utilized machine learning to identify cliffs that are more vulnerable, but this was conducted over a larger region."

By employing ML methodologies, this research holds promise for various stakeholders. Understanding the root causes of erosion enables the prediction of more effective remedies for specific situations. For instance, engineers tasked with designing structures near cliffs could benefit from this method by tailoring solutions based on a knowledge of erosion causation.

This approach facilitates a deeper understanding of cliff stability issues, enabling decision-makers to develop targeted solutions for specific causes, such as addressing instability due to undercutting or slope material characteristics.

1.2 Project history

The research for this PhD thesis commenced in November 2020 and was supervised by the University of Ferrara (Italy) and the University of Cadiz (Spain) from October 2022 to January 2023. The first year of a PhD involved a literature review and the selection of a case study, while the second year was dedicated to conducting fieldwork and data analysis. In the third year, a crucial stage of interpreting findings was carried out and regularly updated, leading to the development of the suggested approach.

1.3 Thesis outline

This thesis is structured into three principal parts:

Part I.

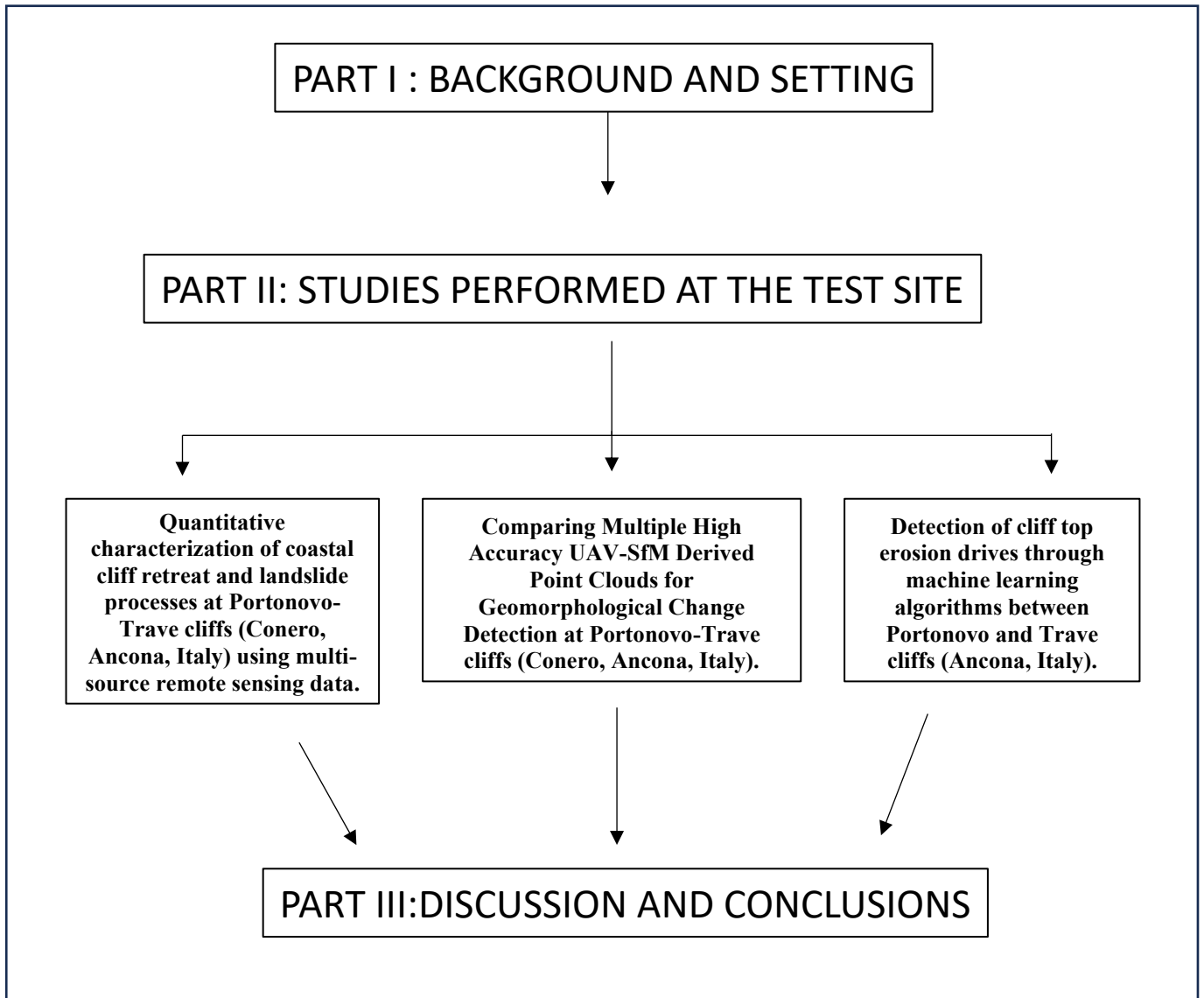
Serves as an introductory section, covering fundamental themes essential for the development of subsequent analyses. It starts by providing an overview of the rocky coast environment, displaying the interplay of complex processes. Following this, a brief exposition of rock mechanics and slope stability concepts is presented, laying the groundwork for a comprehensive understanding of the analyses employed in Part II. Lastly, a chapter dedicated to Machine Learning provides fundamental insights into the algorithms and techniques utilized to assess the significance of factors influencing erosion.

Part II.

Comprises three distinct sections, each addressing studies conducted within the Portonovo-Trave cliffs site. The initial two studies examine the geomorphological evolution of the area across different temporal spans, employing varied input data and processing techniques. The third study employs a Machine Learning approach to search into the influence of diverse factors on cliff-top erosion.

Part III.

Comprises the findings and subsequent discussions. It first explores and evaluates individual findings before merging them comprehensively. The section ends by outlining the primary conclusions drawn from the whole research work. A visual representation of the structure of the thesis is provided below to offer a clearer understanding.



1.4 List of figures

Figure 1: *Rocky coasts distribution around the world.*

Figure 2: *Rocky shores main morphologies: (a) Type-A shore platform, characterized by a sloping profile; (b) Type-B shore platform, featuring a horizontal or sub-horizontal configuration; and (c) plunging cliff.*

Figure 3: *Combination of elements that affect sea cliff toe erosion. Sunamura mod..*

Figure 4: *Factors affecting the sea cliff profiles' shapes. According to M and Sa, marine and subaerial processes, respectively, the impact of processes and rock hardness, and the impact of Quaternary variations in sea level and climate, are represented. Two-story cliffs form where the last glacial stage's talus barely reached halfway up the cliff, whereas hog's-back cliffs formed where the scree reached the rock's peak*

Figure 5: *Pros and cons of the existing remote-sensing technologies (Image from Zhang et al. 2020).*

Figure 6: *Advantages and limitations of photogrammetry and laser scanning techniques (after Petrie and Toth 2018).*

Figure 7: *Schematic illustration of the indirect approach for orthophoto generation.*

Figure 8: *Range measurement using Time Of Flight laser scanner (<https://www.seeedstudio.com/blog/2020/01/08/what-is-a-time-of-flight-sensor-and-how-does-a-tof-sensor-work/>).*

Figure 9: *Range measurements by means of phase-based laser scanner.*

Figure 10: *(a) At incidence angles larger than 45° , only diffuse reflections reach the receiver. (b) At incidence angles smaller than 45° , both diffuse and specular reflections can be received. The red dotted lines are perpendicular to the reflection directions.*

Figure 11: *Original SIFT algorithm flow.*

Figure 12: *Sketch showing the relationships between the extrinsic and intrinsic camera parameters, the col-linearity equations and the projection line.*

Figure 13: *Structure from Motion (SfM) process is illustrated. The structure in the world (cube) is imaged from multiple viewpoints (Image 1, Image 2, Image 3). By tracking (see dashed lines) the pixel locations ($p_{1,1}$, $p_{1,2}$, ...) of specific features (x_1, x_2 ...) in the images, both the camera motion (R_1 , T_1 ; R_2 , T_2 , ...) and the 3D model of the structure is estimated.*

Figure 14: *Important fracture characteristics for engineering rock mechanics.*

Figure 15: *Q-slope stability chart.*

Figure 16: *Characterization of rock masses by means of GSI system.*

Figure 17: *A new GSI classification chart for heterogeneous rock masses such as flysch*

Figure 18: *Summary of the updated version of the Varnes classification system. With the apex a are indicated movement types that usually reach extremely rapid velocities as defined by Cruden and Varnes (1996). The other landslide types are most often (but not always) extremely slow to very rapid.*

Figure 19: *Applications of the Finite Element Method to rock slope stability: example of the 2014 San Leo rockslide (Italy).*

Figure 20: *Typical workflow for analysis with DSAS plugin.*

Figure 21: *Principal methods of learning in Machine Learning applications*

Figure 22: *a) Location map of the study area. b) Satellite image showing the study area delimited by a red line (image taken from GeoEye satellite database, 2020).*

Figure 23: *Geological setting of the study area and “Sectors”: 1) Portonovo; 2) Mezzavalle; 3) Trave. Bedrock legend: SAA (Scaglia Rossa Fm., Upper Cretaceous-Medium Eocene); VAS (Scaglia Variegata Fm., Medium Eocene-Upper Eocene), SCC (Scaglia Cinerea Fm., Upper Eocene-Upper Oligocene), BIS (Bisciaro Fm., Lower Miocene), SCH (Schlier Fm., Lower Miocene-Upper Miocene), GNOa (Sapigno Fm. Upper Miocene), FCO (Colombacci Fm., Upper Miocene), Tv (Trave horizon, Lower Pliocene), FAA (Argille Azzurre Fm., Lower Pliocene-Lower Pleistocene). The Trave horizon is a natural stratum that forms a ridge outcropping from the sea in the northern section of the study area.*

Figure 24: *Coastal points defined in front of the area of interest. The points are positioned on the 20 m depth contour of the bathymetric dataset provided by ARPAE.*

Figure 25: *Methodology followed in DSAS elaboration. a) We used as cliff top the edge between vegetated slope and the bare cliff (showed by the red line). b) The baseline (the blue line), i.e. the line from which all the transects origin, was created using a buffer of the identified shoreline, with the aim of obtaining transects as much perpendicular as possible respect to the coastline. c) Image showing the baseline (in green) and the transects (in violet) obtained by DSAS elaboration.*

Figure 26: *Picture showing distribution of different data through time. The overlap window is between 1998 and 2021.*

Figure 27: *At Trave sector. a) The Sapigno Fm., composed by gypsum, is thrust on the younger Argille Azzurre Fm.. The trend of coastline in this picture is N-NW/S-SE and the attitude of the fault plane is 205/40 in Dip Direction and Dip convention. b) Outcrop of the Argille Azzurre Fm. composed of marls, completely fractured in blocks of few centimeters*

Figure 28: *a) Values of slope and b) elevation: Trave sector shows the highest values for both the considered parameters.*

Figure 29: *Summary of wave and rainfall parameters: a) POT analysis of CNR-ISMAR data between 1994-2019 for the significant wave height (hs) for coastal point CP005, showing the*

identified events. The peak value is highlighted by a red dot. b) Precipitation recorded by the stations “Ancona Torrette” and “Ancona Regione RT-1638” in the period 1990-2021.

Figure 30: NSM values calculated along transects, referred to the period 1978-2021: Portonovo and Trave sector showed the highest values of retreat. a) computed transects for the whole study area. b) Focus at Portonovo sector. c) Focus at Mezzavalle sector. d) Focus at Trave sector.

Figure 31: NSM values calculated along transects, referred to the period 1998-2007: Trave sector results the most active sector. a) computed transects for the study area. b) Focus at Portonovo sector. c) Focus at Mezzavalle sector. d) Focus at Trave sector.

Figure 32: NSM values calculated along transects, referred to the period 2010-2021: Portonovo and Trave sectors result the sectors most affected by retreating of the cliff top edge. a) computed transects for the study area. b) Focus at Portonovo sector. c) Focus at Mezzavalle sector. d) Focus at Trave sector.

Figure 33: Results of DoDs comparison in the period 2021-2012. Every sector is displayed in detail in scale 1:10.000. Analysis shows that the biggest height differences were recorded in Trave sector. a) computed DoDs for the study area. b) Focus at Portonovo sector. c) Focus at Mezzavalle sector. d) Focus at Trave sector.

Figure 34: The geological structure of Trave cliff (GNOa (Sapigno Fm. Upper Miocene) and FAA (Argille Azzurre Fm., Lower Pliocene-Lower Pleistocene)). The main thrusts are highlighted with red lines, the red arrows indicate the sense of movement between hangingwall and footwall. In orange secondary thrusts with a lower slip. The trend of coastline in this picture is N/S and the average attitude of the fault planes identified is 200/45 in Dip Direction and Dip convention.

Figure 35: Satellite image showing the study area delimited by a violet line (image taken from GeoEye satellite database, 2020). 3 sectors are identified: 1) Portonovo; 2) Mezzavalle; 3) Trave.

Figure 36: 2022 UAV derived orthophoto showing the segment identified by a red line. 4 sections are displayed in violet in the tract with a higher computed change.

Figure 37: Histograms of PMC (a) and TC (b) C2C analysis.

Figure 38: M3C2 results are displayed in the pictures showing M3C2 distance above and significant changes below for each area. Segment a) it is shown in 38a) and 38aa), then part b) it is shown in 38b) and 38bb).

Figure 39: M3C2 results are displayed in the pictures showing M3C2 distance above and significant changes below for each area. Segment c) it is shown in 39c) and 39cc), then part b) it is shown in 39d) and 39dd).

Figure 40: M3C2 results are displayed in the pictures showing M3C2 distance above and significant changes below for each area. Segment e) it is shown in 40e) and 40ee), then part f) it is shown in 40f) and 40ff).

Figure 41: M3C2 results are displayed in the pictures showing M3C2 distance above and significant changes below for each area. Segment g) it is shown in 41g) and 41gg).

Figure 42: *Extracted sections are shown to highlights the main changes in the coastline (Figure 36). The topography of 2021 is represented in red while the one of 2022 in green. All the profile are seen from south to north.*

Figure 43: *Map displaying the position of the study area: a) Satellite image showing the study area and the three sectors called Portonovo, Mezzavalle and Trave. (image taken from GeoEye satellite database, 2020). b) Collocation of the study area respect to Italy.*

Figure 44: *Workflow sketch: 1) Fieldwork; 2) Data analyses and surveys. 3) Parameters extraction. 4) Machine learning analysis. 5) Slope stability analysis.*

Figure 45: *Representation of Random Forest (image from <https://kenhoffman.medium.com/random-forest-hyperparameters-explained-8081a93ce23d>).*

Figure 46: *Representation of eXtreme Gradient Boosting (Image created by Michele Fraccaroli).*

Figure 47: *Extracted sections are highlighted in violet and numbered.*

Figure 48: *Geomorphological map of the study area and “Sectors”: 1) Portonovo; 2) Mezzavalle; 3) Trave. Bedrock legend: SCH (Schlier Fm., Lower Miocene-Upper Miocene), GNOa (Sapigno Fm. Upper Miocene), FCO (Colombacci Fm., Upper Miocene), Tv (Trave horizon, Lower Pliocene), FAA (Argille Azzurre Fm., Lower Pliocene-Lower Pleistocene).*

Figure 49: *Pictures portraying the different configuration in the different sectors. a) Portonovo sector b) Mezzavalle sector c) Trave sector.*

Figure 50: *Horizontal georeferencing uncertainty measured between 1978 and 2022 Orthophotos.*

Figure 51: *NSM values calculated along transects, referred to the period 1978-2022: Portonovo and Trave sector showed the highest values of retreat. Computed transects a) at Portonovo sector b) Mezzavalle sector c) at Trave sector.*

Figure 52: *Picture resuming ML results and analysis performed using RF and XGB algorithms. 1) Sketch displaying the parameters used in the analysis. 2) Illustration of the ML algorithm used. 3) Picture illustrating ML results. 3a) Graph showing feature importance resulting from RF algorithm. 3b) Confusion matrix of RF elaboration. 3c) Graph illustrating the feature importance extracted using XGB algorithm. 3d) Confusion matrix of XGB analysis.*

Figure 53: *Graph comparing FS and Cliff Height values in the ten extracted sections. The number behind the dot refers to the section number.*

1.5 List of tables

Table 1: *Rock Mass Quality according to the RQD System.*

Table 2: *Rock mass classification according to the RMR system.*

Table 3: *Rock mass classification according to the SMR system.*

Table 4: *Rock mass classification according to the Q system.*

Table 5: *Rock mass classification according to the RMi system.*

Table 6: *Spatial resolution of the orthophotos used for the cliff top retreat analysis.*

Table 7: *Range of GSI and UCS values for the 3 sectors.*

Table 8: *DSAS results for each period analyzed. Mean EPR and ECI are reported.*

Table 9: *Volume variations computed for each sector are reported together with their uncertainty.*

Table 10: *Summary of parameters used in ML analyses.*

Table 11: *List of the parameters used for numerical modeling.*

Table 12: *Range of GSI and UCS values for the 3 sectors according to different transects.*

Table 13: *DSAS results for each period analyzed. Mean EPR and ECI are reported.*

Table 14: *Results from LEM analysis along the extracted sections.*

2. PART I: BACKGROUND AND SETTING

2.1 Rocky Coasts

The boundary between sea and lands extends for 1,634,701 km around the world (Martínez et al., 2007) an astonishing distance considering that the Earth-to-Moon distance is “only” 384 400 km (Fig.1). These coastal areas are closely tied to human social expansion. Thanks to a generally warmer climate, proximity to food sources, and opportunities for trade routes, they provide the ideal setting for the stabilization and construction of settlements (Martínez et al., 2007).

Since the beginning of the 20th century, a fundamental dichotomy has been established in describing this environment, distinguishing between high and low coast (Broc and Giusti, 2007). The former accounts for between 75% and 52% of the world’s coastline (Williams and Pranzini, 2018; Adam P Young and Carilli, 2019). High coasts can further be categorized into soft and hard rock coasts, defining the former as cliffs composed of material with a uniaxial compressive strength (UCS) ≤ 5 MPa (Sunamura, 2015) and, consequently, the latter as those with a higher UCS value."

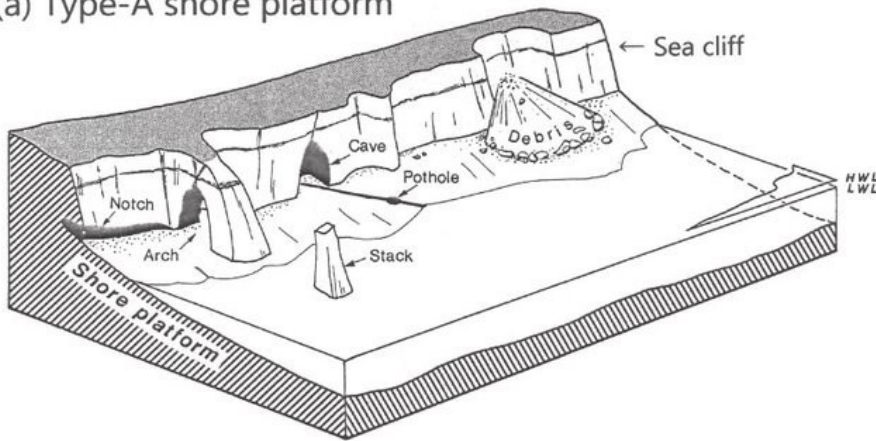


Figure 1: *Rocky coasts distribution around the world* (Emery and Kuhn, 1982).

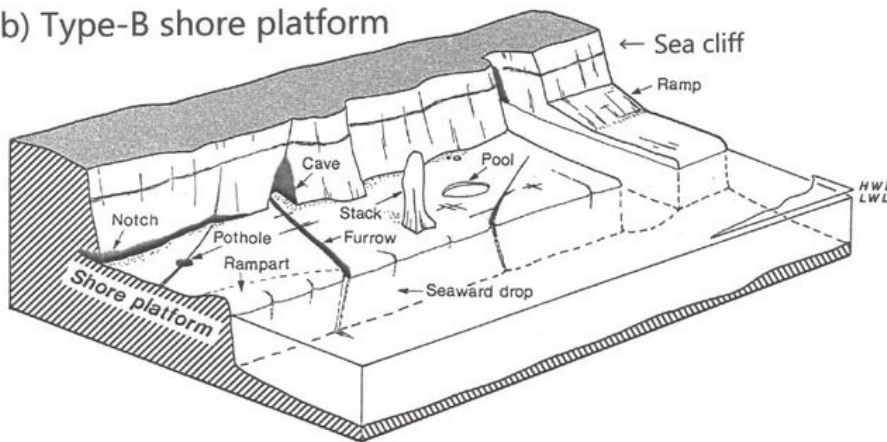
In describing rocky coast, it is essential to understand the various types found in nature. Landforms on rocky coasts are typically characterized by steep sea cliffs and can be broadly categorized into two main types: shore platforms and plunging cliffs. Shore platforms, in turn, can be further classified into two types: sloping (Type A) and horizontal (Type B) (Fig.2).

Type-A platforms feature an erosion surface that gently slopes downward from the base of a sea cliff to below sea level without any evident topographic break. On the other hand, Type-B platforms have a horizontal or sub-horizontal erosion surface that extends in front of a sea cliff and terminates seaward in a marked scarp. In the absence of these platforms, plunging cliffs occur, which are steep slopes extending far below sea level, forming a vertical or semi-vertical face (Sunamura, 2015).

(a) Type-A shore platform



(b) Type-B shore platform



(c) Plunging cliff

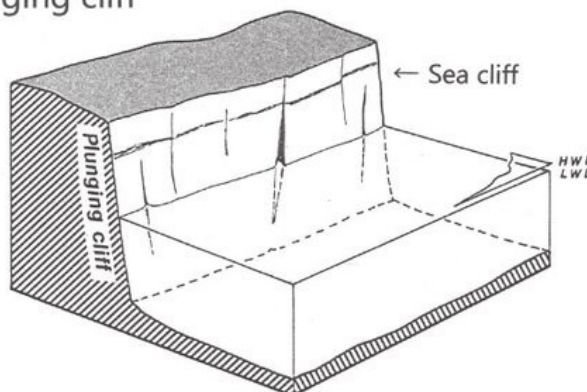


Figure 2: Rocky shores main morphologies: (a) Type-A shore platform, characterized by a sloping profile; (b) Type-B shore platform, featuring a horizontal or sub-horizontal configuration; and (c) plunging cliff (Sunamura T., 1992).

These various morphologies result from the interplay of different processes at different scale in time and space (Trenhaile et al., 2006). There is a feedback loop between hydrodynamic forcing (tide and waves), material response (substrate erosion) and the resulting morphologies that emerge over extended time scales (Ogawa et al., 2016).

Researchers have tried to quantify the connection between certain geological parameters and the rate of cliff erosion. According to Sunamura (Sunamura, 1982)(Eq. 1)

$$dx/dt \propto \ln(f_w/f_r) \quad \text{Eq. 1}$$

where dx/dt is the average rate of cliff erosion, f_w is the wave's assault force, and f_r is the rock's restraining force (Eq 2).

The formula:

$$\rho g H / S_c + C \quad \text{Eq.2}$$

may be used to express the ratio f_w/f_r , where g is the acceleration due to gravity, H is the height of the waves at the foot of the cliff, S_c is the compressive strength of the rock, and C is an arbitrary constant.

Sunamura (Sunamura, 1982; Sunamura T., 1992) provides the information on the lowest wave height (H_{crit}) capable of eroding the base of a cliff as (Eq. 3):

$$H_{crit} = (S_c / \rho g) e^{-\Gamma} \quad \text{Eq.3}$$

where with the symbol Γ is expressed $\ln(A/B)$ a nondimensional constant.

The value of A indicate the abrasive properties of beach sands, while B signify the kind and frequency of cliff's discontinuities.

Tsujimoto (Tsujimoto, 1987) utilizes the number A_p to represent the assailing force of the waves, where p is the wave pressure and A is a nondimensional constant representing abrasion and proposed to represent the resisting force of the rocks as BS_c^* , in which $S_c^* = S_c(V_{pf}/V_{pc})$, where V_{pf}/V_{pc} is the longitudinal ratio of sound wave velocity measured in the rocks in situ to that of cylindrical specimens without visible cracks, measured in the lab, B is a non-dimensional constant related to the effect of weathering.

Furthermore, Tsujimoto postulates that the change from horizontal to gently sloping shore platforms happens when wave-generated bottom shear stress reaches a level high enough to weaken the platform surface and destroy the low-tide cliff, as (Eq.4):

$$\tau_o > 0.005 S_s \quad \text{Eq.4}$$

where S_s is the shear strength, considering the impact of rock discontinuities, and τ_o is the wave-induced shear stress on the bed.

Tsujimoto's model may explain the presence of sloping and horizontal platforms in local regions but might not fully account for the predominance of sloping platforms in high-tidal range settings and sub-horizontal platforms in low-tidal range environments. In any event, wave quarrying at the water's edge rather than shear loads on the ground are considered the primary causes of wave erosion.

On rocky coasts, intense wave action manages to produce vertical or undercut cliff faces, while strong weathering encourages the growth of more smoothly sloping, convex slopes (Fig.3). Whether both process groups are active, with wave erosion dominating at the cliff foot and chemical action in the upper part, the cliff profile might be composed by a steep lower slope and a convex upper one. Plumb cliff profiles are typical in mid-latitudes where we have wave-dominated environments. Vice versa, convex profiles often occur in the humid tropics, due to the combination of strong chemical weathering, weak wave action and shielding bioactivity produces slopes that are enclosed in vegetation. Then, in tropics we can have the presence of steep cliffs with deep biologically eroded

notches develop in limestones. Instead, in high latitudes, the presence of ice prevents wave erosion, and steep slopes are mainly the product of glacial erosion (Trenhaile, 2012).

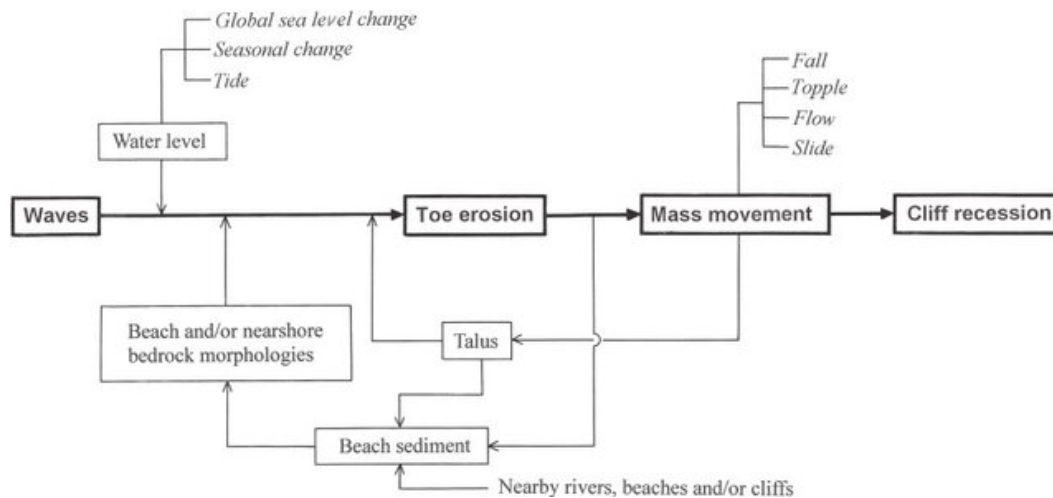


Figure 3: Combination of elements that affect sea cliff toe erosion. (Modified from Sunamura, 1992).

However, the classification of marine cliffs involves numerous special cases, related to different geological factors, which are as crucial as climate and wave regime in determining morphogenesis (Emery and Kuhn, 1982) (Fig.4). For instance, weaker material outcropping in the top part of a cliff can accelerate weathering and the leading to the creation of curved slopes. Meanwhile, tougher cap rocks can protect against weathering, preventing the growth of steep slopes. Additionally, the attitude or orientation of the bedding can influence cliff morphology (Emery and Kuhn, 1980; Trenhaile, 1987). Steep cliffs are usually associated with horizontally or vertically bedding strata, whereas cliff faces develop along bedding or joints in areas where the attitude of strata is seaward or landward. Cliffs can have composite profiles comprising of two or more major slope elements. Generally, cliffs are termed multi-storied when they consist of two or more steep faces separated by more gentle slopes. Another configuration is hog’s back cliffs, characterized by steep wave-cut faces at the bottom and convex or straight seaward-facing slopes above (Fleming, 1965; Orme, 1962). Typically, cliff profiles like this can form where marine and subaerial erosion act simultaneously; however, high composite cliffs in resistant rocks result from Quaternary changes in climate and sea level over extended periods (Hampton and Griggs, 2004).

Plunging cliffs directly descend into deep water without shore platforms or beaches at their base. This type of cliff usually forms in hard rocks with minimal erosion from marine dynamics. Furthermore, the absence of beach/sediment at the cliff foot prevents abrasion. Plunging cliffs are commonly outcropping around resistant coral reef shelters, basaltic islands, and areas where tectonic features provide continuous scarps (Trenhaile, 2012, 1987).

So, it’s evident how these slopes, distinct from inland ones, are subject to a different array of processes that act together with various interactions between them; we cannot consider one process disconnected from another.

For example, cliff erosion through instability generates a new talus, sediment input, (Komar and Shih, 1993) (Moses and Robinson, 2011) acting as a double-edged sword. On one hand, when debris is thick enough, it completely protects the cliff from erosive processes (Kennedy and Milkins, 2015). On the other hand, when sediment is fully mobilized by waves, it acts as an abrasive, increasing erosion rates of both the platform and the cliff at its rear (Kennedy and Milkins, 2015).

Even topography in the offing of the cliffs play a role (Sunamura, 1991; Robinson, 1980) in fact both the gradient and the roughness of shore platforms are expected to play key roles in driving nearshore dynamics through their effect on wave transformation processes, incident wave energy decay, wave setup, and infragravity wave generation (Poate et al., 2018) and yet the width of beach could play an important role. In fact, it has been noted that beach berms less than 20 meters in width offer only a minimal level of protection against wave attack. However, when the berm width is increased to between 20 and 30 meters, there is a significant decrease in seacliff retreat. The most effective level of protection is achieved with a berm that is at least 60 meters wide, which provides near-complete protection against wave attack (Everts, 1991).

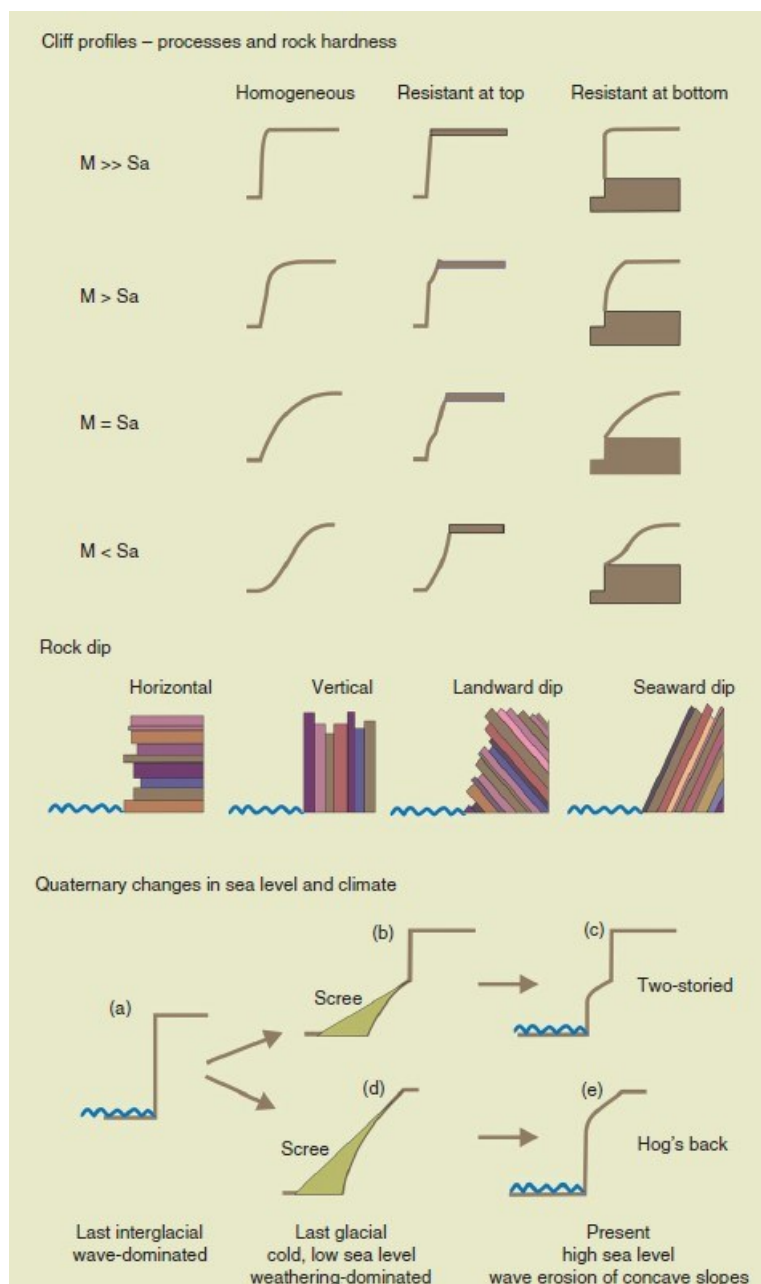


Figure 4: Factors affecting the sea cliff profiles' shapes. According to M and S_a , marine and subaerial processes, respectively, the impact of processes and rock hardness, and the impact of

Quaternary variations in sea level and climate, are represented. Two-story cliffs form where the last glacial stage's talus barely reached halfway up the cliff, whereas hog's-back cliffs formed where the scree reached the rock's peak (Emery and Kuhn, 1982; Trenhaile, 2012, 1987).

As mentioned earlier, waves contribute to the erosion of cliffs (Sunamura T., 1992). The primary physical mechanisms by which they carry out this action are essentially two: Wave quarrying and abrasion.

Quarrying stands out as a significant erosional process in various regions, evidenced by fresh rock scars and the presence of coarse, angular debris composed of jointed blocks and other rock fragments. The effects of high shock pressures, generated by breaking waves as they curl over and trap pockets of air against steep rock faces contribute to this process. However, perhaps most significant for a wide range of rock types is the compression of air trapped in joints, bedding planes, and other discontinuities.

The most productive quarrying occurs in a small zone from the peak of the wave to just below the still water level (Robinson, 1977a, 1977b; Trenhaile, 1987). Quarrying activities result from the alternating forces of air and water. According to wave pressure models, standing, breaking, and broken waves generate the strongest pressures at or just above the mean sea surface. Most erosion likely takes place at the sea's surface due to the surf and swash of broken waves, contingent on precise conditions, including the depth of water in proportion to the wave height. These conditions must exist for unbroken and breaking waves to have an effect on steep coastal slopes.

On rock beaches, there is often a scarcity of abrasive material, especially when fine-grained rock erosion results in suspended sediments that are moved offshore or when the resistant rocks erode too slowly to generate significant material. In such situations, any abrasives that do occur are typically confined to tiny pockets trapped at the foot of scarps, at the bottom of troughs and other topographic depressions, and to narrow zones near the cliff foot. At the base of cliffs and other steep slopes, undercut scarps are created by the back-and-forth movement of abrasive material beneath unbroken and broken waves.

The material can be moved by wave-generated shear stresses at any depth, although abrasion is often most effective at or near the ocean surface. Long-term abrasion rates also decrease with beach thickness due to the challenges in moving material at the bottom of thick deposits. Although some estimates go as high as 0.5 m, the majority of estimates for the greatest beach thickness under which abrasion may occur are less than roughly 0.25 m (Robinson, 1977a, 1977b; Trenhaile, 1997, 1987). Particles beneath heavy accumulations may only be moved by huge waves, but if the bottom is subjected to excessive shear stresses, abrasives may be lifted into suspension and come into less contact with the bedrock.

When a beach deposit is thin enough to be transported over the underlying bedrock, abrasion often occurs in a very limited zone that stretches from a small distance in front of the seaward edge up to a short distance under the beach. Abrasion zones spread (Trenhaile, 2009, 2005) landward through time as the cliffs retreated, even though the process is now only really active over a small region (Blanco-Chao et al., 2007).

There is an ongoing discussion related to the likelihood of tsunamis occurring along rock shores and their potential effects. Large stones, frequently imbricated in a seaward orientation, onshore platforms, coral reefs, and cliff tops have been the subject of much debate.

Some researchers have claimed that these boulders were eroded and deposited by tsunami action (Bryant, 2008; Bryant and Haslett, 2007; Kennedy et al., 2007; Noormets et al., 2002; Scheffers and Kellett, 2006, 2005), asserting that tsunamis were responsible for bedrock sculpturing on shore platforms (Aalto et al., 1999; Bryant, 2008; Bryant and Young, 1996).

However, distinguishing between tsunami deposits and other consequences of strong storms on rock beaches remains challenging. While deep ocean wave heights might suggest that storms historically couldn't erode, transport, and deposit extremely massive blocks high up on a coast, wave heights can significantly increase close to the shore due to shoaling processes and other considerations. Furthermore, big storm waves may compress air in joints, providing enough hydraulic lift to topple massive stones as well as lift and carry smaller boulders (Felton and Crook, 2003).

The distribution of wave energy within the intertidal zone is significantly influenced by tidal range and the type of tidal regime, whether diurnal, semi-diurnal, or mixed. The amount of time (in hours per year or as a percentage of time) that the sea surface spends at each intertidal elevation is represented by tidal duration distributions. The zone of greatest wave erosion subsequently occurs most frequently at or around the mean high and low water neap tidal levels. At the mid-tidal level, frequencies are around one-quarter to one-third lower, and they rapidly decline from the neap to the spring high and low tidal levels. In comparison to macrotidal environments, wave energy is more concentrated in the intertidal zone and occurs more often at each height (Trenhaile, 2012, 1987; Trenhaile et al., 2006; Trenhaile and Porter, 2020).

Although tidal levels typically fall within the mean neap tidal range, other factors such as weather, bottom gradient, water depths, and others all impact how wave energy is used in the intertidal and supratidal zones. During storms, when wind shear and other atmospheric factors elevate the ocean surface, the zones of highest wave-energy expenditure are raised above the tidal duration maxima at the neap high and low tidal levels. Water depth varies from location to location according to tidal range and over time during the tidal cycle, affecting the rate of wave attenuation (Trenhaile, 2012).

Weathering may play a significant, and in some cases dominant, factor in the formation of rock coastlines. Cliff recession often occurs in polar locations and on noncalcareous rocks in the wet tropics due to weathering and removal of debris by mass movement and modest wave action. These mechanisms also function well in protected sections in generally wave-dominated settings. Weathering along joints, bedding planes, and other discontinuities helps to prepare the rock for eventual dislodgment and removal by wave quarrying. On polar shores, this process may be augmented by frost action and grounding ice blocks on the shore platform (Hansom, 1983; Trenhaile, 1997).

Although the significance of weathering processes is well acknowledged, little effort has been made up, until recently, to pinpoint the causative mechanisms or gauge their rates of activity. A laser-scanning method has been utilized on several platforms in western Europe, although slow rates of surface downwearing have typically been measured during the past few decades using MEMs (J. O. H. Swantesson et al., 2006; Williams et al., 2000). While occasional occurrences at certain stations, such the loss of a small piece of surface rock, might result in rates as high as a few centimetres per year, the average rates of downwearing typically range from 0 to a few millimetres per year (Furlani and Cucchi, 2013; Gill and Lang, 1983; Kirk, 1977; Mottershead, 1989; Robinson, 1977b; Stephenson and Kirk, 2001; J. Swantesson et al., 2006; Trenhaile et al., 2006).

The causative processes must be deduced from the erosional data's geographical and temporal properties. Downwearing has often been attributed to weathering and subsequent removal of fine-grained debris by waves where there is a lack of abrasive material. This view has been confirmed by the observation, in certain regions, of quicker downwearing rates in summer, when waves are lower and temperatures are higher, than in winter, when waves are stronger and temperatures are lower (Mottershead, 1989; Robinson, 1977b).

One possible explanation for these apparently conflicting seasonal patterns is that the separation of weathered grains is often dependent on, or aided by, wave-generated turbulence. As a result, the seasonality of surface downwearing may be affected by the wave environment, the type of rock cement, and other factors that influence the strength of the bindings between rock grains. Downwearing may be performed in summer by weathering operating alone or with the help of weak,

seasonal waves in weak rocks or those that are particularly vulnerable to weathering. The detachment and removal of grains already loosened by summer weathering, or of grains in weather-resistant rocks, may be dependent on the heavier waves of fall and winter in more cohesive rocks (Trenhaile, 2012).

Surface downwearing on rock coastlines has typically been associated with alternating wetting and drying, salt crystallization, and other salt weathering processes in the intertidal and lower supratidal zones. Salt weathering occurs in rock capillaries through crystal formation and growth, crystal swelling through the absorption of water, and crystal expansion due to changes in temperature. Tidally induced wetting and drying result from cycles of expansion and contraction in the rock. Additionally, a few studies have noted cases of surface elevation or swelling that might reach several millimetres. These occurrences can last anywhere from a few months to many years and have typically been linked to salt crystallization-related expansion, while expansion brought on by wetting and drying may also have a minor impact (Kirk, 1977; Mottershead, 1989; Stephenson and Kirk, 2001).

In eastern Canada, experiments have been conducted in the lab over three years using tidal simulators to compare and distinguish the downwearing rates caused by salt weathering and wetting and drying on basalt, sandstone, and argillitic rocks (Kanyaya and Trenhaile, 2005; Trenhaile et al., 2006). A recent study (Porter and Trenhaile, 2007) highlighted that, at least within the elevational zone generally flooded twice a day by the tides, downwearing is caused by alternating wetting and drying rather than salt crystallization

On rock coastlines, chemical weathering is accelerated by alternating immersion and exposure in the intertidal zone and spray and splash in the supratidal zone. Coastal zones thus supply the water required for chemical reactions as well as the runoff required to remove the soluble products. Chemical weathering diminishes rock hardness, which is particularly critical at discontinuities and in hot, rainy climates where cliff retreat may be predominantly caused by the removal of fine-grained, weathered material by relatively weak waves (Trenhaile, 2012).

Tafoni and honeycombs can be produced by chemical and salt weathering, and they contribute significantly to water-layer levelling, a set of processes that operates around the edges of pools of standing water to lower, smooth, and level shore platform surfaces (Turner and Bartrum, 1928). Chemical weathering can cause hardening or strengthening of rock surfaces by evaporating saline solutions containing silica, iron, and other cementing agents or vice versa softening and breaking of rock.

The passage of dissolved ions along joint planes, which can deplete or saturate them with precipitates, causes frame weathering, which commonly happens in connection with water-layer levelling. If the impregnated joints become more resistant than the joint blocks, weathering pits with higher rims appear, but if the joints are weaker, small plateaus, sometimes resembling tiny volcanoes, can form.

In the intertidal and spray and splash zones, where the rocks can reach high degrees of saturation, coasts may offer nearly ideal conditions for efficient frost action (Trenhaile and Mercan, 1984). The salinity of saltwater and more concentrated solutions in rock pools may be particularly favourable to successful frost action since studies have shown that frost cycles result in the largest levels of rock breakup in solutions that contain 2-6% of their weight in salt (Trenhaile, 2012).

Frost and temperature-dependent wetting and drying processes are only successful in regions with the correct type of rocks and sufficient wave action to prevent the beach from progressively getting buried under debris."

Frost cycles are most common in chilly, storm wave settings, and mechanical wave erosion and frost action frequently work best on the same types of rock, especially if they are tightly jointed and thinly bedded. Therefore, the consequences of frost action in these regions may be obscured or inhibited by vigorous quarrying by waves or intertidally grounded ice, including the removal of joint blocks that have been weakened by frost (Trenhaile, 1987).

Biological activity as well as inanimate factors have an impact on coastal evolution.

The removal of rock by direct organic action is referred to as bioerosion. It comprises the work of boring organisms that use mechanical or chemical ways to drill holes into rocks and grazing organisms that scrape off the surface of rocks while feeding on the roots of epi- and endolithic microflora. The boring and grazing impacts of gastropods, barnacles, bivalve molluscs, sponges, echinoids, worms, and other marine fauna, as well as bioerosion by algae, particularly Cyanophyta and other microflora, have been widely reported in the literature (Spencer, 1988a, 1988b; Spencer and Viles, 2002; Trenhaile, 1987).

On protected coral, aeolianite, and other calcareous substrates in the tropics, where the collapse of deep, biologically eroded notches is a major contributor to cliff retreat (Trenhaile, 2012).

Although there is a lot of information on bioerosional rates, there is a lot of variety in their accuracy and usefulness. When analyzing the data, it is important to take into account the kind of organism; grazers work across greater areas than borers, while their work is concentrated in a smaller area (Trenhaile, 2012).

Sharp ridges, pinnacles, grooves, and circular basins in the spray and splash zones of limestone beaches have historically been attributed to chemical solution, especially since they resemble karren created by freshwater on land. Surface seawater is normally saturated or supersaturated with calcium carbonate, but faunal respiration in pools produces carbon dioxide that is not removed by algal respiration at night, lowering the pH and causing calcium carbonate to be transformed into more soluble bicarbonate (Trenhaile, 2012).

Anyway, there is rising evidence to support the idea that marine karren and other distinctive characteristics of limestone beaches are largely bioerosional in origin, despite the possibility of chemical solution occurring in saltwater (Schneider and Sadler, 1976; Spencer, 1988a; Trudgill, 1987).

Until now, we have focused mostly on one component of the rocky shore, the cliff, but there are different morphologies typical of this environment that we will now discuss.

Crenulated coastlines, which consist of a series of headlands and bays, typically reflect variations in the resistance of the rock to erosion, in some cases due to lithological differences caused by faulting or folding, and in others due to the influence of rock structure, such as differences in joint density, orientation of discontinuities, and thickness, strike, and dip of the bedding. Bays and headlands can also form in practically homogenous rocks as a result of the lower cliffs around stream outlets retreating faster than the higher cliffs on nearby interflaves, and the Holocene submergence of valley mouths (Trenhaile, 1987).

Beaches in rocks with varying resistance to erosion may ultimately reach an equilibrium that restricts their degree of irregularity. This would happen if fewer refracted waves eroded the more resistant rocks on exposed headlands at the same rate as more refracted waves eroded the weaker rocks in the bays, keeping the plan form as the coast retreated landward over time. Unfortunately, due to the episodic nature of cliff retreat and a lack of good long-term records, it is now hard to assess whether rock coast plan forms are still developing (Trenhaile, 2012).

In rocks strong enough to support high, nearly vertical slopes as well as in the roofs of caves, tunnels, and arches, erosion along well-defined and well-spaced planes of weakness can produce a variety of coves, narrow inlets, blowholes, caves, arches, stacks, and related features. Long tunnels, caverns,

and inlets can also form as a result of the sea crashing into underground karstic systems or lava tunnels in volcanic rocks (Shepard and Kuhn, 1983; Trenhaile, 1987; Trenhaile et al., 1998).

Another element of important relevance in rocky coast is the shore platform.

Platforms have historically been divided into two categories within larger geographic areas: sub-horizontal surfaces that suddenly end in a low-tide cliff or generally gently sloping surfaces that stretch below the low-tidal level without a significant break in slope (Sunamura T., 1992; Trenhaile, 2012).

Some researcher argued that horizontal platforms develop at a level of permanent seawater saturation as weak, weathered material is washed away by weak waves in sheltered areas or eroded by waves in more exposed areas (Bartrum, 1916; Edwards, 1958). Some workers claimed that horizontal platforms are cut by waves (Bartrum, 1926; Cotton, 1963; Edwards, 1951). But research over the last several decades has demonstrated that the mean regional platform gradient and tidal range have a reasonably substantial association (Trenhaile, 1999, 1997, 1987).

While it is still debatable whether weathering can construct broad shore platforms on its own, it is now widely acknowledged that shore platforms are produced by the combined effects of waves and weathering. The relative and absolute significance of these processes varies geographically in response to changes in the substratum's characteristics and morphogenetic causes, as well as momentarily in response to variations in climate, sea level, and intertidal and subtidal morphology (Trenhaile, 2012). Where waves, surf, and swash can impact upstanding irregularities, such as in horizontally bedded rocks with seaward-facing scarps, and in steeply dipping strata in which differences in rock resistance generate uneven corrugated platform surfaces with upstanding beds of resistant strata, wave quarrying is most effective. Mechanical wave erosion is substantially less effective in the absence of abrasive material on platforms with generally smooth profiles and few apparent abnormalities, especially if they have low slopes and low-tide cliffs that force waves to break at the seaward edge. As previously stated, sub-horizontal platforms in certain regions may have been carved by waves in the early to mid-Holocene, when sea level was higher than now. Weathering now commonly dominates these surfaces, especially if they are composed of argillaceous and other weathering-susceptible rocks. As wave-dominated platforms expand broader over time, their gradient diminishes, resulting in increased wave attenuation, waves breaking further from shore, and more energy dissipation in wider, turbulent surf zones. Consequently, weathering must grow increasingly prominent over time, although the relatively large equilibrium gradients of shore platforms in macrotidal settings may allow waves to remain the primary erosional agent (Trenhaile, 2001).

Many researchers have attempted to simulate the long-term evolution of slowly shifting rock coast (Horikawa and Sunamura, 1970; Scheidegger, 2012; Sunamura, 1982, 1978a, 1978b, 1973; Trenhaile, 2003). The qualitative models of the early twentieth century were supplanted in the latter half of the century by very basic mathematical models that took just a few factors into account. These models were built on the premise that most erosion occurs at the water's surface or by underwater mechanisms in a tideless sea (Fleming, 1965; Horikawa and Sunamura, 1967), more recently including tidal duration distributions (Trenhaile, 2000).

Recently, Trenhaile (2009) developed a model that considers mechanical wave erosion at the water surface on bare cliff and shore platform surfaces, as well as the abrasive and protective role of beach material, depending on the thickness of the deposits and the ability of the waves to move them.

One of the most difficult issues for rock coast workers is determining whether they have been inherited from interglacial phases when sea level and temperature were comparable to today's, and from glacial stages when circumstances were very different. During the Quaternary, rock coasts were subjected to changes in the focus of wave attack and other marine processes, as well as climatically

induced changes in storm frequency and intensity, weathering processes and efficacy, and tidal range, which determined the extent of the marine and subaerial domains (Trenhaile, 2012).

Deep-sea cores regarding paleo-sea level records (Bintanja et al., 2005) suggest that wave attack during warmer interglacials periods, when sea levels were similar to today, occurred more frequently on temperate coasts. In contrast, during cold glacial stages when sea levels were much lower than today, frost shattering and periglacial mass movements were more prominent.

The impact of mechanical wave erosion may have been particularly effective during the transitions from glacial to nonglacial conditions, when the rising sea was able to operate on inherited platforms and cliffs that had been severely weakened by the effects of frost during the previous glacial stages. Frost-riven clasts may also have provided an abundant supply of abrasive material at those times (Blanco-Chao et al., 2007).

Although rock coastlines are often very difficult to date, there is frequently qualitative evidence suggesting that some of them are quite ancient. For instance, shore platforms frequently appear to be too large and to be expanding too slowly to be attributed to the few thousand years since the water reached its current level. These shore platforms are found in strong, resistant rocks. These platforms usually have historic composite or hog's-back cliffs, glacial or periglacial deposits, emerging beaches, and erosional ledges as their backs. According to studies (Brooke et al., 1994; Stone et al., 1996; Young and Bryant, 1993), resistant rocky coasts contain some inherited shore platforms and other coastal features.

Modelling reveals that inheritance may be crucial to the evolution of the coastline. The impact of sea level variations over the past 2 million years on the formation of rock coasts was examined by Trenhaile (2001a). Most modelled platforms were, at least in part, take over from one or more interglacial periods when sea level was comparable to that now. The effectiveness of wave erosion determined whether the present beach platform was totally contemporaneous, modified from an inherited surface, or altogether new. The findings indicated that shore platforms' over-steepening and truncation during glacial phases result in their alteration over the following interglacials, which is mostly done by erosion at the high-tidal level, unless platforms are in a condition of perfect static equilibrium.

Another important issue to address in modelling is sea level rising. Between 1961 and 2003, sea level rose globally at an average rate of 1.8 ± 0.5 mm per year, and from 1993 to 2007, the pace climbed to 3.41 mm per year (Beckley et al., 2007). According to various climate change scenarios, the sea level would increase between 0.5 and 1 m in the twenty-first century, according to the Sixth Assessment Report of the Intergovernmental Panel on Climatic Change of the United Nations (Pörtner et al., 2022). The sea level, however, may be 0.5–1.6 m higher than it is now by 2100, according to recent estimates on the rapid melting of Greenland and Antarctica ice (Hanna et al., 2008; Pritchard and Vaughan, 2007).

It is commonly accepted that as sea levels rise, rocky coasts will erode more quickly, in part because deeper water would slow the attenuation of waves. Rock beaches will also be affected by global warming and sea level rise due to changes in tidal range, wave refraction patterns, biological processes, precipitation, and, probably most significantly, an increase in storm frequency and severity.

According to a clay coast model, erosion rates will grow as sea levels rise. Because this will have an impact on how long waves will assault each elevation, the gradient of equilibrium profiles will also rise as sea levels rise (Dickson et al., 2007; Walkden and Dickson, 2008).

2.2 Remote sensing

The ability to capture and handle massive datasets has resulted in a modernized approach to geosciences during the last two decades, owing to the outstanding advancement of geospatial technology such as Differential Global Positioning Systems (DGPS) and robotic equipment.

Remote sensing techniques can be defined as passive or active, depending on the subject of research (Schowengerdt, 2006) (Fig.5).

Passive techniques such as satellite imaging, photography, and infrared thermography capture data by utilizing natural radiation (such as sunlight) emitted or reflected by an object (Zhang et al., 2020).

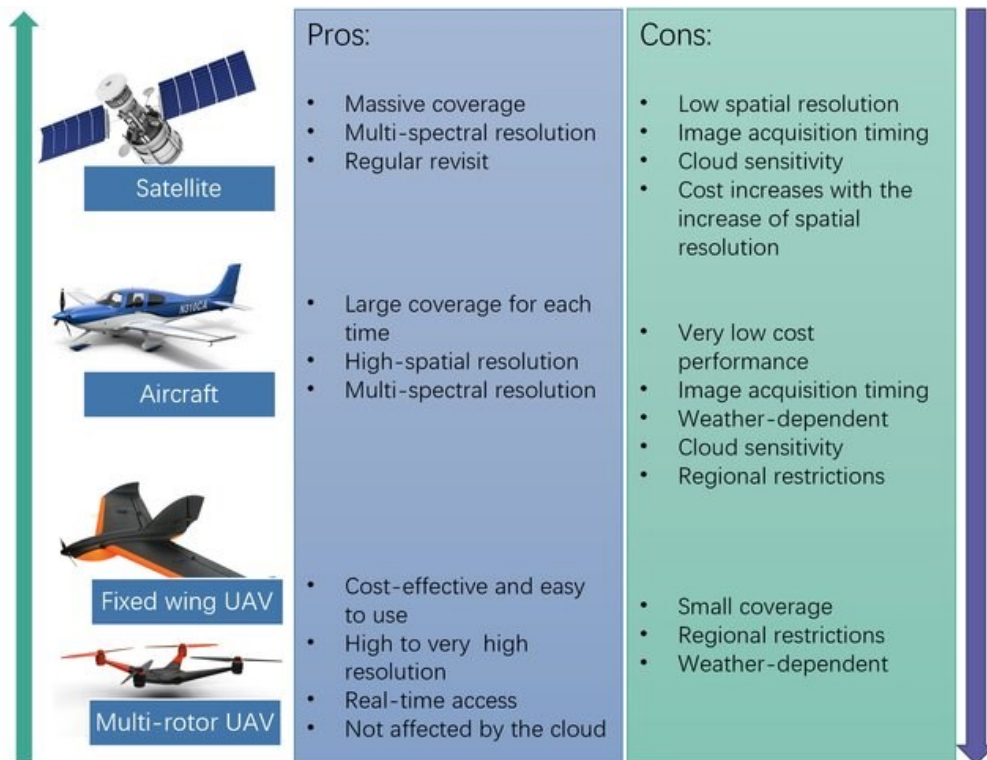


Figure 5: Pros and cons of the existing remote-sensing technologies (Zhang et al., 2020).

Active techniques, on the contrary, such as LiDAR (Light Detection And Ranging) or Radar, deliver an impulse that strikes the target and is measured by the instrument after being reflected. In terms of rock slope studies, while remote sensing techniques can overcome various concerns commonly encountered during field surveys, the huge variety of accessible technologies might be intimidating. According to Derron et al. (2013), the most crucial stage in selecting the proper methodology is understanding the benefits and limits of each method. Petrie and Toth (2018) attempt to resolve these ambiguities by comparing the two most commonly used technologies for rock slope assessment, laser scanning and photogrammetry (Fig.6). Furthermore, the characteristics of the investigated area (e.g., extension, morphology, meteorological conditions), the goals of the surveys (e.g., needed resolution, accuracy, ease of reproducibility), time availability, and budget should all be taken into account in order to find the best solution.

Photogrammetric Weaknesses, Contrasted with LiDAR Strengths	
LiDAR Pros	Photogrammetric Cons
Dense information along homogeneous surfaces	Almost no positional information along homogeneous surfaces
Day or night data collection	Day time data collection only
Direct acquisition of 3D coordinates	Complicated and sometimes unreliable matching procedures
The vertical accuracy is better than the planimetric accuracy	The vertical accuracy is worse than the planimetric accuracy

LiDAR Weaknesses, Contrasted with Photogrammetric Strengths	
Photogrammetric Pros	LiDAR Cons
High redundancy	No inherent redundancy
Rich in semantic information	Positional information; difficult to derive semantic information
Dense positional information along object space break lines	Almost no positional information along break lines
The planimetric accuracy is better than the vertical accuracy	The planimetric accuracy is worse than the vertical accuracy

Figure 6: *Advantages and limitations of photogrammetry and laser scanning techniques* (Petrie and Toth (2018)).

2.2.1 Orthophotos

Orthophotography, developed in the 1960s (Smith, 1995), was costly and time-consuming to create. By the early 1970s (Lin et al., 2021), technical advancements had made this data source inexpensive for commercial purposes, and its use convenient. Computer-driven optical technologies and equipment were used to create the first orthophotography. Today, computer workstations and sophisticated computer software algorithms have mostly supplanted these pieces of equipment (Smith, 1995). This method produces a digital image that may stand on its own aesthetic merits or be incorporated and used inside a geographic information system (Wiesel, 1985).

Orthophoto imagery provides the benefits of a regular map product, but unlike a standard map, the orthophoto may depict actual ground characteristics rather than cartographic renderings of such elements (Wiesel, 1985). Until around 1990, the orthophoto was made by combining optical and computer processing. Because of the rising availability of more powerful computers at lower rates, the digital orthophotograph has become a commercial production reality. To create the orthophoto, four fundamental procedures or adjustments must be made to the conventional vertical aerial image, regardless of the technique of fabrication (Lin et al., 2021; Rau et al., 2002; Wiesel, 1985) (Fig.7).

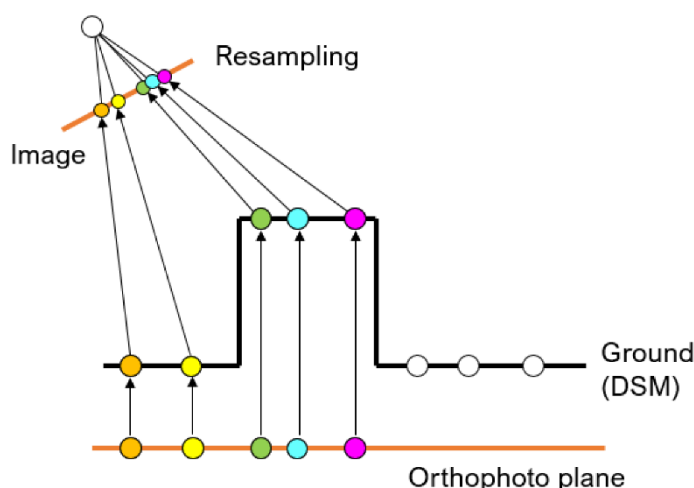


Figure 7: Scheme of the indirect approach for orthophoto generation (Lin et al., 2021).

The initial modification is to standardize the image's scale. The second adjustment entails eliminating the relief displacement in order to reposition the terrain in its right location. The third process involves assigning X and Y coordinate values to the picture. The final job is to make radiometric or tonal modifications to the image so that it blends with nearby photos. Understanding orthophoto imagery requires first knowing the geometric features of conventional vertical aerial photography, which is the source of all orthophoto images (Smith, 1995; Wiesel, 1985).

Traditional aerial mapping photography is shot vertically with highly sophisticated cameras and lenses. These cameras, mounted on gyro stabilized mounts, are directed straight down at the earth's surface and record their pictures in flight lines. Within the flight path, each subsequent shot overlaps the preceding image frame by 60% to 80%. The overlap region between the two succeeding frames enables stereo (3-D) viewing of the common area as well as the following gathering of the digital elevation model (DEM). Additional flight lines are flown with between 20% and 30% duplication (sidelap) between flight lines when more than one flight line is necessary to cover the geographic region of interest (Rau et al., 2002; Smith, 1995).

The scale of this imagery will change across the photograph in accordance with the camera's height above the ground. Using the photo's center as a reference point, landscape at a lower height (far from the camera) will be depicted at a smaller size, while territory at a higher elevation will be photographed at a bigger scale.

The image's spatial precision is altered by a distortion known as relief displacement. Simply said, locations that are higher than the nadir are moved away from the center of the image, and locations that are lower in elevation are moved toward the center of the image instead of away from it. Since the terrain's relief displacement is eliminated throughout the orthophoto processing, the hills and valleys will be shown in their actual locations. So, the top and bottom of the objects are located at the same X and Y coordinates on the ground, relief displacement of flagpoles, buildings, trees, and other characteristics of a similar kind will stay on the image. Particularly at the connection between orthophoto sheets, this phenomenon of relief displacement might result in various visual distortions or illusions (Baltsavias, 1996).

2.2.2 LiDAR technique

Laser scanners make it possible to quickly and accurately capture 3-D data across wide regions. Even though laser scanners were created in the 1960s, direct georeferencing technologies and computer technology advancements in the mid-1990s were fundamental to the successful development of this technology (Petrie and Toth, 2018). The earliest laser scanners used for slope assessments were installed on aerial platforms; later, ground-based laser scanners were developed (Heritage and Large, 2009).

LiDAR surveys are conducted using equipment that uses the Light Amplification by Stimulated Emission of Radiation (LASER) technology to estimate distances with a high degree of accuracy. Laser scanners are optical devices made up of a scanning mechanism and a highly collimated, directional, coherent, and in-phase transmitter/receiver of electromagnetic radiation. Laser scanners are divided into two categories: airborne laser scanners (ALS) and terrestrial laser scanners (TLS), depending on where the device is used (Jaboyedoff et al., 2012b).

According to Baltsavias (1999), the formers are commonly employed to scan wide regions with decimetrical accuracy and precision. As a result, ALS techniques are used to map regional structures (Humair et al., 2013; Loye et al., 2012; Matasci et al., 2011), obtain Digital Elevation Models (DEMs) for small-scale landslide modelling and susceptibility assessment (Chigira et al., 2004; Haneberg et al., 2009; Michoud et al., 2015). TLS systems, on the other hand, operate on static positions and frequently capture many scans from various places to get an overall picture of the region under investigation, although they may be constrained by topographic features (Lato et al., 2015).

Given that they may be positioned within reasonable distances from the target, ground-based laser scanners are advised for sub-vertical or overhanging slopes that are not suitable for ALS approaches (Bremer and Sass, 2012; Oppikofer et al., 2009; Stock et al., 2011).

Distance or range measurement can be accomplished using one of two approaches for both techniques:

Time of Flight (TOF): the laser scanner emits a very brief and powerful pulse of radiation that is reflected back to the instrument (Fig.8). The time it takes for the pulse released at point A to strike the item at position B and return to the laser scanner allows us to calculate the distance using the following formula (Eq.5):

$$R = vt/2 \quad \text{Eq.5}$$

where t is the recorded time interval, v is the electro-magnetic radiation's (or light's) speed, and R is the distance between the sensor and the object.

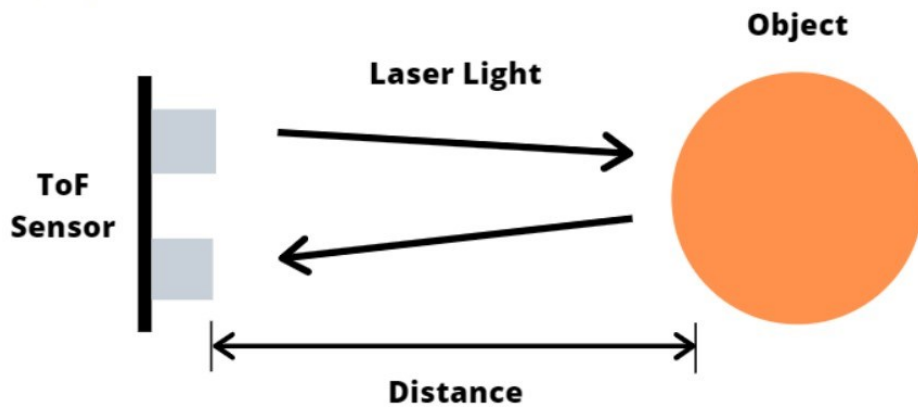


Figure 8: Range measurement using Time Of Flight laser scanner (<https://www.seeedstudio.com/blog/2020/01/08/what-is-a-time-of-flight-sensor-and-how-does-a-tof-sensor-work/>).

Phase pulse: instead of a pulse, the laser scanner generates a continuous stream of laser energy (Fig.9). The phase difference between the transmitted and received sinusoidal waves of the beam is used to calculate the object's distance (Eq.6).

$$R = M\lambda + \Delta\lambda / 2 \quad \text{Eq.6}$$

where M is the integer number of wavelengths, λ is the known value of the wavelength and $\Delta\lambda$ is the fractional part of the wavelength ($=\phi/2\pi$, with ϕ being the phase angle).

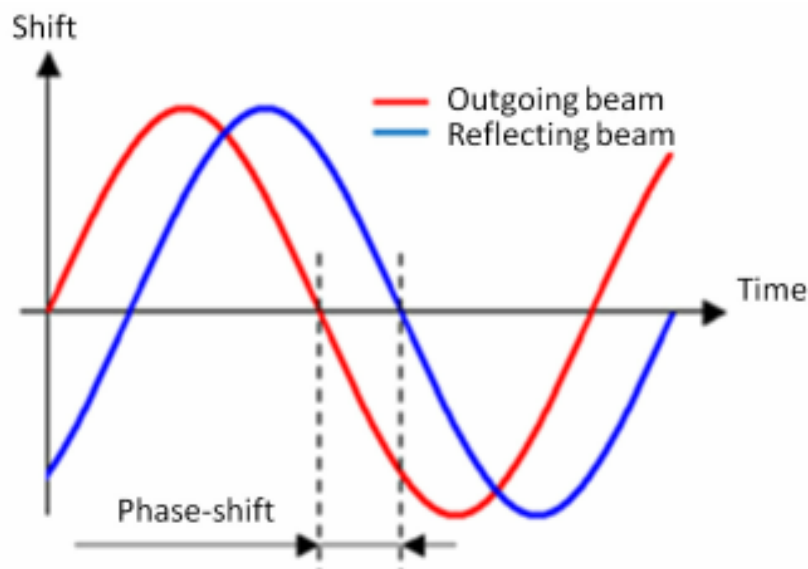


Figure 9: Range measurements by means of phase-based laser scanner (Mill et al., 2023)

Phase-based laser scanners offer more precise distance measurements but are restricted to small ranges, typically up to 100 m (Petrie and Toth, 2018). Because of this, these methods are only appropriate in certain contexts, such as displacement monitoring, whereas TOF methods, which enable the measurement of greater distances, are commonly employed for observations of the Earth's

surface (Wehr and Lohr, 1999). Ground-based laser scanners move in the azimuth direction to measure a sequence of elevation profiles (a line of closely spaced points) all the way around the device's vertical axis. In contrast, airborne systems use profile measurements in a direction perpendicular to the flight line to scan the target region.

Due to the divergence effect, the scanned area grows as the distance between the device and the item increases and is equal to the laser beam directed into the target object (Petrie and Toth, 2018). It is feasible to estimate the location x , y , and z of the target object with respect to the instrument by knowing the origin of the laser beam (LOS, Line Of Sight), as well as the attitude of the device (Jaboyedoff et al., 2012b). In reality, GPS devices are furthermore employed during surveys to precisely specify attitude and position of the laser scanner and to sequentially georeferenced the obtained data in a global coordinate system if they are not built into the laser scanners themselves.

The location and elevation of thousands of points that make up a 3-D representation of the scanned object, also known as a LiDAR point cloud, are provided by both techniques.

In addition to revealing the location of the scanned item, laser rangefinders reveal its reflectivity, which is determined by dividing the radiation incident on a surface by the radiation that surface reflects. Diffuse reflectivity scatters into a hemispherical pattern on "hard surfaces" like rocks and buildings, with the highest intensity perpendicular to the target (Fig. 10). The wavelength of the device's emission, the distance between the laser rangefinder and the target, the roughness and humidity of the target region, as well as the laser beam's incidence angle, all have an impact on reflectivity (Carrea et al., 2016; Jaboyedoff et al., 2012a; Lato et al., 2013; Petrie and Toth, 2018).

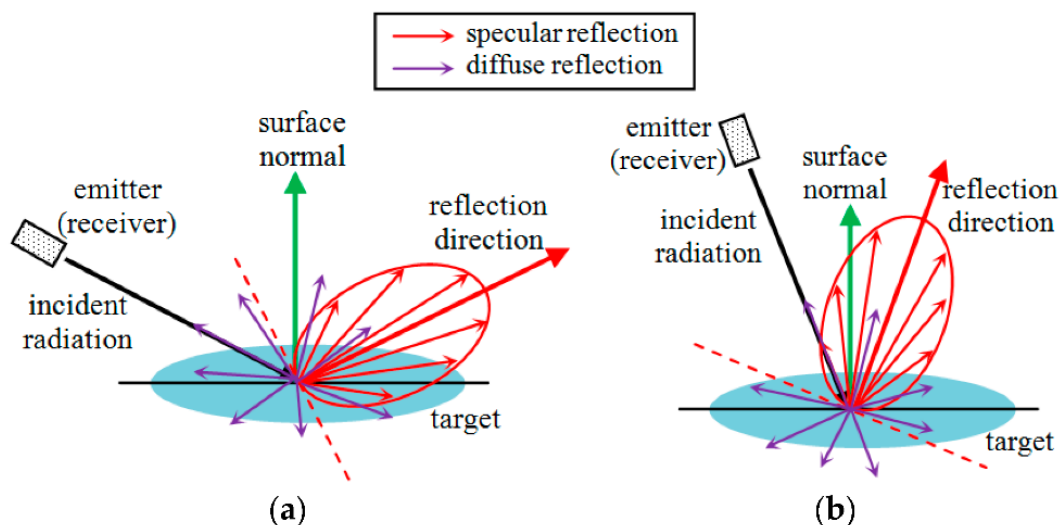


Figure 10: (a) At incidence angles larger than 45° , only diffuse reflections reach the receiver. (b) At incidence angles smaller than 45° , both diffuse and specular reflections can be received. The red dotted lines are perpendicular to the reflection directions (Tan and Cheng, 2017).

The capacity to identify small objects in a point cloud, or the amount of detail that can be viewed inside a point cloud, is generally referred to as laser scanner resolution (Pesci et al., 2011). Resolution is generally regarded as the inverse of point spacing, which is affected by survey parameters such as laser scanner-target distance and angular separation between adjacent scanlines (Jaboyedoff et al., 2012a). Furthermore, the dimension of the laser footprint influences the effective resolution: a larger diameter results in greater point spacing and, as a result, a smaller resolution (Abellán et al., 2014).

The term "accuracy" is used in a more precise context to denote the measurement's intrinsic range of error, or how closely a range measurement corresponds to the real distance (Abellán et al., 2014). Range accuracy and angular accuracy are the two categories (Jaboyedoff et al., 2012a; Kamerman,

1993; Lichti, 2007). The capacity of a laser scanner to resolve two items on the same line of sight is referred to as range accuracy, whereas the ability to resolve two things on neighbouring lines of sight is referred to as angular accuracy. Accuracy of laser scanners reduces with increasing range, surface roughness, and angle of incidence, as well as with temperature, humidity, and interfering radiation from lamps and the sun (Abellán et al., 2009; Boehler et al., 2003; Ingensand, 2006; Lichti, 2007; Voegtle et al., 2008).

While early laser scanners could offer accuracy of between 5 and 15 centimeters for airborne systems (Habib, 2017) and between 1.5 and 2 centimeters for ground-based systems at a distance of 300 meters (Jaboyedoff et al., 2012b; Oppikofer et al., 2009), newer generation technologies now enable reaching, respectively, a few centimeters and a few millimeters (Jaboyedoff et al., 2012a).

2.2.3 Structure from Motion (SfM) and Unmanned Aerial Vehicles (UAV)

Structure from Motion (SfM) is the technique for applying photogrammetry to moving objects using terrestrial, unmanned aerial vehicles (UAV), or aircraft platforms. It was first developed for multimedia applications (Beardsley et al., 1997; Koenderink and Van Doorn, 1991; Shashua, 1994). The ability to generate high-quality point clouds of landforms at various scales for a relatively low price makes SfM, which was only recently introduced to the Earth Sciences, increasingly popular (Anderson et al., 2019; Carrivick et al., 2016; Eltner et al., 2016; Remondino and El-Hakim, 2006; Westoby et al., 2012).

By using triangulation techniques, traditional photogrammetric techniques enabled the reconstruction of 3-D scenes from pictures obtained by compact and single lens reflex (SLR) cameras. However, the exact placement and attitude of the camera had to be known in advance. Alternately, the camera positions might be established using the precise locations of control points on the surveyed area (resectioning process). Early 1990s advancements in computer vision (Boufama et al., 1993; Spetsakis and Aloimonos, 1991; Szeliski and Kang, 1994) and the development of feature-matching algorithms (Förstner, 1986; Harris et al., 1988) resulted in the introduction of techniques that could automatically solve the geometry of the scene, camera positions, and orientations without the need to know the locations of the control points (Lucieer et al., 2014; Turner et al., 2012; Westoby et al., 2012).

As a result, SfM approaches employ highly redundant, iterative bundle adjustment processes (Snavely et al., 2008) to estimate the positions of various features by overlaying the photos taken by a moving sensor.

The generated point clouds are situated in a relative "image-space" coordinate system because the SfM approach does not need the use of points with known coordinates that are part of the real scene (Fonstad et al., 2013; James and Robson, 2014; Turner et al., 2012; Westoby et al., 2012). Contrary to the conventional photogrammetric approaches, the produced point cloud or polygonal surface will not be georeferenced and scaled (Carrivick et al., 2016; Clapuyt et al., 2016; Favalli et al., 2012). With the use of Ground Control Points (GCPs) with known coordinates, roto-translation matrices may be applied to the point cloud to orient and scale the model into an absolute coordinate system.

Today, a variety of commercial software programs, such as Agisoft Metashape (<https://www.agisoft.com/>), Pix4D (<https://www.pix4d.com/>), and Zephyr (<https://www.3dflow.net/it/software-di-fotogrammetria-3df-zephyr/>), are available to conduct the SfM approach on images captured by handheld cameras or more sophisticated UAV systems using normal desktop computers. Despite the possibility of certain commands changing, the procedure generally follows this main pattern:

- Image acquisition
- Keypoints detection and matching
- Collinearity, bundle adjustment and sparse point cloud
- Absolute registration
- Dense 3D reconstruction
- Polygonal surface and orthophotos

The gathering of pictures with adequate overlap (preferably 80-90%) and from multiple locations and/or perspectives is the initial stage in obtaining a 3-D reconstruction of the object (James and Robson, 2012; Lucieer et al., 2014). Ground-based systems are ideal for investigating large-scale and steep areas, whereas aerial platforms are more appropriate for collecting data on vast and low-relief zones (Westoby et al., 2012).

Beginning with image matching, which identifies similar features in several photographs, the captured pictures are processed. These characteristics, known as keypoints, might take the form of points, edges, or distinctive patterns (Bay et al., 2008; Calonder et al., 2010; Lowe, 2004; Strecha et al., 2011), and they need to be resistant to changes in scale, orientation, and lighting conditions (Carrivick et al., 2016). By using certain algorithms as the Scale Invariant Feature Transform (SIFT) presented by Snavely (2008) or the Random Sample Consensus (RANSAC) by Fischler and Bolles (1981), the keypoints are automatically retrieved and matched in each picture (Fig.11).

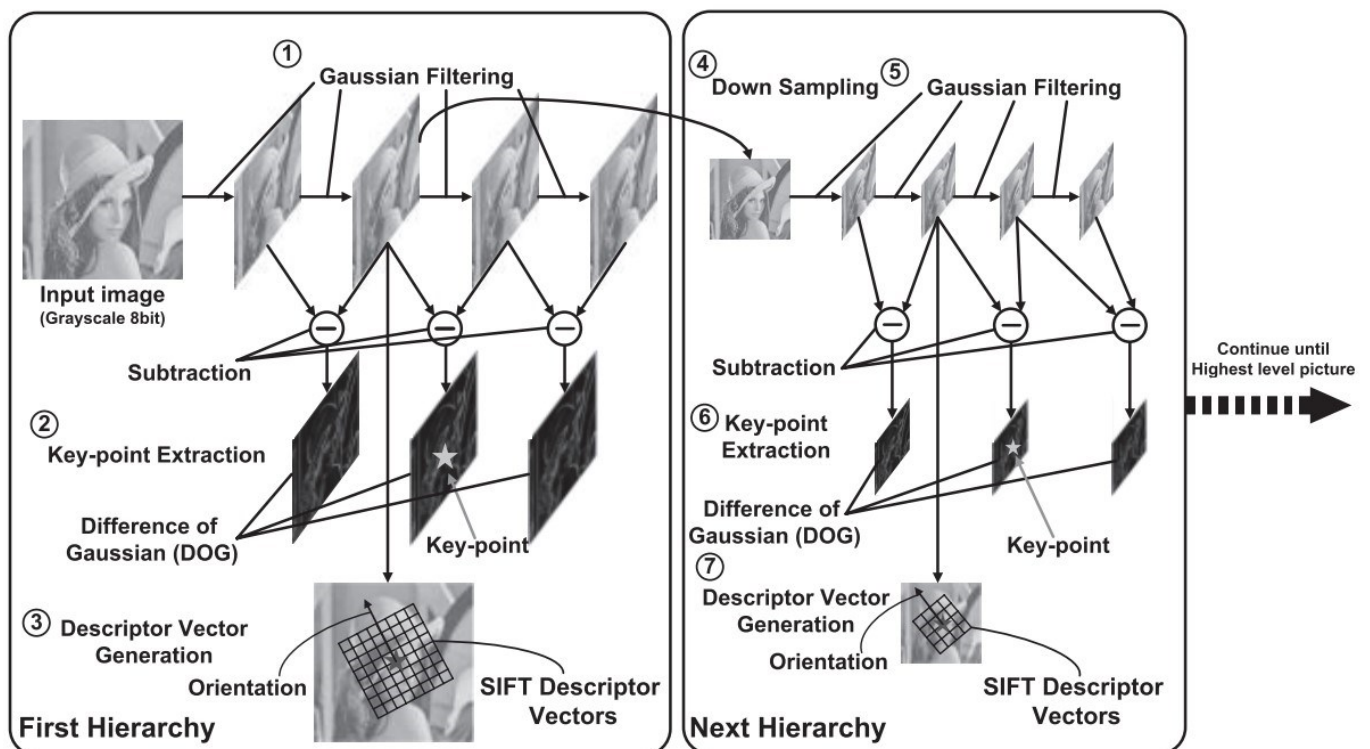


Figure 11: Original SIFT algorithm flow (Mizuno et al., 2011).

To eliminate disturbances like items moving on the scene during the surveys, the pathways between particular keypoints are connected before the 3-D reconstruction starts (Snavely et al., 2008). Despite the fact that keypoints on moving objects may be recognized in many photographs, the distances between the keypoints and other characteristics are continually varying, making it possible to filter out the disturbance using visibility and regularization restrictions (Furukawa and Ponce, 2006).

In order to retain collinearity, a 3-D scene is recreated from a pair of 2-D images using a set of equations (Fonstad et al., 2013; Liu et al., 2006; Roncella et al., 2011). The camera optic center, a point belonging to the surveyed item, and its representation in an image are all determined to be aligned along a straight line by the collinearity equation (Fig.12).

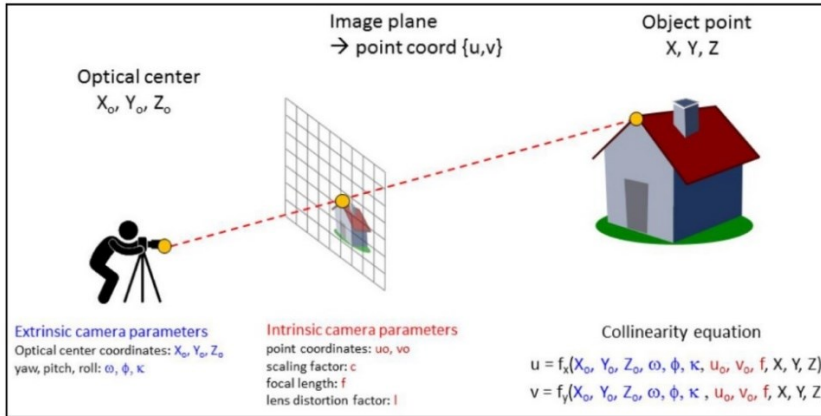


Figure 12: Sketch showing the relationships between the extrinsic and intrinsic camera parameters, the collinearity equations and the projection line (Loiotine, 2022).

One of the major goals of photogrammetry is to create a 3-D scene by translating the coordinates of a point in an image (measured in pixels) into geographic coordinates. The extrinsic and intrinsic camera parameters must be known for this purpose. The optic center coordinates (X_0, Y_0, Z_0) and the instrument's orientation (yaw, pitch, roll) are the extrinsic camera parameters. The (u, v) coordinates of the point in the picture, scaling factor k , focal length f , and lens distortion factor l make up the intrinsic camera parameters. According to the collinearity equation (Mikhail et al., 2001), the coordinates of the point in the picture are expressed as a function of the geographic coordinates of the same point (Eq.7).

$$\begin{cases} u = fx(X_0, Y_0, Z_0, \omega, \phi, \kappa, u_0, v_0, f, X, Y, Z) \\ v = fy(X_0, Y_0, Z_0, \omega, \phi, \kappa, u_0, v_0, f, X, Y, Z) \end{cases} \quad \text{Eq.7}$$

The collinearity equation can be expressed in matrix form as (Eq.8):

$$\begin{bmatrix} u - u_0 \\ v - v_0 \\ f \end{bmatrix} = kM \begin{bmatrix} X - X_0 \\ Y - Y_0 \\ Z - Z_0 \end{bmatrix} \quad \text{Eq.8}$$

where k and M , respectively, are the rotation matrix and scaling factor that account for the camera's orientation. This is the rotation matrix in more detail (Eq.9):

$$M = \begin{bmatrix} \cos\Phi\cos\kappa & \cos\omega\sin\kappa + \sin\omega\sin\Phi\cos\kappa & \sin\omega\sin\kappa - \cos\omega\sin\Phi\cos\kappa \\ -\cos\Phi\sin\kappa & \cos\omega\cos\kappa - \sin\omega\sin\Phi\sin\kappa & \sin\omega\cos\kappa + \cos\omega\sin\Phi\sin\kappa \\ \sin\Phi & \sin\omega\cos\Phi & \cos\omega\cos\Phi \end{bmatrix} = \begin{bmatrix} m_{11} & m_{12} & m_{13} \\ m_{21} & m_{22} & m_{23} \\ m_{31} & m_{32} & m_{33} \end{bmatrix} \quad \text{Eq.9}$$

The following relationships are then achieved from the previous equations (Eq.10):

$$\begin{cases} u - u_0 = -f \frac{m_{11}(X-X_0)+m_{12}(Y-Y_0)+m_{13}(Z-Z_0)}{m_{31}(X-X_0)+m_{32}(Y-Y_0)+m_{33}(Z-Z_0)} \\ v - v_0 = -f \frac{m_{21}(X-X_0)+m_{22}(Y-Y_0)+m_{23}(Z-Z_0)}{m_{31}(X-X_0)+m_{32}(Y-Y_0)+m_{33}(Z-Z_0)} \end{cases} \quad \text{Eq.10}$$

Because there are fewer equations than there are X, Y, and Z unknowns, the issue is still unsolved. Additionally, there will be 2 additional equations and 3 additional unknowns for each additional point in the picture under analysis. With the help of multiple views and the Structure from Motion technique, it is possible to solve the issue and determine the target point's three-dimensional coordinates. If additional images of the same point are examined, the three unknown coordinates will remain the same, but the number of equations will rise (two additional equations will be provided for each image). By analysing all key points, a 3-D scene will be able to be created since the number of equations will significantly outnumber the number of unknowns (Fig. 13, Eq. 11).

$$N_p = \frac{6NV+3}{3NV-3} \quad \text{Eq. 11}$$

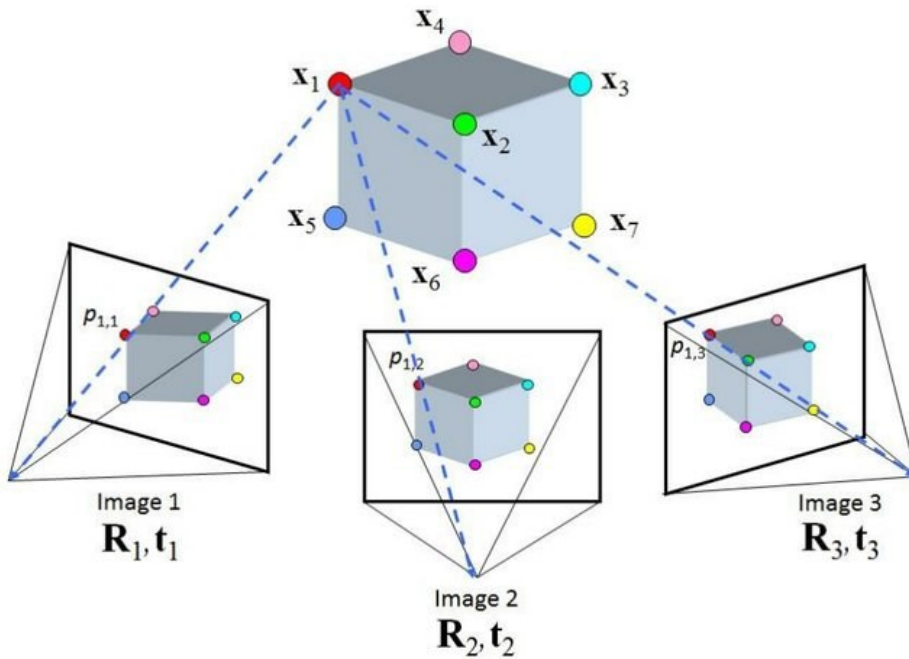


Figure 13: Structure from Motion (SfM) process. The structure in the world (cube) is imaged from multiple viewpoints (Image 1, Image 2, Image 3). By tracking (see dashed lines) the pixel locations ($p_{1,1}, p_{1,2}, \dots$) of specific features ($x_1, x_2 \dots$) in the images, both the camera motion ($R_1, T_1; R_2, T_2, \dots$) and the 3D model of the structure is estimated (Yilmaz and Karakus, 2013).

For each detected key point and each photograph inserted into the model, the common SfM software automatically solve the collinearity equations using least-square bundle adjustment (Brown, 1976; Fonstad et al., 2013; Lucieer et al., 2014; Snavely et al., 2008; Triggs et al., 2000). In order to precisely place the images, the extrinsic and intrinsic camera parameters as well as the XYZ coordinates of the

feature points are determined (Favalli et al., 2012; Ohnishi et al., 2006; Turner et al., 2012). Low-density point cloud with RGB colours taken from the images is generated consequently.

The generated point clouds are positioned in a relative "image-space" coordinate system because the SfM approach does not need the use of known-coordinate points from the real scene (Fonstad et al., 2013; James and Robson, 2014; Turner et al., 2012; Westoby et al., 2012). Contrary to the conventional photogrammetric approaches, the produced point cloud or polygonal surface will not be georeferenced and scaled (Carrivick et al., 2016; Clapuyt et al., 2016; Favalli et al., 2012). With the use of ground-control points (GCPs) with known coordinates, roto-translation matrices may be applied to the point cloud to orient and scale the model into an absolute coordinate system. It is standard procedure to position easily visible objects (targets) on the surveyed area prior to the gathering of images and to get their GPS coordinates.

To prevent mistakes during the 3-D scene reconstruction, the control points should be dispersed across the region (James and Robson, 2012). To scale and orient the point cloud in an absolute reference system, the GCPs are semi-automatically recognized on the pictures during the procedures and their coordinates are assigned in the program. It is recommended to use more targets (5-7) evenly distributed throughout the area, even though 3 GPCs with XYZ coordinates should theoretically be sufficient to locate the scene in a 3-D environment. This will help to reduce deformations caused by camera lens distortions (doming shape deformations) (Eltner et al., 2016; James and Robson, 2014).

Through a dense matching process employing the Multi-View-Stereo (MVS) methods, which enhance the point cloud density by at least two orders of magnitude, a higher resolution point cloud is created (Smith, 2016). The most popular MVS algorithms employed in geosciences, according to Eltner and colleagues (Eltner et al., 2016), are the depth-map merging approach (Li et al., 2010) and Patch-based Multi-view Stereo (PMVS) methods (Furukawa and Ponce, 2006). The second approach, known as depth maps, is based on the distances between the camera location and the 3-D scene, whereas the PMVS methodology reconstructs the 3-D scene from clusters of manageable size. To create a thick point cloud, patches or depth maps are matched and built around the sparse point cloud. The precision of the 3D model may be assessed after it has been scaled and rotated by looking at the Bundle Adjustment residuals: the fewer the reprojection errors, or the distance between each key point's projection and its observations, the better is the result.

The point cloud or dense map may be used to create a polygonal surface (mesh), with various filters (such as vegetation removal), face counts, and quality options available. The mesh can receive a texture produced from the images. Digital elevation models (DEMs) and orthophotos can also be created. It should be explicitly clear that in order to produce dense point clouds and subsequently their products, the SfM approach needs to be linked with the MVS algorithm. Therefore, when referring to the entire procedure (from photo acquisition to point clouds/meshes production), the name SfM-MVS is more applicable. But after intensive matching, the data are also frequently referred to as SfM in the literature. To minimize confusion, the word SfM will be used broadly throughout this work, although it refers to the SfM-MVS coupling.

2.3 Rock-mass and Stability of rock slopes

A rock mass refers to a substantial volume or assemblage of rock materials separated by discontinuities. It encompasses various geological elements such as rock types, structures, fractures, and discontinuities. The properties and behavior of a rock mass are influenced by factors like lithology, structural features, weathering, and the presence of joints or faults. Its characterisation and categorization strive to determine the properties of the rock mass by giving values to a set of rock

parameters. Although continuum mechanics may predict the behaviour of unbroken rock material, most rock masses are extensively fragmented. Since fractures influence the mechanical response of rock masses, the definition of their mechanical behaviour is challenging. Rock mass classifications are often employed in geotechnical engineering and mining to assess the stability, deformation, and strength characteristics of rock formations for construction or excavation purposes.

In this chapter, it will be further addressed a review on discontinuities, rock mass classification and slope stability and related numerical model approaches.

2.3.1 Discontinuities

Numerous works (Attewell and Farmer, 2012; Baecher and Lanney, 1978; Barton, 1978; Blyth and De Freitas, 2017; Fookes and Denness, 1969; Hills, 2012; Marinos and Carter, 2018; Price, 2016; Priest, 1993; Priest and Hudson, 1981; Wyllie, 2017) discuss the different types and characteristics of discontinuities.

Discontinuities are categorized based on their formation as:

- Bedding planes: large discontinuities found within sedimentary rock masses, resulting from interruptions in the sedimentation process. These planes typically exhibit parallel alignment, although they can undergo folding during deformation processes.
- Faults: identifiable discontinuities characterized by relative displacements occurring on opposing sides of the fault plane.
- Joints: discontinuities that lack visible relative displacement and commonly occur as groups of parallel or subparallel structures known as joint sets. Joints are formed because of various geological processes, including rapid cooling of basaltic lava flows (yielding columnar joints), diurnal temperature changes, geological uplift, or tectonic activities.
- Foliation: planar surfaces formed through the recrystallization and parallel alignment of minerals during metamorphism.
- Fractures and cracks: although lacking a universally precise definition, are terms often employed interchangeably with "discontinuity" in general and colloquial discourse. Within the literature, Priest (1993) suggests that "fracture" and "crack" serve as synonyms for the broader concept of "discontinuity."

Quantitative evaluations of discontinuities adhere to the recommendations set forth by the International Society for Rock Mechanics (Barton, 1978) for comprehensive characterization. These guidelines aim to identify ten distinct attributes as follows (Fig. 14):

- Orientation: This attribute describes the spatial attitude of a discontinuity and is measured using geological compasses and clinometers. Orientation will be defined in terms of strike and dip direction/dip for planar representations (top view imagery) and 3-D datasets (point clouds and triangulated surfaces), respectively.
- Set spacing: It refers to the normal distance between two adjacent discontinuities that belong to the same discontinuity set.
- Persistence or continuity: This attribute denotes the length of a discontinuity trace observed in an exposed section.

- Roughness: It signifies the level of asperity exhibited by the surface of a discontinuity at various scales.
- Wall strength: It quantifies the compressive strength of the exposed surface of a discontinuity.
- Aperture: This attribute measures the orthogonal distance between the opposing sides of an open discontinuity, which may be filled with air or water.
- Infilling: It refers to the material that separates the two rock walls of a discontinuity. This material can encompass weaker substances (e.g., soil, weathered material) or more resilient materials (e.g., cement, veins).
- Water seepage: It denotes the presence of water within a discontinuity or the entirety of the rock mass.
- Number of discontinuity sets: This attribute represents the count of distinct sets in which the discontinuity network is organized.
- Block size: It encompasses the dimensions of rock blocks determined by intersecting discontinuities.

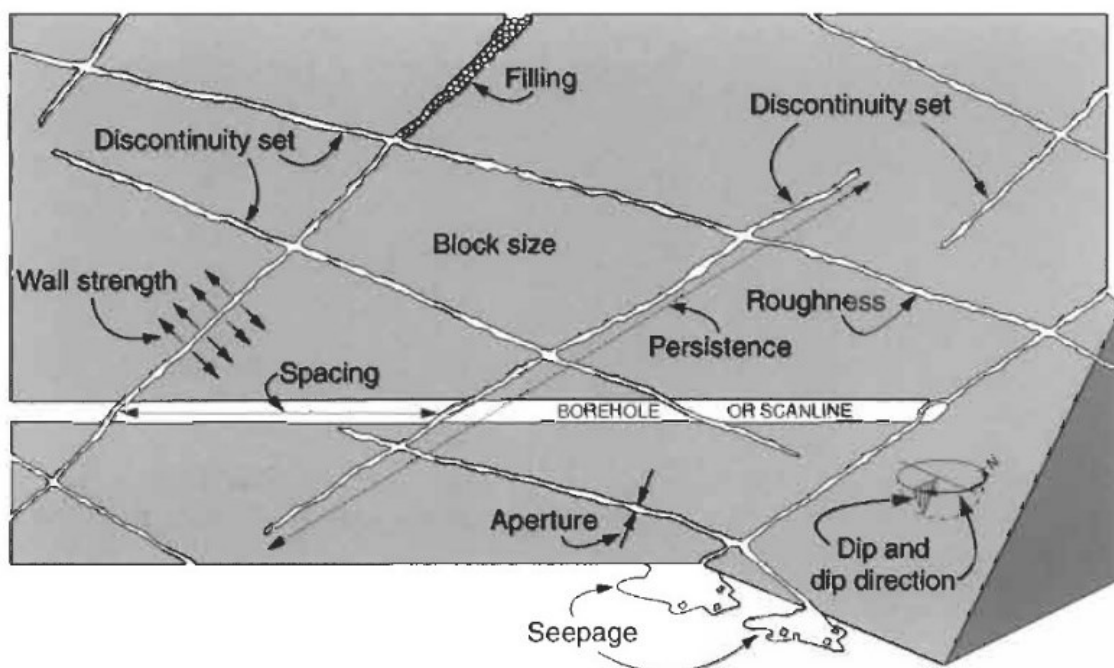


Figure 14: *Rock mass characteristics* (Hudson and Harrison, 2000)

The field-based collection of information on discontinuities commonly employs two primary sampling strategies: scanline surveys and window surveys. The scanline approach involves placing an imaginary or physical line along an exposed rock face that is representative of the study area. Data is then gathered on all the discontinuity traces that intersect this line. To achieve statistical significance, Priest (1993) recommends analysing 150-350 discontinuities, with at least half of them displaying visible terminations. The length of the scanline should be sufficiently long compared to the size and spacing of the discontinuities. For instance, Priest and Hudson (1976) suggest that the linear sample should be at least 50 times the mean spacing of the discontinuity sets. It is also advisable to employ a minimum of three sampling lines orthogonal to each other (Priest, 1993). Further discussions and details on scanlines can be found in La Pointe and Hudson (1985) (La Pointe and Hudson, 1985), Villaescusa (1992) (Villaescusa, 1992), Priest (1993) (Priest, 1993), and Windsor (1997) (Windsor, 1997).

The window sampling technique involves a two-dimensional survey aimed at gathering information on the discontinuities that intersect or lie within a rectangular window. Similar to the scanline approach, the size of the window should be appropriately chosen so that each side intersects a minimum of 30-100 discontinuities Priest (1993). To avoid under-sampling of discontinuities that are parallel to the sampled surface, it is recommended to employ a second window placed perpendicular to the first one.

2.3.2 Rock mass characterizations

In this part, a concise overview of how the properties of discontinuities are incorporated into the prevailing rock mass classification systems, widely utilized for characterizing rock masses and designing engineering structures like tunnels and underground excavations, is provided.

2.3.2.1 Rock Quality Designation (RQD)

The RQD (Rock Quality Designation) system was proposed by Deere (1964) and revolves around the assessment of the RQD index. This index can be obtained directly from drill core logs or indirectly by utilizing correlations such as the discontinuity frequency (Priest and Hudson, 1976). In cases where core samples are unavailable, but the traces of discontinuities are clearly visible in rock exposures, Palmstrom (1996) suggested the following relationship to estimate the RQD (Eq.12) based on the number of discontinuities per unit volume:

$$RQD = 115 - 3.3Jv \quad \text{Eq.12}$$

Where Jv is the volumetric joint count (Palmstrom, 2005).

Employing the volumetric joint count to calculate the RQD index can minimize its dependence on the orientation of the borehole (Hoek, 2007). The classification of rock mass quality is divided into five classes based on the RQD value (Tab.1). However, according to Zhang et al. (2006), relying solely on the RQD index is insufficient for obtaining a comprehensive understanding of the behaviour of the rock mass. This is because the RQD index does not consider the properties of the discontinuities. Consequently, the RQD index is presently utilized as an input parameter in other classification systems.

Table 1: *Rock Mass Quality according to the RQD System* (Deere, 1964; Loiotine, 2022).

RQD (%)	Rock Mass Quality
<25	Very poor
25-50	Poor
50-75	Fair
75-90	Good
90-100	Excellent

2.3.2.2 Rock Mass Rating (RMR) and Slope Mass Rating (SMR)

The Rock Mass Rating (RMR) classification system, initially introduced by Bieniawski (Bieniawski, 1989, 1973) for tunnels and subsequently expanded to encompass rock slopes and foundations

(Romana et al., 2015), revolves around the estimation of the RMR index (Eq.13). This index considers both the strength characteristics of the intact rock and the conditions of the discontinuities:

$$RMRb = R_s + R_{QD} + R_{dj} + R_{cj} + R_w \quad \text{Eq.13}$$

In the RMR system, the RMR index is determined using various parameters. These include R_s , which represents the compressive strength of the intact rock, R_{dj} denoting the joint spacing, R_{cj} indicating the joint conditions, and R_w representing the groundwater conditions. The rock mass quality is then classified into five classes, as outlined in the corresponding Table 2:

Table 2: Rock mass classification according to the RMR system (Bieniawski, 1973; Loiotine, 2022).

RMR	Rock Mass Quality
100-81	Very good
80-61	Good
60-41	Fair
40-21	Poor
<20	Very poor

The Slope Mass Rating (SMR) proposed by Romana (1985) (Romana et al., 2015) modify the RMR method in order to produce a more accurate evaluation of the rock mass quality for slope stability assessment (Eq.14):

$$SMR = RMRb + (F1 \cdot F2 \cdot F3) + F4 \quad \text{Eq.14}$$

The RMRb (basic RMR index) is derived from Bieniawski's classification. It is further modified by incorporating additional factors to obtain the final Stability RMR (SMR) index. The additional factors include $F1$, which accounts for the parallelism between the strike of the discontinuities and the slope face, $F2$, which considers the dip angle of the joints in relation to the planar mode of failure, $F3$, which assesses the relationship between the dip of the discontinuities and the dip of the slope face, and $F4$, a correction factor associated with the excavation method. Based on the SMR value, the rock mass stability is classified into five classes, ranging from completely unstable ($SMR < 20$) to completely stable ($SMR < 81$) (Tab. 3).

Table 3: Rock mass classification according to the SMR system (Loiotine, 2022; Romana et al., 2015)

SMR	Rock Mass Quality
100-81	Very good
80-61	Good
60-41	Normal
40-21	Bad
<20	Very bad

2.3.2.3 Q-System and Q-Slope

Barton (1974) (Barton et al., 1974) introduced the Q-system as a methodology for addressing tunneling and subterranean excavations. Over time, its scope was broadened to encompass various applications within rock formations (Barton, 2002). The assessment of rock mass quality is conducted using the Q index, a metric that incorporates the characteristics of discontinuities in the rock (Eq.15):

$$Q = \frac{RQD}{J_n} \times \frac{J_r}{J_a} \times \frac{J_w}{SRF} \quad (\text{Eq.15})$$

Here, J_n denotes the count of joint sets, J_r represents the parameter for joint roughness, J_a signifies the parameter for joint alteration, J_w accounts for the joint water parameter, and SRF corresponds to the Stress Reduction Factor. To elaborate, the initial ratio pertains to the configuration of the rock mass, the subsequent ratio relates to attributes of the discontinuities (specifically, roughness and wall alteration), and the third ratio reflects the prevailing stress conditions. Detailed guidance on ascertaining these parameters can be located within dedicated tables presented by Barton and colleagues (Barton et al., 1974). Depending on the resultant Q value, classification of the rock mass can be categorized into nine distinct classes (Tab.4).

Table 4: Rock mass classification according to the Q system (Barton et al., 1974; Loiotine, 2022)

Q	Rock Mass Quality
1000-400	Exceptionally good
400-100	Extremely good
100-40	Very good
40-10	Good
10-4	Fair
4-1	Poor
1-0.1	Very poor
0.0-0.01	Extremely poor
0.01-0.001	Exceptionally poor

The Q-slope technique, designed for the purposes of rock slope engineering and rock mass classification, is a product of the collaborative efforts of Barton and Bar (Bar and Barton, 2017). This method quantifies the rock mass's quality concerning slope stability, and it yields the Q-slope value, facilitating the calculation of sustainable slope angles over extended periods without the need for additional reinforcement.

The computation of the Q-slope value involves (Eq.16):

$$Q = \left(\frac{RQD}{J_n} \right) \times \left(\frac{J_r}{J_a} \right)_0 \times \left(\frac{J_{wice}}{SRF_{slope}} \right) \quad \text{Eq.16}$$

The Q-slope methodology draws upon analogous parameters as the Q-system, which has been utilized for more than four decades in formulating ground support strategies for underground excavations and tunnel construction. The initial quartet of parameters, namely RQD (rock quality designation), J_n (joint set count), J_r (joint roughness coefficient), and J_a (joint alteration coefficient), align with those found in the Q-system. Nevertheless, the frictional resistance pair, J_r and J_a , can be applied to specific facets of potentially unstable wedges if necessary. Straightforward orientation factors (denoted as 0), such as $(J_r/J_a)1 \times 0.7$ for the J1 set and $(J_r/J_a) 2 \times 0.9$ for the J2 set, yield approximations of the collective frictional resistance reduction across an entire wedge, as applicable. The Q-system's term, J_w , is substituted with J_{wice} , which considers a broader array of environmental circumstances pertinent to rock slopes exposed to enduring environmental influences.

These circumstances encompass extremes like erosive heavy rainfall and ice wedging, which may transpire seasonally at opposite geological and regional extremities.

Additionally, classifications pertinent to SRF (strength reduction factor) pertinent to slope stability are incorporated. The product of these factors yields the Q-slope value, encompassing a range from 0.001 (indicating extremely suboptimal conditions) to 1000 (indicating exceptionally favourable conditions) across diverse rock masses (Fig. 15).

A concise equation for determining the steepest feasible slope angle (β) in degrees, without necessitating reinforcement or auxiliary support, is provided as follows (Eq.17):

$$\beta = 20 \log_{10} Q_{slope} + 65^\circ \quad \text{Eq.17}$$

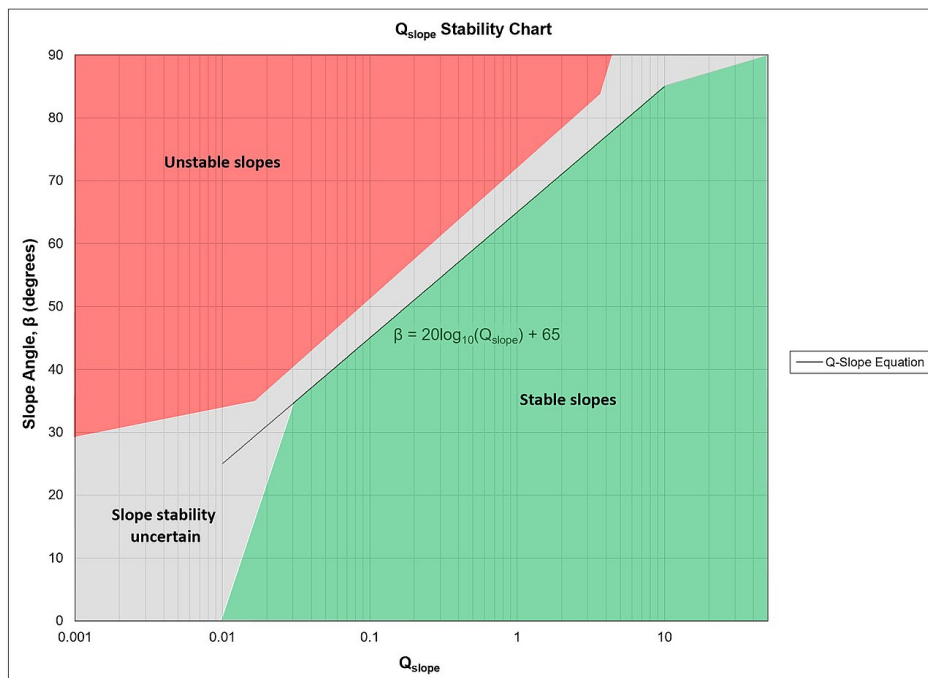


Figure 15: Q-slope stability chart (Bar and Barton, 2017).

2.3.2.4 Rock Mass index (RMi)

Palmstrom's Rock Mass Index (RMi) (Palmstrøm, 1996) classifies rock masses by taking into account the qualities of the discontinuities that tend to lower their strength.

The RMi is written as (Eq.18):

$$Rmi = \sigma_c JP \quad \text{Eq.18}$$

where σ_c is the intact rock's uniaxial compressive strength and JP is the jointing parameter, which reflects the strength drop induced by the joints.

The jointing parameter is made up of the joint condition factor (jC) and the block volume (Vb), as shown below (Eq.19):

$$jC = jR \frac{jL}{jA} \quad \text{Eq.19}$$

where jR, jL, and ja are the joint roughness factor, joint size and continuity factor, and joint alteration factor, respectively.

Table 5 depicts all the range of values in RMi classification. Further discussion is provided in Zhang (2016)(Zhang, 2016).

Table 5: Rock mass classification according to the RMi system (Loiotine, 2022; Palmstrom, 1996)

RMi	Rock Mass Quality
<0.001	Extremely weak
0.001-0.01	Very weak
0.01-0.1	Weak
0.1-1	Medium
1-10	Strong
10-100	Very strong
>100	Extremely strong

2.3.2.5 Geological Strength Index (GSI)

Hoek and Brown (Hoek and Brown, 1997) proposed the GSI categorization system, which is based on the Hoek-Brown strength criteria for rock masses. This criteria was first developed for intact rock (Brown and Hoek, 1980) as follows (Eq.20):

$$\sigma'_1 = \sigma'_3 + \sigma_{ci} \left(mi \frac{\sigma'_3}{\sigma_{ci}} + 1 \right)^{0.5} \quad \text{Eq.20}$$

where σ_{ci} is the rock unconfined compressive strength, mi is a material constant for the intact rock, and σ'_1 and σ'_3 are the effective major and minor primary stresses, respectively.

The generalized Hoek-Brown strength criteria (Hoek and Brown, 1997) which is defined using the following equation, was later used to apply the criterion to rock masses (Eq.21).

$$\sigma'_1 = \sigma'_3 + \sigma_{ci} \left(mb \frac{\sigma'_3}{\sigma_{ci}} + s \right)^\alpha \quad \text{Eq.21}$$

where the rock mass material's specified constants are mb , s , and α .

By using the GSI index, which is based on the rock mass structure (range from intact to disintegrated) and the discontinuity conditions (from very good to very poor), the GSI classification system offers a qualitative assessment of the rock mass quality. Hoek and Brown recommended identifying a range of GSI rather than a single figure because the assessment of the GSI is somewhat arbitrary. Figure 16 presents the initial GSI categorization scheme. The method has recently been modified to account for various types of rock masses (Hoek et al., 2005, 2002, 1998; Hoek and Brown, 2019; Hoek and Marinos, 2007, 2000; Marinos and Hoek, 2018; Marinos et al., 2005; Marinos and Carter, 2018; Marinos, 2017) as Flysch (Fig.17).

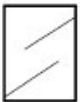





GEOLOGICAL STRENGTH INDEX FOR JOINTED ROCKS (Hoek and Marinos, 2000) From the lithology, structure and surface conditions of the discontinuities, estimate the average value of GSI. Do not try to be too precise. Quoting a range from 33 to 37 is more realistic than stating that GSI = 35. Note that the table does not apply to structurally controlled failures. Where weak planar structural planes are present in an unfavourable orientation with respect to the excavation face, these will dominate the rock mass behaviour. The shear strength of surfaces in rocks that are prone to deterioration as a result of changes in moisture content will be reduced if water is present. When working with rocks in the fair to very poor categories, a shift to the right may be made for wet conditions. Water pressure is dealt with by effective stress analysis.		SURFACE CONDITIONS				
		VERY GOOD Very rough, fresh unweathered surfaces	GOOD Rough, slightly weathered, iron stained surfaces	FAIR Smooth, moderately weathered and altered surfaces	POOR Slickensided, highly weathered surfaces with compact coatings or fillings or angular fragments	VERY POOR Slickensided, highly weathered surfaces with soft clay coatings or fillings
STRUCTURE		DECREASING SURFACE QUALITY →				
	INTACT OR MASSIVE - intact rock specimens or massive in situ rock with few widely spaced discontinuities	90			N/A	N/A
	BLOCKY - well interlocked undisturbed rock mass consisting of cubical blocks formed by three intersecting discontinuity sets	80	70			
	VERY BLOCKY- interlocked, partially disturbed mass with multi-faceted angular blocks formed by 4 or more joint sets		60	50		
	BLOCKY/DISTURBED/SEAMY - folded with angular blocks formed by many intersecting discontinuity sets. Persistence of bedding planes or schistosity			40	30	
	DISINTEGRATED - poorly interlocked, heavily broken rock mass with mixture of angular and rounded rock pieces				20	
	LAMINATED/SHEARED - Lack of blockiness due to close spacing of weak schistosity or shear planes	N/A	N/A			10

Figure 16: GSI classification chart (Hoek and Marinos, 2000)

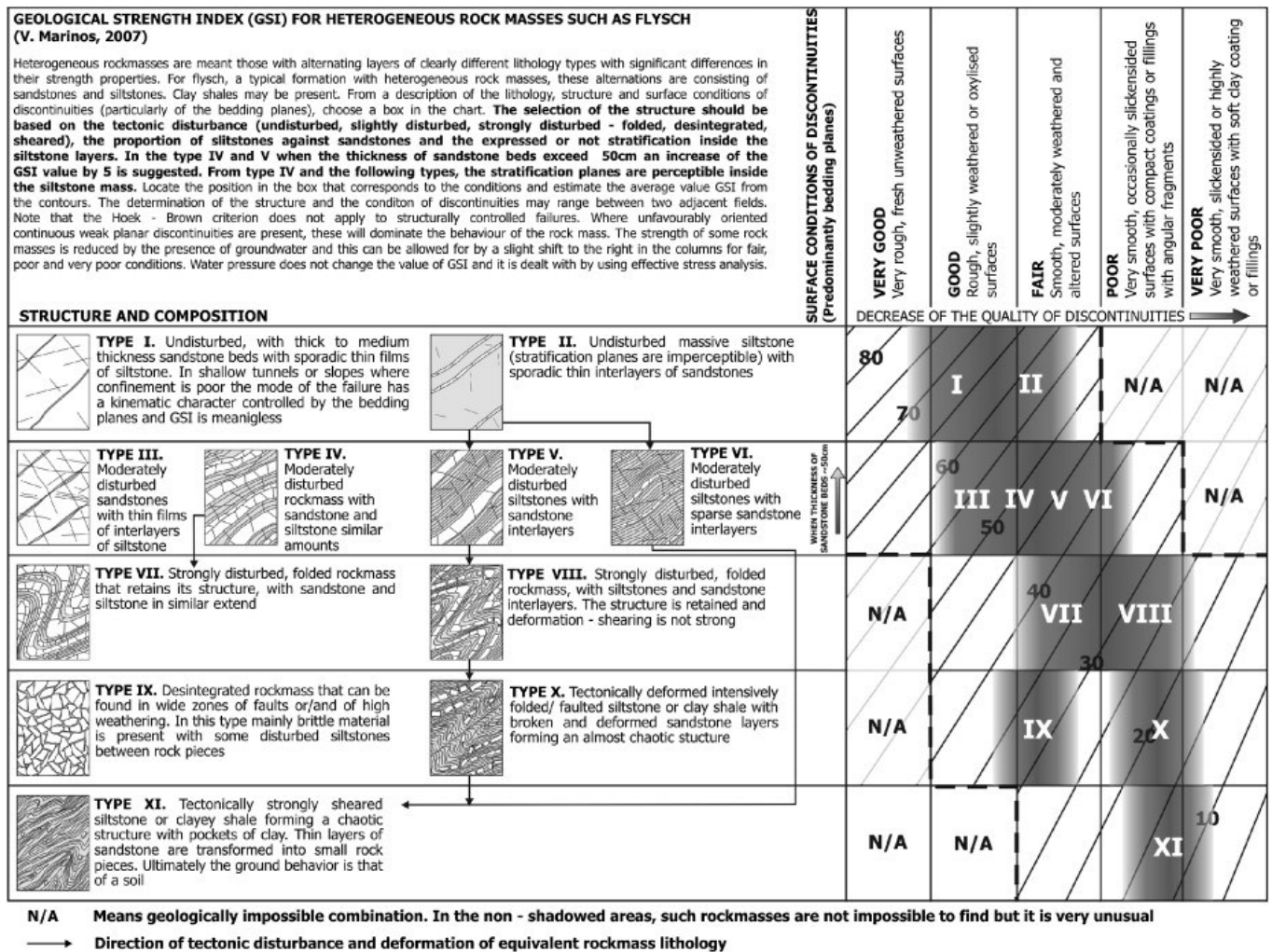


Figure 17: GSI classification chart for heterogeneous rock masses such as flysch (Marinos, 2017).

2.3.3 Classification of landslides

In the majority of instances, occurrences of rock mass failures are regulated by geological structures, with their kinematic characteristics contingent upon the geometric interplay between the slope and the structural discontinuities (Stead and Wolter, 2015). Multiple notable failure mechanisms, including planar sliding, wedge sliding, rotational sliding, and toppling, have been extensively documented (Cruden, D.M., Varnes, 1996; Cruden, 2003; Giani, 1992; Goodman and Shi, 1985; Hoek, 2007; Hoek and Bray, 1981). Nevertheless, additional forms of failure have been identified, characterized primarily by the observed phenomena rather than the spatial arrangement of the slope and joints (Hantz et al., 2003; Hungr et al., 2014; Hungr and Evans, 2004).

An update of the Varnes Classification of Landslide Types, is proposed by Hungr et al. (2014)(Hungr et al., 2014). In accordance with this classification, the principal landslides are as follows and in Figure 18:

- Rock/ice fall: Detachment, fall, rolling, and bouncing of rock or ice fragments. May occur singly or in clusters, but there is little dynamic interaction between the most mobile moving fragments, which interact mainly with the substrate (path). Fragment deformation is unimportant, although fragments can break during impacts. Usually of limited volume.

- Boulder/debris/silt fall: Detachment, fall, rolling and bouncing of soil fragments such as large clasts in soil deposits, or blocks of cohesive (cemented or unsaturated) soil. The mechanism of propagation is similar to rock fall, although impacts may be strongly reduced by the weakness of the moving particles.
- Rock block topple: Forward rotation and overturning of rock columns or plates (one or many), separated by steeply dipping joints. The rock is relatively massive, and rotation occurs on well-defined basal discontinuities. Movement may begin slowly, but the last stage of failure can be extremely rapid. Occurs at all scales.
- Rock flexural topple: Bending and forward rotation of a rock mass characterized by very closely spaced, steeply dipping joints or schistose partings, striking perpendicular to the fall line of the slope. The rock is relatively weak and fissile. There are no well-defined basal joints, so that rotation of the strata must be facilitated by bending. The movement is generally slow and tends to self-stabilize. However, secondary rotational sliding may develop in the hinge zone of the topple. Occurs at large scale.
- Gravel/sand/silt block topple: Block toppling of columns of cohesive (cemented) soil, separated by vertical joints.
- Rock rotational slide (“rock slump”): Sliding of a mass of weak rock on a cylindrical or other rotational rupture surface which is not structurally controlled. The morphology is characterized by a prominent main scarp, a characteristic back-tilted bench at the head and limited internal deformation. Usually slow to moderately slow.
- Rock planar slide (“block slide”): Sliding of a mass of rock on a planar rupture surface. The surface may be stepped forward. Little or no internal deformation. The slide head may be separating from stable rock along a deep, vertical tension crack. Usually extremely rapid.
- Rock wedge slide: Sliding of a mass of rock on a rupture surface formed of two planes with a downslope-oriented intersection. No internal deformation. Usually extremely rapid.
- Rock compound slide: Sliding of a mass of rock on a rupture surface consisting of several planes, or a surface of uneven curvature, so that motion is kinematically possible only if accompanied by significant internal distortion of the moving mass. Horst-and-graben features at the head and many secondary shear surfaces are typical. Slow or rapid.
- Rock irregular slide (“rock collapse”): Sliding of a rock mass on an irregular rupture surface consisting of a number of randomly oriented joints, separated by segments of intact rock (“rock bridges”). Occurs in strong rocks with non-systematic structure. Failure mechanism is complex and often difficult to describe. May include elements of toppling. Often very sudden and extremely rapid.
- Clay/silt rotational slide (“soil slump”): Sliding of a mass of (homogeneous and usually cohesive) soil on a rotational rupture surface. Little internal deformation. Prominent main scarp and back-tilted landslide head. Normally slow to rapid but may be extremely rapid in sensitive or collapsible soils.
- Clay/silt planar slide: Sliding of a block of cohesive soil on an inclined planar rupture surface, formed by a weak layer (often pre-sheared). The head of the slide mass separates from stable soil along a deep tension crack (no active wedge). May be slow or rapid.
- Gravel/sand/debris slide: Sliding of a mass of granular material on a shallow, planar surface parallel with the ground. Usually, the sliding mass is a veneer of colluvium, weathered soil, or pyroclastic deposits sliding over a stronger substrate. Many debris slides become flow-like after moving a short distance and transform into extremely rapid debris avalanches.
- Clay/silt compound slide: Sliding of a mass of soil on a rupture surface consisting of several planes, or a surface of uneven curvature, so that motion is kinematically possible only if accompanied by significant internal distortion of the moving mass. Horst-and-graben features

at the head and many secondary shear surfaces are observed. The basal segment of the rupture surface often follows a weak horizon in the soil stratigraphy.

- Rock slope spread: Near-horizontal stretching (elongation) of a mass of coherent blocks of rock as a result of intensive deformation of an underlying weak material, or by multiple retrogressive sliding controlled by a weak basal surface. Usually with limited total displacement and slow.
- Sand/silt liquefaction spread: Extremely rapid lateral spreading of a series of soil blocks, floating on a layer of saturated (loose) granular soil, liquefied by earthquake shaking or spontaneous liquefaction.
- Sensitive clay spread: Extremely rapid lateral spreading of a series of coherent clay blocks, floating on a layer of remoulded sensitive clay.
- Rock/ice avalanche: Extremely rapid, massive, flow-like motion of fragmented rock from a large rockslide or rock fall.
- Dry (or non-liquefied) sand/silt/gravel/debris flow: Slow or rapid flow-like movement of loose dry, moist, or subaqueous, sorted, or unsorted granular material, without excess pore pressure.
- Sand/silt/debris flowslide: Very rapid to extremely rapid flow of sorted or unsorted saturated granular material on moderate slopes, involving excess pore-pressure or liquefaction of material originating from the landslide source. The material may range from loose sand to loose debris (fill or mine waste), loess and silt. Usually originates as a multiple retrogressive failure. May occur subaerially, or under water.
- Sensitive clay flowslide: Very rapid to extremely rapid flow of liquefied sensitive clay, due to remolding during a multiple retrogressive slide failure at, or close to the original water content.
- Debris flow: Very rapid to extremely rapid surging flow of saturated debris in a steep channel. Strong entrainment of material and water from the flow path.
- Mud flow: Very rapid to extremely rapid surging flow of saturated plastic soil in a steep channel, involving significantly greater water content relative to the source material. Strong entrainment of material and water from the flow path (Plasticity Index > 5 %).
- Debris flood: Very rapid flow of water, heavily charged with debris, in a steep channel. Peak discharge comparable to that of a water flood.
- Debris avalanche: Very rapid to extremely rapid shallow flow of partially or fully saturated debris on a steep slope, without confinement in an established channel. Occurs at all scales.
- Earthflow: Rapid or slower, intermittent flow-like movement of plastic, clayey soil, facilitated by a combination of sliding along multiple discrete shear surfaces, and internal shear strains. Long periods of relative dormancy alternate with more rapid “surges”.
- Peat flow: Rapid flow of liquefied peat, caused by an undrained failure.
- Mountain slope deformation: Large-scale gravitational deformation of steep, high mountain slopes, manifested by scarps, benches, cracks, trenches and bulges, but lacking a fully defined rupture surface. Extremely slow or unmeasurable movement rates.
- Rock slope deformation: Deep-seated slow to extremely slow deformation of valley or hill slopes. Sagging of slope crests and development of cracks or faults, without a well-defined rupture surface. Extremely slow movement rates.
- Soil slope deformation: Deep-seated, slow to extremely slow deformation of valley or hill slopes formed of (usually cohesive) soils. Often present in permafrost slopes with high ice content.

- Soil creep: Extremely slow movement of surficial soil layers on a slope (typically less than 1 m deep), as a result of climate-driven cyclical volume changes (wetting and drying, frost heave).
- Solifluction: Very slow but intensive shallow soil creep involving the active layer in Alpine or polar permafrost. Forms characteristic solifluction lobes.

Type of movement	Rock	Soil
Fall	1. <i>Rock/ice</i> fall ^a	2. <i>Boulder/debris/silt</i> fall ^a
Topple	3. Rock block topple ^a	5. <i>Gravel/sand/silt</i> topple ^a
	4. Rock flexural topple	
Slide	6. Rock rotational slide	11. <i>Clay/silt</i> rotational slide
	7. Rock planar slide ^a	12. <i>Clay/silt</i> planar slide
	8. Rock wedge slide ^a	13. <i>Gravel/sand/debris</i> slide ^a
	9. Rock compound slide	14. <i>Clay/silt</i> compound slide
	10. Rock irregular slide ^a	
Spread	15. Rock slope spread	16. <i>Sand/silt</i> liquefaction spread ^a
		17. Sensitive clay spread ^a
Flow	18. <i>Rock/ice</i> avalanche ^a	19. <i>Sand/silt/debris</i> dry flow
		20. <i>Sand/silt/debris</i> flowslide ^a
		21. Sensitive clay flowslide ^a
		22. Debris flow ^a
		23. Mud flow ^a
		24. Debris flood
		25. Debris avalanche ^a
		26. Earthflow
27. Peat flow		
Slope deformation	28. Mountain slope deformation	30. Soil slope deformation
	29. Rock slope deformation	31. Soil creep
		32. Solifluction

Figure 18: Summary of the updated version of the Varnes classification system (Hungr et al., 2014). With the apex *a* are indicated movement types that usually reach extremely rapid velocities as defined by Cruden and Varnes (1996) (Cruden, D.M., Varnes, 1996). The other landslide types are most often (but not always) extremely slow to very rapid.

2.3.4 Numerical modelling approaches for rock slope analysis

The utilization of numerical techniques for the assessment of the stability of rock slopes has witnessed a significant upsurge in the last two decades (Stead and Coggan, 2012). Numerous methodologies are available to explore progressively intricate processes of slope failure. Initial evaluations of rock slope stability can be conducted through basic kinematic analyses, hinging on the alignment of the slope and the documented structural discontinuities. The employment of limit equilibrium methods permits the appraisal of slope stability by quantifying the ratio between propelling and opposing forces within the system (Hoek and Bray, 1981).

Continuum and Discontinuum numerical methodologies offer a means to incorporate the deformation and failure tendencies of the materials constituting the slope. This facilitates the investigation of more intricate mechanisms such as material deterioration, step path failures, and the accumulation of damage. Complex hybrid methodologies can be adopted to simulate the fragile conduct of the unbroken rock, replicating the progression of fractures within unbroken material. These approaches

also enable the exploration of the impact of rock bridges and the potency of unbroken rock on slope stability (Elmo and Stead, 2010; Lisjak et al., 2014).

In recent times, the utilization of lattice-spring scheme methods for modelling brittle fractures has gained prominence, driven by the development of modern, user-friendly numerical codes and the enhanced computational capabilities of contemporary workstations (Cundall, 2011). This has resulted in a growing prevalence of such methods. This passage furnishes a synopsis of the most employed techniques for the analysis of slope stability, with specific emphasis on limit equilibrium techniques and continuum.

2.3.4.1 Kinematic analyses and Limit Equilibrium techniques

During an initial stage, deterministic or probabilistic evaluations of rock slopes stability can be conducted through kinematic analyses utilizing stereographic projections. These assessments involve the execution of kinematic feasibility tests (Markland, 1972)(e.g., Markland 1972) to recognize potential failure mechanisms and determine movement directions. These determinations rely on the spatial orientation of both the rock slope and its discontinuities. Various commercial software packages, such as Dips (<https://www.rocscience.com/>) and Dips Analyst (Admassu and Shakoor, 2013), are accessible for performing kinematic analyses encompassing different failure modes, including planar sliding, wedge sliding, direct toppling, and oblique toppling.

Limit Equilibrium methods are specialized tools employed for evaluating the stability of rock slopes impacted by planar or circular failure surfaces. In this context, the slope is treated as a rigid entity, and its stability hinges on the factor of safety (Eq.22). This factor signifies the ratio between the resisting force along a distinct failure surface (ultimate stress) and the driving force exerted on the same surface (working stress). In instances of shear-type failures, the values of resisting and working stresses are defined in terms of shear strength τ (Wyllie, 2017):

$$FS = \frac{\text{Ultimate stress}}{\text{Working stress}} = \frac{\tau}{\tau_s} \quad \text{Eq.22}$$

Here, τ represents the resisting shear strength, and τ_s the shear strength along the displacing sliding surface. The equilibrium condition is attained in limit equilibrium when the driving forces equate the resisting forces, denoted as $FS=1$. The literature has documented various Limit Equilibrium methods, differing in the investigated failure mechanisms and the underlying assumptions that render the problem statistically determinate. For example, Fellenius (1936) (Fellenius, 1936), Bishop (1955)(Bishop, 1955), and Janbu (1973)(Janbu, 1973) addressed mechanisms involving both circular and non-circular failure surfaces. Subsequently, Morgenstern-Price (1965)(Morgenstern and Price, 1965), Spencer (1967)(Spencer, 1967), and Sarma (1973)(Sarma, 1973) considered inter-slice forces. Commercial software such as RocPlane (<https://www.rocscience.com/>), Swedge (<https://www.rocscience.com/>), Slide3 (<https://www.rocscience.com/>), enable the swift application of these methods and facilitate sensitivity analyses. These analyses estimate the factor of safety by varying discontinuity parameters within a specified range, rather than assuming fixed values. However, these software tools are restricted to simulating relatively straightforward block configurations and are unsuitable for more intricate geometries and conditions. Indeed, the limitations of limit equilibrium methods and associated computer codes become apparent in scenarios involving non-persistent failure planes (Stead et al., 2006). While some researchers have made efforts in this direction (Baczynski, 2000; Jennings, 1970; Kemeny, 2003), methods do not accommodate the simulation of progressive failures (Bjerrum, 1967; Chowdhury and A-Grivas, 1982) or the internal deformation of the rock mass.

2.3.4.2 Continuum methods: FEM and FDM

Continuum methods rank among the most extensively employed techniques for examining the stability of soil and rock slopes (Stead and Coggan, 2012). They facilitate the integration of intricate rock mass attributes and processes, including stiffness, anisotropy, water pore pressure, and material degradation (Stead et al., 2006). The classification of continuum methods commonly distinguishes between Finite Element Methods (FEM) and Finite Difference Methods (FDM). While the mathematical methodologies for solving the models differ, they yield similar outcomes in practical terms (<https://www.itascacg.com/>). A comprehensive exposition of the theories underlying these methods lies beyond the scope of this summary; for an in-depth, technical elucidation, Peiró and Sherwin (2005) are recommended.

Both FEM and FDM partition the model domain (e.g., the slope) into a grid of elements or zones within which stress and strain calculations are performed. The model solution can be achieved through either an implicit or explicit scheme. Codes utilizing an implicit scheme resolve the model iteratively, reaching equilibrium if a solution exists. Implicit schemes are generally unsuited for investigating unstable slopes with significant displacements, but they accommodate the use of large time-steps, leading to relatively short runtimes. On the other hand, explicit codes employ a time-stepping scheme that computes stress, strain, displacement, and velocity at each node during each cycle, utilizing Newton's second law (<https://www.itascacg.com/>). Consequently, realistic modeling of substantial failures and displacements is feasible, although smaller time-steps are required for mathematical stability, resulting in longer runtimes. Prominent FEM geomechanical codes that use an implicit solution scheme include RS2 (<https://www.rocscience.com/>) and RS3 (<https://www.rocscience.com/>). FLAC (<https://www.itascacg.com/>) and FLAC3D (<https://www.itascacg.com/>) utilize an FDM with an explicit time-stepping scheme for solving slope stability problems.

Continuum methods are well-suited for assessing rock slopes or subterranean excavations where failure hinges on the rock mass's strength, represented as a "continuum equivalent" (Grøneng et al., 2010; Hoek and Guevara, 2009; Zhao et al., 2015), a limited number of discontinuities can be incorporated to investigate the impact of discrete fractures on slope stability (Hammah et al., 2008; Jing, 2003; Spreafico et al., 2017) (Fig. 19).

Exploring the stability of rock slopes often involves the Shear Strength Reduction (SSR) method (Diederichs et al., 2007; Matsui and San, 1992), which entails a gradual weakening (or strengthening) of material (or discontinuity) strength parameters until a state of limit equilibrium is attained. SSR analyses are now commonplace in both two-dimensional (De Caro et al., 2018; Spreafico et al., 2017) and three-dimensional models (Shen and Karakus, 2014).

Continuum methods, albeit to a more constrained extent, have also been tailored for the exploration of brittle fracturing in rock formations. Notably, the Fracture Analysis Code (FRANC) emerged as one of the initial software to adopt a Finite Element Method (FEM) approach for analyzing the brittle fracturing of intact rock material (Wawrzynek and Ingraffea, 1987). The FEM-based Rock Failure Process Analysis (RFPA) code serves to replicate the development and propagation of cracks within a cohesive, unbroken medium (Tang, 1997; Tang and others, 2011). The RFPA methodology has also been employed to investigate the accrual of brittle damage and the ensuing acoustic emissions in the right bank slope of the Jinping hydropower project (Xu et al., 2011) as well as the Dagangshan Hydropower Station (Xu et al., 2012). More recently, FEM Voronoi tessellation techniques have been deployed to simulate the brittle fracturing of rock bridges preceding rock slope failures (Spreafico et al., 2017).

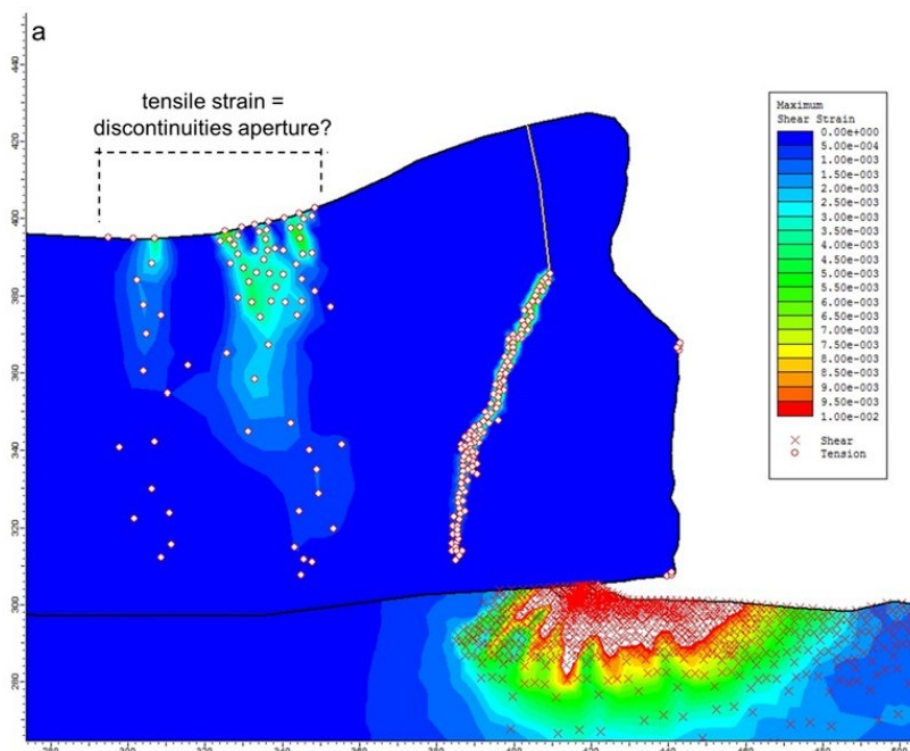


Figure 19: Applications of the Finite Element Method to rock slope stability: example of the 2014 San Leo rockslide (Italy) (Donati, 2016; Spreafico et al., 2017).

2.4 Digital Shoreline Analysis System (DSAS)

The Digital Shoreline Analysis System (DSAS) (Himmelstoss et al., 2018) plugin is an ArcGIS tool designed for coastal scientists, geographers, and environmental professionals. DSAS is an essential component of shoreline change analysis, enabling users to assess coastal dynamics and monitor shoreline shifts (Baig et al., 2020; Mutaqin, 2017; Nassar et al., 2019). Recently it founded applications not only in shoreline shifts but even in the quantification of the evolution in other coastal features, like dune fields and cliff top (Fabbri et al., 2021a; Gómez-Pazo et al., 2021; Lollino et al., 2021).

DSAS workflow begins by importing geospatial data, primarily historical and contemporary shoreline data, which may include: Shoreline vectors (polygons or lines), aerial or satellite imagery, topographic maps, LiDAR (Light Detection and Ranging) data, bathymetric data. Once the data is imported, DSAS offers tools to calibrate and georeference it accurately, ensuring alignment with the spatial coordinate system. The first step in shoreline analysis is identifying the shoreline positions in the historical and contemporary datasets. DSAS employs various techniques for shoreline identification as manual digitization; users can trace the shoreline positions on maps or images. Another technique is automated shoreline extraction; algorithms may be employed to identify shorelines from imagery or LiDAR data (Swirad and Young, 2021).

DSAS excels at detecting and quantifying shoreline changes over time. This involves many steps: Calculating distances between corresponding points in historical and contemporary shorelines, analyzing spatial shifts and changes, including erosion, accretion, or stability, generating change rate statistics to assess the speed of shoreline alterations.

Then, the software allows users to define analysis zones, which can be customized based on specific research or management objectives. These zones can vary in size, location, and shape, enabling targeted analysis of coastal areas.

DSAS provides a rich suite of statistical tools and visualization options, including: Shoreline change statistics mean, standard deviation, and rates of change, graphical representations, charts, graphs, and maps displaying shoreline change patterns, time series analysis studying long-term trends in coastal dynamics.

Coastal analysis often deals with intrinsic uncertainties (Casella et al., 2020; Del Río and Gracia, 2013). DSAS offers tools to assess and quantify uncertainty in shoreline change measurements.

Here a typical workflow of how DSAS (Fig. 20) can be used for shoreline analysis:

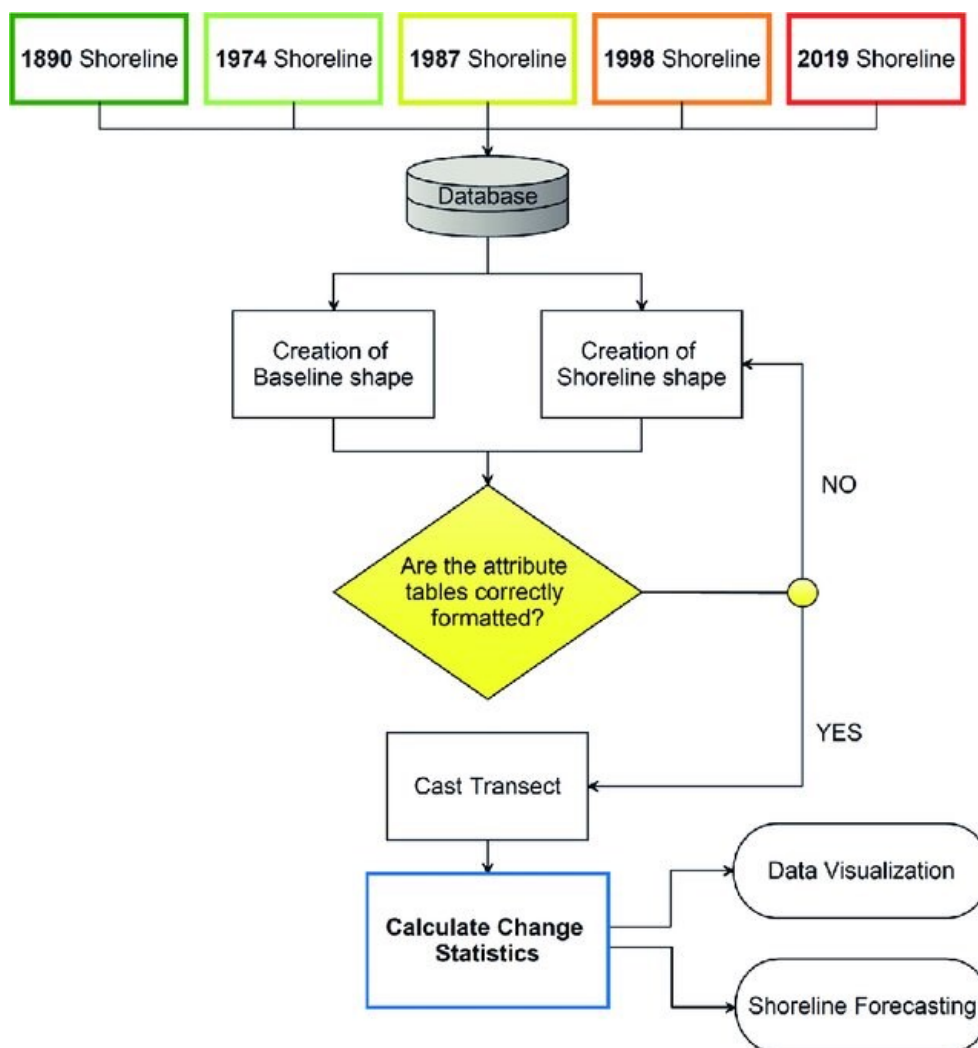


Figure 20: Typical workflow for analysis with DSAS plugin (Pepe et al., 2023).

- Data Import: Import historical and contemporary shoreline data, as well as relevant geospatial datasets such as imagery and topographic data.
- Data Calibration: Ensure accurate georeferencing and alignment of all datasets.
- Shoreline Identification: Identify shoreline positions using manual or automated methods.
- Change Detection: Calculate shoreline change by comparing historical and contemporary shorelines.

- **Analysis Zones:** Define analysis zones based on study objectives and specific coastal areas of interest.
- **Statistics and Visualization:** Generate shoreline change statistics, charts, graphs, and maps to visualize coastal dynamics.
- **Uncertainty Assessment:** Evaluate and quantify uncertainties associated with shoreline change measurements.
- **Reporting and Export:** Create detailed reports and export data for dissemination and decision-making.

2.5 Machine learning

Algorithms are indispensable for resolving computer-related issues (Alpaydin, 2020). They serve as a set of instructions guiding the transformation of input into output. For instance, one can formulate an algorithm to sort a set of numbers, rearranging an unordered list into an ascending order. Nonetheless, certain tasks lack pre-established algorithms (Rebala et al., 2019).

To bridge this knowledge gap, we turn to data. Essentially, we seek to automate the extraction of the algorithm for these tasks, empowering the computer (machine) without the need for explicit coding. While we have well-established algorithms for tasks such as numerical sorting, numerous applications require no predefined algorithms but rely on accessible example data (Alpaydin, 2020).

The advancement of computer technology has provided us with the capacity to store and process vast volumes of data, along with remote access through computer networks. Many data acquisition devices now generate digital and dependable data (Han et al., 2012a).

In the absence of complete knowledge regarding a process, data collection becomes the key, with the hope of extracting answers from the data (Alpaydin, 2020).

Despite not having a complete understanding of the data generation process, we believe it follows a non-random pattern. While we may not be able to comprehensively explain the process, we can construct useful approximations. Although these approximations may not account for everything, they capture a portion of the data's patterns. This is where machine learning plays a critical role. These patterns facilitate our understanding of the process and support predictions based on the assumption that the near future will resemble the past when the sample data was collected (Alpaydin, 2020).

In essence, machine learning entails programming computers to optimize performance criteria through example data or past experiences. It involves defining a model with parameters and then executing a computer program to optimize these parameters based on training data or prior experiences. The model may be predictive, aiming to make future predictions, or descriptive, with the goal of acquiring knowledge from data, or a combination of both (Han et al., 2012b).

Machine learning relies on statistical theory to construct mathematical models, given that the primary task involves drawing inferences from a sample. Computer science plays a dual role in this context. First, during training, efficient algorithms are essential to solve the optimization problem efficiently and manage vast data volumes (Han et al., 2012c). Second, once a model is learned, the representation and algorithm for inference must also be efficient. In specific applications, the efficiency of the learning or inference algorithm, holding space and time complexity, assumes equal importance alongside predictive accuracy (Alpaydin, 2020).

For an in-depth exploration of the diverse applications and types of machine learning, let's focus on the main subdivision of machine learning techniques in supervised, unsupervised and reinforced learning (Fig. 21) (Badillo et al., 2020). Then, the algorithms used in this work, Random Forest (RF) (Breiman, 2001) and eXtreme Gradient Boosting (Chen and He, 2014) will be presented together with Mean Decrease of Impurity (MDI) method (Louppe et al., 2013).

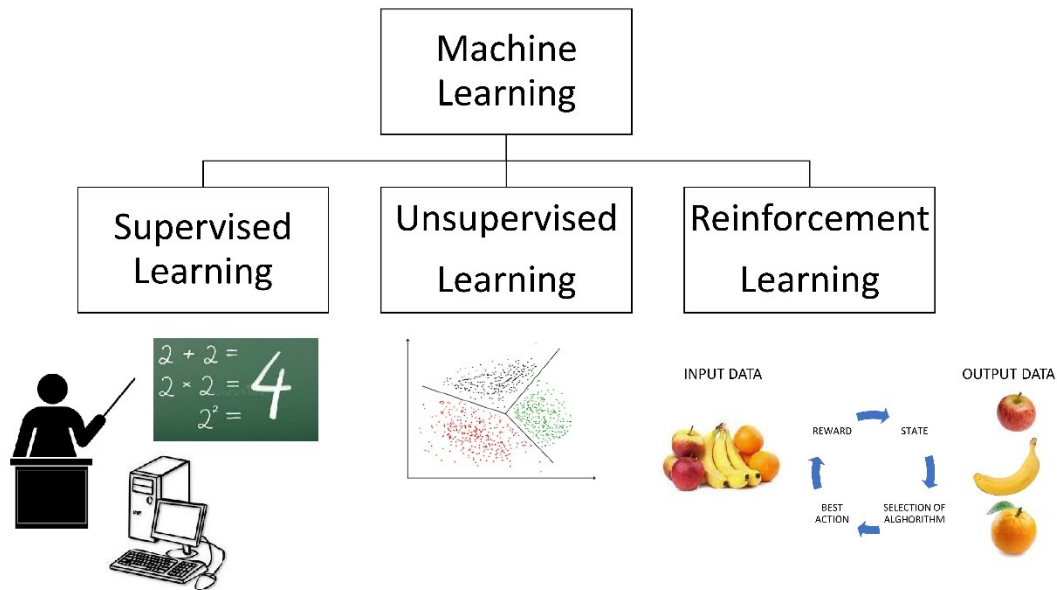


Figure 21: *Principal methods of learning in Machine Learning applications.*

2.5.1 Supervised machine learning

Supervised machine learning stands as an extensively utilized approach within the domain of artificial intelligence and data science (Burkart and Huber, 2021). It serves as a methodology enabling computer systems to acquire knowledge from data and subsequently formulate predictions or decisions predicated on this acquired information. In the supervised learning paradigm, the algorithm is presented with a dataset characterized by labelled instances. This dataset comprises input-output pairs, where the inputs represent the data's features or attributes, and the outputs correspond to the associated target values or labels. The principal objective of supervised learning is to facilitate the training of a model capable of generalizing from the furnished examples, thereby accurately predicting outcomes for novel, unseen data (Alpaydin, 2020).

At the core of supervised learning is the conceptual analogy of a teacher instructing a student. In this analogy, the algorithm functions as the student, while the labelled dataset assumes the role of the "teacher". The teacher's responsibility is to provide correct answers or labels during the training phase, thereby guiding the model as it iteratively adjusts its parameters to enhance its predictive performance. This process of learning from labelled data positions supervised learning as a fundamental tool across a diverse spectrum of applications, ranging from image recognition and natural language processing to medical diagnosis, financial forecasting, and geosciences application (Alpaydin, 2020).

2.5.2 Unsupervised machine learning

Unsupervised learning is an important facet of machine learning, distinct from its supervised counterpart (Hastie et al., 2009). In contrast to supervised learning, which deals with labelled data to make predictions or classifications, unsupervised learning operates on unlabelled data, seeking to discover intrinsic patterns, structures, and relationships within the information. It is a branch of

machine learning where algorithms delve into data without predefined categories or target outcomes, allowing them to extract hidden insights and generate valuable knowledge from unstructured information.

Unsupervised learning is an effective tool for uncovering hidden information within large datasets, clustering similar data points, reducing dimensionality, and providing valuable guidance for downstream decision-making (Alpaydin, 2020). Whether in anomaly detection, recommendation systems, or exploratory data analysis, unsupervised learning is instrumental in revealing the intrinsic organization of data and advancing our understanding of the intricate patterns that surround us (Han et al., 2012d).

2.5.3 Reinforced machine learning

Reinforcement Learning (RL) stands as a highly specialized domain within the field of machine learning (Kaelbling et al., 1996). Unlike supervised and unsupervised learning, which rely on labelled data or intrinsic data patterns, reinforcement learning operates in a distinctive paradigm where an autonomous agent interacts with an environment, learning by making a sequence of decisions and receiving feedback in the form of rewards or punishments (Alpaydin, 2020).

In RL, the agent's primary objective is to plan a strategy or policy that maximizes cumulative rewards over time. This results in making a series of decisions, known as actions, in response to the state of the environment. These actions influence the state transitions and, consequently, the rewards received by the agent. The essence of RL lies in the agent's ability to learn from its interactions with the environment and adapt its decision-making process to optimize long-term outcomes (Kaelbling et al., 1996).

Reinforcement learning is particularly well-suited for tasks that involve sequential decision-making, where the optimal strategy may not be readily apparent and must be acquired through trial and error (Rogova et al., 2002). This methodology has gained prominence in various domains, including robotics, autonomous systems, game playing, and recommendation systems. It allows machines to operate autonomously, make complex decisions, and continually refine their strategies to achieve goals in dynamic and uncertain environments (Alpaydin, 2020).

2.5.4 Decision trees and ensemble models

Machine learning has witnessed remarkable growth and innovation in recent years, reshaping industries by automating complex tasks, predicting outcomes, and uncovering hidden patterns within vast datasets. Decision trees and ensemble models have emerged as important and versatile techniques within this dynamic landscape, providing valuable tools for predictive modelling and data analysis (Alpaydin, 2020).

Decision trees are a fundamental class of algorithms in machine learning that excel in both classification and regression tasks (Kotsiantis, 2013). These models emulate human decision-making processes by partitioning the input data space into regions through a hierarchical structure of nodes and branches. Each internal node of the tree represents a decision based on a particular feature, and the leaves yield the final predictions. In the construction of a decision tree, selecting the most appropriate features for splitting the data at each internal node is a challenge. The choice of these features significantly influences the model's accuracy, interpretability, and overall performance, making an understanding of feature importance essential (Alpaydin, 2020).

Ensemble models (Sagi and Rokach, 2018) exploit the strength of multiple base models, such as decision trees, to create an aggregated prediction that often outperforms any individual component. The ensemble approach mitigates overfitting and reduces the risk of being influenced by outliers or noise in the data (Alpaydin, 2020).

Decision trees and ensemble models have proven to be useful tools with numerous applications in various domains:

- **Classification and Regression:** Decision trees are adept at managing classification tasks, where the goal is to categorize data into distinct classes, as well as regression tasks, which involve predicting continuous values (Loh, 2011).
- **Interpretability:** Decision trees are highly interpretable, making them valuable in domains where model transparency and comprehensibility are crucial (Carvalho et al., 2019).
- **Feature Importance:** The concepts of feature importance, enable researchers and practitioners to understand the impact of individual features on model predictions (Zien et al., 2009).
- **Model Robustness:** Ensemble models enhance model robustness by aggregating predictions from multiple base models, reducing the risk of overfitting and increasing generalization (Hancox-Li, 2020).

2.5.5 Random Forest (RF)

Random Forest algorithm is a prominent example of an ensemble learning method (Breiman, 2001). It operates by constructing multiple decision trees based on bootstrapped subsets of the dataset and employing a random subgroup of features at each node. These individual decision trees, when aggregated into an ensemble, aim to mitigate overfitting, and enhance the generalization of the model. By accounting the diversity of the constituent trees, Random Forest excels in predictive accuracy across various tasks (Azar et al., 2014; Deng et al., 2021; He et al., 2021; Kardani et al., 2021).

The Random Forest algorithm can be summarized as follows:

- **Bootstrap Sampling:** A random selection of data points, with replacement, creates multiple subsets from the original dataset. This introduces variability into the training data for each decision tree (Tsamardinos et al., 2018).
- **Feature Subset Selection:** At each node in a decision tree, a random subset of features is considered for splitting. This decorrelates the individual trees, leading to a more robust ensemble.
- **Voting or Averaging:** The predictions from all the decision trees in the forest are combined to produce the final ensemble prediction. In classification tasks, this is often done through majority voting, while regression tasks use averaging.

2.5.6 eXtreme Gradient Boosting (XGB)

Gradient Boosting is a machine learning technique that builds predictive models by combining the outputs of several weaker models, typically decision trees (Chen and He, 2014). The core idea is to iteratively train new models that correct the errors made by the ensemble of previous models. Each new model focuses on the mistakes of its predecessors, gradually improving the overall predictive accuracy (Chen and He, 2014).

XGB, is an advanced implementation of the Gradient Boosting framework (Friedman, 2001). It is specifically designed to optimize performance, speed, and scalability, making valid in various machine learning competitions and applications.

XGB introduces several key innovations and optimizations:

- **Regularization Techniques:** XGB incorporates Lasso and Ridge regularization (McDonald, 2009; Tibshirani, 1996) to control overfitting, allowing it to build more robust models.
- **Parallel and Distributed Computing:** It powers parallel processing and distributed computing, making it highly efficient even on large datasets.
- **Tree Pruning:** XGB employs an advanced tree condensing algorithm to create simpler trees, reducing computational complexity and increasing model generalization (Chen and He, 2014).
- **Customizable Loss Functions:** Users can define custom loss functions, enabling the model to be shaped to specific objectives, such as ranking, survival analysis, and more (Chen and He, 2014).

2.5.7 Mean Decrease of Impurity (MDI)

The concept of Mean Decrease of Impurity (MDI) is a powerful tool for evaluating feature importance in decision tree-based models (Breiman, 2017, 2001).

MDI is a concept established in the decision tree algorithm, with a particular focus on ensemble learning methods. Individual decision trees, when combined into an ensemble, yield robust and high-performing models. MDI, therefore, serves as a quantitative measure to evaluate the importance of each feature in constructing these decision trees (Breiman, 2017). The core idea behind MDI is to assess the reduction in impurity when a specific feature is used to split the data at a node. The impurity is typically measured using metrics such as Gini impurity or information gain (Breiman, 2017). By calculating the mean decrease in impurity across all the decision trees in the ensemble, MDI provides a feature importance score for each variable (Breiman, 2017).

The insights derived from MDI are important in various aspects of machine learning:

- **Feature Selection:** MDI aids in feature selection by ranking features based on their importance. This process not only simplifies models but also leads to better interpretability and, in some cases, improved generalization.

- **Model Interpretability:** Understanding the contribution of each feature through MDI enhances the interpretability of machine learning models.
- **Anomaly Detection:** MDI can be applied in anomaly detection to identify features with unexpected or significant deviations in their importance, potentially signalling data quality issues or unusual patterns.
- **Model Validation:** Consistency in MDI values across different subsets of data can be indicative of model robustness and reliability.

3. PART II: STUDIES PERFORMED AT THE TEST SITE

The second part of this thesis comprises three distinct studies conducted within the Portonovo-Trave Cliffs test site. The initial two studies delineate the geomorphological evolution of the area, examining it through various spatial and temporal resolutions. Conversely, the final study searches into the significance of driving forces by employing a Machine Learning (ML) approach.

The following works are enumerated, explaining their publication status and briefly synthesizing the key aspects related to methodologies and findings:

1. **Quantitative Characterization of Coastal Cliff Retreat and Landslide Processes at Portonovo-Trave Cliffs (Conero, Ancona, Italy) Using Multi-Source Remote Sensing Data:**

This study involves the computation of cliff top retreat at Portonovo-Trave cliffs over the last forty years (1978-2021) through the utilization of combined remote sensing technologies such as UAV and historical orthophotos. Dem Of Difference (DODs) analysis completes DSAS to confirm the determined geomorphological evolution. The findings identify the Trave sector as the most active part of the coastline. The outcomes of this research have been published in the journal Remote Sensing (MDPI) with the reference <https://doi.org/10.3390/rs15174120>.

Fullin, N., Duo, E., Fabbri, S., Francioni, M., Ghirotti, M., Ciavola, P., 2023. Quantitative Characterization of Coastal Cliff Retreat and Landslide Processes at Portonovo – Trave Cliffs (Conero , Ancona , Italy) Using Multi-Source Remote Sensing Data.

2. **Comparing Multiple High Accuracy UAV-SfM Derived Point Clouds for Geomorphological Change Detection at Portonovo-Trave Cliffs (Conero, Ancona, Italy):**

This study focuses on comparing two UAV surveys conducted in 2021 and 2022 at the Portonovo-Trave cliffs. The resulting point clouds are examined, and the annual geomorphological evolution is discussed. The outcomes reveal the presence of localized notching not identified in previous analyses, particularly in the Mezzavalle sector, underscoring the significance of integrating high spatial and temporal resolution data. The Trave sector remains notably highlighted as the most active part of the coastline. This work is currently in draft form and awaits revision by the research group.

3. **Detection of Cliff Top Erosion Drives through Machine Learning Algorithms between Portonovo and Trave Cliffs (Ancona, Italy):**

In this research, the computation of cliff top erosion between 1978 and 2022 in the Portonovo-Trave region is accomplished. Topographic, marine, and geological parameters are extracted along Digital Shoreline Analysis System (DSAS) transects. Machine learning algorithms, including Random Forest (RF) and XGBoost (XGB), are employed to assess the importance of each driving factor relative to erosion. The study highlights cliff height as the most critical factor correlated with cliff top retreat. This work is ready for submission to an academic journal.

3.1 Quantitative characterization of coastal cliff retreat and landslide processes at Portonovo-Trave cliffs (Conero, Ancona, Italy) using multi-source remote sensing data.

3.1.1 Introduction

High coasts represent about 75% of the world's coastline (Williams and Pranzini, 2018) and can be composed by both soft and hard rocks, with soft rocks usually characterized by an uniaxial compressive strength (UCS) ≤ 5 MPa and hard rocks by UCS > 5 MPa (Sunamura, 2015).

The study of cliffed areas, with particular focus on coastal retreat and slope failures, involves several factors such as geological, geomorphological and structural settings (Sunamura T., 1992; Trenhaile, 2012), wave action (Brideau et al., 2009; Budetta et al., 2000; Kennedy et al., 2011; Naylor et al., 2010; Piacentini et al., 2021; Sunamura, 2015; Sunamura T., 1992; Trenhaile, 1987), sediment input (Kennedy and Milkins, 2015; Komar and Shih, 1993), cliff topography (Robinson, 1980; Sunamura, 1991), beach width (Everts, 1991) and energy contents of waves (Poate et al., 2018).

In particular, geological structures can play a key role in controlling the morphology and stability of high coastlines (Prémaillon et al., 2021; Stead and Wolter, 2015), changing asymmetrically the values of shear strength and uniaxial compressive strength along the cliff. Furthermore, wave action and sea level rise can lead to the creation of coastal notches and progressively to the collapse of large parts of the cliffs (Fazio et al., 2019; Sunamura, 2015).

In this already complex scenario, it must be considered the effect of climate change which tends to modify the frequency and intensity of instability factors, such as storminess, storm energy and sea level rise. In fact, although the role of such phenomena is well known in coastal failures and retreats (even in case of single major events, Brooks and Spencer, 2016) (H.-O. Pörtner, D.C. Roberts, M. Tignor, E.S. Poloczanska, K. Mintenbeck, A. Alegría, M. Craig, S. Langsdorf, S. Löschke, V. Möller, A. Okem, 2022), their prediction is becoming more and more difficult. Examples of the effect of sea level rise in coastal areas has been presented by Bruun 1962 (Bruun, 1962) and Ashton et al., 2011 (Ashton et al., 2011). Diversely from the model proposed by Bruun (Bruun, 1962) for sandy coast, Ashton et al., (Ashton et al., 2011) demonstrated how, in case of high rocky coastline, the rate of sea-level rise results in increased profile of slopes.

In the last decades, along with these new environmental challenges, new technologies have been developed and adapted for more accurate analysis. In particular, for cliffs, Terrestrial Laser Scanning (TLS) (Caputo et al., 2018; Esposito et al., 2020; Matano et al., 2015; Rosser et al., 2005a), orthophotos (Del Río et al., 2020; Warrick et al., 2017), UAV (Esposito et al., 2017; Francioni et al., 2018a; Koukouvelas et al., 2020; Martino and Mazzanti, 2014; Westoby et al., 2012) and Persistent Scatterer Interferometry Synthetic Aperture Radar (PSInSAR) (Mateos et al., 2017) were successfully used for monitoring their temporal and morphometric evolution.

The use of aerial photographs can be very useful for the assessment and evolution of cliff behavior along wide coastal sections. However the spatial and temporal resolution of aerial photography is often not suitable to gather significant results (Del Río et al., 2020). The adoption of more recent survey techniques (when available) for reconstructing coastal topography, such as Aiborne and Terrestrial Laser Scanning (ALS/TLS) and UAV, remarkably improve the evaluation of short- to medium-term cliff erosion processes and rates (Calligaro et al., 2013; Koukouvelas et al., 2020; Piacentini et al., 2021; Young, 2018). TLS has very high accuracy, but it may be difficult to be used in coastal areas because of the inaccessibility of many slopes. The use of ALS overcomes the problem connected with the TLS by, on the other hand, it may be very expensive. As for the TLS and ALS, the UAV can be used to derive DEMs of the investigated areas and, although the lower accuracy of the products (Casella et al., 2020; Duo et al., 2021; Seymour et al., 2018; Turner et al., 2016), they represent a low-cost solution to acquire data at local and large scale, also in inaccessible areas, constituting one of the best cost-effective choice in coastal monitoring (Godfrey et al., 2020). In some

cases, the combination of the above mentioned techniques become very important (although challenging) to obtain a more complete dataset (in terms of spatial and temporal data) (Cenci et al., 2018; Colica et al., 2023; Del Río et al., 2020; Francioni et al., 2018a; Martino and Mazzanti, 2014). In this context, this paper aims to study erosion processes in the area between Portonovo and Trave (Ancona, Italy, Fig.1) through the combined use of aerial photography, UAV photogrammetry and LiDAR data. It is important to note that these remote sensing techniques played an outstanding role, giving the possibility to study the entire area decreasing the risk for surveyor. The integration of these remote sensing techniques with conventional geological and geomorphological surveys allowed to recognize the coastline sectors with higher retreat values and, at the same time, to explore the potential and more important factors contributing to the retreat. In particular, we have considered geological, geomorphological, structural, meteorological and marine factors.

The cliff top retreat analysis has been carried out through the Digital Shoreline Analysis System (DSAS) (Thieler et al., 2009) and DoD calculations. The DSAS was applied to orthophotos spanning from 1978 to 2021. A DSM of the area was created from a UAV survey conducted in 2021 and compared with 2012 LiDAR data DTM for the DoD calculations.

3.1.2 Study Area Description

The study area is located in the central Adriatic coast, a few kilometers south of Ancona, between Portonovo and Trave in the Conero promontory (Fig.22). This area is characterized by high cliffs ranging from tens to hundred meters in elevation and slopes from almost flat to 80° of steepness.

From a geological point of view, the Conero promontory belongs to the central sector of the present-day foredeep basin and foreland ramp of the Outer Northern Apennine fold and thrust belt (Calamita et al., 1999; Cello and Coppola, 1989; Coltorti et al., 1987; Iaccarino et al., 2008). In the study area Neogenic formations from Miocene to present time outcrop. These formations, Schlier, Formazione a Colombacci, Formazione di Sapigno, Orizzonte del Trave and Argille Azzurre (Coltorti and Sarti, 2011) are mainly composed by marls, clays, sandstones and gypsum. The bedrock is often covered by landslide deposits, well recognizable along the whole study area (Montanari et al., 2016).

The structural setting of the area is characterized by the presence of two principal thrusts with typical Apennine lineaments NW-SE oriented, well known in literature (Coltorti and Sarti, 2011). The first one is well exposed between Portonovo and Mezzavalle and brings the Schlier Fm. on top of the Colombacci Fm.; the second thrust, close to the Trave, brings the Sapigno Fm. over the Argille Azzurre Fm.

From the geomorphological point of view, intense processes of erosion and many landslides characterize this part/sector of the coastline, giving a badland-like appearance to these slopes.

The landslides are well documented in the landslide database of Istituto Superiore per la Ricerca e Protezione Ambientale (ISPRA) IdroGEO, occurring mostly in Trave sector (<https://idrogeo.isprambiente.it/app/iffi/>). The study area is characterized by composite landslides, rock rotational slide, clay/silt rotational slide, rock fall, rock block topple and earthflow (Hungar et al., 2014). Landslides identified in the study area are active or re-activated state of activity (Cruden, D.M., Varnes, 1996).

Their crown is prevalently located along the morphological edge that separates the inland from the coast. The area interested by landslide phenomena is estimated to be approximately 280000 m².

With regard to the pedology and soil cover these have been documented and described by the Parco Nazionale del Conero authority (https://www.regione.marche.it/natura2000/public/allegati_blog/1682/File%20non%20disponibile.pdf). The soil covering the marls and calcareous bedrock is called regosol or lithosol Xerorthents typic and lithic. Unluckily, no information was reported about the different depth of this level along the coastline.

Further available data from Corine Land Cover (<https://land.copernicus.eu/pan-european/corine-land-cover>) of 1990 and 2018 were checked in order to find information regarding land use change and vegetation.

It has been founded that the area corresponding to the Trave sector was classified from 1990 with the code 141 as “Green urban areas” and the other two sectors with the code 311 as “Broad-leaved forest”. From 2018 the Trave sector was classified with the code 323 “Sclerophyllous vegetation”, while the other two sectors remained under the code 311 as “Broad-leaved forest”.

According to morphology and geological characteristics, the coastline has been divided in three different sectors (Fig. 23) defined from South to North: Sector “1”, named Portonovo, is E-O/NW-SE oriented and stretches from Portonovo to the beginning of the Mezzavalle sector. This sector is mainly characterized by the Schlier Fm.. Sector “2”, called Mezzavalle, is approximately NW-SE oriented and mainly covered by landslide deposits. Sector “3”, entitled Trave, approximately N-S/NW-SE oriented, is characterized by high and steep cliffs (± 200 meters) along which tectonized flyschoid formation (Argille Azzurre Fm.) largely outcrop.

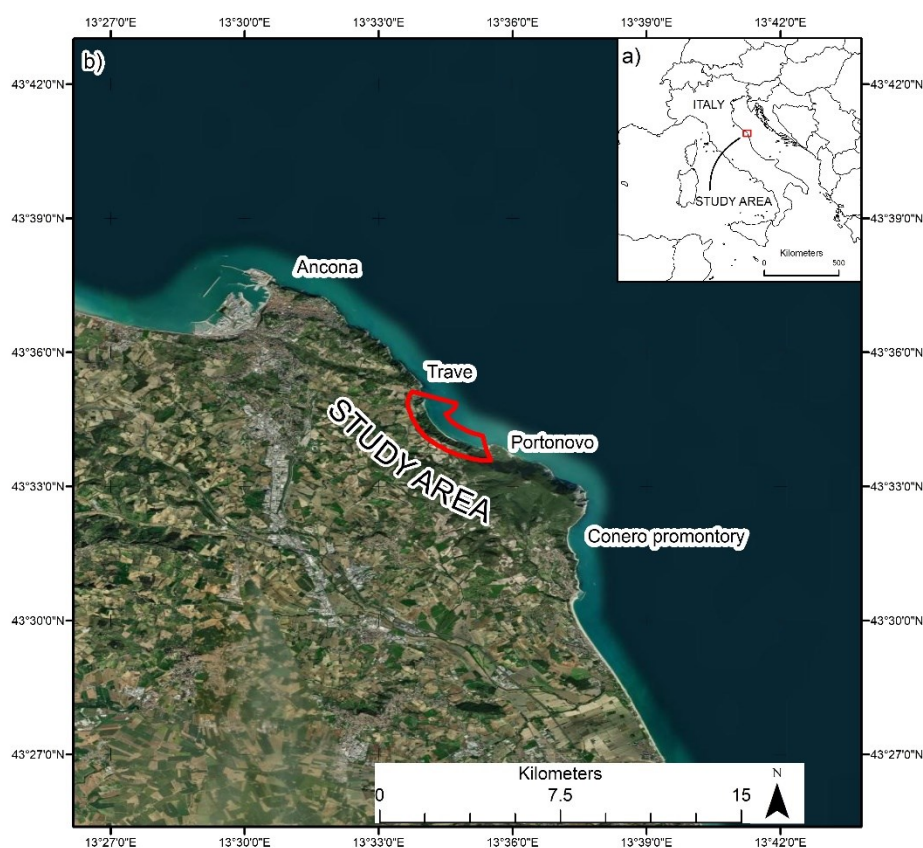


Figure 22: a) Location map of the study area. b) Satellite image showing the study area delimited by a red line (image taken from GeoEye satellite database, 2020).

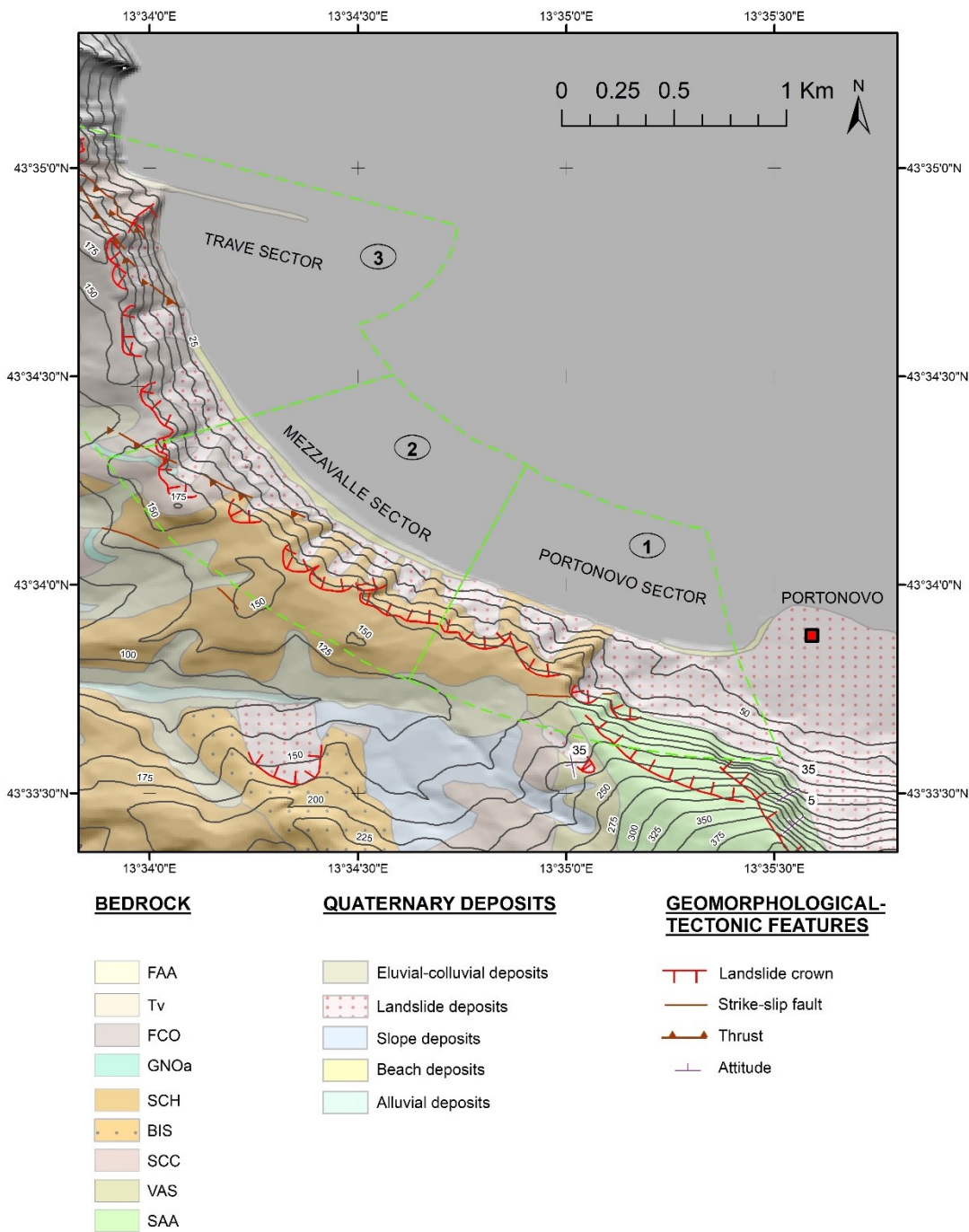


Figure 23: Geological setting of the study area (Coltorti M., 2011) and “Sectors”: 1) Portonovo; 2) Mezzavalle; 3) Trave. Bedrock legend: SAA (Scaglia Rossa Fm., Upper Cretaceous-Medium Eocene); VAS (Scaglia Variegata Fm., Medium Eocene-Upper Eocene), SCC (Scaglia Cinerea Fm., Upper Eocene-Upper Oligocene), BIS (Bisciaro Fm., Lower Miocene), SCH (Schlier Fm., Lower Miocene-Upper Miocene), GNOa (Sapigno Fm. Upper Miocene), FCO (Colombacci Fm., Upper Miocene), Tv (Trave horizon, Lower Pliocene), FAA (Argille Azzurre Fm., Lower Pliocene-Lower Pleistocene). The Trave horizon is a natural stratum that forms a ridge outcropping from the sea in the northern section of the study area.

The coastline object of this study overlooks on the northern-central Adriatic Sea (Bisci, Carlo; Cantalamessa, Gino; de Marco, Rocco; Spagnoli, Federico; Tramontana, 2021). The Adriatic sea is a microtidal environment (Bisci, Carlo; Cantalamessa, Gino; de Marco, Rocco; Spagnoli, Federico; Tramontana, 2021) and this sector is characterized by two different prevalent seas, reigning sea coming from S-SE (Sirocco), namely the most frequent direction of wave storm events and conjoined winds and dominant sea from NE (Bora), the direction of wave storm with major intensity (Acciarri et al., 2021; Perini, L.; Calabrese, L.; Marco, D.; Valentini, A.; Ciavola, P.; Armaroli, 2011). Additionally, it is possible identify along the coast of this region a littoral drift moving northwards (Grottoli et al., 2015).

3.1.3 Materials and Methods

With the aim of quantifying morphodynamical processes acting on these cliffs, we have performed an interdisciplinary study which includes:

Fieldwork.

The analysis of meteorological and marine data.

Cliff-top retreat in different periods, using the DSAS tool for ArcGis. (<https://www.arcgis.com/home/index.html>).

DoD between an available 2012 Lidar data and a 2021 DSM extracted from UAV photographs, to improve our understanding of cliffs retreat rate and validate results from multitemporal orthoimages analysis.

3.1.3.1 Fieldwork and GIS Topographic Analysis

During the fieldwork a geological survey of the area was performed with the goal of improving the details of the existing maps/information integrated through the use of a pocket penetrometer and a Schmidt hammer according with ISRM guidelines (Ulusay, 2014). This allowed to gather values of uniaxial compressive strength (UCS) both for deposits and bedrock in the three studied sectors. Furthermore, to improve the information about rock mass quality along the coastline the rock mass classification “geological strength index” (GSI) was performed (Hoek et al., 2005; Marinos and Hoek, 2018, 2001; Marinos et al., 2005; Marinos, 2017). Starting from the 2012 DTM provided by Marche region in GIS environment, an elevation model was carried out working in the symbology of the raster and a slope model was created thanks the tool *slope*.

Furthermore, the beach width in the different sectors was extracted in GIS, starting from an orthophoto taken on 28/29 September 2021. Profiles spaced 30 meters, for a total of 104, were traced perpendicularly respect the shoreline and width measured along their length between the berm crest and the cliff base. Then, all the values obtained were stored in a table and a mean value for each sector identified.

3.1.3.2 Analysis of Meteo and Marine Data

The analysis of marine data was implemented using the 1994-2019 wave hindcast produced by CNR-ISMAR for the Adriatic Sea in the framework of a collaboration between the University of Ferrara, the CNR-ISMAR and the Autorità di Bacino del Fiume Po (ADBPO). This was part of the Research Programme Venezia 2021, coordinated by CORILA, with the contribution of the Provveditorato for the Public Works of Veneto, Trentino Alto Adige and Friuli Venezia Giulia (Benetazzo et al., 2022). The wave dataset is based on the WaveWatch3 (WW3) numerical model implemented for the Adriatic Sea using a grid with spatial resolution ~2.5 km using high resolution (~80 m) bathymetry from

EMODnet. The model was forced with an edited version of ERA5 to correct the bias due to the general underestimation of the wind intensity on the Mediterranean Sea of the original dataset. The wave dataset is provided in NETCDF format (i.e. 1 file for each year, hourly data). The 2018 high-resolution bathymetry from ARPAE was used to extract the 20 m depth bathymetric contour as source to extract coastal points as reference positions for the analysis. A set of coastal points were defined in front of the Mezzavalle-Trave area (Fig. 24).



Figure 24: Coastal points defined in front of the area of interest. The points are positioned on the 20 m depth contour of the bathymetric dataset provided by ARPAE.

The significant wave height (h_s) timeseries was extracted from the gridded data of the CNR-ISMAR datasets for each defined coastal points using the nearest point method. The yearly timeseries were merged. Independent extremes were identified through a Peak-over-Threshold analysis where the threshold was calculated as quantile of the provided timeseries, and the independence criteria was based on a time window.

The analysis was implemented using the python library `pyextremes` (<https://georgebv.github.io/pyextremes/>).

Regarding the rainfall data, these were retrieved from Sistema Informativo Regionale Protezione Civile Marche. The data are available on Regione Marche website (<https://www.regione.marche.it/Regione-Utile/Protezione-Civile/Progetti-e-Pubblicazioni/Annali-Idrologici#Annali-Idrologici---Parte-1>) from 1990 and are related to the meteorological station “Ancona Torrette” with a daily sample frequency and without gaps. From 2003, another station was used “Ancona Regione RT-1638”, data are available in the website after registration (<http://app.protezionecivile.marche.it/sol/indexjs.sol?lang=it>) with a sample frequency of 15 minutes and no gaps in the record. Both stations are ca 5-8 km norther from the cliffs object of this study.

3.1.3.3 UAV Survey and Data Elaboration

Because of the extension of the study area (about 1.5 km²), the UAV data acquisition was accomplished in two consequent days, 28/29 September 2021 using a commercial drone DJI Phantom Vision 3+ Pro equipped with a camera: FC300X (focal length: 3.61 mm; pixel size: 1.56 × 1.56 μm). Flights were conducted at a constant elevation of 120 m covering the top cliff, and 60-70 m covering the beach area, using automated flight plans created using the “Drone deploy” opensource application (<https://www.dronedeploy.com/>). Front and side overlap between each photo was ~70% and flight speed 8-10 m/s.

The UAV survey was supported by an RTK-GNSS survey using a Trimble RTK-DGPS R8 (i.e., stop and go technique; horizontal accuracy of 8 mm and vertical accuracy of 15 mm) which was used to acquire the position of 22 ground control points (GCPs). These were made of white and red wooden square targets, measuring 60 × 60 cm, and distributed within the study area. The Universal Transversal Mercatore WGS84 zone 33N was used as coordinate system and the ellipsoidal height was converted to orthometric height using national grids using the software “Convergo” (https://www.cisis.it/?page_id=3214). Estimate error during the RTK-GNSS survey was approx 6 cm horizontally and vertically.

“Agisoft Metashape” (version 1.5.1 <https://www.agisoft.com>) was used to manage and process UAV data and GCP coordinates. Using the procedure suggested by different authors (Brunetta et al., 2021; Duo et al., 2021; Fabbri et al., 2021b; Gindraux et al., 2017; Talavera et al., 2021) it was possible to create the DSM and orthophoto of the surveyed area.

3.1.3.4 Morphological analysis

Although the DSAS tool was created to analyse the shoreline movements, its use in cliff retreat studies is widely documented in the literature (Brooks et al., 2012; Gómez-Pazo et al., 2021; Hapke and Plant, 2010; Lollino et al., 2021).

The study was performed using orthophoto acquired in 1978, 1998, 2007, 2010 and 2021. The first four (1978, 1998, 2007 and 2010) are available on institutional websites (<http://www.pcn.minambiente.it/viewer/index.php>, <http://wms.cartografia.marche.it/geoserver/Ortofoto/wms>). The 2021 orthophoto is the one extracted from UAV photographs. Spatial resolutions of such orthophotos are reported in Table 6.

Table 6: *Spatial resolution of the orthophotos used for the cliff top retreat analysis.*

Date (yr)	1978	1998	2007	2010	2021
Cell size (m)	1.28 x 1.28	1 x 1	0.5 x 0.5	0.5 x 0.5	0.1 x 0.1

The DSAS analysis is based on the comparison of different cliff top edge mapped over the years. The comparison is made using the cliff tops edges and a baseline as reference line. Cliff top edges was manually mapped on the orthophotos, keeping the same visual scale on all the photos (Scale 1:3000) and using the limit between vegetation and bare slope as edge of the cliff (Fig.25a). The accuracy of manual mapping was defined following the example of Crowell et al. (1991), Fletcher et al. (2003) and Del Río and Gracia (2013) (Crowell et al., 1991; Del Río and Gracia, 2013; Fletcher et al., 2003). The approach used is based on the use of the Spatial Adjustment tool in ArcGIS (Buchanan et al., 2020; Cenci et al., 2013; Fabbri et al., 2021b; Viridis et al., 2012); the cliff top edge is mapped 4 different times and the difference between each line is then calculated measuring the offset between a couple of line per time, along several perpendicular thick profiles. Once each couple of the data set (for each image) were tested, the highest error was taken as reference. For what concerns DSAS calculations, as reference line and base line, we have used the shoreline, which was mapped in the 2021 orthophoto, thanks to the different color between the sand and the sea. The same procedure described before was used to calculate the error in the digitalization of the shoreline. Hence, a 100 m buffer of this line was performed in GIS environment (being sure that the buffer was beyond the cliff top edges) (Fig.25b). Starting from this baseline, the software creates a series of transects. In this case we have defined a distance between each transects of 10 meters, for a total of 310 transects. An example of transects created during the DSAS analysis is shown in Figure 25c. Along them, the software verifies the changes in the cliff top edges and calculates the Net Shoreline Movement (NSM,

the total movement measured in meters) and the End Point Rate (EPR, the rate of movement calculated in meters per years). Hence, Confidence of End Point Rate (ECI or EPR_{unc} in newer versions of DSAS) was calculated. This is an index which takes into consideration the uncertainty of lines (accuracy error) as a factor for calculating the EPR confidence.

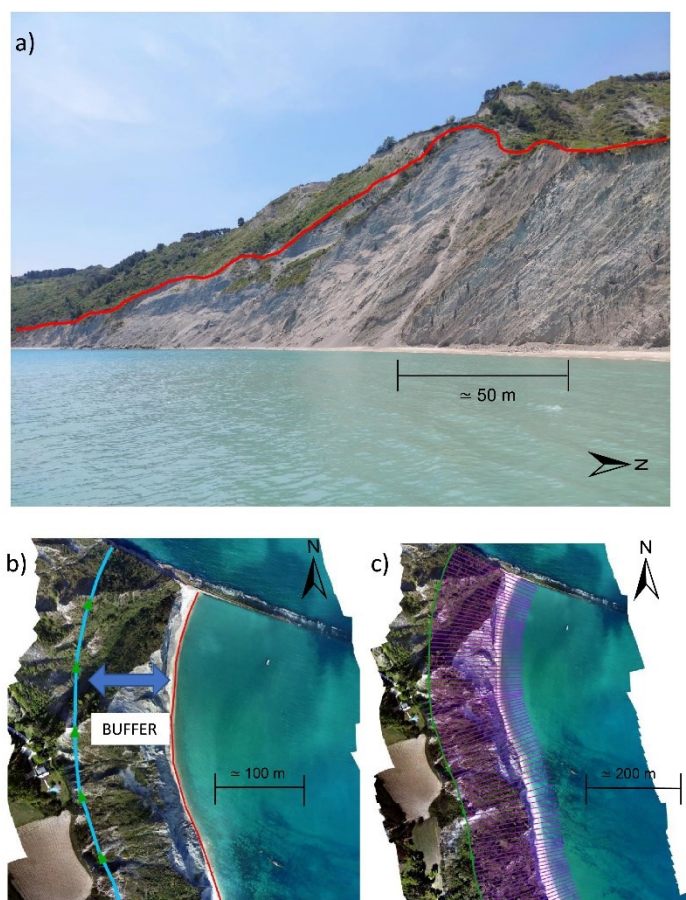


Figure 25: Methodology followed in DSAS elaboration. a) We used as cliff top the edge between vegetated slope and the bare cliff (showed by the red line). b) The baseline (the blue line), i.e. the line from which all the transects origin, was created using a buffer of the identified shoreline, with the aim of obtaining transects as much perpendicular as possible respect to the coastline. c) Image showing the baseline (in green) and the transects (in violet) obtained by DSAS elaboration.

Considering the available information about waves (1994-2019) and precipitation (1990 to current), it was decided to perform DSAS analysis using 1998-2007 and 2010–2021 time spans, in order to have a temporal correspondence between computed erosion processes and external drives (Fig. 26). A further analysis was also undertaken for the period 1978-2021 (although no wave and precipitation were available until 1990) to verify the coastal retreat in the whole 40 years and compare such results with other periods.

Finally, to further verify the results of DSAS analysis, a DoD analysis was carried out. The use of DoD is becoming a common practice in geosciences (Gómez-Pazo et al., 2021; Jaboyedoff et al., 2012b; Williams, 2012). In this case we have used the 2012 airborne Lidar (near infrared and green) DTM with a cell size of 4x4 m given by Marche Region and the 2021 UAV extracted DSM with a cell size of 0,25x0,25 m. The accuracy of UAV extracted DSM product was computed checking the differences between control points coordinates acquired through RTK-DGPS and the coordinates of same points on UAV's extracted DSM, computing the mean error and the RMSE. In particular, we have found a planimetric mean error of 31 cm with RMSE of 12 cm and a vertical mean error of 5

cm with a RMSE of 6 cm (Committee and others, 1998). The 2012 airborne Lidar has a vertical RMSE < 10 cm and a planimetric RMSE <10 cm, as reported by the Marche Region. The two rasters were compared after a resample, keeping the coarsest resolution through the GIS tools resample and clip. Vegetated areas were excluded from the analysis and the UAV DSM was resampled at the same resolution of the Lidar based DTM. The raster calculator was used to compute the differences between the two rasters in elevation. Statistical analysis on resulting data was performed for each sector, obtaining mean, maximum and minimum values of variation for each sector.

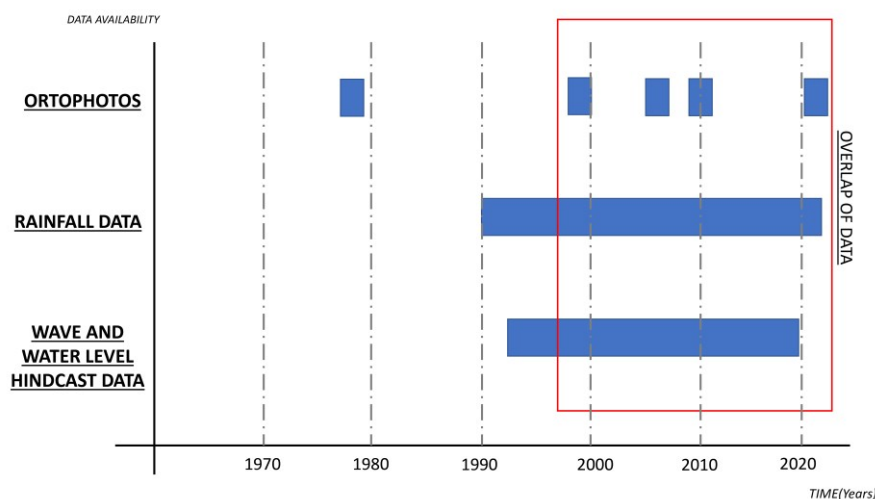


Figure 26: Picture showing distribution of different data through time. The overlap window is between 1998 and 2021.

3.1.4 Results

3.1.4.1 Fieldwork and GIS analysis

The geological and structural surveys highlighted the main differences between the 3 sectors. Moving from Portonovo to Trave we found different geological formations, i.e. Schlier Fm. / Sapigno Fm. / Argille Azzurre Fm. and, Colombacci Fm. with different geotechnical characteristics as evidenced by the values of GSI and UCS gathered through pocket penetrometer and a Schmidt hammer (Table 7). Rock mass classification together with UCS, have been shown as factors of unneglectable importance in coastal cliff erosion, predisposing slopes to more frequent failures (Budetta et al., 2000; Prémaillon et al., 2018; Sunamura, 2015). We have therefore considered that GSI and UCS represent the more suitable geotechnical parameters to characterize, according to the lithotypes outcropping in the area, soil or weak rocks.

Table 7: Range of GSI and UCS values for the 3 sectors.

	GSI (Flysch)	UCS (MPa)
PORTONOVO	50-60	30-35
MEZZAVALLE	/	0.5-5
TRAVE	15-30	5-30

We obtained the smallest values of UCS along the Mezzavalle sector, which is basically characterized by landslide deposits (for them the GSI classification it is not applicable). In the Portonovo sector we obtained the highest values of GSI and UCS. In the Trave sector these values are very variable and

depend on the structural features present which determine high fracturing degree, as in corresponding to the tectonic contact between the Sapigno Fm. and the Argille Azzurre Fm. (Figure 27a) which gave rise to a completely fractured zone in the Argille Azzurre Fm. itself (Figure 27b).

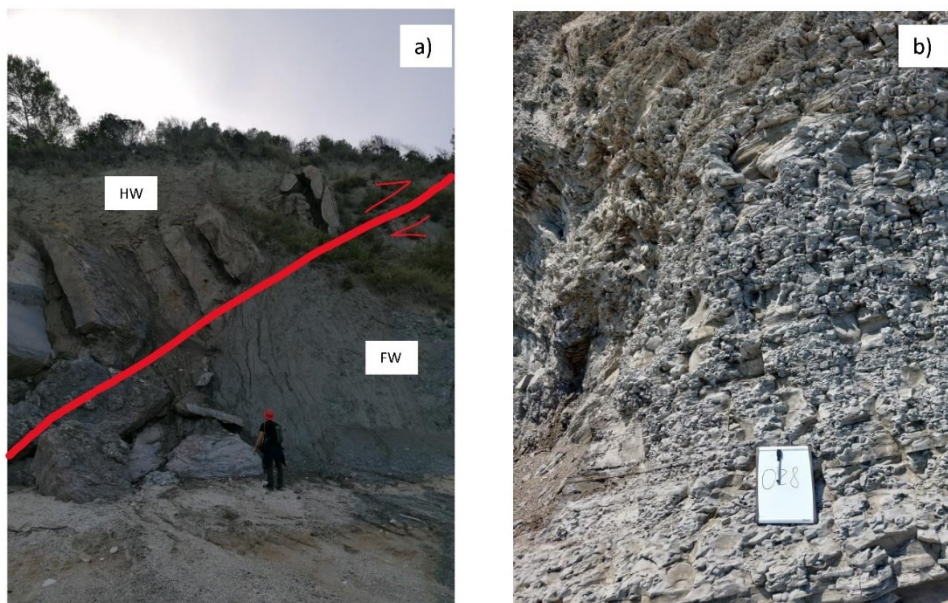
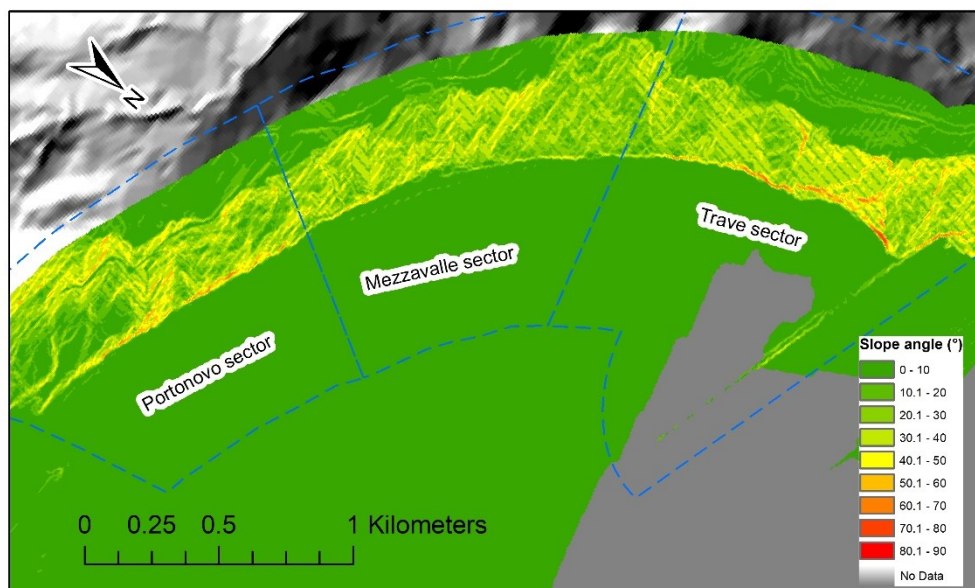


Figure 27: At Trave sector. a) The Sapigno Fm., composed by gypsum, is thrust on the younger Argille Azzurre Fm.. The trend of coastline in this picture is N-NW/S-SE and the attitude of the fault plane is 205/40 in Dip Direction and Dip convention. b) Outcrop of the Argille Azzurre Fm. composed of marls, completely fractured in blocks of few centimeters.

Furthermore, thematic maps developed in GIS using LiDAR data show that, among the three sectors, the Trave sector is characterized by the steepest and highest cliffs (Fig.28). The mean beach width computed of the three sectors was 6.7 m, 23.5 m and 7.6 m for Portonovo, Mezzavalle and Trave respectively.

a) **SLOPE MAP DISTRIBUTION**



b) **ELEVATION MAP DISTRIBUTION**

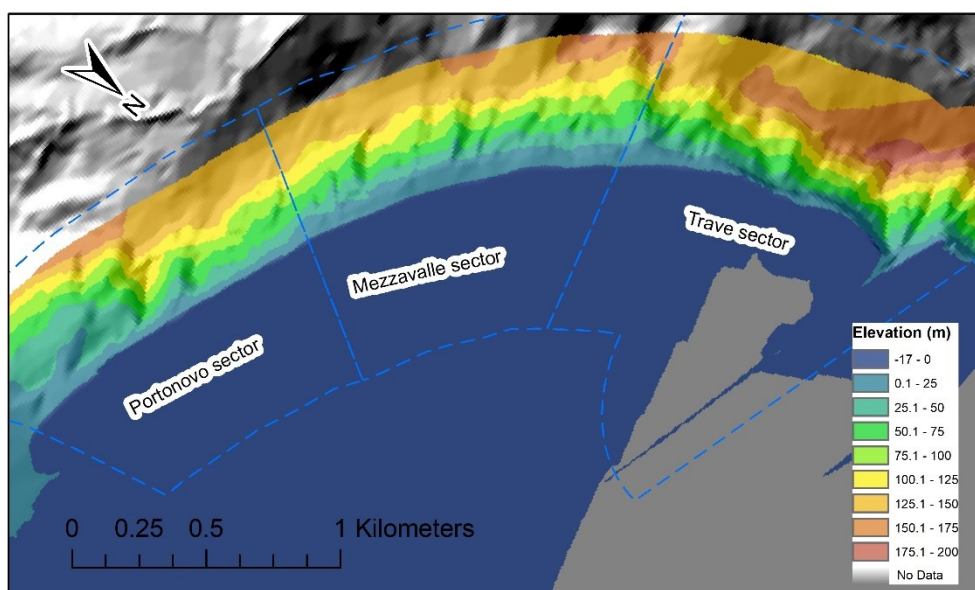


Figure 28: a) Values of slope and b) elevation: Trave sector shows the highest values for both the considered parameters.

3.1.4.2 Analysis of Meteo and Marine Data

Data from CNR-ISMAR are displayed in Fig. 29 along with the results of the POT analysis (threshold: 99.5 percentile; independence criteria: 48 hours) for the significant wave height (hs) for the coastal point CP005. Here, the hindcasted over-threshold events between 1994 and 2019 are reported. The average number of events per year is 4.5, which is in line with the expected range (3-5) for traditional POT analysis. It is not possible to identify any kind of trend in the rate of storminess in the whole period considered, it can be only noted that after 2012 the number of events with $hs > 4,5$ m is higher respect the period before (1994-2012).

Regarding the rainfall data, the annual average precipitation recorded between 1990 and 2021 is 664 mm. It is possible to identify two years where precipitation exceeded mean values, 2010 (with 1034 mm) and 2014 (with 966 mm), and two years with dryer conditions, 2011 and 2012, with 433 mm and 447 mm of precipitation, respectively (Fig. 29).

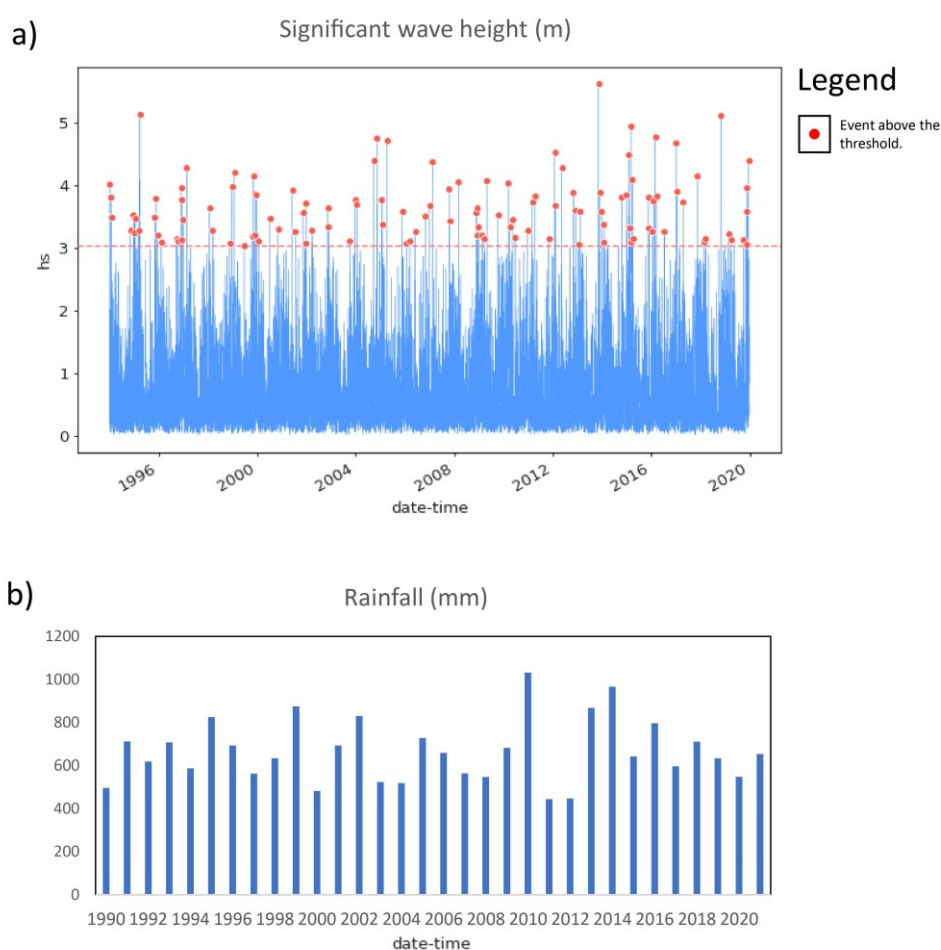


Figure 29: Summary of wave and rainfall parameters: a) POT analysis of CNR-ISMAR data between 1994-2019 for the significant wave height (hs) for coastal point CP005, showing the identified events. The peak value is highlighted by a red dot. b) Precipitation recorded by the stations “Ancona Torrette” and “Ancona Regione RT-1638” in the period 1990-2021.

3.1.4.3 Morphological analysis

Digitalization of the cliff top and the shoreline has been performed and maximum Root Mean Square Error (RMSE) of this operation calculated. In particular, it has been found that the maximum RMSE for cliff top digitalization is obtained for 1978 orthophoto, with a value of 3,89 m. Shoreline digitalization was performed on 2021 orthophoto and resulted in a RMSE of 0.85 m.

Considering the whole period 1978-2021 (Fig.30), Trave sector is the portion with the highest mean value of EPR, Portonovo sector show a similar behavior while Mezzavalle sector shows a marginally positive value. Moreover, focusing on specific area within each sector, values of almost -1 m/yr of EPR are reached between transects 21-31 and 251-291 in Portonovo and Trave sector respectively. ECI computed for this time span is 0.16 m.

Furthermore, the analysis shows that in the period 1998-2007 (Fig.31) cliff top retreat was more concentrated in Trave sector, where we calculated an average mean EPR three times higher than the value obtained for Portonovo and Mezzavalle sectors in the same period. The highest values of EPR were recorded between transects 26 and 44 in Portonovo sector, with values around -2 m/yr and between transects 266 and 286 in Trave sector where we reached the value of -3 m/yr in the EPR. ECI in this time span is 0.79 m.

During the period 2010-2021 (Fig.32), Trave sector resulted to have the highest negative values of EPR, very similar to Portonovo sector and 4 time higher than in Mezzavalle sector. Between transects 226-236 (Trave sector) the EPR overcame -2 m/yr. ECI for this period is 0.62 m. All the values regarding mean EPR and ECI are illustrated in Table 8, while NSM values are represented in Fig. 30,31,32.

Table 8: DSAS results for each period analyzed. Mean EPR and ECI are reported.

Periods	Portonovo		Mezzavalle		Trave	
	EPR (m/yr)	ECI (m)	EPR (m/yr)	ECI (m)	EPR (m/yr)	ECI (m)
1978-2021	-0.20	0.16	0.09	0.16	-0.25	0.16
1998-2007	-0.21	0.79	-0.27	0.79	-0.72	0.79
2010-2021	-0.40	0.62	-0.09	0.62	-0.42	0.62

For what concern the DoD analysis (Fig. 33) Portonovo sector presents a negative mean value of variation from 2012 to 2021 of -2.2 m in elevation. The highest negative value recorded was -16.3 m between transects 51-57 in the middle part of Portonovo sector, where landslides deposits nowadays overly the bedrock.

The DoDs analysis allows to compare the 2012 DTM and the 2021 DSM and highlights difference in elevation between this period. Negative values indicate the loss of material, while positive values, accumulation. Mezzavalle sector displays negative mean values of DoDs of -1,4 m, the maximum height difference is -12.6 m in southern part of the area, between transects 87-94, were Schlier Fm. outcrops. In the rest of the sector no other clear difference was recorded, except for a single pixel value that shows increase for 6.4 m and associated probably with the presence of vegetation yet (Fig.33). In Trave sector a negative mean variation of -3.7 m was recorded for the whole area, with the highest value of -31.2 m, between transects 289-301 near Trave rock. Others negative height differences greater than -10 m were recorded close the edge of cliff top, from transect 230 to 282. Evident areas characterized by positive (accumulation) values were not found. This is probably related to sea action which tend to remove landslide deposits.

The uncertainty of the DoD was computed propagating the uncertainty of the input DEMs, by applying the root of the sum of the square (Brasington et al., 2003) and obtaining values of 11.18 cm for z and 15,62 cm for planimetric component. Furthermore we refined this result multiplying the error values for a t-value of 1.96 (Duo et al., 2021; Wheaton et al., 2010) obtaining an uncertainty of 21.98 cm for z and 30.61 cm for planimetric component.

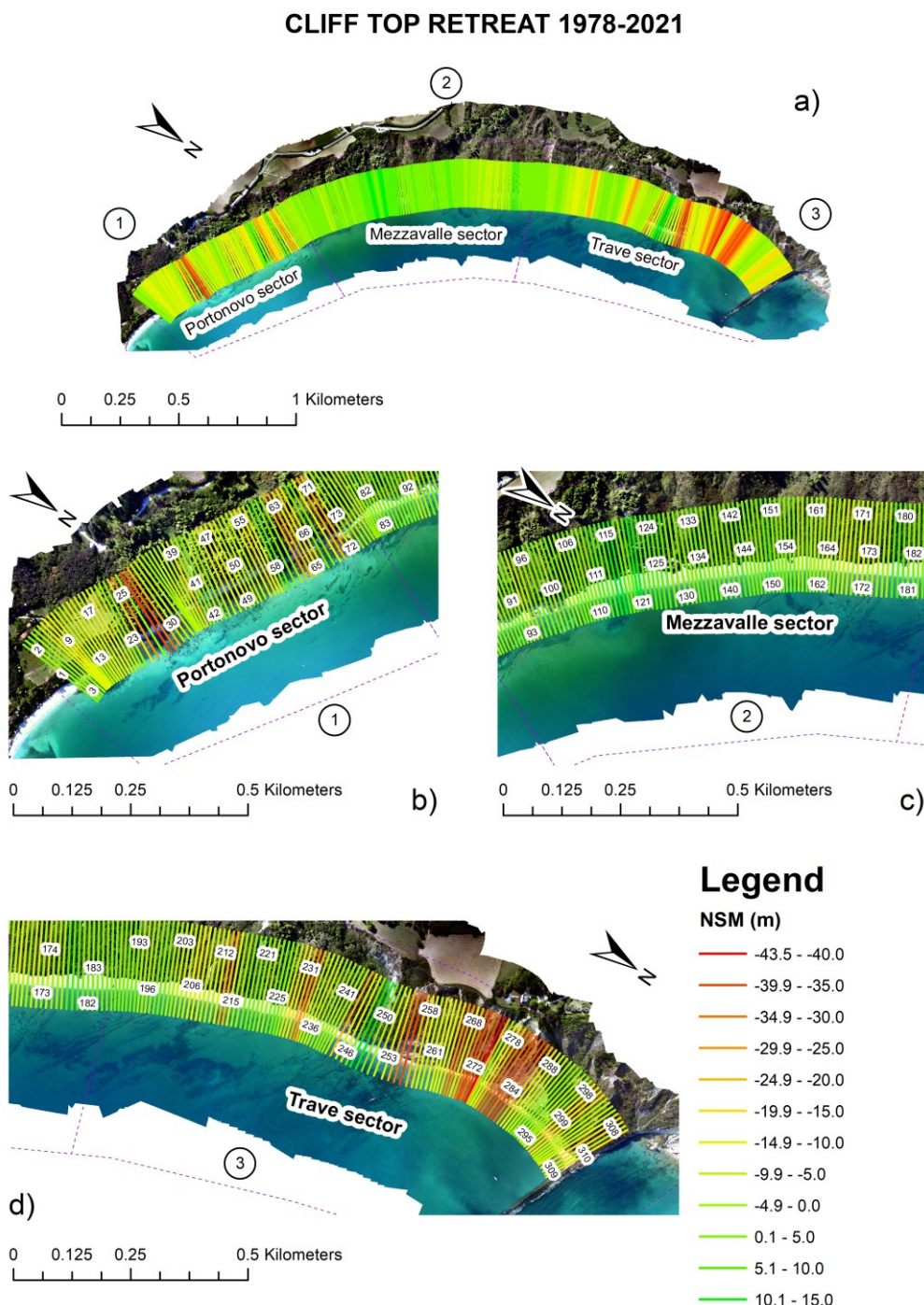


Figure 30: NSM values calculated along transects, referred to the period 1978-2021: Portonovo and Trave sector showed the highest values of retreat. a) computed transects for the whole study area. b) Focus at Portonovo sector. c) Focus at Mezzavalle sector. d) Focus at Trave sector.

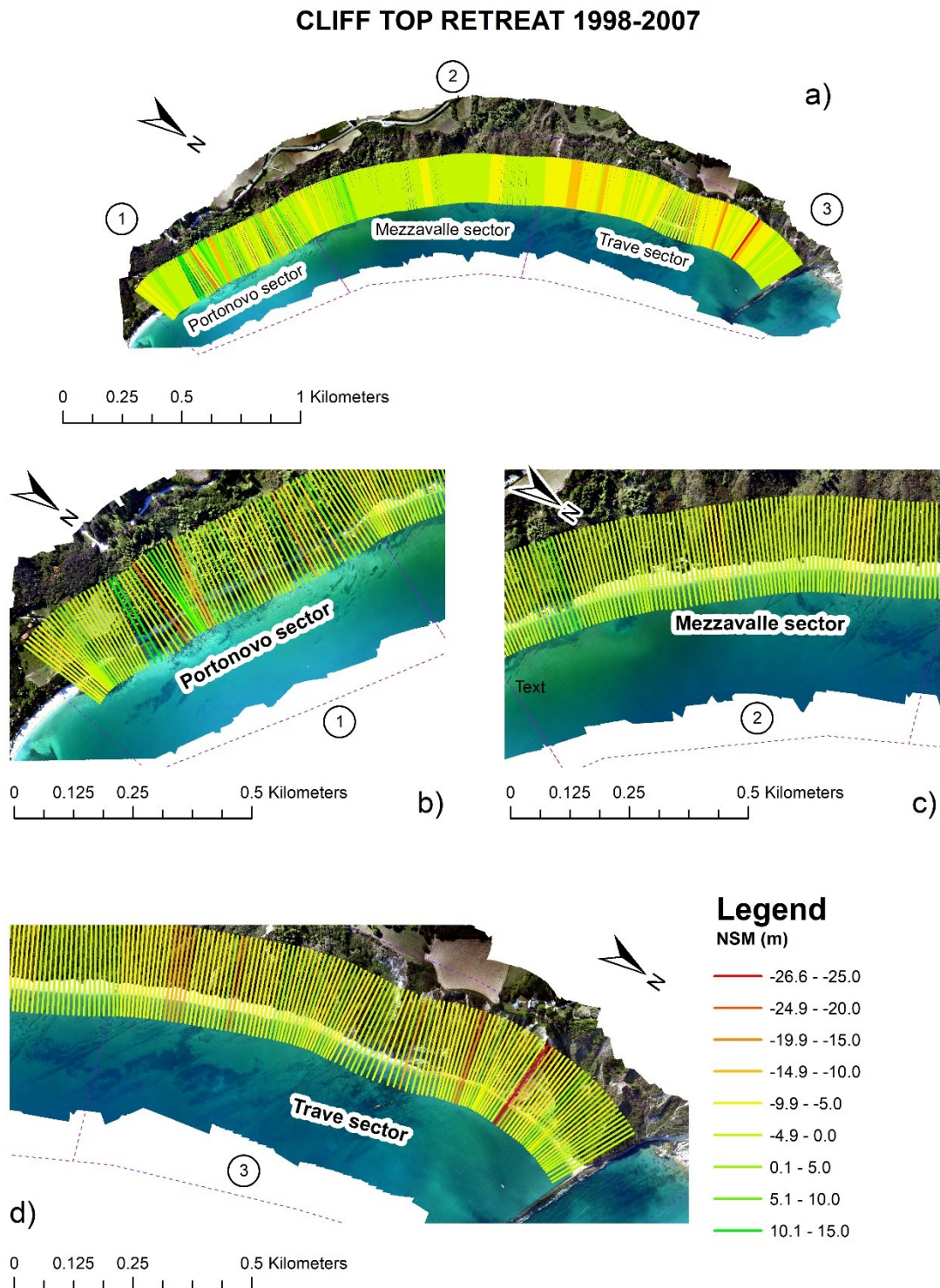


Figure 31: NSM values calculated along transects, referred to the period 1998-2007: Trave sector results the most active sector. a) computed transects for the study area. b) Focus at Portonovo sector. c) Focus at Mezzavalle sector. d) Focus at Trave sector.

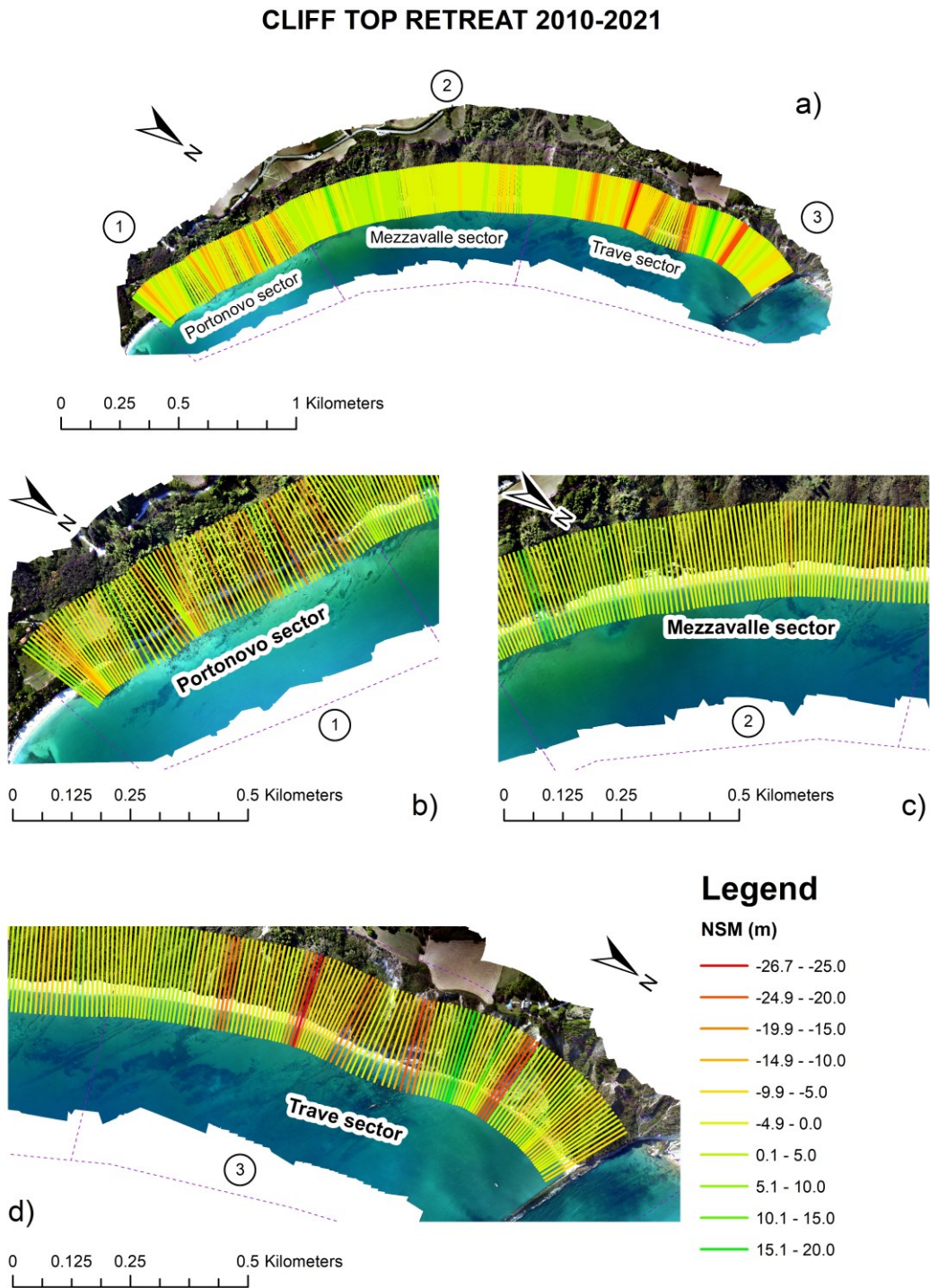


Figure 32: NSM values calculated along transects, referred to the period 2010-2021: Portonovo and Trave sectors result the sectors most affected by retreating of the cliff top edge. a) computed transects for the study area. b) Focus at Portonovo sector. c) Focus at Mezzavalle sector. d) Focus at Trave sector.

DoDs ANALYSIS 2012-2021

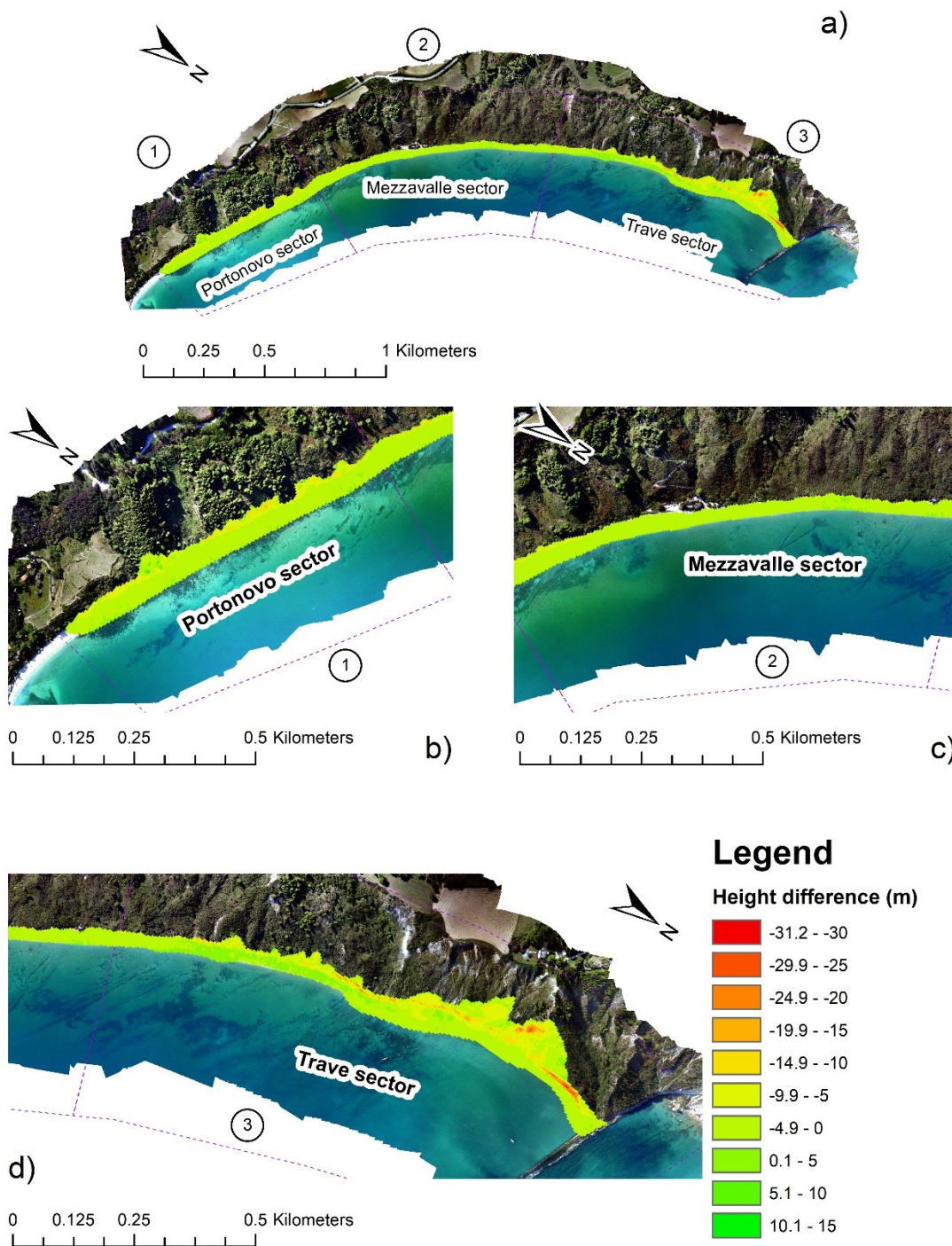


Figure 33: Results of DoDs comparison in the period 2021-2012. Every sector is displayed in detail in scale 1:10.000. Analysis shows that the biggest height differences were recorded in Trave sector. a) computed DoDs for the study area. b) Focus at Portonovo sector. c) Focus at Mezzavalle sector. d) Focus at Trave sector.

3.1.5 Discussion

Results from DSAS analysis show how this coastline is geomorphologically an active area. The average retreat rate calculated in the period 1978-2021 was - 0.25 m/yr. More specifically, in the three sector we can summarize the following outcome.

Trave sector shows the highest rate of cliff retreat, in the period 1998-2007 where the mean is -0.72 m/yr (almost 3 times higher than the average retreat calculate in the whole area). Mezzavalle sector results to be the one with less retreat rate during all the time spans. Despite this, the latter sector is mainly characterized by landslide deposits with poor geotechnical properties and, it is well known as geotechnical properties play a key role in cliff erosion/retreat (Prémaillon et al., 2018). Portonovo sector shows an intermediate behavior between the other two sectors, more similar to Trave, exhibiting in the period 2010-2021 a retreat rate doubled respect the entire period 1978-2021. Many authors has drawn attention to the range of coastal cliff retreat (Gómez-Pazo et al., 2021; Prémaillon et al., 2018; Sunamura T., 1992; Woodroffe, 2002) focusing especially on weak rocks, and obtaining average values of -0,25 m/yr (Prémaillon et al., 2018). Interestingly, while average retreat gathered by other authors is perfectly comparable with our values, the Trave sector shows values nearly 3 times higher than the mean value reported in GlobR2C2 (Prémaillon et al., 2018). Looking to other Italian case studies we can see that in Punta Caleo headland (Campania region), a retreat of 15 m over 30 years was founded (0.5 m/yr). In the close locality of Torre la Punta (1 km far from Punta Caleo), a retreat rate of 0.8 m/yr was assessed, showing how the rate of erosion can suddenly vary in the same coastal areas (Budetta et al., 2000). Regarding other cases in Adriatic Sea, in Torre dell'Orso (Apulia region) the rate of erosion (in fine limestones) was found between 0.08 m/yr and 0.12 m/yr (Delle Rose and Parise, 2005; Lollino et al., 2021), while in the Abruzzo region (on Pleistocene clay-sand-sandstone-conglomerate marine sequence) the retreat rate ranged between 0.15 m/yr and 1 m/yr (Miccadei et al., 2019). In the area between Gabicce and Pesaro, few kilometers on the North of our case study (characterized by similar lithologies), a mean retreat rate of 0.16 m/yr was calculated in the last 6000 year (Colantoni et al., 2004). Considering the much smaller time span considered in our study these values cannot be compared.

In relation to what discussed above, information about precipitation, waves, geology, and land cover has been examined in order to understand the main factors controlling such erosion processes. Although a complete time overlap between precipitation and wave data it is not present, the coverage is enough only in the 1998-2021 temporal window (Fig. 26) to understand potential correlation between these factors and cliff retried. It has been above commented that the highest rate of retreat has been measured in the Trave sector in the period 1998-2007. Considering that extreme events for precipitations and waves, respectively, it results that there is no correlation between the highest rate of cliff retried measured in the period 1998-2007 in the Trave sector and these two parameters. It is difficult with the available data to perfectly match cliff top retreat occurrence and singular meteo/marine events, because orthophotos are yearly distributed and even marine data are not completely reliable cause they come from an hindcast elaboration. Yet, performing an extreme value analysis of marine data will be useless without the possibility to assess with photos the effect of waves on the slopes. The same issue is related even to rainfall data. From the September 2003 it is possible to have information on the precipitation every 15 minutes; however, the lack of data does not allow a cause-consequence analysis that correlate the main raining events and landslide triggering. As numerous authors has demonstrated, soft-rock cliff recession is an episodic and localized phenomenon (Sunamura, 2015). For example, on September 14, 1944, a storm on Long Island, New York, cut back a cliff made of glacial deposits by a horizontal distance of more than 12m in a single day (Davies et al., 1974). At Santa Cruz, during storms in January 1983, waves eroded around 14 m of the bluff top in Miocene mudstone-siltstone cliffs. Due to this, it is challenging to constrain which events and

drives can have a greater impact on the cliffs without a complete dataset (Griggs and Savoy, 1985). Since this, other parameters have to be used to understand possible correlations.

Other important features that have to be taken into account are: beaches width, geotechnical properties and slope cliff elevation/steepness (Everts, 1991; Prémaillon et al., 2018; Wolters and Müller, 2008) Regarding the beach width, it has been noted that Mezzavalle sector has the widest beach, followed by Portonovo and Trave sectors with almost the same beach width mean.

The sector with highest geotechnical properties is Portonovo sector while the one with the lowest values is Mezzavalle (made prevalently by landslide deposits).

The geological survey shows that the Trave sector is the area more interested by tectonic features, with two main thrusts present (Fig. 34). Furthermore, Trave sector is the one with highest cliff elevation and steepness. Clearly, such highly fractured remarkably decrease the geotechnical properties (lower values of GSI) of rock masses and their stability (Brideau et al., 2009). This is also confirmed by the landslide inventory of ISPRA, where most of the landslide documented occurred in Trave sector (<https://idrogeo.isprambiente.it/app/iffi/>).

Additionally, as observed on the California coast, fracture spacing play a very important role in retreat rates. (Benumof and Griggs, 1999; Moore et al., 1999).

Another important aspect to be discussed is related to the land cover of the study area. No information was reported about the different depth of soil cover along the coastline, but many considerations can be made. The fieldwork has pointed out that the landslide deposits outcropping in Portonovo sector are more granular than those present in Mezzavalle (composed mainly by clays). This, combined with the higher steepness of the Portonovo and Trave sector, leads to hypothesize that the soil cover depth in Mezzavalle sector could be higher than the others sectors (pedogenesis is usually more prone to develop in flatter area (Brosens et al., 2020)). This can also be linked with the resulted higher occurrence of flow like landslides in Mezzavalle sector, reported by IdroGEO in the areas behind the active cliffs.

Another issue to be discussed is related to the presence of vegetation in the three sectors. The analysis of UAV photographs highlighted that the Trave sector, compared with the other sectors, presents in the cliff top a lower vegetation rate and a different land cover (in agreement with Corine Land Cover, which define the vegetation on that sector as Sclerophyllous vegetation).

From a geomorphological point of view this evidence can give us more insight regarding the process acting on the cliff. In fact, it is possible to state that with a lower vegetation rate, run-off processes can be more severe, increasing the instability of the rock mass. These observations agree with what showed by the DoDs analysis, where the sector with the major negative differences (loss of material) is the Trave one. Observing the shape and distribution of the area with higher DoD values, it is also possible to notice that these are mainly localized along the cliff-top. This evidence, combined with the lack of evidence of detectable notches at the cliff base, lead us to think that the erosive process is more influenced by slope processes than marine forcing. Dods analysis showed even that Mezzavalle sector presents the lowest variation and Portonovo an intermediate behavior between the other two. This datum completely agrees with the results gathered from the DSAS analysis: area with positive difference (accumulation) is very minor less wide and this is probably related to the capacity of the sea to quickly remove slope collapsed material.

The integration of DSAS and DoDs analysis guarantee confirmed areas with major failures/erosions activity. These results confirm as the continuation of multitemporal survey can represent a good method in monitoring the evolution of this coastline.

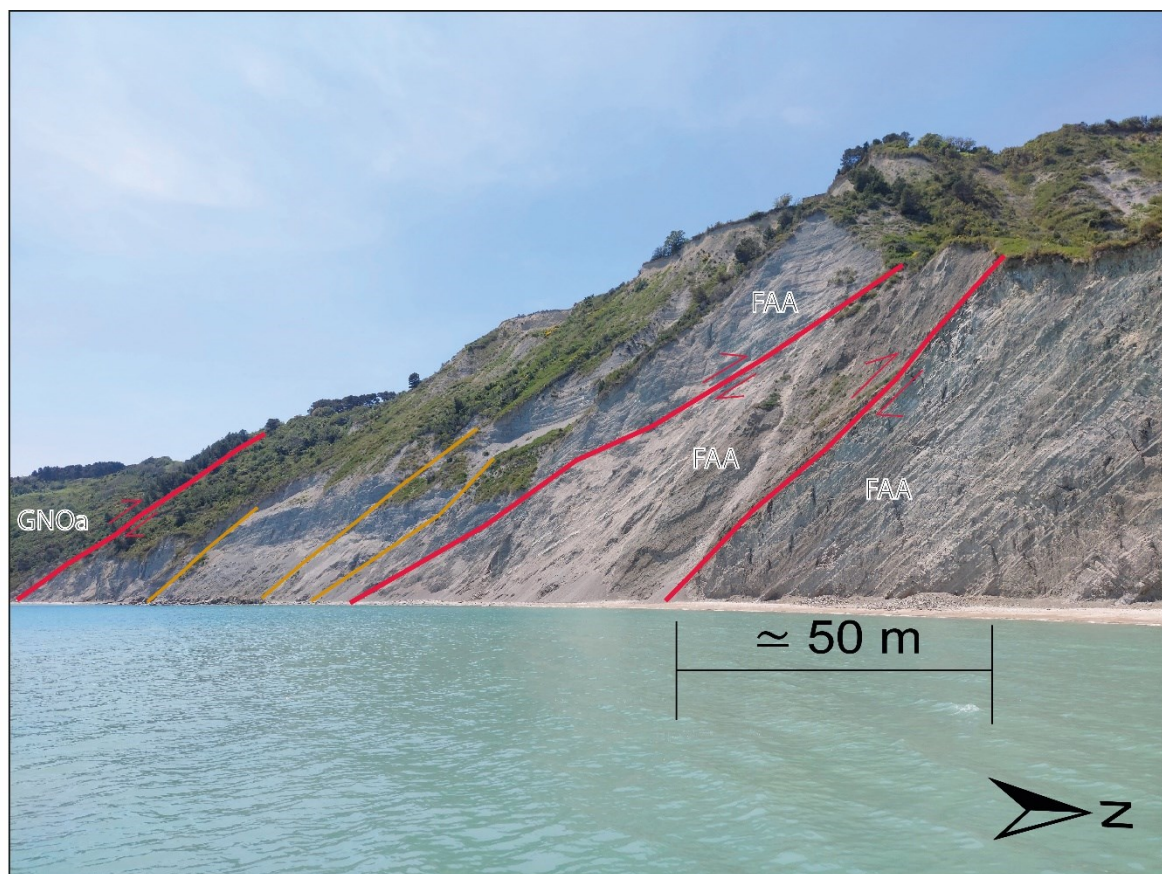


Figure 34: *The geological structure of Trave cliff (GNOa (Sapigno Fm. Upper Miocene) and FAA (Argille Azzurre Fm., Lower Pliocene-Lower Pleistocene)). The main thrusts are highlighted with red lines, the red arrows indicate the sense of movement between hangingwall and footwall. In orange secondary thrusts with a lower slip. The trend of coastline in this picture is N/S and the average attitude of the fault planes identified is 200/45 in Dip Direction and Dip convention.*

3.1.6 Conclusions

This study presents the first-time attempt of quantifying morphodynamical processes acting on Portonovo-Mezzavalle-Trave cliffs.

It has been performed an interdisciplinary study which include fieldworks, analysis of meteorological and marine data, geological and land cover information, and cliff-top retreat in different periods, using the DSAS tool for ArcGis. Moreover, to improve our understanding of cliffs retreat rate and validate results from multitemporal orthoimages analysis, we performed a DoD between available 2012 DTM data and a 2021 DSM extracted from UAV photographs.

The results gathered from the study can be summarized as follow:

- The coastal area that shows the highest variation in all the time spans considered is Trave sector, showing NSM maximum retreat of -43.5 m and a maximum height difference of -31 m.
- Comparing different time periods, it results an augmented cliff top erosion trend the last 20 years if compared to the whole period of analysis (1978-2021).
- The Trave sector shows values of retreat nearly 3 times higher than the mean value reported in GlobR2C2 (Prémaillon et al., 2018).

We conclude that the higher retreat rate localized at Trave sector is related to a combination of factors:

- Mechanical properties of the rockmass are decreased due to the presence of tectonic disturbances, that increase fracture intensity and resulting in a decreasing GSI.
- The steepness and elevation of this sector which is the highest in the entire investigated coastline (both are landslide-predisposing factors and finally).
- One of the lowest values of beach width, that increases the role of wave action.
- Variations of vegetation rate and land cover may affect the run-off and the erosion in the upper slope.

Different is the situation at Mezzavalle sector: it is characterized by the lowest values of geotechnical properties, the highest values of beach width and by value of elevation of the cliff much lower than the Trave sector. The Mezzavalle sector is the area with the lowest rate of cliff retreat.

Portonovo sector shows an intermediate behavior between the other two, more similar to Trave sector. Precipitations and waves data don't seem to have correlation with the different erosional process in the different sectors. In fact, there is no correlation between years of high rate of precipitation and waves data and the high rate of cliff retreat measured in the Trave sector between 1998-2007. From a geomorphological perspective, the data gathered in the study let us to hypothesize that the evolution of this coastline is more controlled by slope factors than marine drives, leading to a progressive retrogression of the cliff-top edge.

3.2 Comparing Multiple High Accuracy UAV-SfM Derived Point Clouds for Geomorphological Change Detection at Portonovo-Trave cliffs (Conero, Ancona, Italy).

3.2.1 Introduction

Rocky coastal regions are increasingly susceptible to the impacts of human activities and the associated infrastructure (Martínez et al., 2007; Small and Nicholls, 2003). Moreover, these areas face a growing vulnerability to natural hazards exacerbated by climate change, including the risk of rising sea levels and potentially heightened storm events (Coco and Ciavola, 2017; Del Río and Gracia, 2009; Gómez-Pazo et al., 2021; Alan S. Trenhaile, 2010). The evolution of rocky coasts is influenced by several factors, such as geological, geomorphological, and structural characteristics (Sunamura T., 1992; Trenhaile, 2012), wave dynamics (Brideau et al., 2009; Budetta et al., 2000; Kennedy et al., 2011; Naylor et al., 2010; Piacentini et al., 2021; Sunamura, 2015; Sunamura T., 1992; Trenhaile, 1987), sediment inputs (Kennedy and Milkins, 2015; Komar and Shih, 1993), cliff topography (Robinson, 1980; Sunamura, 1991), beach width (Everts, 1991), and the energy content of waves (Poate et al., 2018).

Continuous monitoring over time to document the ongoing changes in these coastal areas can significantly contribute to assess risk assessment, hazard mitigation, and coastal management (Esposito et al., 2017; Godfrey et al., 2020; Rosser et al., 2005a). However, obtaining the necessary data from rocky coastlines, characterized by steep and unstable slopes as well as high cliffs, has historically presented challenges. In recent decades, in response to these environmental challenges, new technologies have been developed and adapted to facilitate more accurate analysis (Caputo et al., 2018; Del Río et al., 2020; Esposito et al., 2020, 2017; Francioni et al., 2018a; Koukouvelas et al., 2020; Martino and Mazzanti, 2014; Matano et al., 2015; Rosser et al., 2005a; Warrick et al., 2017; Westoby et al., 2012).

Unmanned aerial vehicles (UAVs) offer promising opportunities for monitoring these coastal areas, as they can operate at low altitudes and cross challenging terrain (Westoby et al., 2012). When combined with Structure-from-Motion (SfM) photogrammetric techniques, UAVs enable high-precision analyses at relatively affordable costs (Brunetta et al., 2021; Buchanan et al., 2020; Duo et al., 2021; Westoby et al., 2018). Furthermore, in cases of landslides, other commonly used techniques, such as satellite imagery, often prove inadequate in providing the required level of information (Koukouvelas et al., 2020). To address these challenges, assessments based on high-resolution imagery collected from UAVs in combination with ground control points (GCPs) measured using a Global Navigation Satellite System (GNSS) have been increasingly employed (Vanneschi et al., 2017). This approach is becoming more prevalent, thanks to technological advancements, including autopilot systems, high-quality digital cameras, miniature and accurate global positioning systems, and improvements in SfM software (Lucieer et al., 2013). Examining an area through UAV imagery poses intrinsic complexity, attributed to various factors like dense vegetation, untextured surfaces, diverse slopes, water-filled areas, and more (Alexiou et al., 2021). Among these factors, vegetation stands out as the most crucial element impeding a clear ground view when employing UAV-based photogrammetry methods (Dandois and Ellis, 2010). Anyway, UAV found in the recent past high-quality application on determining bare cliff characteristics and evolution (Casagli et al., 2017; Fazio et al., 2019; Fullin et al., 2023; He et al., 2022; Koukouvelas et al., 2020; Melis et al., 2020).

UAV derived Digital surface (DSM) or terrain (DTM) models, known as DEMs, find widespread application in various geomorphic contexts for conducting spatial assessments, both static and

dynamic (Earlie et al., 2015; Jaboyedoff et al., 2012b; Piacentini et al., 2021; Turner et al., 2016). Wheaton et al. (2010) (Wheaton et al., 2010) standardized these methods for determining notable variations in elevation and volume between DEMs, incorporating evaluations of uncertainty. This can be applied even using point clouds products (Esposito et al., 2020, 2018; Lague et al., 2013; Matano et al., 2014).

In this context, the present study aims to investigate the one-year evolution in the area spanning from Portonovo to Trave (Ancona, Italy, Fig. 35) through the utilization of UAV photogrammetry-derived products. UAVs have played an important role, even in ground truth operations, offering the possibility to inspect the entire cliffs without introducing additional risks. The change detection between two Digital Surface Models (DSMs) generated in 2021 and 2022 using UAV technology underscores the significance of this approach in the context of rocky coastal environments. Comparing these remote sensing techniques with prior studies has allowed for the identification of coastline segments experiencing higher rates of evolution with enhanced spatial resolution, permitting to recognize processes that were before ignored using other remote sensing techniques.

3.2.2 Study Area Description

The study area, positioned on the central Adriatic coast between Portonovo and Trave in the Conero promontory, a few kilometers north of Conero promontory (Fig. 35), exhibits distinctive characteristics. This region features high cliffs ranging from tens to hundreds of meters in elevation and slopes varying from nearly flat to steep inclinations of up to 80°/90°. The particular stretch of coastline under investigation overlooks the northern-central Adriatic Sea (Bisci et al., 2021). The Adriatic sea is a microtidal environment (Bisci et al., 2021) and it experiences two predominant winds: the Sirocco from the S-SE and the Bora from the NE (Acciarri et al., 2021; Perini et al., 2011). Moreover, a littoral drift moving northwards is presumed along this coastal area (Grottoli et al., 2015).

The coastline morphology has led to its division into three sectors, progressing from South to North (Fig 35):

- Sector “1” (Portonovo) with an E-O/NW-SE orientation, characterized by the Schlier Fm.;
- Sector “2” (Mezzavalle), approximately NW-SE oriented and predominantly covered by landslide deposits;
- Sector “3” (Trave), approximately N-S/NW-SE oriented, featuring high and steep cliffs (\pm 200 meters) with tectonized flyschoid formations (Argille Azzurre Fm.).

In terms of geological attributes, the Conero promontory is situated in the central sector of the present-day foredeep basin and foreland ramp of the Outer Northern Apennine fold and thrust belt (Calamita et al., 1999; Cello and Coppola, 1989; Coltorti et al., 1987; Iaccarino et al., 2008). The study area includes Neogenic formations dating from the Miocene to the present, including the Schlier, Formazione a Colombacci, Formazione di Sapigno, Orizzonte del Trave, and Argille Azzurre (Coltorti and Sarti, 2011) These formations primarily consist of marls, clays, sandstones, and gypsum, often masked by landslide deposits observed throughout the study area (Montanari et al., 2016).

Geologically, the structural setting in the area is marked by two principal thrusts, both NW-SE oriented, resulting in the exposure of different formations in specific sectors. Intense erosion processes and numerous landslides contribute to a badland-like appearance along this part of the coastline. In particular, the Portonovo sector displays the activation of landslides in the upper sedimentary cover, causing cliff top retreats. The Mezzavalle sector is mainly comprised of landslide deposits, with occasional bedrock outcroppings near the morphological edge separating inland from the cliff. The Trave sector exhibits a high incidence of active landslides with various kinematic mechanisms, indicating a predisposition to landslide movements due to multiple thrusts cutting through the rock mass.

Landslide occurrences are well-documented in the landslide database of the Istituto Superiore per la Ricerca e Protezione Ambientale (ISPRA) IdroGEO, primarily concentrated in the Trave sector (<https://idrogeo.isprambiente.it/app/iffi/>). The study area experiences diverse landslide types, including rotational slides, earthflows, falls/topples, and complex movements, categorized by their activity state (Cruden, D.M., Varnes, 1996). The crown of these landslides is predominantly situated along the morphological edge separating inland from the coast, with the affected area estimated to be approximately 280,000 m².

Pedological and soil cover perspectives were also addressed. Official documents from the Parco Nazionale del Conero (https://www.regione.marche.it/natura2000/public/allegati_blog/1682/File%20non%20disponibile.pdf) describe the soil covering the marls and calcareous bedrock as regosol or lithosol Xerorthents

typic and lithic. Unfortunately, no information is available regarding the varying depth of this soil level along the coastline.

To further comprehend land use changes and vegetation, data from Corine Land Cover (<https://land.copernicus.eu/pan-european/corine-land-cover>) for 1990 and 2018 were examined. In 1990, the Trave sector was classified as "Green urban areas" (code 141), while the other two sectors were classified as "Broad-leaved forest" (code 311). By 2018, the Trave sector was classified as "Sclerophyllous vegetation" (code 323), whereas the other two sectors remained under the code 311 as "Broad-leaved forest."

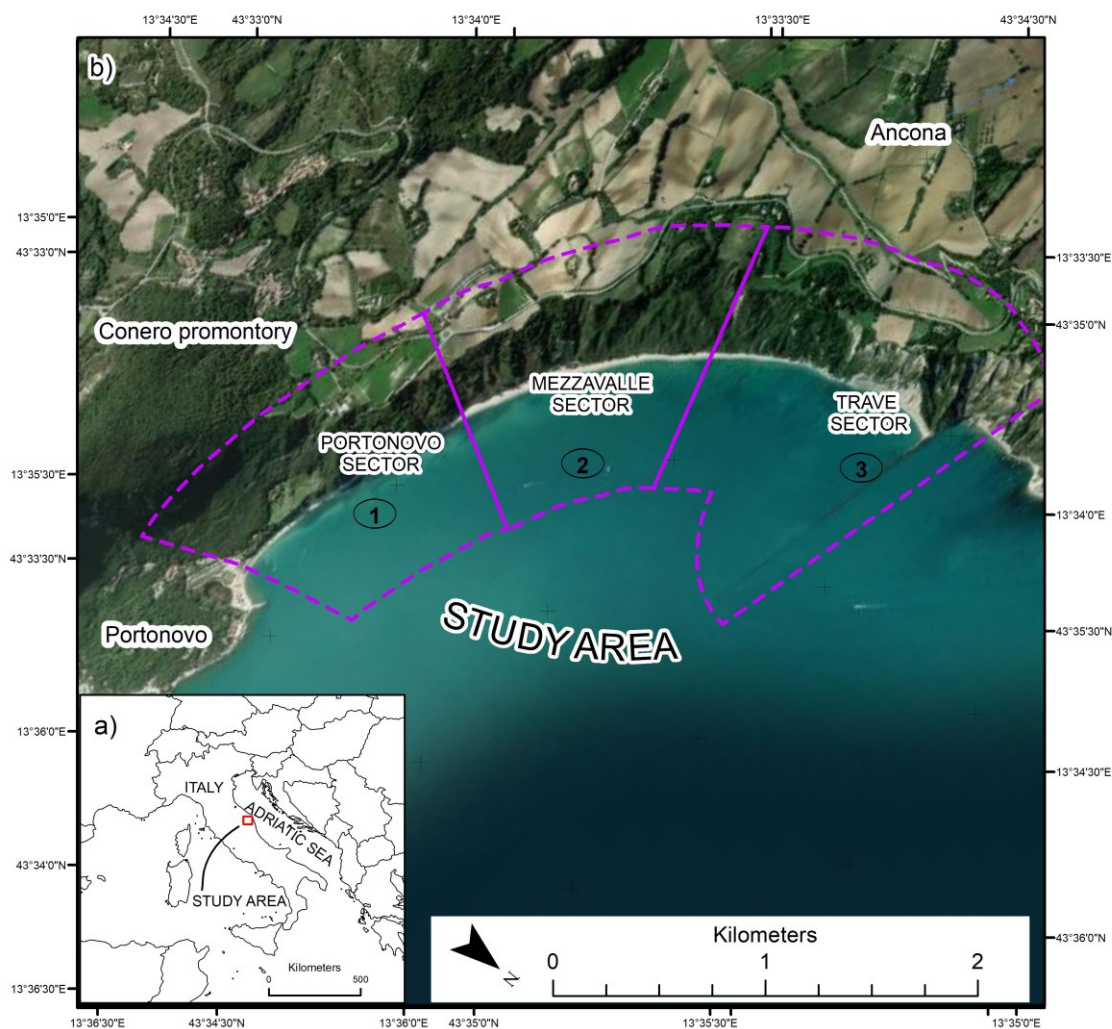


Figure 35: Satellite image showing the study area delimited by a violet line (image taken from GeoEye satellite database, 2020). 3 sectors are identified: 1) Portonovo; 2) Mezzavalle; 3) Trave.

3.2.3 Materials and Methods

With the aim of quantifying morphological evolution between 2021-2022 on these cliffs, we have performed the following methodology:

- 2 distinct UAV survey with nearly 1 year of delay
- Change detection between 2021 and 2022 UAV derived point clouds.

3.2.3.1 UAV Surveys and Data Elaboration

Surveys were completed in two separate fieldworks, the first on the end of September 2021 and the second in the beginning of October 2022, trying to fly always in the morning in order to keep almost the same light condition (Tziavou et al., 2018).

3.2.3.1.1 28/29 September 2021 survey

Because of the extension of the study area (about 1.5 km²), the UAV data acquisition was accomplished in two consequent days, 28/29 September 2021 using a commercial drone DJI Phantom Vision 3+ Pro equipped with a camera: FC300X (focal length: 3.61 mm; pixel size: 1.56 × 1.56 μm). Flights were conducted at a constant elevation of 120 m covering the top cliff, and 60-70 m covering the beach area, using automated flight plans created using the “Drone deploy” opensource application (<https://www.dronedeploy.com/>). Front and side overlap between each photo was ~70% and flight speed 8-10 m/s.

The UAV survey was supported by an NRTK-GNSS survey using a Trimble RTK-DGPS R8 (i.e., stop and go technique; horizontal accuracy of 8 mm and vertical accuracy of 15 mm) which was used to acquire the position of 22 ground control points (GCPs). These were made of white and red wooden square targets, measuring 60 × 60 cm, and distributed within the study area. The Universal Transversal Mercatore WGS84 zone 33N was used as coordinate system and the ellipsoidal height was converted to orthometric height using national grids using the software “Convergo” (https://www.cisis.it/?page_id=3214). Estimate error during the NRTK-GNSS survey was approx 6 cm horizontally and vertically.

“Agisoft Metashape” (version 1.5.1 <https://www.agisoft.com>) was used to manage and process UAV data and GCP coordinates. Using the procedure suggested by different authors (Brunetta et al., 2021; Duo et al., 2021; Fabbri et al., 2021b; Gindraux et al., 2017; Talavera et al., 2021) it was possible to create the DSM and orthophoto of the surveyed area.

3.2.3.1.2 06/07 October 2022 Survey

The UAV data acquisition was accomplished in two consequent days, 06/07 October 2022, covering the extension of the study area (about 1.5 km²). The drone used for the survey was a DJI Mavic 2 Pro. Characteristics of the drone camera were: 20 megapixel resolution; 28 mm focal length with f/2.8 to f/11 aperture and maximum image size of 5472×3648 px.

In order to get the same photographs ground resolution, the flights were conducted at a constant elevation, 120 m above the area, using programmed flight plans created through the BLY3D software of Aermatica3D application (<https://www.aermatica.com/app-bly3d/>). Photographs overlap was kept at 80% and flight speed at 8 m/s.

Trimble RTK-DGPS R8 (i.e., stop and go technique; horizontal accuracy of 8 mm and vertical accuracy of 15 mm) was used to support the UAV survey with an NRTK-GNSS measure to acquire the position of 13 Ground Control Points (GCPs), based on the national net of Leica. These were white and red wooden square targets, measuring 60 × 60 cm, uniformly distributed within the study

area. The Universal Transversal Mercatore WGS84 zone 33 N was used as coordinate system and the ellipsoidal height was converted to orthometric height using national grids in the software “Convergo” (https://www.cisis.it/?page_id=3214). Estimate error during the NRTK-GNSS survey was approx. 3 cm horizontally and vertically.

GCP coordinates and UAV data were managed and processed using "Agisoft Metashape" (version 1.5.1, available at <https://www.agisoft.com>). The Digital Surface Model (DSM) and orthophoto of the surveyed region were produced following existing methods (Brunetta et al., 2021; Duo et al., 2021; Fabbri et al., 2021a; Gindraux et al., 2017; Talavera et al., 2021).

3.2.3.3 Change detection analysis

Change detection is becoming a common practice in geosciences (Gómez-Pazo et al., 2021; Jaboyedoff et al., 2012b; Williams, 2012). In this case we have performed this analysis using two points clouds extracted by UAV survey in September 2021 and October 2022 in the software CloudCompare (<https://www.danielgm.net/cc/>). Georeferencing error between the 2 clouds was extracted through the CloudCompare tool Cloud-to-Cloud (C2C) that highlighted different errors along the whole coastline. In fact, due to the continuous activity of Trave Cliffs, in the October 2022 less GCPs were ubicated close this sector. Hence, it was decided to study separately the surveys, by dividing the cloud in Trave (hereafter Trave-Cloud (TC)) from the clouds of 2021 and 2022 from the other part (hereafter Portonovo-Mezzavalle-Cloud (PMC)) with different georeferencing error.

In order to reduce this existing error in TC, multitemporal point clouds underwent alignment using the iterative closest point (ICP) best-fit algorithm implemented in CloudCompare. This alignment method, known as ICP best-fit, offers a rapid and faithful approach that can help in aligning clouds where it is not possible to safely positioning GCPs across extensive areas with complex morphology or steep inclines. Furthermore, it mitigates uncertainty arising from matching point clouds exhibiting variable densities (Fey and Wichmann, 2017).

Within the ICP algorithm, one point cloud remains fixed as the reference while the other is adjusted to achieve the optimal alignment with the reference. Through iterative processes, the algorithm refines the transformation, involving translation and rotation, to minimize the distance between the moving and reference point clouds.

At the end of this process for both the clouds TC and PMC the Multiscale Model to Model Cloud Comparison (M3C2) algorithm within CloudCompare was used.

The M3C2 algorithm facilitated the assessment of differences between two point clouds by measuring the spatial distance between points within a 3D space, enabling the identification and characterization of volumetric and morphological alterations, as showed by Lague et al. in 2013 (Lague et al., 2013). The M3C2 algorithm considered surface roughness and alignment errors between clouds, while also allowing for the determination of the analysis scale, contingent upon the density of the sub-sampled cloud (Lague et al., 2013). We utilized the automatically estimated values provided by the plug-in, except for the co-registration errors specifically related to the comparison between the point clouds, also known as the level of detection (LOD) (Esposito et al., 2020).

These values were introduced differently according to the results obtained by C2C for TC and PMC. Specifically, the decision was made to employ a value equivalent to twice the standard deviation (2σ) derived from C2C histograms as the Level of Detection (LOD) for each respective cloud (Lague et al., 2013; Taylor and Thompson, 1982; Wheaton et al., 2010). Vegetation was removed masking the clouds and through segmentation tool.

3.2.3.4 Volume variation analysis

The study area was divided into seven segments (labeled as a, b, c, d, e, f, g) to effectively document the erosion and accretion that emerged between 2021 and 2022 (Fig. 36). Each segment was isolated from the M3C2 clouds, with segments a, b, c, d, e, and f attributed to PMC, and segment g to TC. Volume variations were determined by isolating significant changes (according to LOD) within the 2022 cloud data through M3C2 analysis and subsequently comparing these variations with the 2021 point cloud. The CloudCompare tool, specifically the "Volume 2.5D" feature, was employed to calculate the volumetric changes using a grid size of 0.10 meters. Uncertainty in volumetric variation was computed according to Nourbakhshbeidokhti et al. (2019). A more detailed representation of the observed evolution was made defining four distinct detailed sections (Fig. 36).

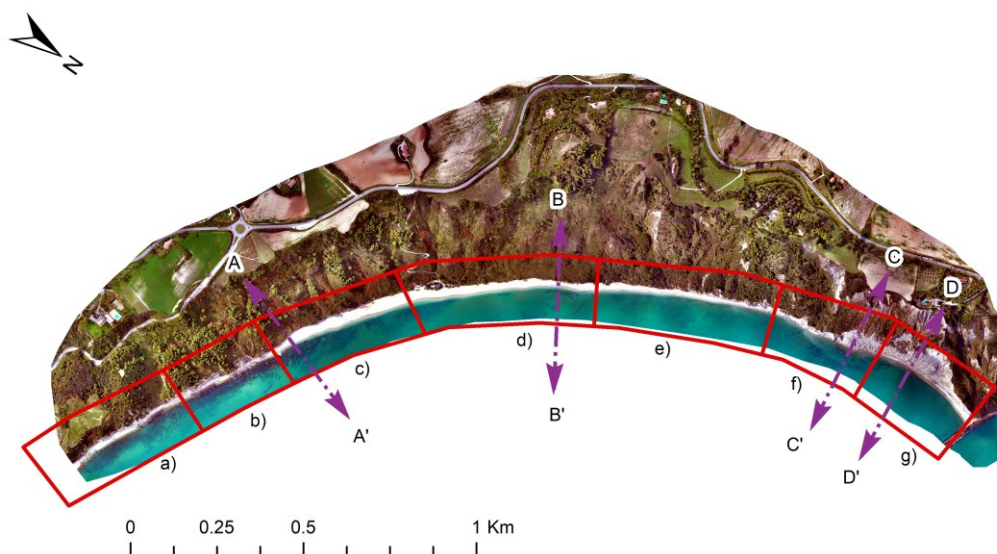


Figure 36: 2022 UAV derived orthophoto showing the segment identified by a red line. 4 sections are displayed in violet in the tract with a higher computed change.

3.2.4. Results

3.2.4.1 UAV derived points clouds

2021 and 2022 dense clouds had respectively a mean point density of 19 points for square meters (p/m^2) and 67 p/m^2 .

The C2C histograms retrieved from TC and PMC products are reported in Figure 37.

Hence the values added into the M3C2 plugin for co-registration were respectively 0.70 m and 0.80 m for PMC and TC (Taylor and Thompson, 1982).

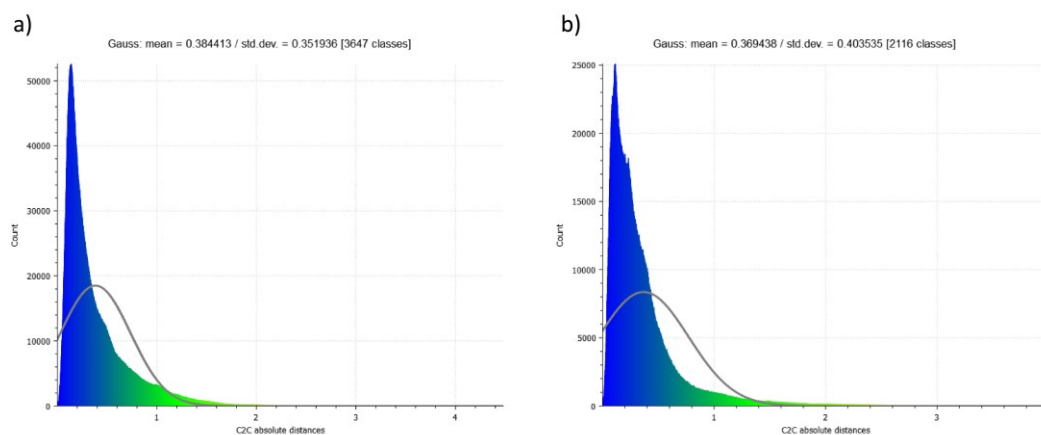


Figure 37: Histograms of PMC (a) and TC (b) C2C analysis.

3.2.4.2 Change Detection and Volume Variation Analysis

The analysis conducted between 2021 and 2022 delineates the detection of changes across diverse coastal sections, synthesized in the Figures 38,39,40,41. The four sections extracted as reported in Figure 36 are reported in Figure 42.

All values acquired from the volume variation analysis have been collected within Table 9 for the convenience of presenting the results.

Table 9: Volume variations computed for each sector are reported together with their uncertainty.

	Volume variation (m ³)		Uncertainty (m ³)
	Positive	Negative	
a)	/	11.67	0.74
b)	/	4.36	0.40
c)	56.94	24.24	12.24 and 1.68
d)	/	111.25	9.89
e)	/	43.18	4.35
f)	/	512.41	50.81
g)	/	105.26	8.88

Summarizing the outcomes for each segment:

In area a), minimal changes were recorded (Fig. 38), with slightly over 10 m^3 being eroded from the cliffs according to volume analysis. Examining the shape of these removed sections suggests they may have detached as small falls or toppled fragments. No accretion was detected on the beach or talus of these cliffs above the LOD (Limit of Detection). Picture a) shows a slight linear increase in the volume of the beach upon the cliff's southern side, potentially indicating a storm berm, but given its data's proximity to the LOD, it could be affected by noise.

Segment b) displayed a similarly modest evolution, with less than 5 m^3 eroded (Fig. 38), solely in erosion. The small sections involved in this movement might also be categorized as results of falls or toppling. Considering their lower position, marine action might have contributed to the detachment of these volumes.

Area c) exhibited an evolution involving both accretion and erosion (Fig. 39), notably prominent in the southern part of this segment. It showcased a local increase in beach height exceeding 1.5 m and a substantial notch in the cliffs, particularly depicted in section A-A' (Fig. 42a). The volume removed from the cliff was quantified at 24 m^3 , while beach accretion ranged between 50 and 60 m^3 .

Segment d) demonstrated a significant notching at the northern cliff base (Fig. 39), as also illustrated in section B-B' (Fig. 42b). Although appreciable volumetric accretion was not measured here, erosion of approximately 110 m^3 was detected, primarily affecting patches of the cliff at low elevations, 2-4 m above sea level.

Area e) recorded the most substantial morphological evolution at the cliff base (Fig. 40), particularly in the southern part of the segment. Similar to d), the areas affected by erosion are situated closer to sea level, indicating a potential link between wave action and the observed erosion. Volume loss was estimated at around 40 m^3 of material.

Area f) evidenced the highest recorded erosion along the entire coastline (Fig. 40), reaching values of 500 m^3 . This erosion concentrated on both the cliff base and face, potentially involving landslides such as falls or topplings. Additionally, a possible slide was detected in the northern part of this area, with section C-C' (Fig. 42c) highlighting the change observed between 2021 and 2022.

Area g), akin to d) and f), displayed significant erosion, up to 100 m^3 , concentrating on both the cliff face and base (Fig. 41). Section D-D' (Fig. 42d) emphasized a zone where two distinct landslides occurred, one at the top of the active cliff and another close to the base. This indicates that the material might not have been deposited immediately off the cliff but could have been reworked and relocated either offshore or elsewhere along the coastline (as potentially observed in c)).

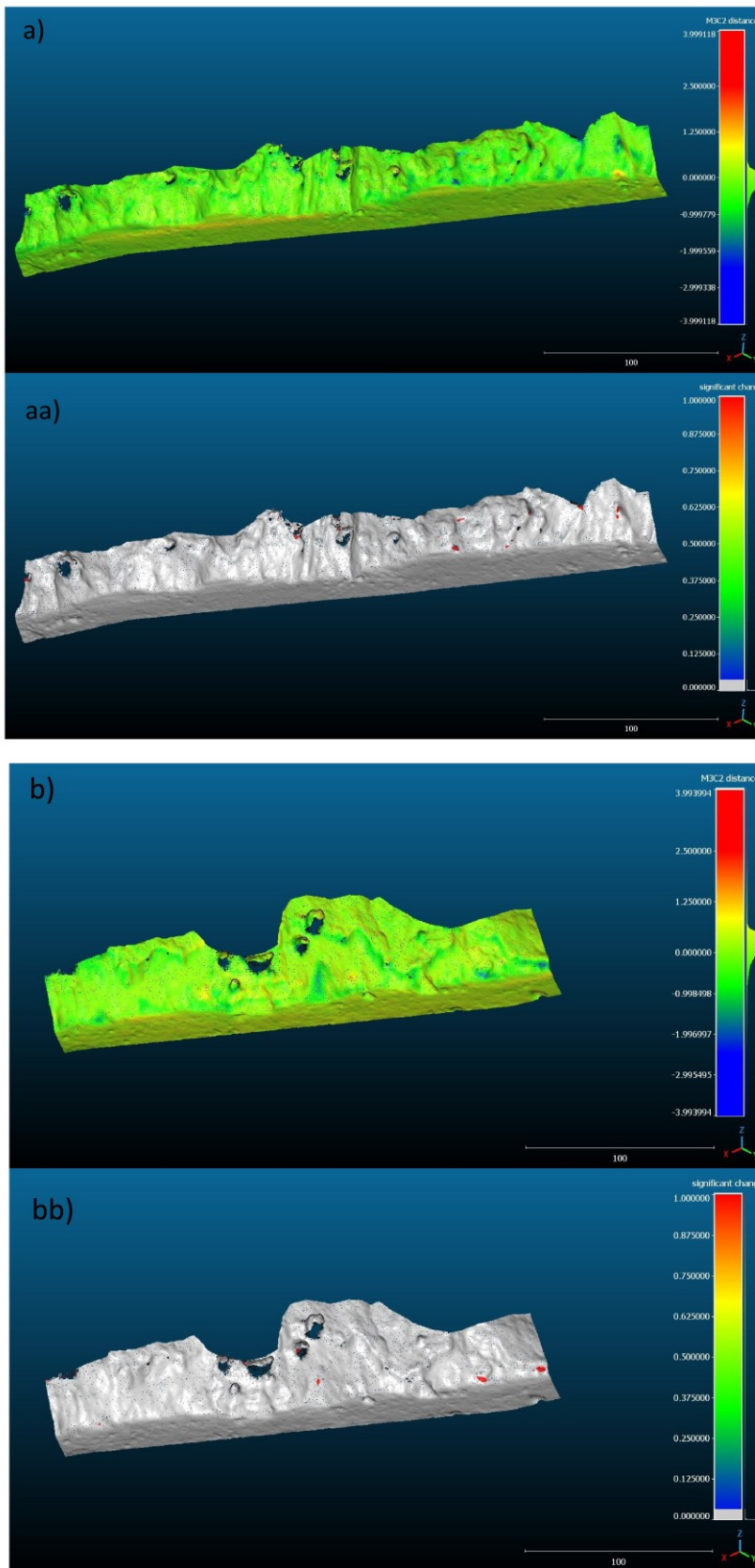


Figure 38: *M3C2 results are displayed in the pictures showing M3C2 distance above and significant changes below for each area. Segment a) it is shown in 38a) and 38aa), then part b) it is shown in 38b) and 38bb).*

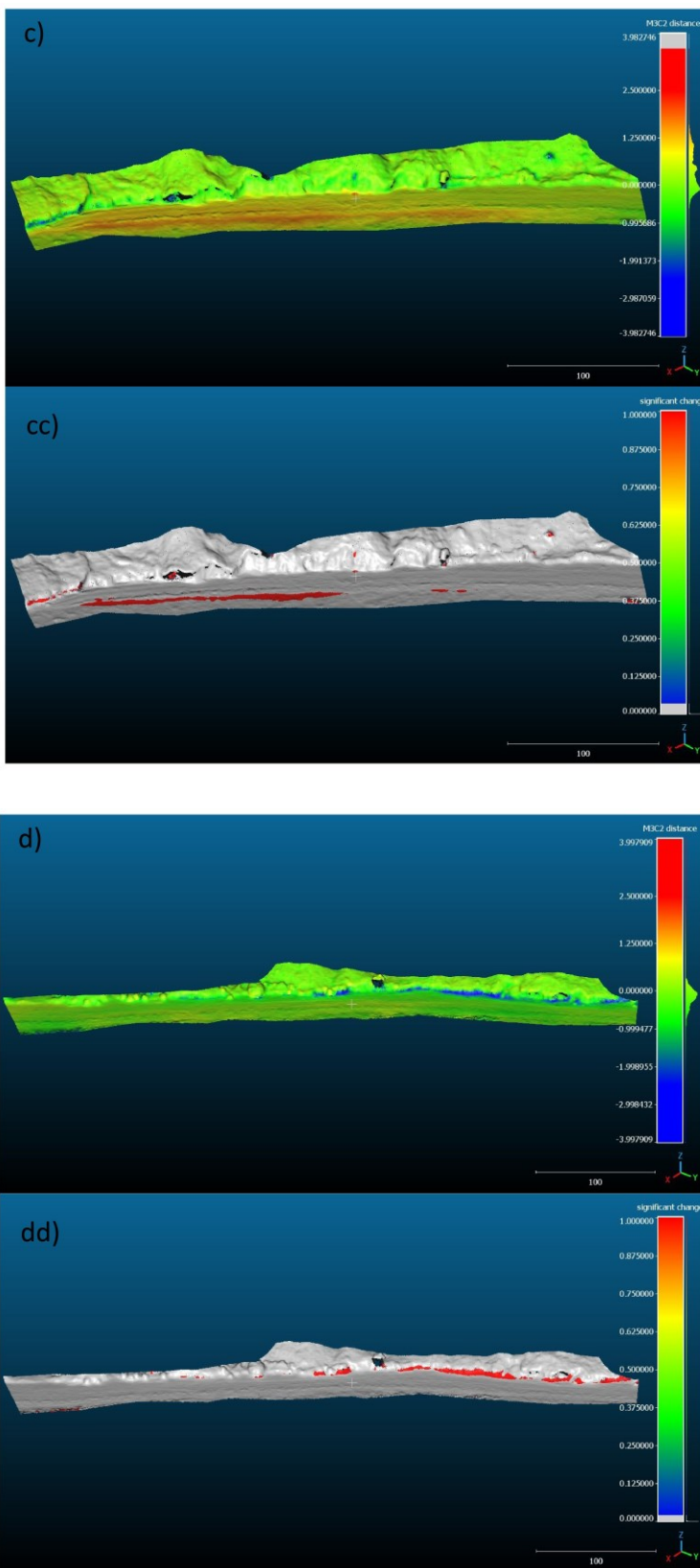


Figure 39: M3C2 results are displayed in the pictures showing M3C2 distance above and significant changes below for each area. Segment c) it is shown in 39c) and 39cc), then part b) it is shown in 39d) and 39dd).

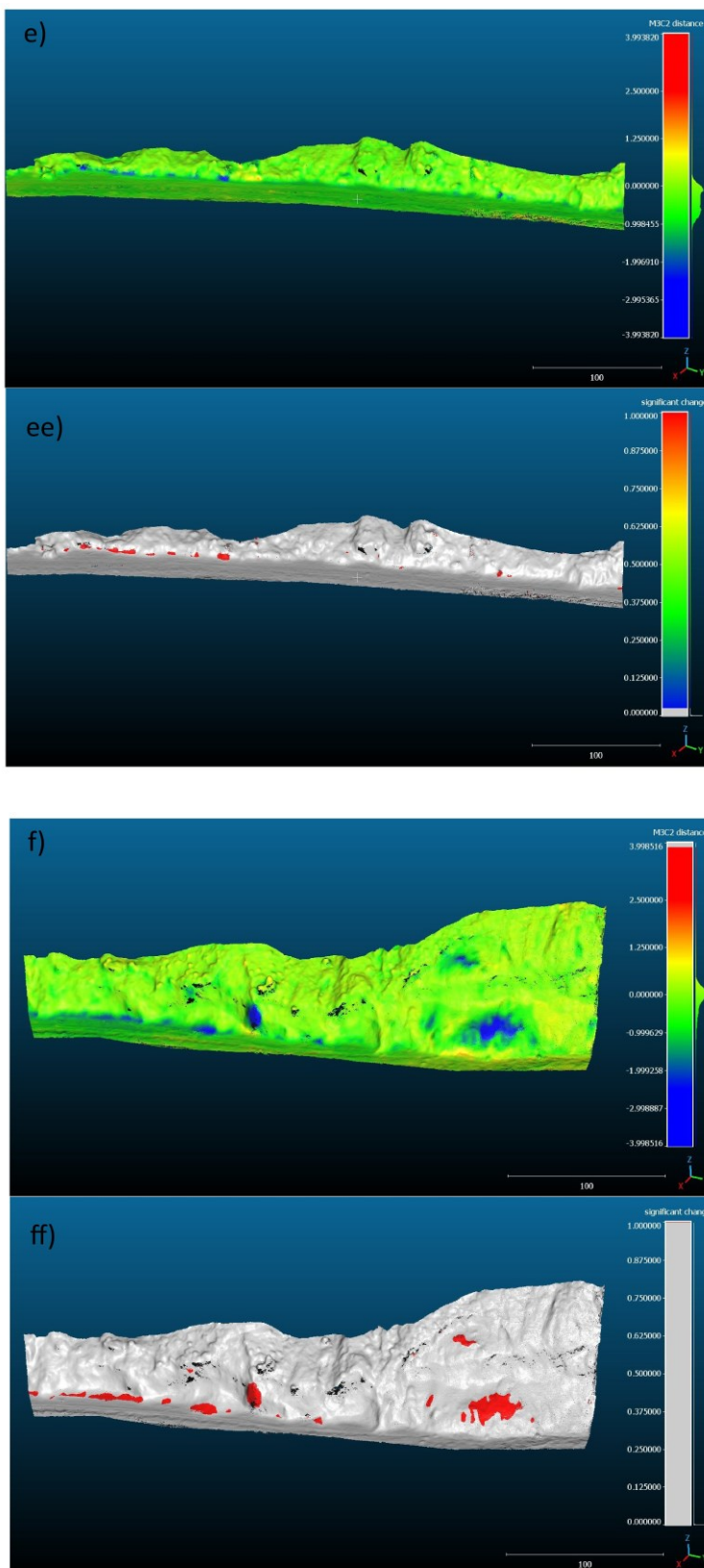


Figure 40: M3C2 results are displayed in the pictures showing M3C2 distance above and significant changes below for each area. Segment e) it is shown in 40e) and 40ee), then part f) it is shown in 40f) and 40ff).

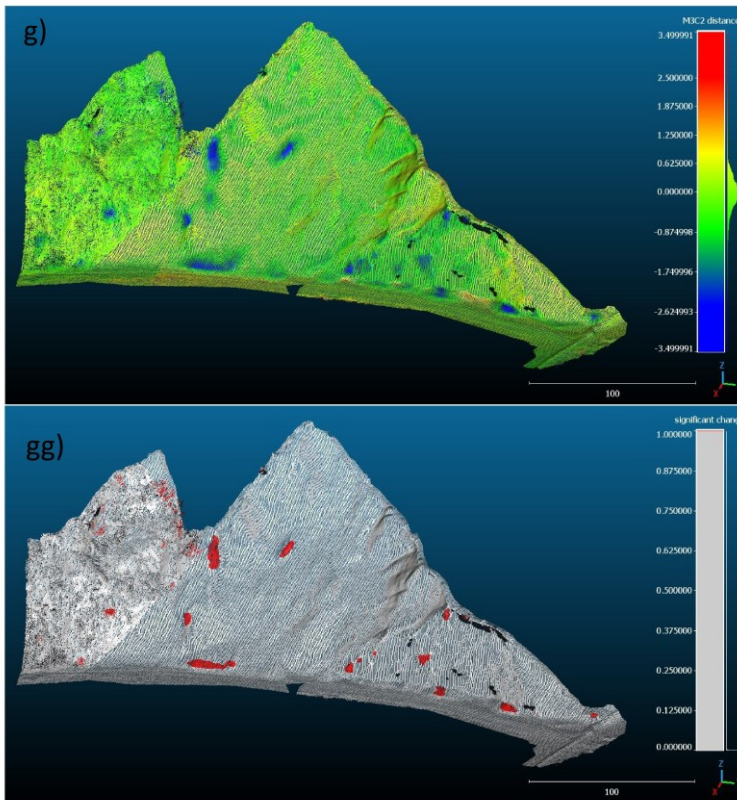


Figure 41: M3C2 results are displayed in the pictures showing M3C2 distance above and significant changes below for each area. Segment g) it is shown in 41g) and 41gg).

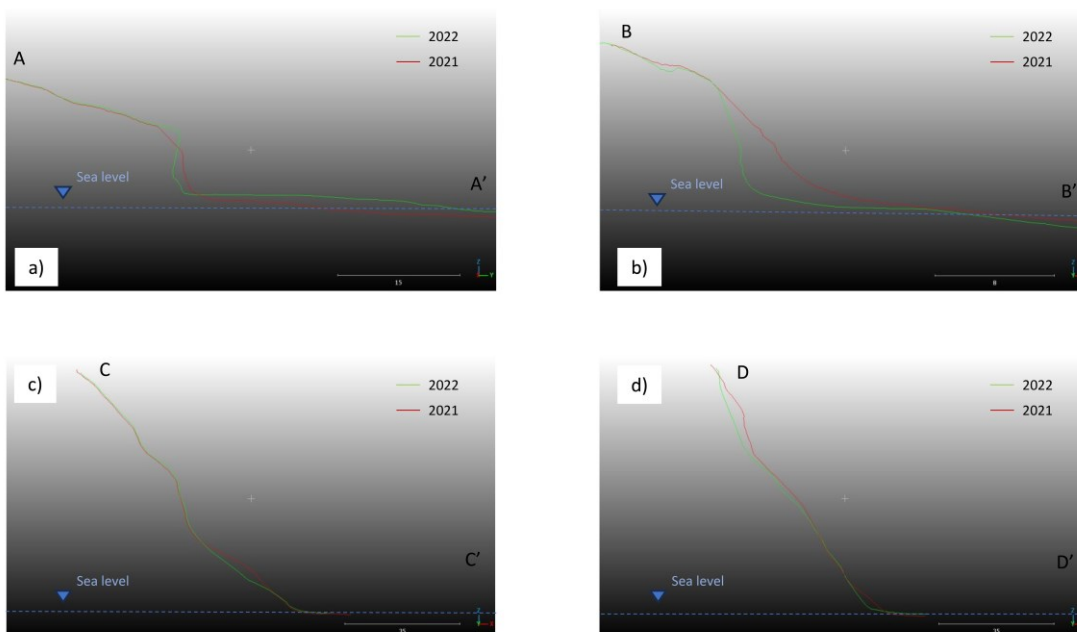


Figure 42: Extracted sections are shown to highlights the main changes in the coastline (Figure 36). The topography of 2021 is represented in red while the one of 2022 in green. All the profile are seen from south to north.

3.2.5 Discussion

The findings obtained from the change detection analysis emphasized the dynamic nature of the entire coastal region. Specifically, sections d), f), and g) exhibited a notably higher volumetric loss compared to other areas, while segment c) displayed accretion above the LOD threshold, distinct from the rest. Across this stretch of rocky coast, an average erosion rate of $0.29 \text{ m}^3 \text{ yr}^{-1}$ per meter of coastline was observed, with segment f) demonstrating a maximum erosion rate of $2.04 \text{ m}^3 \text{ yr}^{-1}$. These values, when compared to documented ones in different contexts such as California (Alessio and Keller, 2020; Swirad and Young, 2021), Japan (Obanawa and Hayakawa, 2018) and even in Mediterranean (Giuliano et al., 2022) were lower.

A comparison between the outcomes of this study and those from Fullin et al. (2023) is of interest. The repeated UAV surveys conducted in this research offered a higher temporal resolution and finer detail compared to the preceding analysis. However, due to the intricate nature of the study area and its hazardous configurations, especially in the Trave sector, repeating the UAV surveys with an identical arrangement of Ground Control Points (GCPs) was unfeasible. Consequently, the spatial resolution in this study was lower than in other applications (Brunetta et al., 2021; Fabbri et al., 2021b; Turner et al., 2016; Westoby et al., 2018). Additionally, the use of two different flights at varying altitudes (September 2021) and an automated flight (October 2022) may have introduced discrepancies in the final data products (Aicardi et al., 2016; Eisenbeiss and Sauerbier, 2011; Tziavou et al., 2018). Nonetheless, the analysis results have provided new insights compared to previous work. Within the timeframe of 2021-2022, clear cliff top retreats were not distinctly evident, and notching was observed at the base of cliffs in contrast to Fullin et al. (2023), where lower spatial resolution hindered such analysis. Particularly notable was the detection of notching in the Mezzavalle sector, despite the absence of significant cliff top retreats over the past four decades. This discrepancy might be attributed to processes that are not readily discernible from orthophotos. Moreover, even if sections of the cliff collapse, it may not necessarily result in a retreat of the boundary between the bare cliff and vegetation, making detection impossible without higher resolution data. Thus, comprehensive understanding of cliff evolution necessitates utilizing high-temporal and high-spatial resolution products (Bernatchez et al., 2021; Lim et al., 2005; Rosser et al., 2005b).

The data from this analysis confirm that a majority of the removed coastline material originates from the Trave sector (particularly segments f) and g)), consistent with existing literature (Fullin et al., 2023). This eroded material has a dual origin: from the base of cliffs due to notching and from various landslide processes, mainly topples and falls. A potential landslide was identified in segment f), as depicted in the lower part of section C-C' (Fig. 42c). However, establishing a clear pattern interconnecting these landslide events (e.g., notching leading to landslides) remains challenging. Although in section D-D', two distinct landslides were identified along the same slice, without knowledge of their chronological order, reconstructing the evolution of the instability process is infeasible.

Furthermore, accretion was observed in segment c) across a considerable portion of the beach, contrasting with the prevalent erosion in the northern segments (especially f) and g)). This observation suggests a potential along-coast transport of sediments from north to south in this region, in opposition to findings near Portonovo, indicating a northward drift (Grottoli et al., 2015). Further investigation is necessitated to establish if this material is locally generated or transported from the Esino or Musone rivers, despite their respective distances of 20 and 10 kilometers from this area.

Thus, this study underscores the significance of recurrent UAV surveys and their resultant data products, both for the high spatial resolution achievable and their ease of repetition. In handling a complex and unsafe environment such as this study area, equipping UAVs with Real-Time Kinematic (RTK) GPS for GCP disposition would be advantageous. Processes identified in this analysis were previously unobserved due to the application of techniques with lower spatial resolutions (Fullin et

al., 2023). Advancing understanding of these cliffs evolution could imply the installation of cameras in various locations to continuously capture images over time. This approach could facilitate the identification of causes behind erosion and discrete landslide events, alongside external triggering conditions (Godfrey et al., 2020). In areas densely covered with vegetation, combining UAV techniques with Lidar surveys could yield Digital Terrain Model (DTM) products (Swirad and Young, 2021).

3.2.6 Conclusions

This research attempts to quantify morphodynamic processes impacting the Portonovo-Mezzavalle-Trave cliffs during the period between 2021 and 2022, employing UAV-derived products. Two UAV surveys were conducted in September 2021 and October 2022, yielding respective Digital Surface Models (DSMs). Change detection analysis covering the entire coastline was executed using CloudCompare software.

The outcomes of this study can be succinctly summarized as follows:

- An average erosion rate of $0.29 \text{ m}^3 \text{ yr}^{-1}$ per meter of coastline was observed.
- A maximum erosion rate of $2.04 \text{ m}^3 \text{ yr}^{-1}$ was computed for segment f) in Trave sector.
- Notch erosion was identified in segments c), d), e) and f) corresponding even in the Mezzavalle sector where no erosion was previously identified (Fullin et al., 2023).
- Accretion on beach height and width was noted in segment c), differently from the other parts here studied.
- Segments a) and b) in Portonovo sector showed a limited erosion if compared with the other areas.

The loss of volume in the area is attributed to both landslides and notch erosion. UAV-derived products facilitated a more accurate comprehension of the cliff's evolutionary dynamics. The utilization of high spatial and temporal resolution data is imperative for a comprehensive understanding of processes within these intricate environments.

3.3 Detection of cliff top erosion drives through machine learning algorithms between Portonovo and Trave cliffs (Ancona, Italy).

3.3.1 Introduction:

The coastal environment holds significant importance due to its high population density and extensive human activities (Martínez et al., 2007; Small and Nicholls, 2003). Approximately 52 to 80 percent of coastlines worldwide are characterized by high coasts (Emery and Kuhn, 1982; Williams and Pranzini, 2018; Adam P. Young and Carilli, 2019). Despite numerous studies presented over the years, the intricate processes governing coastal evolution remain not well-understood (Naylor et al., 2010).

The morphological evolution of coastal cliffs results from a complicated interplay of various processes, including the influence of waves and their spectrum (Kennedy et al., 2011; Poate et al., 2018; Sunamura, 2015), beach width and sediments balance (Everts, 1991; Kennedy and Milkins, 2015; Komar and Shih, 1993; Moses and Robinson, 2011), as well as the slope and roughness of the seabed. These factors play fundamental roles in shaping nearshore dynamics in proximity to cliffs (Robinson, 1980; Sunamura, 1991).

Moreover, the intrinsic nature of the cliff slope itself plays a decisive role in the evolution of rocky coasts (Sunamura, 2015; Troiani et al., 2020). Therefore, it is essential to consider the lithotype and structural attributes of both the cliff and the shore platform (Naylor and Stephenson, 2010) in combination with ongoing rock mass processes such as brittle rock fracturing, creeping, and damage (Brideau et al., 2009; Donati et al., 2020; Marmoni et al., 2023; Stead and Wolter, 2015). Recent innovations in remote sensing technology have ushered in an era of higher spatial and temporal resolution topographic data, thanks to a plethora of innovative techniques now routinely employed, including Unmanned Aerial Vehicles (UAV) and Terrestrial Laser Scanning (TLS) (Caputo et al., 2018; Esposito et al., 2017; Francioni et al., 2018b, 2018a; Lim et al., 2005; Loiotine et al., 2021; Matano et al., 2015; Rosser et al., 2013, 2005b). These advancements have paved the way for numerous works aimed at recognizing local and regional processes occurring on cliffs (Gómez-Pazo et al., 2021; Jaud et al., 2019; Piacentini et al., 2021; Prémaillon et al., 2021; Young et al., 2021) often merging marine and slope stability perspectives (Bergillos et al., 2022; Earlie et al., 2015; Lollino et al., 2021). In this regard, numerical slope stability modelling can provide further insights into the current and future evolution of rocky coasts (He et al., 2022; Lollino et al., 2021; Mantovani et al., 2013; Styles et al., 2011).

While several authors have qualitatively classified hazards and risks on rocky coasts (Anfuso et al., 2013; Budetta et al., 2000; Del Río and Gracia, 2009; Di Luccio et al., 2023; Tursi et al., 2023), there remains a lack of research aimed at quantifying the specific significance of individual factors within the evolution process.

Combined with remotely sensed data, some efforts have been made to automatically assess the importance of each factor in driving instability using both Bayesian and Machine Learning (ML) algorithms on a regional scale (Dickson and Perry, 2016; Hapke and Plant, 2010; He et al., 2021). Nevertheless, there is currently a lack of site-specific applications of ML algorithms that employ a comprehensive set of quantified parameters to determine their relevance in instability and erosion processes affecting cliffs.

In this study, we examined a segment of rocky coast located in the eastern part of Italy (Ancona). We employed an integrated methodology that effectively combined field and remote sensing data. A Digital Surface Model (DSM), generated from a UAV survey conducted in 2022, was used to extract topographic parameters, while geomechanical data were collected during fieldwork. Cliff top erosion was computed in the time span 1978-2022 thanks to the USGS tool DSAS (Digital

Shoreline Analysis System) (Himmelstoss et al., 2018). These quantified datasets were subjected to an ML analysis, using XGB (Chen and He, 2014) and RF (Breiman, 2001) algorithms to obtain MDI, resulting in an output that ranks the significance of each driving factor concerning cliff top erosion. ML findings were further validated using Limit Equilibrium Method (LEM) codes (Stead and Coggan, 2012).

The results described represent the initial step of research aiming at the investigation of the potential of ML in forecasting the relative importance of various factors affecting a cliff top erosion process.

3.3.1.1 Setting

The area object of this study is located south of Ancona, between the sites of Portonovo and Trave in the Conero promontory with an area of approximately 1.5 km² (Fig.43). The coastline here is facing the Adriatic Sea, through high cliffs with an elevation that can exceed two hundred meters. Together with the San Bartolo promontory, these cliffs make up the only rocky coastline from Central Italy to Trieste that faces the Adriatic Sea.

The rocky coasts are primarily composed of Neogenic rocks, mainly marls, clays, sandstones, and gypsum (Cello and Coppola, 1989; Coltorti and Sarti, 2011) and, are partially covered by landslide deposits (Montanari et al., 2016). Two principal thrusts outcrop in this coastal sector, having a typical Apenninic orientation NW-SE (Coltorti and Sarti, 2011) bringing Miocenic formations upon Pliocenic rocks.

In this study, we divided the area of study into three different sectors according to geological characteristics (Fullin et al., 2023): Sector “1” Portonovo, here the cliffs are composed by marls of the Schlier Fm., Sector “2” Mezzavalle where cliffs are made of landslide deposits and Sector “3” Trave, with cliffs constituted by tectonized flyschoid formations (Fig.48).

The landslides have been extensively documented in the landslide database IdroGEO (<https://idrogeo.isprambiente.it/app/iffi/>). These landslides exhibit various kinematics, including composite landslides, rock rotational slides, clay/silt rotational slides, rock falls, rock block topples, and earthflows (Hungar et al., 2014). It should be noted that the landslides identified in this area are either currently active or in a reactivated state (Cruden, D.M., Varnes, 1996).

Regarding soil composition and coverage, comprehensive documentation is available through the Parco Nazionale del Conero authority (https://www.regione.marche.it/natura2000/public/allegati_blog/1682/File%20non%20disponibile.pdf). The soil that lies on top of the marls and calcareous bedrock is known as "regosoil" or "lithosoil Xerorthents typic and lithic." Unfortunately, there is a lack of information available about the different depths of this soil layer along the shore.

The Adriatic sea is classified as a microtidal environment (Bisci et al., 2021) and within this region, there are two predominant wave directions: the first is from the south-southeast (Scirocco), which corresponds to the most common direction of storm events and associated winds. The second prevailing storms are from the northeast (Bora), representing the dominant sea, namely the direction

of wave storms with greater intensity (Acciarri et al., 2021). A littoral drift observed along this coastal area is moving in a northward direction (Grottoli et al., 2015).

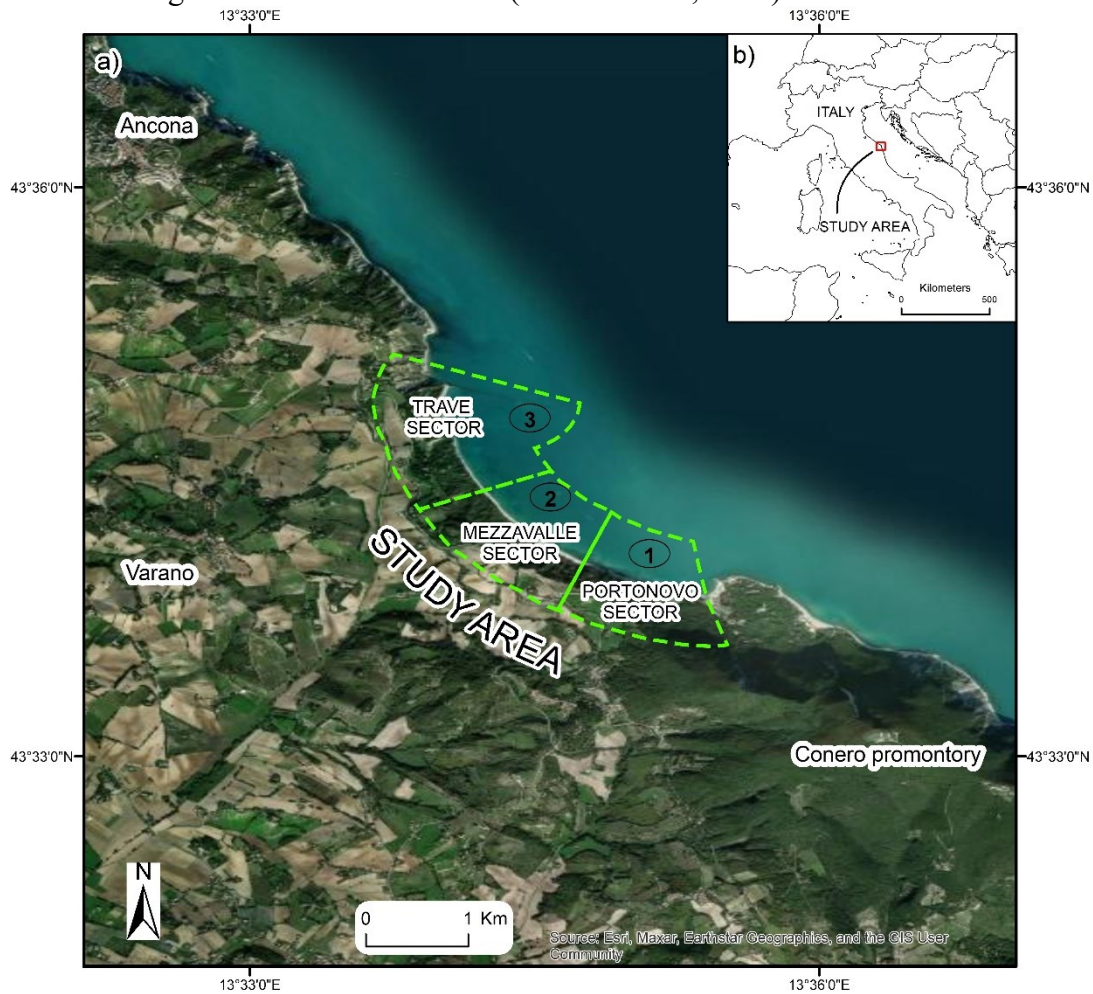


Figure 43: Map displaying the position of the study area: a) Satellite image showing the study area and the three sectors called Portonovo, Mezzavalle and Trave. (image taken from GeoEye satellite database, 2020). b) Collocation of the study area respect to Italy.

3.3.2 Methodology

It is possible to resume the paper’s methodology in 5 steps (Fig. 44): 1) Fieldwork, 2) Data analyses and surveys, 3) Parameters extraction, 4) Machine learning analysis and 5) Slope stability analysis.

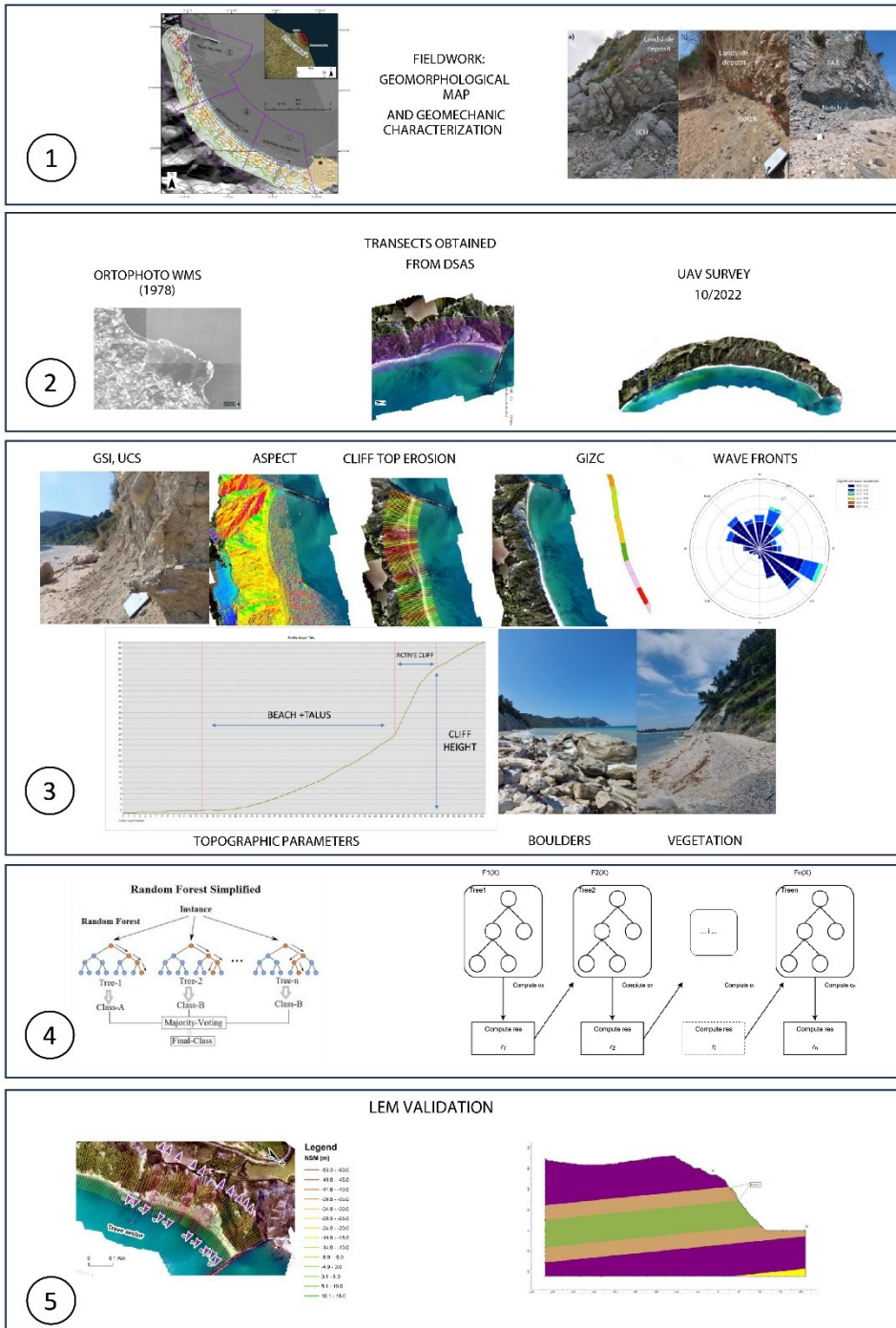


Figure 44: Workflow sketch: 1) Fieldwork; 2) Data analyses and surveys. 3) Parameters extraction. 4) Machine learning analysis. 5) Slope stability analysis.

3.3.2.1 Fieldwork

Fieldwork was performed to collect and map information regarding geological and mechanical characteristics of the exposed lithotypes.

According to ISRM guidelines (Barton, 1978), in situ uniaxial compressive strength (UCS) values, both for soil deposits and rocks were determined (Barton, 1978). The rock masses outcropping along the coastline were classified by means of the “Geological Strength Index” (GSI) for heterogeneous rock masses (Hoek et al., 2005; Marinos, 2017). Approximately every 10 meters along the cliff base, outcrops were analysed, and geomechanical parameters were recorded. Subsequently, all this data was compiled, categorized, and represented as polygons in a GIS environment. This approach allowed for the subdivision of the coastline on geomechanically homogeneous areas on which subsequent analyses will be performed.

3.3.2.2 Data analyses and surveys

The UAV data acquisition was accomplished in two consequent days, 06/07 October 2022, covering the extension of the study area (about 1.5 km²). The drone used for the survey was a DJI Mavic 2 Pro. Characteristics of the drone camera were: 20 megapixel resolution; 28 mm focal length with f/2.8 to f/11 aperture and maximum image size of 5472×3648 px.

In order to get the same ground resolution of the photographs, the flights were conducted at a constant elevation, 120 m above the area, using programmed flight plans created through the BLY3D software of Aermatica3D application (<https://www.aermatica.com/app-bly3d/>). Photographs overlap was kept at 80% and flight speed at 8 m/s.

Trimble RTK-DGPS R8 (i.e., stop and go technique; horizontal accuracy of 8 mm and vertical accuracy of 15 mm) was used to support the UAV survey with an NRTK-GNSS measure to acquire the position of 13 Ground Control Points (GCPs), based on the national net of Leica. These were white and red wooden square targets, measuring 60 × 60 cm, uniformly distributed within the study area. The Universal Transversal Mercatore WGS84 zone 33 N was used as coordinate system and the ellipsoidal height was converted to orthometric height using national grids in the software “Convergo” (https://www.cisis.it/?page_id=3214). Estimate error during the NRTK-GNSS survey was approx. 3 cm horizontally and vertically.

GCP coordinates and UAV data were managed and processed using "Agisoft Metashape" (version 1.5.1, available at <https://www.agisoft.com>). The Digital Surface Model (DSM) and orthophoto of the surveyed region were produced following existing methods (Brunetta et al., 2021; Duo et al., 2021; Fabbri et al., 2021a; Gindraux et al., 2017; Talavera et al., 2021).

3.3.2.3 Parameters extraction: Cliff top retreat analysis and transects identification.

Cliff top retreat was determined through the application of DSAS analysis. Specifically designed for analyzing shoreline movements, this tool's frequent inclusion in literature attests to its common use in studies focusing on cliff retreat (Brooks et al., 2012; Gómez-Pazo et al., 2021; Hapke and Plant, 2010; Lollino et al., 2021).

1978 and 2022 orthophotos were used for the study. The 1978 version is publicly accessible on the "Regione Marche" website at <http://wms.cartografia.marche.it/geoserver/Ortofoto/wms>. The 2022 orthophotos were generated using UAV photos, and the spatial resolutions of these orthophotos are respectively 1.28 m for the 1978 one and 0.1 m for the 2022 one.

The cliff top edges were delineated in both orthophotos, and the linear distance between the distinct cliff top edges and a baseline (transects) was measured. The 2022 orthophoto was resampled to a cell size of 1.28 m, consistent with the 1978 orthophoto. Subsequently, a uniform visual scale (1:3000) was applied to both photos. The mapping of cliff top edges on the orthophotos involved a manual process, relying on the boundary between vegetation and bare slope to define the edge of the cliff. The cliff top edge was calculated separately 4 times, and the variations between each line were identified (Buchanan et al., 2020; Cenci et al., 2013; Viridis et al., 2012) to account for digitalization errors. The manual mapping process was performed according to established methodologies outlined in existing literature (Crowell et al., 1991; Del Río and Gracia, 2013; Fletcher et al., 2003). Additional specifics regarding the adopted procedure can be found in Fullin et al., 2023.

To calculate georeferencing error between the two orthophotos the subsequent procedure has been followed. We selected scattered control points within the coastline for 1978 orthophoto, georeferenced by regional authority using benchmark topographic, and compared these control points with the 2022 product, georeferenced using GCPs. We calculated the Euclidean distance between the matched control points, assigning an uncertainty value to each one based on this horizontal distance. We used inverse distance-weighted interpolation in ArcGIS to interpolate our uncertainty as a continuous grid at a resolution of 50 meters per pixel across the research region, because the uncertainty is not constant across orthophotos (Bloom et al., 2023).

Shoreline has been used as reference line to obtain the baseline (with a 100 m buffer). The 2022 orthophoto was used for mapping and the shoreline was identified by the color changing between the sand and the sea. A series of transects is generated starting from this baseline crossing the two cliff edges detected and computing the linear distance between them. In this case we have defined a distance between each transects of 10 meters, for a total of 310 transects. In order to obtain coastal profiles, it was used a smoothing factor of 100 to avoid any crosscut between these lines and keeping each transect as much perpendicular to the coastline as possible. Net Shoreline Movement (NSM, the total movement measured in meters) and the End Point Rate (EPR, the rate of movement calculated in meters per years) along these transects were calculated, together with Confidence of End Point Rate (ECI or EPRunc in newer versions of DSAS), an index which takes into account the uncertainty of lines (accuracy error) as a factor for calculating the EPR confidence. DSAS analysis was conducted for the period 1978-2022 to assess coastal retreat over the entire 40-year span, given that these were the most recent and older orthophotos available for the area.

3.3.2.4 Machine learning analysis: Parameters.

For Machine Learning analyses we considered a list of 13 parameters, as detailed in Table 10. To acquire topographical data, we utilized the 2022 DSM in a GIS environment. Transects generated from DSAS enabled the extraction of profiles corresponding to the 2022 topography, from which morphological elements like Cliff Height, Cliff Slope, Aspect, Beach and Talus width, and Cliff base slope were derived. Geomorphological edges were manually identified on these profiles, and the corresponding values were recorded in a table (Appendix 1), associating transect numbers with the relevant information. The geological/geomorphological parameters taken into account included UCS, GSI, Cliff Top Retreat, the presence of boulders on the cliff base, beach erosion, and the existence of vegetation on the cliff top. UCS and GSI data were collected during fieldwork and subsequently imported into the GIS environment. Polygons were utilized to represent the variations in parameters, and the values within each polygon were recorded in a table, aligned with the

existing DSAS transects (see Appendix 1). The DSAS tool was employed to measure cliff top retreat, and the automatically computed values were stored for each corresponding transect. The occurrence of boulders at the cliff base was identified using the 2022 orthophoto. A value of 1 was assigned when boulders were present along the transect, and 0 when they were not. Beach erosion data for the period between 2008 and 2019 were calculated by Regione Marche as part of the Gestione Integrata delle Zone Costiere (GIZC) project (<https://www.regione.marche.it/Regione-Utile/Paesaggio-Territorio-Urbanistica-Genio-Civile/Difesa-della-costa#Piano-GIZC-2019>) and made available in a .kmz file, which can be freely downloaded from their website. The .kmz file was imported into a GIS environment and buffered along the shoreline to capture values along the created transects. This data, along with beach width, holds significance in representing wave impact (Earlie et al., 2018; Everts, 1991; Sunamura T., 1992). The presence of vegetation at the cliff top was analyzed in a manner similar to boulder occurrence. Additionally, two marine parameters were computed by considering the angle between the normal of the 2022 shoreline and the wave fronts (Emery and Kuhn, 1982). The direction of dominant wave fronts, Bora and Scirocco (Bisci et al., 2021), were chosen according to Rete Ondametrica Nazionale (RON) data (<https://www.mareografico.it/>).

The selection of drives presented in Table 10 is not an exhaustive catalog of all potential factors influencing cliff failure. The choice is based on reviews of previous studies (Dickson and Perry, 2016; Hapke and Plant, 2010; Sunamura, 2015; Trenhaile, 2012) and field data.

Table 10. *Summary of parameters used in ML analyses.*

Drives	Description	Mapping Method	Data type
Cliff height	The height of the cliff above sea level. It can influence slope stability (Dickson and Perry, 2016; Wolters and Müller, 2008)	Data were extracted from 2022 DSM sampling the highest point of the active cliff	Number
Cliff slope	The slope of the active cliff wall. It can affect the frictional resistances	It was manually computed on the extracted profile in GIS environment, starting from the highest point of the active cliff down to the cliff base	Number
Aspect	The exposure of the cliff wall might be changing the erosion rate through differential weathering rates and different exposure to winds (Dickson and Perry, 2016)	It was automatically computed in GIS environment. The aspect was reported measured in degree clockwise respect to Nord	Number

UCS (MPa)	The uniaxial compressive strength measured at the cliff base is related to cliff retreat (Prémaillon et al., 2018; Sunamura T., 1992)	It was collected during the fieldwork using a Pocket Penetrometer and a Schmidt Hammer	Number
GSI	Classification of the rockmass which takes in account the quality of discontinuities that controls cliff erosion (Earlie et al., 2015)	It was obtained during the fieldwork using the most updated versions of the classification for complex formation (Marinos, 2017)	Number
Cliff top retreat	Values of the cliff top retreat computed in the period 1978-2022, target value for the ML analysis	It was computed in GIS environment using the tool DSAS of USGS	Number
Beach and talus width	The corridor that separates the cliff base from the sea. This parameter determines if the cliff wall might be hit by waves (Everts, 1991)	It was manually measured on GIS environment for every transect, starting from the cliff base until the shoreline	Number
Cliff base slope	The slope of the space between the sea and the cliff base. It can affect wave run-up (Stockdon et al., 2006)	It was manually measured on GIS environment for every transect on the tract starting from the cliff base until the shoreline	Number
Boulders at cliff base	Boulders at the base of the cliff can reduce the erosive power of waves, in fact they are used even as revetment (Goda, 2010)	It was manually added for each transect looking at the 2022 orthophoto	Binary (0 absence, 1 presence)
Beach retreat (GIZC)	Beach retreat between 2008-2019 computed by Regione Marche in the project Gestione	The values reported in the GIZC were reported by a buffer in the shoreline and the	Number

	Integrata Zone Costiere (GIZC)	values attributed for each transect	
Vegetation at cliff top	Trees and their roots in the upper part of the cliff can give more cohesion to soil or remove it when they are uprooted	It was manually added for each transect using the 2022 orthophoto	Binary (0 absence, 1 presence)
Angle between shoreline and NE storms (Bora)	The angle between the normals of the shoreline and the wave front (Emery and Kuhn, 1982). The direction of Bora wave front was chosen according to RON data*	It was manually measured on GIS environment for every transect	Number
Angle between shoreline and SE storms (Scirocco)	The angle between the normals of the shoreline and the wave front (Emery and Kuhn, 1982). The direction of Scirocco wave front was chosen according to RON data*	It was manually measured on GIS environment for every transect	Number

* <https://www.mareografico.it/>

3.3.2.5 Application of machine learning models

To discern the primary factors influencing cliff erosion, we adopted two Machine Learning (ML) models: the Random Forest (RF) Ensemble Model (Tin Kam Ho, 1995) and eXtreme Gradient Boosting (XGB) (Chen and He, 2014) (code is included in Appendix 2). These models categorized two classes – erosion or non-erosion – based on whether the values were greater or less than 0.

RF (Azar et al., 2014; Breiman, 2001) consists of different Decision Trees (Quinlan, 1993) that operate together as an ensemble (Fig. 45). The concept of RF is that many uncorrelated trees, operating as the voting population, will outperform any of the individual trees. Indeed, one of the most important aspects of RF is the uncorrelation between trees. While some trees may be wrong, many others in the class prediction are correct. So, a set of trees can move in the right direction due to the uncorrelatedness of the trees. Another advantage of RF is the simplicity of extraction of the most important features in a prediction. The relative importance of each feature on prediction can be calculated by measuring how much the tree node reduces impurity to all trees in the forest using that feature, as described in Equation 23:

$$N_k^i = w_k C_k - w_{left(k)} C_{left(k)} - w_{right(k)} C_{right(k)} \quad \text{Eq. 23}$$

where w_k is the weighted number of samples in node k as a fraction of total weighted number of samples, C_k is the impurity in node k , and $left(k)$ and $right(k)$ are its respective children's nodes. To get a complete map of which features are important for the final classification, we compute a score for each feature after the training phase (Equation 24) and normalize the results so that the sum of all importances equals 1.

$$FI_i = \frac{\sum_{k: \text{node } k \text{ splits on feature } i} N_k^i}{\sum_{j \in \text{all nodes}} N_j^i} \quad \text{Eq. 24}$$

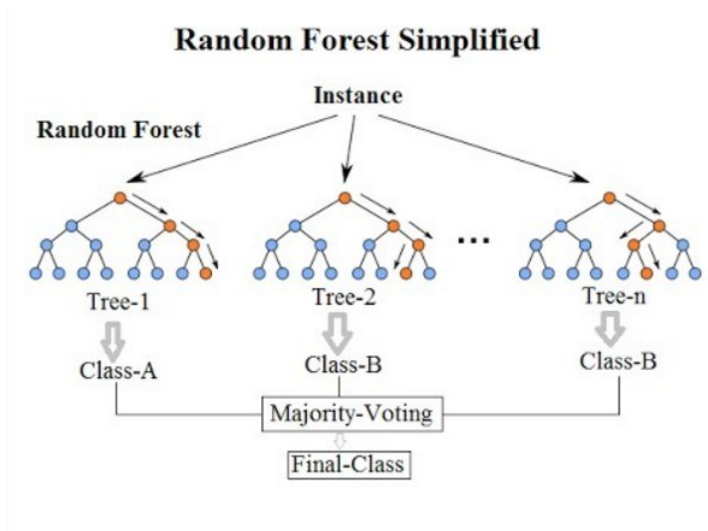


Figure 45: Representation of Random Forest (image from <https://kenhoffman.medium.com/random-forest-hyperparameters-explained-8081a93ce23d>).

XGB (Chen and Guestrin, 2016; Chen et al., 2018) is built on the concept of Gradient Boosting (Friedman, 2001)(Fig. 46). Each weak learner that composes the ensemble (i.e., Decision Tree) maps input data to one of its leaves that contains a class. The XGB algorithm minimizes a regularized loss function (difference between the predicted and target outputs). XGB is trained iteratively. Trees are individually added to the ensemble and adjusted to correct prediction errors from previous models. XGB uses a gradient descent algorithm (Ruder, 2016) to minimize loss when adding new weaker models.

In Equation 25 we can see the result of XGB as the sum of previous output $K_{n-1}(X)$ and the result of function h_n trained to predict result r_{m-1} multiplied by the regularization term α_n . The r_i term represent the output of the i^{th} weaker learner. In Equation 26 we can see how to compute the regularization term (α_i) where O_i and $K_{i-1}(Xi)$ are the target output and prediction of the model respectively. Equation 27 is the differentiable loss function. As for RF, it is possible to obtain the feature importance from XGB by measuring how much the tree nodes which use a feature reduce impurity across all trees in the model.

$$K_n(X) = K_{n-1}(X) + \alpha_n h_n(X, r_{m-1}) \quad \text{Eq.25}$$

$$\text{argmin}_{\alpha} = \sum_{i=1}^n L(O_i, K_{i-1}(Xi) + \alpha h_i(X_i, r_{i-1})) \quad \text{Eq. 26}$$

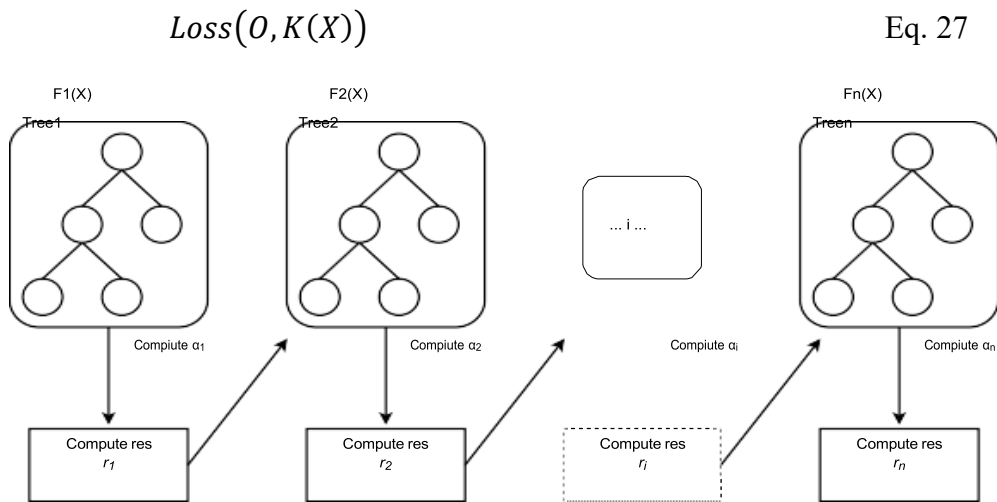


Figure 46: Representation of eXtreme Gradient Boosting (Image created by Michele Fraccaroli).

The simulations were performed splitting the dataset in 80% of training and 20% of test (Guyon and others, 1997). Oversampling was used to avoid inconsistency due to the difference between the size of the two addressed classes (Bej et al., 2021) and a grid search approach was used for the tuning of hyperparameters (Liashchynskiy and Liashchynskiy, 2019) owing to the moderate size of the dataset.

3.3.2.6 Slope stability numerical modelling

The stability of Trave sector, i.e. the area most affected by erosion processes in the time span 1978-2022 and with the highest elevation, has been investigated by 2D Limit Equilibrium Method (LEM). Ten topographic sections were extracted (Fig. 47) from Lidar data provided by Regione Marche in 2012 (Fullin et al., 2023), and the Factor of Safety (FS) was calculated for each of them.

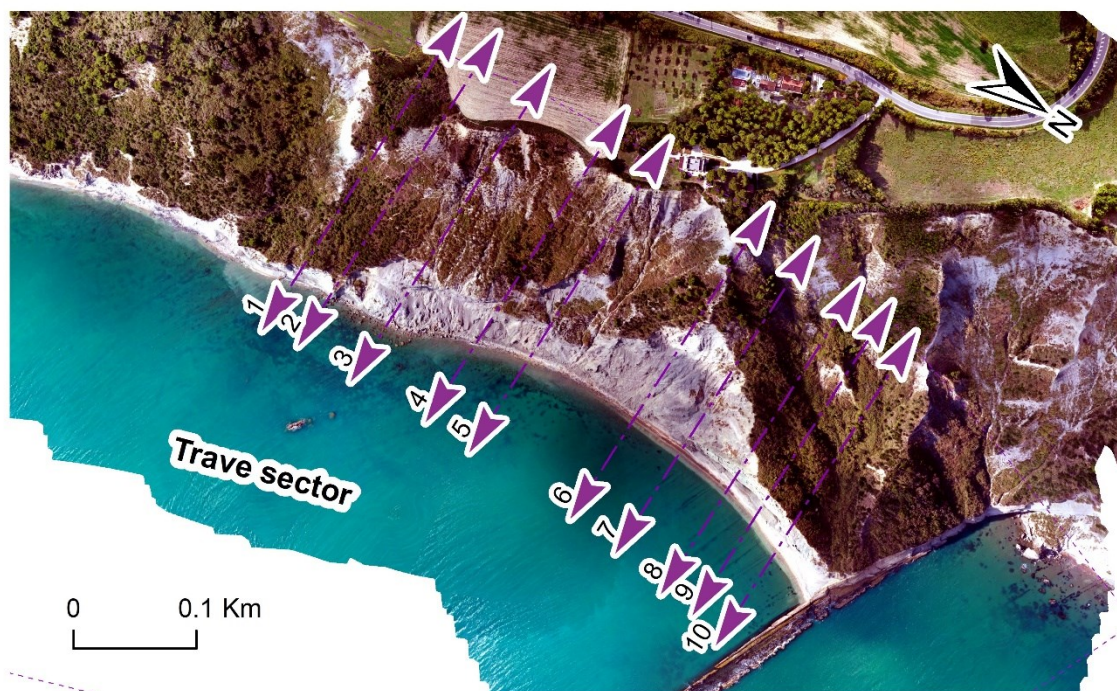


Figure 47: *Extracted sections are highlighted in violet and numbered.*

In particular, the slope stability conditions were investigated using the Morgenstern-Price method implemented in the Slide2 code (<https://www.roccscience.com/>), on 2012 sections, i.e. pre-erosional retreat, in order to calculate their F.S. (Morgenstern and Price, 1965) (Appendix 3).

The input parameters were derived from the field surveys (UCS and GSI classification for complex formation (Marinos, 2017)). The Geological Strength Index (GSI) provides a method of relating geological field observations to the quality of the rock mass. This classification is based on the density of jointing and amount of weathering/alteration observed in the rock mass. As part of the Hoek–Brown Failure Criterion, GSI can be extended to determine strength and material characteristics of in situ rock masses. The analyses were run assigning to the slope materials the Hoek-Brown (H-B) failure criterion (Cai and Kaiser, 2007). GSI was estimated in situ for the different formations and ranges between 50 and 20 and m_i (material constant for the intact rock) and γ (specific weight) were derived from typical values quoted for each lithotype (Brown, 2008). D is a factor which depends upon the degree of disturbance to which the rock mass has been subjected by blast damage and stress relaxation. It varies from 0 for undisturbed in situ rock masses to 1 for very disturbed rock masses. Values of D different from zero indicate disturbed tectonic conditions. Representative values of the materials used in the analyses are listed in Table 11), grouped on the basis of GSI values. The models assume dry conditions of the slopes, as there is a lack of available data regarding the water table.

Table 11: List of the parameters used for numerical modeling (refer to Figure 51 for the number of the transects reported).

LITHOLOGY	γ (KN/m3)	GSI	mi	D	UCS (MPa)
Argille Azzurre Fm. (228-265)	24	35	7	0	25
Faulted rocks (266-276)	23	25	4	0.6	20
Argille Azzurre Fm. (277-290)	24	35	7	0	25
Argille Azzurre Fm. (291-310)	24	45	7	0	30
Orizzonte del Trave	25	50	17	0	50

3.3.3 Results

3.3.3.1 Fieldwork

A revised geological-geomorphological setting of the study area was generated based on the field survey findings (Fig. 48). The Portonovo sector is characterized by the outcropping of the Schlier Fm. mostly covered by landslides deposits. The cliff top retreat is here mainly ascribing to landslides in the upper portion of the slope, with vertical or sub-vertical faces in corresponding with the crown portion of the landslide (Fig.49a).

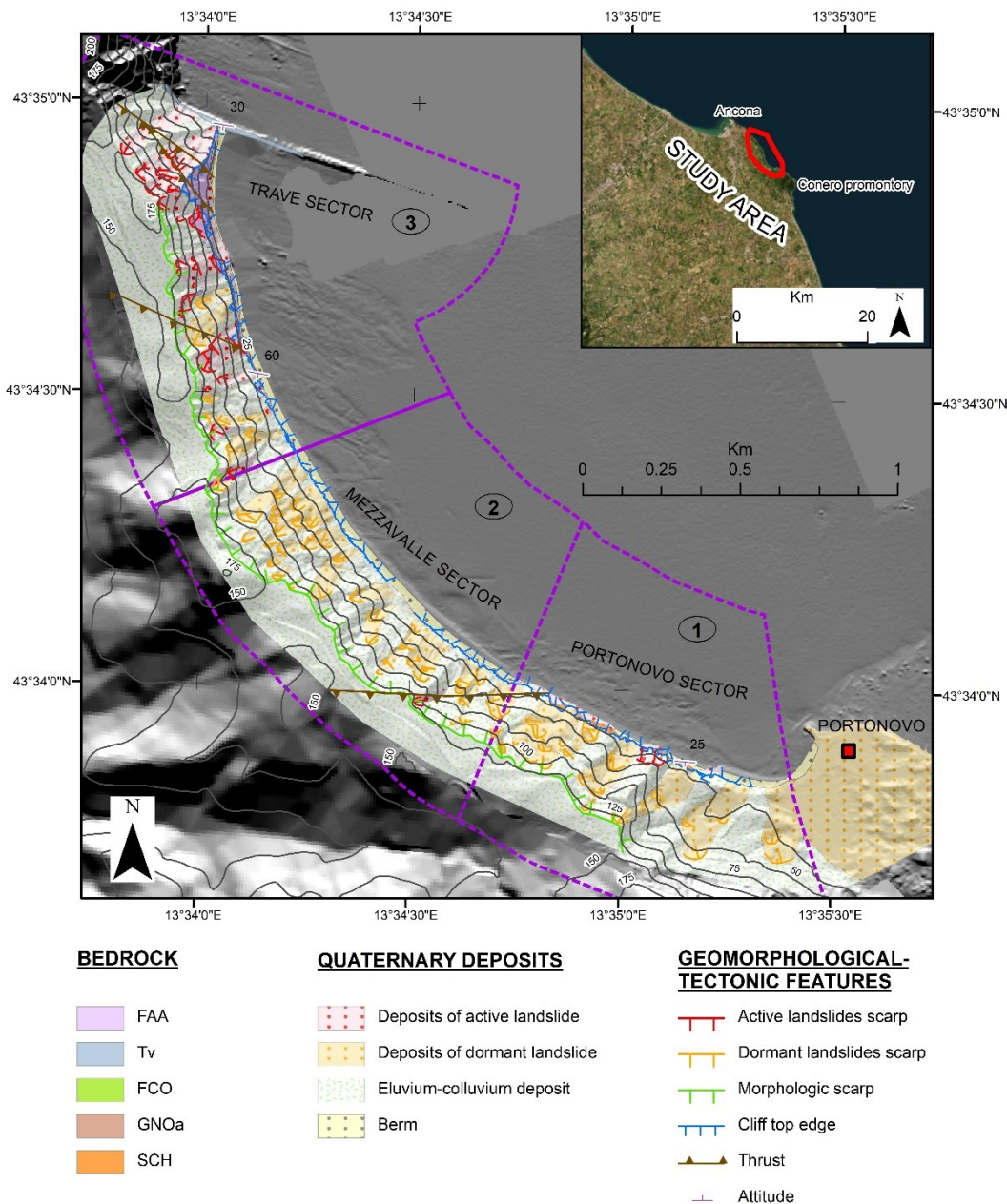


Figure 48: Geological-geomorphological setting of the study area and “Sectors”: 1) Portonovo; 2) Mezzavalle; 3) Trave. Bedrock legend: SCH (Schlier Fm., Lower Miocene-Upper Miocene), GNOa (Sapigno Fm. Upper Miocene), FCO (Colombacci Fm., Upper Miocene), Tv (Trave horizon, Lower Pliocene), FAA (Argille Azzurre Fm., Lower Pliocene-Lower Pleistocene).

Mezzavalle sector is principally composed by landslide deposit (Fig. 49b), only close the morphological edge that separate inland from the steep cliff, it is possible to observe the bedrock outcropping in landslides scars. The Trave sector presents the higher numbers of active landslides of different type, mainly falls, block toppling, earth flow and complex. An important feature that characterizes this sector is the high fracturing degree of the rock mass (Fig. 49c), it occurs in corresponding with many thrusts which cut the rock mass, so diminishing the mechanical characteristics of the rock mass and predisposing it to landslides.

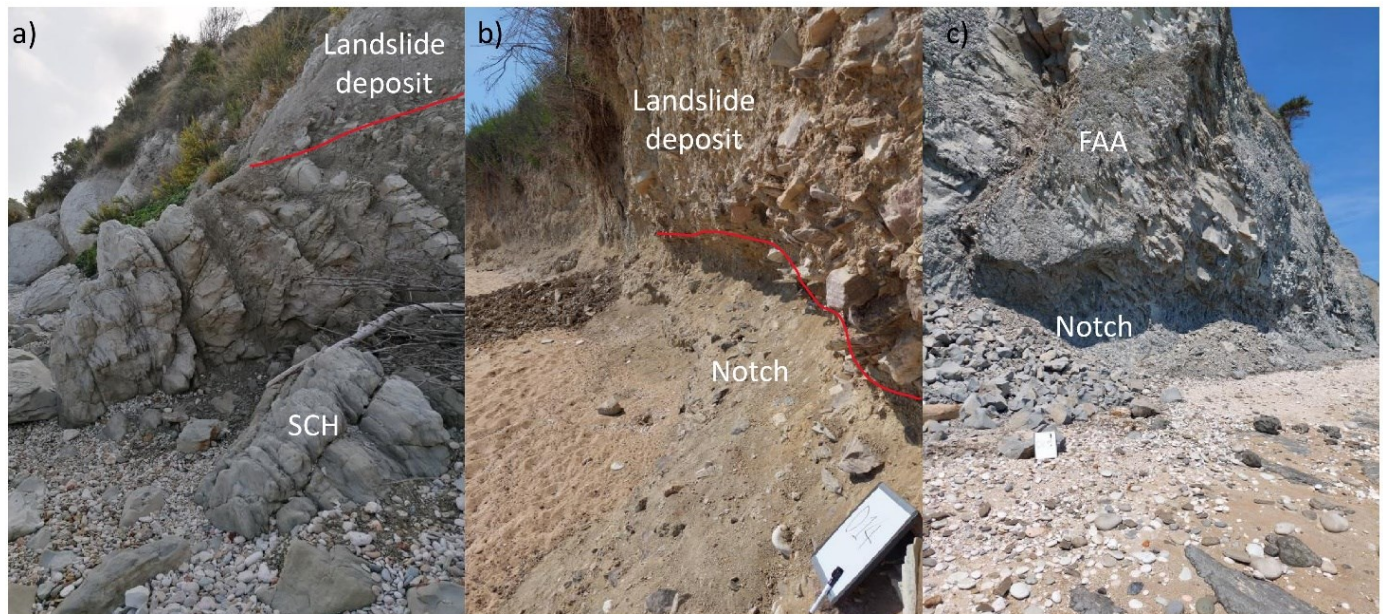


Figure 49: Pictures portraying the different configurations of the cliff base. a) Portonovo sector b) Mezzavalle sector c) Trave sector.

The UCS values gathered through pocket penetrometer and Schmidt hammer are reported in Table 12. Rock mass quality, expressed by the GSI value, and UCS are factors of crucial importance in coastal cliff erosion processes (Budetta et al., 2000; Prémaillon et al., 2018; Sunamura, 2015). Therefore, we decided that GSI and UCS were the most suitable geotechnical parameters to be used, according to the lithotypes outcropping in the area (soil or weak rocks). Because weak rock masses consist of alternating layers of marls and layers of calcareous marls, an average UCS value was computed across various levels in order to obtain a single representative value for each site. Since landslide deposits make up the cliffs in Mezzavalle, a GSI of zero was assigned to them in order to represent GSI numerically along the entire coastline, even in areas where the rock is not outcropping. This was done to explicit GSI values along the whole coastline, to highlight that these deposits are weathered, and with lower mechanical resistance than the nearby rocks (as reported even by UCS).

Table 12: *Range of GSI and UCS values for the 3 sectors according to different transects.*

SECTOR	TRANSECTS	GSI	UCS (MPa)
PORTONOVO	1-79	50	35
MEZZAVALLE	80-184	0	5
	185-215	0	1
TRAVE	216-227	45	30
	228-265	35	25
	266-276	25	20
	277-290	35	25
	291-310	45	30

3.3.3.2 *Cliff top retreat analysis*

The maximum Root Mean Square Error (RMSE) for the digitalization of the cliff top and the shoreline was calculated. An RMSE of 3.89 meters was recorded for cliff-top digitalization using the 1978 orthophoto, while shoreline digitalization in the 2022 orthophoto yielded an RMSE of 1.65 meters. Georeferencing error for the UAV orthophotos using GCPs resulted in a horizontal uncertainty of 5 cm. The horizontal uncertainty between UAV 2022 orthophoto and 1978 orthophoto was computed as described in Bloom et al., 2023 and it is reported in Figure 50.

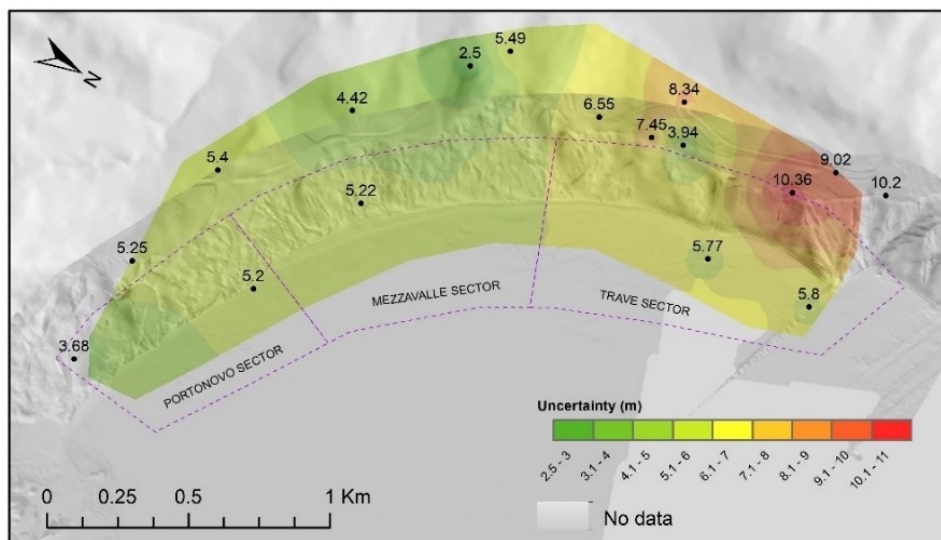


Figure 50: Horizontal georeferencing uncertainty measured between 1978 and 2022 Orthophotos. The cliff top erosion in whole period 1978-2022 was considered in this analysis: Trave sector is the portion with the highest mean value of EPR, Portonovo sector shows a similar behavior while Mezzavalle sector shows a marginally negative value (Tab. 13). Moreover, focusing on specific area within each sector, values of almost -0.6 m/yr and -1.2 m/yr of EPR are reached between transects 61-66 and 251-288 in Portonovo and Trave sector respectively (Fig. 51). ECI computed for this time span is 0.09 m.

Table 13: DSAS results for each period analyzed. Mean EPR and ECI are reported.

Periods	Portonovo		Mezzavalle		Trave	
	EPR (m/yr)	ECI (m)	EPR (m/yr)	ECI (m)	EPR (m/yr)	ECI (m)
1978-2022	-0.24	0.09	-0.09	0.09	-0.25	0.09

CLIFF TOP RETREAT 1978-2022

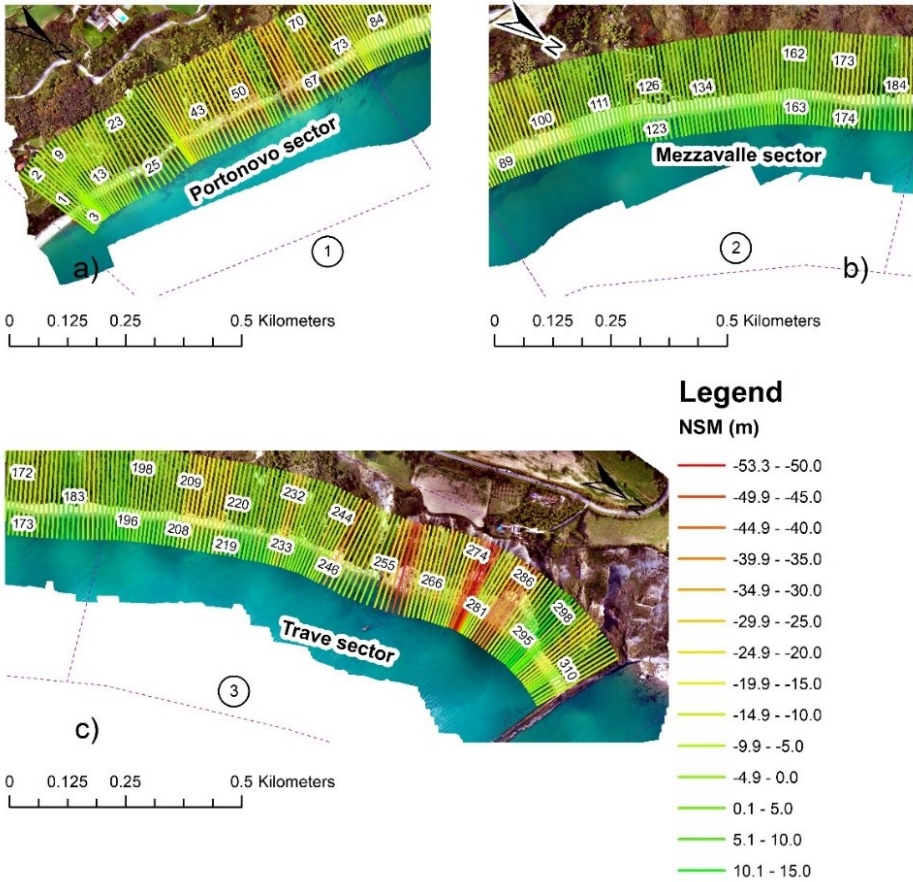


Figure 51: NSM values calculated along transects, referred to the period 1978-2022: Portonovo and Trave sector showed the highest values of retreat. Computed transects a) at Portonovo sector b) Mezzavalle sector c) at Trave sector.

3.3.3.3 *Machine learning*

The parameters shown in Table 10 were extracted for each transect acquired via DSAS elaboration, yielding a table with 310 lines correspondent the number of transects and 13 columns denoting the extracted or derived parameters (Appendix 1). This data was processed through two ML algorithm, RF and XGB as described in methodology.

Each algorithm gave two different graphs: a confusion matrix and a table with feature importance. RF analysis gave a test score of 0.95 on test data and a confusion matrix showing only 4 false predictions (Fig. 52, 3b). The feature significance graph (Fig. 52, 3a) revealed that "Cliff height" is the most important parameter for class prediction, with a relative relevance twice that of the other drivers.

Then, analysis was performed using XGB algorithm, giving a test score of 0.95 on test data. The confusion matrix (Fig. 52, 3d) for XGB revealed 4 erroneous predictions, and the feature importance graph (Fig. 52, 3c) revealed the same order of RF algorithm driving importance. Even in this analysis, "Cliff Height" was shown to be the most relevant characteristic in class recognition, although with a magnitude less than twice that of the others.

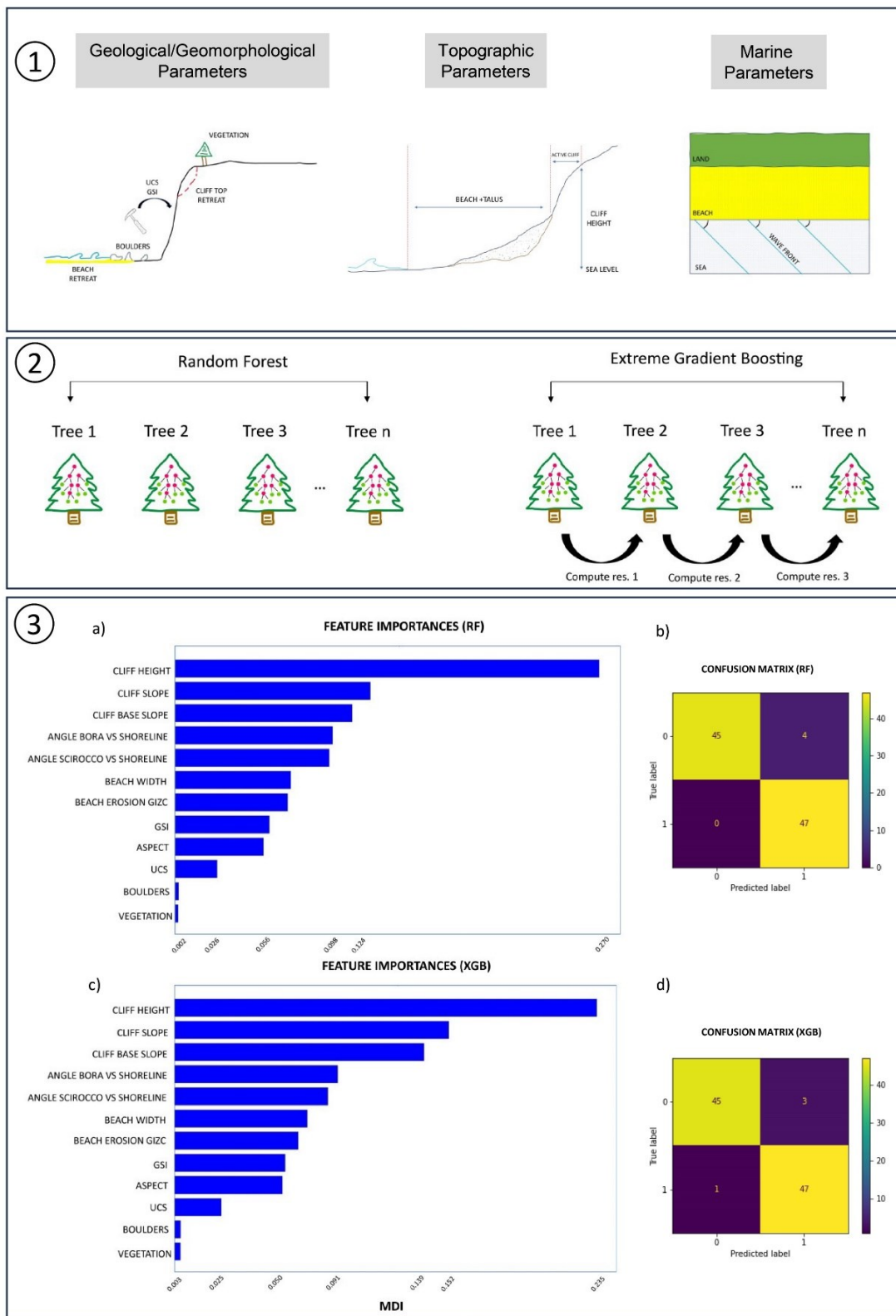


Figure 52: ML results and analysis performed using RF and XGB algorithms. 1) Sketch displaying the parameters used in the analysis. 2) Illustration of the ML algorithm used. 3) Picture illustrating ML results. 3a) Graph showing feature importance resulting from RF algorithm. 3b) Confusion matrix of RF elaboration. 3c) Graph illustrating the feature importance extracted using XGB algorithm. 3d) Confusion matrix of XGB analysis.

3.3.3.4 Slope stability

Numerical modeling outputs are reported for easiness in Table 14, summarizing FS and cliff height values obtained. Values of FS below 1 are present for section 6 and 8, and the range of values obtained is from 4.37 to 0.91. Notably, these are indicative of the greater and lower cliff heights, respectively.

Table 14: Results from LEM analysis along the extracted sections.

SECTION	FS	Cliff Height (m)
1	2.04	37
2	1.86	42
3	1.52	50
4	1.12	73
5	1.21	80
6	0.91	120
7	1.14	97
8	0.98	60
9	2.26	50
10	4.37	25

The graph in Figure 53 shows as it exists a dependency between FS decrease and cliff height increase ($R^2 = 0.84$). Section n. 6 with a FS of 0.91 cross the slope between transects 280-290 where values of retreat above 40 m in the period 1978-2022 were computed.

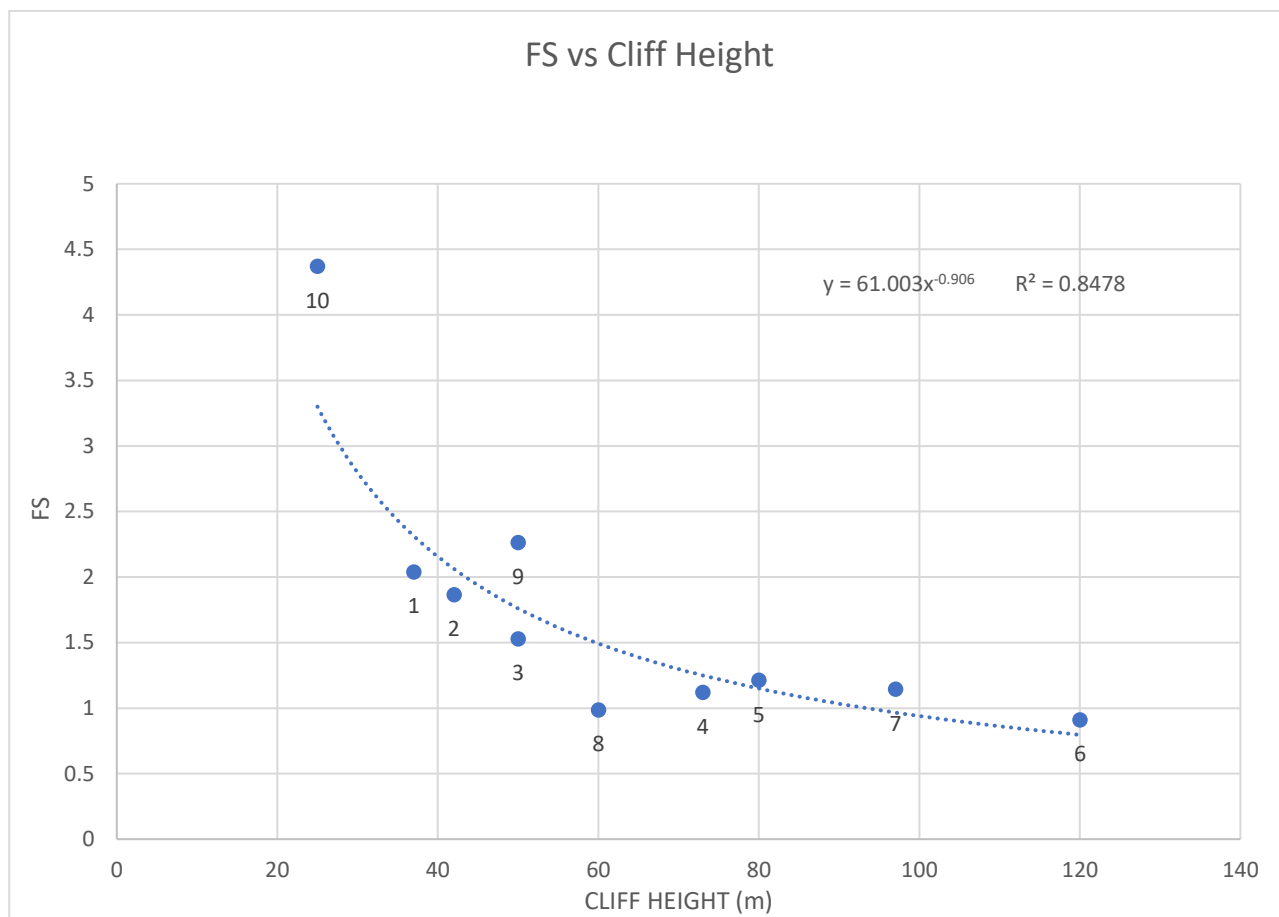


Figure 53: Graph comparing FS and Cliff Height values in the ten extracted sections. The number below the dot refers to the section number.

3.3.4 Discussion

This research aimed to show a multidisciplinary approach to the study of coastal cliff retreat based on the use of DSAS, ML analysis and numerical modelling. The cliff top retreat analysis closely corroborate with the results gathered by precedent research Fullin et al., 2023. Notably, this analysis reaffirms that the Trave sector remains the most precarious and unstable segment, manifesting higher NSM in certain transects when compared to the Portonovo sector. Only the mean EPR shows similar patterns for these latter two sectors. Nevertheless, the Mezzavalle sector continues to exhibit a distinct lack of evolution when compared with the others. However, it is necessary to emphasize that further research, employing enhanced spatial resolution techniques, is required to discern the seasonal variations in the evolution of these cliffs, predominantly constituted by landslide deposits. Coastal cliff retreat on weak rocks calculated on other works showed an average retreat similar with what calculated in our area , with the exception of the Trave sector, where the erosion rate is three times higher than the average in GlobR2C2 (Gómez-Pazo et al., 2021; Prémaillon et al., 2018; Sunamura T., 1992; Woodroffe, 2002). Still, in Adriatic sea mean EPR values similar to the ones estimated in our research were found in two areas in the Puglia Region (0.08 m/yr and 0.12 m/yr) (Delle Rose and Parise, 2005; Lollino et al., 2021), two areas in the Abruzzo Region (0.15 m/yr and 1 m/yr) (Miccadei et al., 2019) and in the Marche Region (0.16 m/yr) (Colantoni et al., 2004).

Numerous works have attempted to comprehend the drivers behind cliff retreat (Brooks et al., 2012; Hursta et al., 2016; Limber et al., 2018; Prémaillon et al., 2018; Sunamura, 2015, 1977; Alan S Trenhaile, 2010; Trenhaile, 2019, 2012). In this context we presented in this research a new and

innovative approach to investigate cliff top erosion. Few attempts were made in a similar manner: Dickson and Perry 2016 (Dickson and Perry, 2016) focused on different ML techniques, as classification and regression trees (CART), maximum entropy models (MAXENT) and boosted regression trees (BRT) and applied to wide scales to identify more dangerous areas, He et al. 2021 (He et al., 2021) used RF algorithm and support vector machine (SVM), multilayer perceptron (MLP) and deep learning neural network (DLNN) models to evaluate the role of discontinuities orientation in landslide processes. None of these attempts focused on a so site-specific case considering this plethora of drives and proposing a particular methodology to assess the importance of the different factors in erosion. ML applications similar to the ones presented in this research have previously demonstrated their efficacy in various scientific domains (Fadja et al., 2022; Fraccaroli et al., 2021; Kardani et al., 2021; Loggenberg et al., 2018; Parsa, 2021; Zeng et al., 2022). The robustness of results and the absence of overfitting in relation to the training dataset are ensured by the high-test scores achieved through ML analysis, coupled with the utilization of grid search, oversampling techniques and bagging.

In the context of the parameters chosen for the ML algorithms, it is important to acknowledge that the compilation of driving factors presented herein does not represent an exhaustive inventory encompassing all imaginable elements influencing cliff failure. The selection of these factors has been guided by comprehensive reviews of prior research (Hapke and Plant, 2010; Ogawa et al., 2016; Sunamura, 2015; Trenhaile, 2012), on-site investigations, and the practical constraints inherent in fieldwork. It is worth noting that future research endeavors may consider expanding the analysis to encompass marine drivers. A study of nearshore bathymetry, followed by numerical wave propagation modeling to derive significant wave height values at the cliff base, could be performed (Bergillos et al., 2022; Booij et al., 1999; Sunamura T., 1992). Consequently, we intend to make the ML code we employed available on GitHub (<https://github.com/micheleFraccaroli/Machine-Learning-for-Coastal-Retreat>). This will facilitate the potential application of our methodology by other researchers to diverse sites, permitting the assessment of its consistency and the incorporation of additional parameters in other contexts.

The most significant result from both Mean Decrease in Impurity (MDI) studies emphasizes the importance of cliff height in connection to cliff top erosion. This linkage between these two parameters has previously been documented in the literature (Barton et al., 2020; Barton and Shen, 2018; Dickson and Perry, 2016; Quinn et al., 2010; Wolters and Müller, 2008). To further investigate retreat mechanism and the role of cliff height, numerical modeling of the slopes was undertaken.

Particularly, ten sections were extracted in Trave sector, where the greatest height and NSM were recorded. In this context, LEM approach, considering circular surfaces of slip was judged appropriate, as the slope can be approximated as isotropic continua with respect to its lithological properties (Stead and Coggan, 2012). The simulation results align with the ML findings, confirming the link between FS and cliff height. However, it is remarkable that in many sections, the calculated Safety Factor (SRF) remains near 1 or below. This agrees with the frequent, almost daily, activity observed in these slopes, characterized by isolated falls or toppling events. Any perturbations, either resulting from changes in pore pressure, seismic activity, or clay shrinkage, can trigger landslide events. Previous research on rocky coastlines has undertaken numerical slope modeling, taking into account the evolving notches at various locations on the cliffs (e.g., base, middle, particularly in cases of pronounced lithological contrasts) to elucidate the stress-strain response within the changed topographic configuration (Lollino et al., 2021; Styles et al., 2011). To complete these objectives, further research such as laboratory testing, borehole explorations, and more sophisticated software such as Finite Element Methods (FEM) are required. The present study did not pursue this line of investigation; instead, it focused on assessing correlation between cliff height and retrieved FS, just to underpin or not ML finding. Furthermore, implicit within the cliff height parameter lies the geological complexity of the slope. Although geological structural information is embedded in the

parameters of Geological Strength Index (GSI) and Unconfined Compressive Strength (UCS), it is essential to consider that these parameters were gathered at the cliff base because of logistical difficulty (e.g. operator’s safety) in accessing the slope itself.

This study serves as a site-specific analysis employing an ML approach to discern the significance of diverse parameters in cliff top retreat. If successfully replicated in other locations, this methodology holds the potential to play a role in informing engineering design solutions. It offers valuable insights into which specific factors, among the multitude of influencing variables, permit targeted interventions to mitigate instability.

3.3.5 Conclusion

In this study, a segment of rocky coast located in the eastern part of Italy (Ancona, AN) was examined. An integrated methodology was employed wherein marine, geological, and remote sensing data were effectively combined. A Digital Surface Model (DSM), generated from a UAV survey conducted in 2022, was used to extract topographic parameters and compute cliff top erosion in the time span 1978-2022. Geomechanical data were collected during fieldwork. These datasets were subjected to an ML analysis, resulting in an output that ranks the significance of each individual driving factor concerning cliff top erosion. Then slope stability analysis was performed along 10 sections to check the consistency of ML results analyzing the relation between FS and cliff height.

The main achievements of this research can be summarized as follows:

1. Cliff top retreat calculations spanning the period from 1978 to 2022 reaffirm the findings of previous research Fullin et al., 2023, indicating notably higher values of NSM in the Trave sector.
2. The Mean Decrease in Impurity (MDI) analysis, conducted utilizing Random Forest (RF) and XGBoost (XGB) ML algorithms, identified cliff height as the parameter most strongly associated with cliff top erosion.
3. Limit Equilibrium Method (LEM) modeling corroborate the presence of a correlation between FS and cliff height.

Subsequent investigations will require the use of more refined remote sensing techniques (e.g. fixed cameras), involving both heightened spatial and temporal resolutions. Furthermore, a thorough analysis of marine parameters (e.g. significant wave height, high resolution bathymetry) could be conducted in various additional site cases to evaluate the efficacy of the algorithms.

A GitHub repository containing the machine learning (ML) code employed for this analysis has been made available to facilitate the reproducibility of this study in different locations (<https://github.com/micheleFraccaroli/Machine-Learning-for-Coastal-Retreat>).

If successfully applied to diverse settings, this methodology carries the potential to contribute to the proposal of solutions for coastal instabilities cases. It provides valuable insights into the specific factors, among the myriad influencing variables, that imply precise interventions to ease instability processes.

4. PART III: DISCUSSION AND CONCLUSIONS

4.1 General discussion

This PhD thesis has focused on examining a specific site to identify the primary factors driving erosion along the cliffs of the Portonovo-Trave rocky coast in the Marche region.

Three main phases of research were conducted. Initially, the study involved analyzing cliff erosion by utilizing orthophotos, Lidar, and UAV surveys at distinct intervals. Subsequently, the data from drone surveys were combined to assess the annual evolution of the cliff. Finally, the last study applied ML algorithms in conjunction with geomorphological analysis and LEM methods to investigate the role of various factors in the erosion process.

The initial analysis revealed significant morphodynamical activity in the area. Over the period 1978-2021, the average retreat rate measured at -0.25 m/yr, with the Trave sector exhibiting the highest retreat rate between 1998-2007, nearly three times greater than the area's average. The Mezzavalle sector displayed the lowest retreat rate, even if primarily characterized by landslide deposits with poor geotechnical properties (Prémaillon et al., 2018). The Portonovo sector showed an intermediate behavior, resembling Trave in retreat rate during the period of 2010-2021, doubling compared to the entire 1978-2021 span.

Comparing these data with existing literature highlighted Trave sector values significantly higher than reported averages, aligning with similar Italian case studies (Budetta et al., 2000; Colantoni et al., 2004; Delle Rose and Parise, 2005; Lollino et al., 2021; Miccadei et al., 2019; Prémaillon et al., 2018).

The analysis of precipitation, waves, geology, and land cover aimed to clarify the primary factors driving erosion. However, correlating extreme events for precipitation and waves with the highest retreat rate in the Trave sector between 1998-2007 proved challenging due to limited data availability and the episodic nature of soft-rock cliff recession (Sunamura, 2015).

Hence, important considerations involved beach width, geotechnical properties, slope elevation, and steepness (Everts, 1991; Prémaillon et al., 2018; Wolters and Müller, 2008).

A detailed analysis across different sectors revealed distinct patterns and characteristics. Notably, Mezzavalle had the widest beach, while the Portonovo sector exhibited better geotechnical properties. The Trave sector, marked by tectonic features, elevated cliff height, and steepness, presented lower geotechnical properties (Benumof and Griggs, 1999; Brideau et al., 2009; Moore et al., 1999).

These observations align with the findings of the DoDs analysis, where the Trave sector emerges as the area experiencing the most significant negative differences, indicating material loss. Moreover, an examination of the configuration and distribution of areas showing higher DoD values reveals their predominant localization along the cliff-top. This evidence, coupled with the absence of detectable notches at the cliff base, leads to the implication that slope processes might exert a more pronounced influence on the erosive dynamics than marine factors. The DoDs analysis further illustrates that the Mezzavalle sector displays the least variation, while Portonovo exhibits an intermediate behavior between the other two sectors. This evidence aligns well with the outcomes derived from the DSAS analysis, where areas displaying positive differences (accumulation) are notably narrower. This phenomenon is likely linked to the sea's efficacy in quickly removing collapsed material from the slopes.

The combination of DSAS and DoDs analyses certifies delineated regions experiencing substantial failures or erosion activity. These findings emphasize the practicality of sustained multitemporal surveys as an effective methodology for monitoring the ongoing evolution of this coastline.

The second study, involving a comparative analysis between the September 2021 UAV survey and a subsequent 2022 assessment, has significantly enriched our understanding of current morphodynamic processes. The increased resolution of the available data from this comparison has facilitated a deeper understanding of the dynamics of this rocky coast. Notably, the observed average erosion rate stood at $0.29 \text{ m}^3 \text{ yr}^{-1}$ per meter of coastline, with segment f) displaying a maximum erosion rate of $2.04 \text{ m}^3 \text{ yr}^{-1}$. These values, although slightly lower, align with findings from different contexts (Alessio and Keller, 2020; Giuliano et al., 2022; Obanawa and Hayakawa, 2018; Swirad and Young, 2021).

An interesting comparison between the outcomes of this study and the preceding research (Fullin et al., 2023) unveils the advancements achieved. The repeated UAV surveys conducted in this study provided enhanced temporal resolution and finer detail compared to the previous analysis. However, complexities inherent in the study area, particularly in the Trave sector, posed challenges in replicating UAV surveys with identical Ground Control Points (GCPs). Consequently, the spatial resolution in this study was somewhat limited compared to other applications (Brunetta et al., 2021; Fabbri et al., 2021b; Turner et al., 2016; Westoby et al., 2018). Moreover, variations in flight technique between the surveys conducted in September 2021 and October 2022 might have contributed to some discrepancies in the final data products (Aicardi et al., 2016; Eisenbeiss and Sauerbier, 2011; Tziavou et al., 2018). Anyway, results obtained by this analysis had brought new insights compared to the precedent work. Notably, within the timeframe of 2021-2022, distinct cliff top retreats were not prominently evident. Interestingly, notching was observed at the base of cliffs in deviation from the previous study (Fullin et al., 2023), where lower spatial resolution disadvantaged the analysis. The detection of notching in the Mezzavalle sector, despite the absence of significant cliff top retreats over several decades, suggests underlying processes that may not be readily detectable from orthophotos alone. Moreover, cases of cliff collapse may not necessarily manifest as a retreat in the boundary between the exposed cliff and vegetation, rendering detection challenging without higher resolution data. Hence, reaching a comprehensive insight of cliff evolution requires the utilization of high-temporal and high-spatial resolution data (Bernatchez et al., 2021; Lim et al., 2005; Rosser et al., 2005b).

The insights gathered from this analysis affirm that a significant portion of the coastal material removal originates primarily from the Trave sector, notably segments f) and g) as highlighted in the first study (Fullin et al., 2023). The erosion of this material stems from a dual origin: one arising from the base of cliffs due to notching, while the other results from diverse landslide processes, predominantly topples and falls. A translational slide was identified within segment f), specifically delineated in the lower part of section C-C' (Fig. 42c). However, establishing a pattern of landslide occurrences linking notching and subsequent landslides, remains a challenging endeavor. Despite the identification of two distinct landslides in section D-D', the reconstruction of the chronological order of these events proves to be impracticable without precise temporal information, impeding a comprehensive understanding of the instability process's evolution.

Additionally, interesting observations of accretion in segment c) across a substantial beach area contrast completely with prevalent erosion in the northern segments, especially segments f) and g). This variance suggests a potential transport of sediments along the coastline from north to south, contrary to findings near Portonovo indicating a northward drift (Grottoli et al., 2015). Supplementary research is needed to determine if this material is locally generated or transported.

Consequently, this study underscores the fundamental importance of recurrent UAV surveys and their resultant products, principally due to the high spatial resolution and the ease of repetition they offer. In traversing the complexities and hazards of this study area, using UAVs equipped with Real-Time

Kinematic (RTK) GPS would be advantageous. Advancing understanding of these cliffs' evolution could involve the installation of cameras in various locations to continuously capture images over time. Such an approach could significantly help in detecting erosion causes and discrete landslide events, together with external triggering conditions (Godfrey et al., 2020). UAV techniques with Lidar surveys could generate DTM in vegetation heavily covered ranges (Swirad and Young, 2021). Combining techniques hold great potential in unraveling the complexities of coastal erosion processes.

The final study introduces a novel methodological approach, employing Machine Learning (ML) algorithms to identify the primary factors driving erosion along cliffs. Initially, a new analysis of cliff top erosion spanning the period from 1978 to 2022 was conducted using DSAS. The results of this cliff top retreat analysis closely match with the findings of the first investigation (Fullin et al., 2023). Remarkably, this confirms the vulnerability of the Trave sector as the most unstable area, displaying higher NSM in specific transects compared to the Portonovo sector. Moreover, the mean EPR exhibits similar patterns for these latter two sectors. However, the Mezzavalle sector continues to showcase a distinct lack of erosion in comparison to the others, surely due to the loss of enhanced spatial resolution, necessary to discern seasonal variations in the evolution of these cliffs.

Then, a new and innovative methodology aimed at examining cliff top erosion dynamics is presented. Few prior attempts searched into similar approaches, they were principally centered on different ML techniques and scales (Dickson and Perry, 2016; He et al., 2021). ML applications akin to those presented in this study have previously exhibited their effectiveness across diverse scientific domains (Fadja et al., 2022; Fraccaroli et al., 2021; Kardani et al., 2021; Loggenberg et al., 2018; Parsa, 2021; Zeng et al., 2022). The reliability of the results and the absence of overfitting concerning the training dataset are sustained by the high-test scores derived from the ML analysis. This robustness is further fortified by the application of techniques such as grid search, oversampling, and bagging, ensuring a rigorous and comprehensive evaluation of the data. Within the context of the parameters utilized for the ML algorithms, it is crucial to acknowledge that the compilation of driving factors outlined in this study does not represent an exhaustive inventory about all possible elements influencing cliff failure. The selection of these factors was guided by complete reviews of prior research (Hapke and Plant, 2010; Ogawa et al., 2016; Sunamura, 2015; Trenhaile, 2012), inspections, and the practical constraints inherent the field topography. It is important that future research works could consider expanding the analysis to include marine drives. Surveying nearshore bathymetry, combined with numerical wave propagation modeling to get significant wave height values at the cliff base, could led to a more comprehensive analysis (Bergillos et al., 2022; Booij et al., 1999; Sunamura T., 1992). To facilitate further research, we share the ML code used in this study on GitHub (<https://github.com/micheleFraccaroli/Machine-Learning-for-Coastal-Retreat>) and in appendix.

The principal outcome derived from both Mean Decrease in Impurity (MDI) studies highlights the correlation between cliff height and cliff top erosion, a linkage well-documented in literature (Barton et al., 2020; Barton and Shen, 2018; Dickson and Perry, 2016; Quinn et al., 2010; Wolters and Müller, 2008).

To examine deeper into the retreat mechanisms, numerical modeling of the slopes was undertaken. Specifically, ten sections were delineated within the Trave sector, where the greatest height and NSM were recorded by the previous analyses. In this context, the Limit Equilibrium Method LEM, was employed, considering circular surfaces of slip, and the material approximated as an isotropic continuum, with regard to its mechanical properties (Stead and Coggan, 2012). The direct correlation between FS and cliff height obtained with the LEM simulation results, corroborate the ML analysis results. In numerous sections, the calculated Safety Factor either stay close around 1 or falls below it. This aligns with the observed frequent, almost daily, activity characterized by isolated falls or toppling events within these slopes. Minimal variations in external factors can potentially trigger

landslides. Prior research has investigated rocky coastlines stability using numerical slope modeling, considering the evolving notches at various cliff locations to illustrate the stress-strain response within the altered topographic configuration (Lollino et al., 2021; Styles et al., 2011). To comprehensively achieve these objectives, further research involving laboratory testing, borehole explorations, and numerical modeling such as Finite Element (FEM) is needed. In this work we focus on assessing the correlation between cliff height and retrieved FS. The results corroborated and, in some way, reinforce the ML outcomes. Furthermore, the geological complexity of the slope has to be taken into account. The geomechanical information of the rockmass are included into the parameters GSI and UCS, it should be emphasized that they were determined at the bottom of the cliff. Consequently, their possible changes along the slope should not be ignored, and the importance of the cliff height parameter extends to this aspect as well.

This investigation serves as a site-specific study employing an ML approach to recognize the significance of diverse parameters in cliff-top retreat. If successfully replicated in other locations, this methodology could hold the potential to play a role in engineering design solutions. It offers valuable insights into which specific factors, among the multitude of influencing variables, to consider for landslide mitigation.

4.2 Final conclusions and future developments

The findings from these studies can be summarized around three focal points: the erosion mechanism, the spatial distribution of erosion along this particular coastline, and the underlying factors that contribute to its cliff retreat.

A comprehensive understanding of the mechanism driving the cliffs' retreat was proposed but more data are needed to underpin our findings. Despite an extensive collection of information and numerous analyses, a comprehensive coherence among the analyses is hindered by the different methodologies employed. Assessments employing DSAS and DoD techniques indicate significant cliff tops evolution, notably in the Portonovo and Trave sectors, with retreat values reaching approximately 50 meters. Conversely, analyses utilizing UAV datasets in 2021 and 2022 reveal detectable evidence of notching in different coastal areas, along with landslides, but without a marked increase in localized cliff top retreat.

These different outcomes can be ascribed to variations in temporal and spatial resolutions employed in the analyses: A 40-year analysis effectively captures the long-term evolution of cliffs with lower spatial resolution, in contrast, annual analyses employing high-density point clouds reveal slight alterations unnoticed by preceding studies but confined to a limited timeframe. Consequently, determining whether the primary erosion mechanism hinges on notching and the collapse of overlying material or recurrent cliff landslides followed by sea-induced base material elimination remains uncertain solely based on the acquired data and morphological analyses.

For example, notching erosion at the Mezzavalle sector might have occurred without a perceptible top retreat, as material collapsing onto the notch may slightly shift forward without visibly manifesting in orthophoto-based observations. Consequently, stating the dominance of one mechanism over another or its prevalence in one sector over another would be erroneous based on current evidence. What is discernible is the occurrence of both mechanisms along these cliffs, however their comprehension necessitates of further research.

Following this study, a strong recommendation, ever considering site conditions and economic constraints, would be the periodic execution of UAV surveys post-storm events, or the installation of fixed cameras. Given the discrete nature of cliff dynamics, a continuous visual surveillance system could enhance temporal comprehension of ongoing processes, fostering more comprehensive

discussions compared to relying solely on sporadic information and efficiently monitoring erosion processes (Dematteis et al., 2022; Lucieer et al., 2014; Mazzanti et al., 2020; Redweik et al., 2009).

The findings regarding the distribution of erosion align well across conducted studies. These analyses consistently identify the Trave sector as the most dynamically active area along the coastline. Across various observation scales, a significantly higher rate of evolution was observed here if compared to Portonovo and Mezzavalle sectors. However, in Mezzavalle, while both the DSAS study and the annual change detection corroborate each other, neither indicates a retreat of the cliff top in that specific sector. Nevertheless, the annual analysis does reveal the presence of notching in certain sections, suggesting likely erosion at the base due to wave impact.

Concerning the Portonovo sector, the change detection analysis shows minimal alterations, with only sporadic occurrences of landslide movements, such as topples and falls, without clear indications of significant changes at the base. DSAS analysis demonstrates a retreat, particularly at the cliff top. Emphasizing the spatial occurrence of erosion helped over investigating deeper into the underlying causes affecting this rocky coastline section.

The alignment between the findings of the current study and those reported in similar areas underscores the effectiveness of geomatics and remotely sensed techniques in facilitating the monitoring of these intricate environments.

The investigation into erosion causes involved the application of a novel methodology tailored for studies on rocky coasts. The coastline was divided into 10-meter spaced transects, each providing 13 parameters related to geology, topography, and marine influence. The selection of these parameters was based on existing literature, taking into account their recognized influence on cliff erosion dynamics. (Dickson and Perry, 2016; Sunamura T., 1992; Trenhaile, 2012). Machine learning (ML) algorithms were utilized to determine the relative significance of these parameters concerning erosion, as computed by the DSAS method. The assessment involved evaluating 40 years of cliff top retreat through the MDI technique using RF and XGB algorithms. The analysis revealed a robust association between erosion and slope height, a correlation previously acknowledged in the field of slope stability (Bar and Barton, 2017; Wolters and Müller, 2008).

However, this specific finding had not been previously attained using the employed methodology, signifying a notable advancement in research.

Although the analysis focused on a single site and the selected parameters represent the most relevant factors in cliff erosion, it is important to note that they are subject to potential modification or enhancement to better suit different contexts.

The code employed in this study is openly available on GitHub, enabling other researchers to adapt it for their case studies. This inclusive approach aims to expand the database of cases, thereby improving forecasting capabilities and its relevance in decision-making processes related to coastal instability issues. This effort allows for the refinement and validation of the methodology's effectiveness, contributing to more informed decisions in addressing challenges associated with coastal instability.

The primary findings from this doctoral thesis can be summarized as follows:

- The analysis of cliff top retreat spanning from 1978 to 2022 indicates notably increased values of Net Shoreline Movement (NSM) within the Trave sector, recording up to 50 meters of retreat along specific transects. This trend is confirmed by the Difference of Digital Surface Models (DoD) between 2012-2021 and change detection between 2021-2022, indicating a height discrepancy of -31 meters and an erosion rate of 2.04 cubic meters per year, respectively.

- The DSAS analysis suggests relative stability in the Mezzavalle sector. Nevertheless, change detection carried out using Unmanned Aerial Vehicle (UAV) derived products between 2021-2022 reveals significant evolution, due to notching erosion, in specific segments. In contrast, the Portonovo sector lacks detectable notching but experiences small landslide events. The DSAS analysis identifies an evolution primarily linked to cliff top retreat for this sector. These findings emphasize the importance of high-resolution spatial and temporal data in comprehending these dynamics. They shed light on the distinct erosion patterns among sectors, underscoring the importance of employing advanced analysis techniques and comprehensive datasets to understand and address coastal erosion phenomena effectively.
- The Mean Decrease in Impurity (MDI) analysis, employing Random Forest (RF) and XGBoost (XGB) Machine Learning (ML) algorithms, identifies cliff height as the parameter most strongly correlated with cliff top erosion in this site. The validation through Limit Equilibrium Method (LEM) numerical modeling further confirms a relationship between Factor of Safety (FS) and cliff height. This methodology, innovative within this thematic domain, is openly shared through code available at (<https://github.com/micheleFraccaroli/Machine-Learning-for-Coastal-Retreat>) to apply this analysis on different sites.

REFERENCES

- Aalto, K.R., Aalto, R., Garrison-Laney, C.E., Abramson, H.F., 1999. Tsunami (?) sculpturing of the Pebble Beach wave-cut platform, Crescent City area, California. *J. Geol.* 107, 607–622.
- Abellán, A., Jaboyedoff, M., Oppikofer, T., Vilaplana, J.M., 2009. Detection of millimetric deformation using a terrestrial laser scanner: experiment and application to a rockfall event. *Nat. Hazards Earth Syst. Sci.* 9, 365–372.
- Abellán, A., Oppikofer, T., Jaboyedoff, M., Rosser, N.J., Lim, M., Lato, M.J., 2014. Terrestrial laser scanning of rock slope instabilities. *Earth Surf. Process. Landforms* 39, 80–97.
<https://doi.org/10.1002/esp.3493>
- Acciarri, A., Bisci, C., Cantalamessa, G., Cappucci, S., Conti, M., Di Pancrazio, G., Spagnoli, F., Valentini, E., 2021. Metrics for short-term coastal characterization, protection and planning decisions of Sentina Natural Reserve, Italy. *Ocean Coast. Manag.* 201, 105472.
<https://doi.org/10.1016/j.ocecoaman.2020.105472>
- Admassu, Y., Shakoor, A., 2013. DIPANALYST: A computer program for quantitative kinematic analysis of rock slope failures. *Comput. Geosci.* 54, 196–202.
<https://doi.org/https://doi.org/10.1016/j.cageo.2012.11.018>
- Aicardi, I., Chiabrando, F., Grasso, N., Lingua, A.M., Noardo, F., Spanò, A., 2016. UAV photogrammetry with oblique images: First analysis on data acquisition and processing. *Int. Arch. Photogramm. Remote Sens. Spat. Inf. Sci.* 41, 835–842.
- Alessio, P., Keller, E.A., 2020. Short-term patterns and processes of coastal cliff erosion in Santa Barbara, California. *Geomorphology* 353, 106994.
<https://doi.org/https://doi.org/10.1016/j.geomorph.2019.106994>
- Alexiou, S., Deligiannakis, G., Pallikarakis, A., Papanikolaou, I., Psomiadis, E., Reicherter, K., 2021. Comparing high accuracy t-lidar and uav-sfm derived point clouds for geomorphological change detection. *ISPRS Int. J. Geo-Information* 10. <https://doi.org/10.3390/ijgi10060367>
- Alpaydin, E., 2020. Introduction to machine learning. MIT press.
- Anderson, K., Westoby, M.J., James, M.R., 2019. Low-budget topographic surveying comes of age: Structure from motion photogrammetry in geography and the geosciences. *Prog. Phys. Geogr. Earth Environ.*
- Anfuso, G., Gracia, F.J., Battocletti, G., 2013. Determination of cliffed coastline sensitivity and associated risk for human structures: A methodological approach. *J. Coast. Res.* 29, 1292–1296.
<https://doi.org/10.2112/JCOASTRES-D-12-00262.1>
- Ashton, A.D., Walkden, M.J.A., Dickson, M.E., 2011. Equilibrium responses of cliffed coasts to changes in the rate of sea level rise. *Mar. Geol.* <https://doi.org/10.1016/j.margeo.2011.01.007>
- Attewell, P.B., Farmer, I.W., 2012. Principles of engineering geology. Springer Science & Business Media.

- Azar, A.T., Elshazly, H.I., Hassanien, A.E., Elkorany, A.M., 2014. A random forest classifier for lymph diseases. *Comput. Methods Programs Biomed.* 113, 465–473. <https://doi.org/https://doi.org/10.1016/j.cmpb.2013.11.004>
- Baczynski, N.R.P., 2000. STEPSIM4" step-path" method for slope risks, in: *ISRM International Symposium*. p. ISRM--IS.
- Badillo, S., Banfai, B., Birzele, F., Davydov, I.I., Hutchinson, L., Kam-Thong, T., Siebourg-Polster, J., Steiert, B., Zhang, J.D., 2020. An Introduction to Machine Learning. *Clin. Pharmacol. Ther.* 107, 871–885. <https://doi.org/10.1002/cpt.1796>
- Baecher, G.B., Lanney, N.A., 1978. Trace length biases in joint surveys, in: *ARMA US Rock Mechanics/Geomechanics Symposium*. p. ARMA--78.
- Baig, M.R.I., Ahmad, I.A., Shahfahad, Tayyab, M., Rahman, A., 2020. Analysis of shoreline changes in Vishakhapatnam coastal tract of Andhra Pradesh, India: an application of digital shoreline analysis system (DSAS). *Ann. GIS* 26, 361–376.
- Baltsavias, E.P., 1999. Airborne laser scanning: basic relations and formulas. *ISPRS J. Photogramm. Remote Sens.* 54, 199–214.
- Baltsavias, E.P., 1996. Digital ortho-images — a powerful tool for the extraction of spatial- and geo-information. *ISPRS J. Photogramm. Remote Sens.* 51, 63–77. [https://doi.org/https://doi.org/10.1016/0924-2716\(95\)00014-3](https://doi.org/https://doi.org/10.1016/0924-2716(95)00014-3)
- Bar, N., Barton, N., 2017. The Q-Slope Method for Rock Slope Engineering. *Rock Mech. Rock Eng.* 50, 3307–3322. <https://doi.org/10.1007/s00603-017-1305-0>
- Barton, N., 2002. Some new Q-value correlations to assist in site characterisation and tunnel design. *Int. J. rock Mech. Min. Sci.* 39, 185–216.
- Barton, N., 1978. Suggested methods for the quantitative description of discontinuities in rock masses, in: *International Journal of Rock Mechanics and Mining Sciences and Geomechanics Abstracts*. pp. 319–368. [https://doi.org/https://doi.org/10.1016/0148-9062\(79\)91476-1](https://doi.org/https://doi.org/10.1016/0148-9062(79)91476-1)
- Barton, N., Lien, R., Lunde, J., 1974. Engineering classification of rock masses for the design of tunnel support. *Rock Mech.* 6, 189–236.
- Barton, N., Shen, B., 2018. Extension Strain and Rock Strength Limits for Deep Tunnels, Cliffs, Mountain Walls and the Highest Mountains. *Rock Mech. Rock Eng.* 51, 3945–3962. <https://doi.org/10.1007/s00603-018-1558-2>
- Barton, N., Shen, B., Bar, N., 2020. Limited heights of vertical cliffs and mountain walls linked to fracturing in deep tunnels - Q-slope application if jointed slopes. *ISRM VIII Brazilian Symp. Rock Mech. SBMR 2018*.
- Bartrum, J.A., 1926. “Abnormal” shore platforms. *J. Geol.* 34, 793–806.
- Bartrum, J.A., 1916. High-water rock platforms: a phase of shoreline erosion, in: *Trans. Proc. New Zealand Inst.* pp. 132–134.
- Bay, H., Ess, A., Tuytelaars, T., Van Gool, L., 2008. Speeded-up robust features (SURF). *Comput. Vis. image Underst.* 110, 346–359.

- Beardsley, P.A., Zisserman, A., Murray, D.W., 1997. Sequential updating of projective and affine structure from motion. *Int. J. Comput. Vis.* 23, 235–259.
- Beckley, B.D., Lemoine, F.G., Luthcke, S.B., Ray, R.D., Zelensky, N.P., 2007. A reassessment of global and regional mean sea level trends from TOPEX and Jason-1 altimetry based on revised reference frame and orbits. *Geophys. Res. Lett.* 34.
- Bej, S., Davtyan, N., Wolfien, M., Nassar, M., Wolkenhauer, O., 2021. LoRAS: An oversampling approach for imbalanced datasets. *Mach. Learn.* 110, 279–301.
- Benetazzo, A., Davison, S., Barbariol, F., Mercogliano, P., Favaretto, C., Sclavo, M., 2022. Correction of ERA5 wind for regional climate projections of Sea waves. *Water* 14, 1590.
- Benumof, B.T., Griggs, G.B., 1999. The dependence of seacliff erosion rates on cliff material properties and physical processes: San Diego County, California. *Shore \& Beach* 67, 29–41.
- Bergillos, R.J., Rodriguez-Delgado, C., Medina, L., Fernandez-Ruiz, J., Rodriguez-Ortiz, J.M., Iglesias, G., 2022. A combined approach to cliff characterization: Cliff Stability index. *Mar. Geol.* 444, 106706. <https://doi.org/10.1016/j.margeo.2021.106706>
- Bernatchez, P., Boucher-Brossard, G., Corriveau, M., Caulet, C., Barnett, R.L., 2021. Long-term evolution and monitoring at high temporal resolution of a rapidly retreating cliff in a cold temperate climate affected by cryogenic processes, north shore of the st. Lawrence gulf, quebec (canada). *J. Mar. Sci. Eng.* 9, 1418.
- Bieniawski, Z.T., 1989. Engineering rock mass classifications: a complete manual for engineers and geologists in mining, civil, and petroleum engineering. John Wiley \& Sons.
- Bieniawski, Z.T., 1973. Engineering classification of jointed rock masses. *Civ. Eng. Sivele Ingenieurswese* 1973, 335–343.
- Bintanja, R., Van De Wal, R.S.W., Oerlemans, J., 2005. Modelled atmospheric temperatures and global sea levels over the past million years. *Nature* 437, 125–128.
- Bisci, Carlo; Cantalamessa, Gino; de Marco, Rocco; Spagnoli, Federico; Tramontana, M., 2021. Caratteri oceanografici dell’Adriatico centro-settentrionale e della costa marchigiana. *Stud. COSTIERI* 30, 7–12. <https://doi.org/https://hdl.handle.net/11576/2693668>
- Bishop, A.W., 1955. The use of the slip circle in the stability analysis of slopes. *Geotechnique* 5, 7–17.
- Bjerrum, L., 1967. The third Terzaghi lectures; Progressive failure in slopes of overconsolidated plastic clay and clay shales. *J. Soil Mech. Found. Div.* 93, 1–49.
- Blanco-Chao, R., Pérez-Alberti, A., Trenhaile, A.S., Costa-Casais, M., Valcárcel-D\’iaz, M., 2007. Shore platform abrasion in a para-periglacial environment, Galicia, northwestern Spain. *Geomorphology* 83, 136–151.
- Bloom, C.K., Singeisen, C., Stahl, T., Howell, A., Massey, C., 2022. Earthquake Contributions to Coastal Cliff Retreat. *Egusph. [preprint]* 757–778.
- Blyth, F.G.H., De Freitas, M., 2017. A geology for engineers. CRC Press.
- Boehler, W., Vicent, M.B., Marbs, A., others, 2003. Investigating laser scanner accuracy. *Int. Arch. Photogramm. Remote Sens. Spat. Inf. Sci.* 34, 696–701.

- Booij, N., Ris, R.C., Holthuijsen, L.H., 1999. A third-generation wave model for coastal regions 1. Model description and validation. *J. Geophys. Res. Ocean.* 104, 7649–7666.
<https://doi.org/10.1029/98JC02622>
- Boufama, B., Mohr, R., Veillon, F., 1993. Euclidean constraints for uncalibrated reconstruction, in: 1993 (4th) International Conference on Computer Vision. pp. 466–470.
- Brasington, J., Langham, J., Rumsby, B., 2003. Methodological sensitivity of morphometric estimates of coarse fluvial sediment transport. *Geomorphology* 53, 299–316.
- Breiman, L., 2017. *Classification and regression trees*. Routledge.
- Breiman, L., 2001. Random Forests. *Mach. Learn.* 45, 5–32. <https://doi.org/10.1023/A:1010933404324>
- Bremer, M., Sass, O., 2012. Combining airborne and terrestrial laser scanning for quantifying erosion and deposition by a debris flow event. *Geomorphology* 138, 49–60.
- Brideau, M.A., Yan, M., Stead, D., 2009. The role of tectonic damage and brittle rock fracture in the development of large rock slope failures. *Geomorphology*.
<https://doi.org/10.1016/j.geomorph.2008.04.010>
- Broc, N., Giusti, C., 2007. The *Traite de Geographie physique* by Emmanuel deMartonne: from geographical lexicography to geomorphological theory. *Geomorphol. Process. Environ.*
- Brooke, B.P., Young, R.W., Bryant, E.A., Murray-Wallace, C. V, Price, D.M., 1994. A Pleistocene origin for shore platforms along the northern Illawarra coast, New South Wales. *Aust. Geogr.* 25, 178–185.
- Brooks, S., Spencer, T., 2016. Storm Impacts on Cluffed Coastlines. In Ciavola and Coco (Eds.), in: *Coastal Storms: Processes and Impacts*. <https://doi.org/10.1002/9781118937099.ch6>
- Brooks, S.M., Spencer, T., Boreham, S., 2012. Deriving mechanisms and thresholds for cliff retreat in soft-rock cliffs under changing climates: Rapidly retreating cliffs of the Suffolk coast, UK. *Geomorphology* 153–154, 48–60. <https://doi.org/10.1016/j.geomorph.2012.02.007>
- Brosens, L., Campforts, B., Robinet, J., Vanacker, V., Opfergelt, S., Ameijeiras-Mariño, Y., Minella, J.P.G., Govers, G., 2020. Slope Gradient Controls Soil Thickness and Chemical Weathering in Subtropical Brazil: Understanding Rates and Timescales of Regional Soilscape Evolution Through a Combination of Field Data and Modeling. *J. Geophys. Res. Earth Surf.* 125, e2019JF005321.
<https://doi.org/https://doi.org/10.1029/2019JF005321>
- Brown, D.C., 1976. The bundle method--progress and prospects. *Int. Arch. Photogramm.* 21, 1–33.
- Brown, E.T., Hoek, E., 1980. *Underground excavations in rock*. CRC Press.
- Brunetta, R., Duo, E., Ciavola, P., 2021. Evaluating Short-Term Tidal Flat Evolution Through UAV Surveys: A Case Study in the Po Delta (Italy). *Remote Sens.* 13. <https://doi.org/10.3390/rs13122322>
- Bruun, P., 1962. Sea-Level Rise as a Cause of Shore Erosion. *J. Waterw. Harb. Div.* 88, 117–130.
<https://doi.org/10.1061/JWHEAU.0000252>
- Bryant, E., 2008. *Tsunami: The Underrated Hazard (Second Edition)*. <https://doi.org/10.1007/978-3-540-74274-6>

- Bryant, E.A., Haslett, S.K., 2007. Catastrophic wave erosion, Bristol Channel, United Kingdom: impact of tsunami? *J. Geol.* 115, 253–269.
- Bryant, E.A., Young, R.W., 1996. Bedrock-sculpturing by tsunami, south coast New South Wales, Australia. *J. Geol.* 104, 565–582.
- Buchanan, D.H., Naylor, L.A., Hurst, M.D., Stephenson, W.J., 2020. Erosion of rocky shore platforms by block detachment from layered stratigraphy. *Earth Surf. Process. Landforms* 45, 1028–1037. <https://doi.org/10.1002/esp.4797>
- Budetta, P., Galiotta, G., Santo, A., 2000. A methodology for the study of the relation between coastal cliff erosion and the mechanical strength of soils and rock masses. *Eng. Geol.* 56, 243–256. [https://doi.org/10.1016/S0013-7952\(99\)00089-7](https://doi.org/10.1016/S0013-7952(99)00089-7)
- Burkart, N., Huber, M.F., 2021. A survey on the explainability of supervised machine learning. *J. Artif. Intell. Res.* 70, 245–317.
- Cai, M.; Kaiser, P.K., 2007. Obtaining Modeling Parameters for Engineering Design by Rock Mass Characterization. *11th ISRM Congr.*, 381–384.
- Calamita, F., Coltorti, M., Pierucci, P., Pizzi, A., 1999. Evoluzione strutturale e morfogenesi Plio-Quaternaria dell' Appennino Umbro- Marchigiano tra il Pedappennino Umbro e la ... *Boll. della Soc. Geol. Ital.* 118, 125–139.
- Calligaro, S., Sofia, G., Prosdocimi, M., Dalla Fontana, G., Tarolli, P., 2013. Terrestrial laser scanner data to support coastal erosion analysis: The conero case study. *Int. Arch. Photogramm. Remote Sens. Spat. Inf. Sci. - ISPRS Arch.* 40, 125–129. <https://doi.org/10.5194/isprsarchives-XL-5-W3-125-2013>
- Calonder, M., Lepetit, V., Strecha, C., Fua, P., 2010. Brief: Binary robust independent elementary features, in: *Computer Vision--ECCV 2010: 11th European Conference on Computer Vision, Heraklion, Crete, Greece, September 5-11, 2010, Proceedings, Part IV* 11. pp. 778–792.
- Caputo, T., Marino, E., Matano, F., Somma, R., Troise, C., De Natale, G., 2018. Terrestrial Laser Scanning (TLS) data for the analysis of coastal tuff cliff retreat: application to Coroglio cliff, Naples, Italy. *Ann. Geophys. Geophys.* 61. <https://doi.org/10.4401/ag-7494>
- Carrea, D., Abellan, A., Humair, F., Matasci, B., Derron, M.-H., Jaboyedoff, M., 2016. Correction of terrestrial LiDAR intensity channel using Oren--Nayar reflectance model: An application to lithological differentiation. *ISPRS J. Photogramm. Remote Sens.* 113, 17–29.
- Carrivick, J.L., Smith, M.W., Quincey, D.J., 2016. *Structure from Motion in the Geosciences*. John Wiley & Sons.
- Carvalho, D. V, Pereira, E.M., Cardoso, J.S., 2019. Machine learning interpretability: A survey on methods and metrics. *Electronics* 8, 832.
- Casagli, N., Frodella, W., Morelli, S., Tofani, V., Ciampalini, A., Intrieri, E., Raspini, F., Rossi, G., Tanteri, L., Lu, P., 2017. Spaceborne, UAV and ground-based remote sensing techniques for landslide mapping, monitoring and early warning. *Geoenvironmental Disasters* 4, 1–23. <https://doi.org/10.1186/s40677-017-0073-1>

- Casella, E., Drechsel, J., Winter, C., Benninghoff, M., Rovere, A., 2020. Accuracy of sand beach topography surveying by drones and photogrammetry. *Geo-Marine Lett.* 40, 255–268. <https://doi.org/10.1007/s00367-020-00638-8>
- Castedo, R., Murphy, W., Lawrence, J., Paredes, C., 2012. A new process-response coastal recession model of soft rock cliffs. *Geomorphology* 177–178, 128–143. <https://doi.org/10.1016/j.geomorph.2012.07.020>
- Cello G., Coppola, L.M., 1989. Modalità e stili deformativi nell’area anconetana. *Stud. Geol. Camerti* XI, 37–48.
- Cenci, L., Disperati, L., Persichillo, M.G., Oliveira, E.R., Alves, F.L., Phillips, M., 2018. Integrating remote sensing and GIS techniques for monitoring and modeling shoreline evolution to support coastal risk management. *GIScience & Remote Sens.* 55, 355–375. <https://doi.org/10.1080/15481603.2017.1376370>
- Cenci, L., Disperati, L., Sousa, L.P., Phillips, M., Alves, F.L., 2013. Geomatics for Integrated Coastal Zone Management: Multitemporal shoreline analysis and future regional perspective for the Portuguese Central Region. *J. Coast. Res.* 1349–1354. <https://doi.org/10.2112/SI65-228.1>
- Chen, T., Guestrin, C., 2016. XGBoost: A scalable tree boosting system. *Proc. ACM SIGKDD Int. Conf. Knowl. Discov. Data Min.* 13-17-Aug, 785–794. <https://doi.org/10.1145/2939672.2939785>
- Chen, T., He, T., 2014. xgboost: Extreme Gradient Boosting. *R Lect.* 1–84.
- Chen, X., Huang, L., Xie, D., Zhao, Q., 2018. EGBMMDA: Extreme gradient boosting machine for MiRNA-disease association prediction. *Cell Death Dis.* 9. <https://doi.org/10.1038/s41419-017-0003-x>
- Chigira, M., Duan, F., Yagi, H., Furuya, T., 2004. Using an airborne laser scanner for the identification of shallow landslides and susceptibility assessment in an area of ignimbrite overlain by permeable pyroclastics. *Landslides* 1, 203–209.
- Chowdhury, R.N., A-Grivas, D., 1982. Probabilistic model of progressive failure of slopes. *J. Geotech. Eng. Div.* 108, 803–819.
- Clapuyt, F., Vanacker, V., Van Oost, K., 2016. Reproducibility of UAV-based earth topography reconstructions based on Structure-from-Motion algorithms. *Geomorphology* 260, 4–15.
- Coco, G., Ciavola, P., 2017. *Coastal Storms*. Coastal Storms. John Wiley & Sons.
- Colantoni, P., Mencucci, D., Nesci, O., 2004. Coastal processes and cliff recession between Gabicce and Pesaro (northern Adriatic Sea): a case history. *Geomorphology* 62, 257–268. <https://doi.org/https://doi.org/10.1016/j.geomorph.2004.03.003>
- Colica, E., Galone, L., D’Amico, S., Gauci, A., Iannucci, R., Martino, S., Pistillo, D., Iregbeyen, P., Valentino, G., 2023. Evaluating Characteristics of an Active Coastal Spreading Area Combining Geophysical Data with Satellite, Aerial, and Unmanned Aerial Vehicles Images. *Remote Sens.* 15, 1465.
- Coltorti M., Sarti M., 2011. Note Illustrative della Carta Geologica d’Italia alla scala 1:50.000 “Foglio 293 - Osimo”. Progetto CARG-ISPRA, Servizio Geologico d’Italia. Available online: https://www.isprambiente.gov.it/Media/carg/293_OSIMO/Foglio.html

- Coltorti, M., Nanni, T., Rainone, M., 1987. Il contributo delle Scienze della Terra nell'elaborazione di un piano paesistico : l'esempio del M. Conero (Marche).
- Committee, F.G.D., 1998. Geospatial positioning accuracy standards. Fed. Geogr. Data Comm. 3.
- Cotton, C.A., 1963. Levels of planation of marine benches. *Zeitschrift für Geomorphol.* 7, 97–111.
- Crowell, M., Leatherman, S.P., Buckley, M.K., 1991. Historical shoreline change: error analysis and mapping accuracy. *J. Coast. Res.* 7, 839–852.
- Cruden, D., Varnes, D.J., 1996, *Landslide Types and Processes*, Transportation Research Board, U.S. National Academy of Sciences, Special Report, 247: 36-75. Spec. Rep. - Natl. Res. Council. Transp. Res. Board 247, 36–57.
- Cruden, D.M., 2003. The shapes of cold, high mountains in sedimentary rocks. *Geomorphology* 55, 249–261.
- Cundall, P.A., 2011. Lattice method for modeling brittle , jointed rock. *Contin. distinct Elem. Numer. Model. Geomech.* 1–2.
- Dandois, J.P., Ellis, E.C., 2010. Remote Sensing of Vegetation Structure Using Computer Vision. *Remote Sens.* <https://doi.org/10.3390/rs2041157>
- Davies, D.S., Alexrod, E.W.O., Sturges, J., 1974. Erosion of the north shore of Long Island. Technical Report; Marine Sciences Research Center; State University of New York; Stony Brook: Stony Brook, NY, USA; Volume 18, pp. 1–101.
- De Caro, M., Crosta, G.B., Castellanza, R., Agliardi, F., Volpi, G., Alberti, S., 2018. 2D modelling of rockslide displacements by non-linear time dependent relationships, in: *Landslides and Engineered Slopes. Experience, Theory and Practice*. CRC Press, pp. 765–770.
- Deere, D.U., 1964. Technical description of rock cores for engineering purpose. *Rock Mech. Engineering Geol.* 1, 17–22.
- Del Río, L., Gracia, F.J., 2013. Error determination in the photogrammetric assessment of shoreline changes. *Nat. Hazards* 65, 2385–2397. <https://doi.org/10.1007/s11069-012-0407-y>
- Del Río, L., Gracia, F.J., 2009. Erosion risk assessment of active coastal cliffs in temperate environments. *Geomorphology* 112, 82–95. <https://doi.org/10.1016/j.geomorph.2009.05.009>
- Del Río, L., Posanski, D., Gracia, F.J., Pérez-Romero, A.M., 2020. A comparative approach of monitoring techniques to assess erosion processes on soft cliffs. *Bull. Eng. Geol. Environ.* 79, 1797–1814. <https://doi.org/10.1007/s10064-019-01680-2>
- Delle Rose, M., Parise, M., 2005. Speleogenesi e geomorfologia del sistema carsico delle Grotte della Poesia nell'ambito dell'evoluzione quaternaria della costa Adriatica Salentina. *Atti e Mem. Comm. Grotte “E. Boegan* 40, 153–173.
- Dematteis, N., Wrzesniak, A., Allasia, P., Bertolo, D., Giordan, D., 2022. Integration of robotic total station and digital image correlation to assess the three-dimensional surface kinematics of a landslide. *Eng. Geol.* 303, 106655.

- Deng, W., Huang, Z., Zhang, J., Xu, J., 2021. A Data Mining Based System for Transaction Fraud Detection. 2021 IEEE Int. Conf. Consum. Electron. Comput. Eng. ICCECE 2021 542–545. <https://doi.org/10.1109/ICCECE51280.2021.9342376>
- Derron, M.-H., Jaboyedoff, M., Pedrazzini, A., Michoud, C., Villemain, T., 2013. Remote sensing and monitoring techniques for the characterization of rock mass deformation and change detection. *Rockfall Eng.* 39–65.
- Di Luccio, D., Aucelli, P.P.C., Di Paola, G., Pennetta, M., Berti, M., Budillon, G., Florio, A., Benassai, G., 2023. An integrated approach for coastal cliff susceptibility: The case study of Procida Island (southern Italy). *Sci. Total Environ.* 855, 158759. <https://doi.org/10.1016/j.scitotenv.2022.158759>
- Dickson, M.E., Perry, G.L.W., 2016. Identifying the controls on coastal cliff landslides using machine-learning approaches. *Environ. Model. Softw.* 76, 117–127. <https://doi.org/10.1016/j.envsoft.2015.10.029>
- Dickson, M.E., Walkden, M.J.A., Hall, J.W., 2007. Systemic impacts of climate change on an eroding coastal region over the twenty-first century. *Clim. Change* 84, 141–166.
- Diederichs, M.S., Lato, M., Quinn, P., Hammah, R., 2007. Shear strength reduction approach for slope stability analyses, in: ARMA Canada-US Rock Mechanics Symposium. p. ARMA--07.
- Donati, D., 2016. The characterization of slope damage: a combined remote sensing-numerical modelling approach. PhD, Thesis.
- Donati, D., Stead, D., Lato, M., Gaib, S., 2020. Spatio-temporal characterization of slope damage: insights from the Ten Mile Slide, British Columbia, Canada. *Landslides*. <https://doi.org/10.1007/s10346-020-01352-3>
- Duo, E., Fabbri, S., Grottoli, E., Ciavola, P., 2021. Uncertainty of Drone-Derived DEMs and Significance of Detected Morphodynamics in Artificially Scraped Dunes. *Remote Sens.* 13. <https://doi.org/10.3390/rs13091823>
- Earlie, C., Masselink, G., Russell, P., 2018. The role of beach morphology on coastal cliff erosion under extreme waves. *Earth Surf. Process. Landforms* 43, 1213–1228. <https://doi.org/10.1002/esp.4308>
- Earlie, C.S., Masselink, G., Russell, P.E., Shail, R.K., 2015. Application of airborne LiDAR to investigate rates of recession in rocky coast environments. *J. Coast. Conserv.* 19, 831–845. <https://doi.org/10.1007/s11852-014-0340-1>
- Edwards, A.B., 1958. Wave-cut platforms at Yampi Sound, in the Buccaneer Archipelago. *J. R. Soc. West. Aust.* 41, 17–21.
- Edwards, A.B., 1951. Wave action in shore platform formation. *Geol. Mag.* 88, 41–49.
- Eisenbeiss, H., Sauerbier, M., 2011. Investigation of UAV systems and flight modes for photogrammetric applications. *Photogramm. Rec.* 26, 400–421.
- Elmo, D., Stead, D., 2010. An integrated numerical modelling--discrete fracture network approach applied to the characterisation of rock mass strength of naturally fractured pillars. *Rock Mech. Rock Eng.* 43, 3–19.

- Eltner, A., Kaiser, A., Castillo, C., Rock, G., Neugirg, F., Abellán, A., 2016. Image-based surface reconstruction in geomorphometry -- merits, limits and developments. *Earth Surf. Dyn.* 4, 359–389. <https://doi.org/10.5194/esurf-4-359-2016>
- Emery, K.O., Kuhn, G.G., 1982. Sea cliffs: Their processes, profiles, and classification. *GSA Bull.* 93, 644–654. [https://doi.org/10.1130/0016-7606\(1982\)93<644:SCTPPA>2.0.CO;2](https://doi.org/10.1130/0016-7606(1982)93<644:SCTPPA>2.0.CO;2)
- Emery, K.O., Kuhn, G.G., 1980. Erosion of rock shores at La Jolla, California. *Mar. Geol.* 37, 197–208. [https://doi.org/https://doi.org/10.1016/0025-3227\(80\)90101-2](https://doi.org/https://doi.org/10.1016/0025-3227(80)90101-2)
- Esposito, G., Matano, F., Sacchi, M., Salvini, R., 2020. Mechanisms and frequency-size statistics of failures characterizing a coastal cliff partially protected from the wave erosive action. *Rend. Lincei* 31, 337–351. <https://doi.org/10.1007/s12210-020-00902-0>
- Esposito, G., Salvini, R., Matano, F., Sacchi, M., Danzi, M., Somma, R., Troise, C., 2017. Multitemporal monitoring of a coastal landslide through SfM-derived point cloud comparison. *Photogramm. Rec.* 32, 459–479. <https://doi.org/10.1111/phor.12218>
- Esposito, G., Salvini, R., Matano, F., Sacchi, M., Troise, C., 2018. Evaluation of geomorphic changes and retreat rates of a coastal pyroclastic cliff in the Campi Flegrei volcanic district, southern Italy. *J. Coast. Conserv.* 22, 957–972. <https://doi.org/10.1007/s11852-018-0621-1>
- Everts, C.H., 1991. Seacliff retreat and coarse sediment yields in southern California, *Proceeding in Coastal Sediments '91* (American Society Civil Engineering). pp. 1586–1598.
- Fabbri, S., Grottoli, E., Armaroli, C., Ciavola, P., 2021. Using High-Spatial Resolution UAV-Derived Data to Evaluate Vegetation and Geomorphological Changes on a Dune Field Involved in a Restoration Endeavour. *Remote Sens.* 13. <https://doi.org/10.3390/rs13101987>
- Fadja, A.N., Fraccaroli, M., Bizzarri, A., Mazzuchelli, G., Lamma, E., 2022. Neural-Symbolic Ensemble Learning for early-stage prediction of critical state of Covid-19 patients. *Med. Biol. Eng. Comput.* 60, 3461–3474. <https://doi.org/10.1007/s11517-022-02674-1>
- Favalli, M., Fornaciai, A., Isola, I., Tarquini, S., Nannipieri, L., 2012. Multiview 3D reconstruction in geosciences. *Comput. \& Geosci.* 44, 168–176.
- Fazio, N.L., Perrotti, M., Andriani, G.F., Mancini, F., Rossi, P., Castagnetti, C., Lollino, P., 2019. A new methodological approach to assess the stability of discontinuous rocky cliffs using in-situ surveys supported by UAV-based techniques and 3-D finite element model: a case study. *Eng. Geol.* 260. <https://doi.org/10.1016/j.enggeo.2019.105205>
- Fellenius, W., 1936. Calculation of the stability of earth dams, in: *Proc. of the Second Congress on Large Dams*. pp. 445–463.
- Felton, E.A., Crook, K.A.W., 2003. Evaluating the impacts of huge waves on rocky shorelines: an essay review of the book ‘Tsunami--the underrated hazard.’ *Mar. Geol.* 197, 1–12.
- Fey, C., Wichmann, V., 2017. Long-range terrestrial laser scanning for geomorphological change detection in alpine terrain--handling uncertainties. *Earth Surf. Process. Landforms* 42, 789–802.
- Fischler, M.A., Bolles, R.C., 1981. Random sample consensus: a paradigm for model fitting with applications to image analysis and automated cartography. *Commun. ACM* 24, 381–395.

- Fleming, B.C.A., 1965. Two-storied Cliffs at the Auckland Islands. *Royal Society of New Zealand* 3, 171–174.
- Fletcher, C., Rooney, J., Barbee, M., Lim, S., Richmond, B., 2003. Mapping Shoreline Change Using Digital Orthophotogrammetry on Maui , Hawaii. *J. Coast. Res.* 106–124.
<https://doi.org/http://pubs.er.usgs.gov/publication/70025169>
- Fonstad, M.A., Dietrich, J.T., Courville, B.C., Jensen, J.L., Carbonneau, P.E., 2013. Topographic structure from motion: a new development in photogrammetric measurement. *Earth Surf. Process. Landforms* 38, 421–430. <https://doi.org/https://doi.org/10.1002/esp.3366>
- Fookes, P.G., Denness, B., 1969. Observational studies on fissure patterns in cretaceous sediments of South-East England. *Geotechnique* 19, 453–477.
- Förstner, W., 1986. A feature based correspondence algorithm for image matching. *ISPRS ComIII, Rovaniemi* 150–166.
- Fraccaroli, M., Mazzuchelli, G., Bizzarri, A., 2021. Machine Learning Techniques for Extracting Relevant Features from Clinical Data for COVID-19 Mortality Prediction, in: 2021 IEEE Symposium on Computers and Communications (ISCC). pp. 1–7. <https://doi.org/10.1109/ISCC53001.2021.9631477>
- Francioni, M., Coggan, J., Eyre, M., Stead, D., 2018a. A combined field/remote sensing approach for characterizing landslide risk in coastal areas. *Int. J. Appl. Earth Obs. Geoinf.* 67, 79–95.
<https://doi.org/10.1016/j.jag.2017.12.016>
- Francioni, M., Coggan, J., Eyre, M., Stead, D., 2018b. A combined field/remote sensing approach for characterizing landslide risk in coastal areas. *Int. J. Appl. Earth Obs. Geoinf.* 67, 79–95.
- Francioni, M., Salvini, R., Stead, D., Coggan, J., 2018c. Improvements in the integration of remote sensing and rock slope modelling. *Nat. Hazards.* <https://doi.org/10.1007/s11069-017-3116-8>
- Friedman, J.H., 2001. Greedy Function Approximation: A Gradient Boosting Machine. *Ann. Stat.* 29, 1189–1232.
- Fullin, N., Duo, E., Fabbri, S., Francioni, M., Ghirotti, M., Ciavola, P., 2023. Quantitative Characterization of Coastal Cliff Retreat and Landslide Processes at Portonovo – Trave Cliffs (Conero , Ancona , Italy) Using Multi-Source Remote Sensing Data.
- Furlani, S., Cucchi, F., 2013. Downwearing rates of vertical limestone surfaces in the intertidal zone (Gulf of Trieste, Italy). *Mar. Geol.* 343, 92–98.
- Furukawa, Y., Ponce, J., 2006. Carved visual hulls for image-based modeling, in: *Computer Vision--ECCV 2006: 9th European Conference on Computer Vision, Graz, Austria, May 7-13, 2006. Proceedings, Part I* 9. pp. 564–577.
- Giani, G.P., 1992. *Rock slope stability analysis.* CRC Press.
- Gill, E.D., Lang, J.G., 1983. Micro-erosion meter measurements of rock wear on the Otway coast of southeast Australia. *Mar. Geol.* 52, 141–156.
- Gindraux, S., Boesch, R., Farinotti, D., 2017. Accuracy assessment of digital surface models from Unmanned Aerial Vehicles’ imagery on glaciers. *Remote Sens.* 9, 1–15.
<https://doi.org/10.3390/rs9020186>

- Giuliano, J., Dewez, T.J.B., Lebourg, T., Godard, V., Prémaillon, M., Marçot, N., 2022. Mapping Coastal Erosion of a Mediterranean Cliff with a Boat-Borne Laser Scanner: Performance, Processing, and Cliff Erosion Rate, in: 3D Digital Geological Models. pp. 109–132. <https://doi.org/https://doi.org/10.1002/9781119313922.ch7>
- Goda, Y. , 2010. *Random Seas and Design of Maritime Structures*; WORLD SCIENTIFIC; Vol. 33; ISBN 978-981-4282-39-0.
- Godfrey, S., Cooper, J., Bezombes, F., Plater, A., 2020. Monitoring coastal morphology: the potential of low-cost fixed array action cameras for 3D reconstruction. *Earth Surf. Process. Landforms* 45, 2478–2494. <https://doi.org/10.1002/esp.4892>
- Gómez-Pazo, A., Pérez-Alberti, A., Trenhaile, A., 2021. Tracking the behavior of rocky coastal cliffs in northwestern Spain. *Environ. Earth Sci.* 80, 1–18. <https://doi.org/10.1007/s12665-021-09929-4>
- Goodman, R.E., Shi, G., 1985. *Block theory and its application to rock engineering*. Englewood Cliffs, NJ: Prentice-Hall.
- Griggs, G.B., Savoy, L.E., 1985. *Living with the California coast*. Durham, NC: Duke University Press.
- Grøneng, G., Lu, M., Nilsen, B., Jenssen, A.K., 2010. Modelling of time-dependent behavior of the basal sliding surface of the Åknes rockslide area in western Norway. *Eng. Geol.* 114, 414–422.
- Grottoli, E., Bertoni, D., Ciavola, P., Pozzebon, A., 2015. Short term displacements of marked pebbles in the swash zone: Focus on particle shape and size. *Mar. Geol.* 367, 143–158. <https://doi.org/10.1016/j.margeo.2015.06.006>
- Guyon, I., others, 1997. A scaling law for the validation-set training-set size ratio. *AT&T Bell Lab.* 1.
- Pörtner, H.-O., Roberts, D.C., Tignor, M., Poloczanska, E.S., Mintenbeck, K., Alegría, A., Craig, M., Langsdorf, S., Löschke, S., Möller, V., Okem, A.B.R., 2022. *IPCC Climate Change 2022: Impacts, Adaptation, and Vulnerability. Contribution of Working Group II to the Sixth Assessment Report of the Intergovernmental Panel on Climate Change., Global Warming of 1.5°C*. Cambridge. <https://doi.org/doi:10.1017/9781009325844>
- Habib, A., 2017. Accuracy, quality assurance, and quality control of LiDAR data, in: *Topographic Laser Ranging and Scanning*. CRC Press, pp. 269–294.
- Hammah, R.E., Yacoub, T., Corkum, B., Curran, J.H., 2008. The practical modelling of discontinuous rock masses with finite element analysis, in: *ARMA US Rock Mechanics/Geomechanics Symposium*. p. ARMA--08.
- Hampton, M.A., Griggs, G.B., 2004. Formation, Evolution, and Stability of Coastal Cliffs – Status and Trends. *USGS Prof. Pap.* 1693 129.
- Han, J., Kamber, M., Pei, J., 2012a. 2 - Getting to Know Your Data, in: Han, J., Kamber, M., Pei, J.B.T.-D.M. (Third E. (Eds.), *The Morgan Kaufmann Series in Data Management Systems*. Morgan Kaufmann, Boston, pp. 39–82. <https://doi.org/https://doi.org/10.1016/B978-0-12-381479-1.00002-2>
- Han, J., Kamber, M., Pei, J., 2012b. 7 - Advanced Pattern Mining, in: Han, J., Kamber, M., Pei, J.B.T.-D.M. (Third E. (Eds.), *The Morgan Kaufmann Series in Data Management Systems*. Morgan Kaufmann, Boston, pp. 279–325. <https://doi.org/https://doi.org/10.1016/B978-0-12-381479-1.00007-1>

- Han, J., Kamber, M., Pei, J., 2012c. 3 - Data Preprocessing, in: Han, J., Kamber, M., Pei, J.B.T.-D.M. (Third E. (Eds.), The Morgan Kaufmann Series in Data Management Systems. Morgan Kaufmann, Boston, pp. 83–124. <https://doi.org/https://doi.org/10.1016/B978-0-12-381479-1.00003-4>
- Han, J., Kamber, M., Pei, J., 2012d. 10 - Cluster Analysis: Basic Concepts and Methods, in: Han, J., Kamber, M., Pei, J.B.T.-D.M. (Third E. (Eds.), The Morgan Kaufmann Series in Data Management Systems. Morgan Kaufmann, Boston, pp. 443–495. <https://doi.org/https://doi.org/10.1016/B978-0-12-381479-1.00010-1>
- Hancox-Li, L., 2020. Robustness in machine learning explanations: Does it matter?, in: Proceedings of the 2020 Conference on Fairness, Accountability, and Transparency. pp. 640–647.
- Haneberg, W.C., Cole, W.F., Kasali, G., 2009. High-resolution lidar-based landslide hazard mapping and modeling, UCSF Parnassus Campus, San Francisco, USA. *Bull. Eng. Geol. Environ.* 68, 263–276.
- Hanna, E., Huybrechts, P., Steffen, K., Cappelen, J., Huff, R., Shuman, C., Irvine-Fynn, T., Wise, S., Griffiths, M., 2008. Increased runoff from melt from the Greenland Ice Sheet: a response to global warming. *J. Clim.* 21, 331–341.
- Hansom, J.D., 1983. Shore-platform development in the South Shetland islands, Antarctica. *Mar. Geol.* 53, 211–229.
- Hantz, D., Vengeon, J.M., Dussauge-Peisser, C., 2003. An historical, geomechanical and probabilistic approach to rock-fall hazard assessment. *Nat. Hazards Earth Syst. Sci.* 3, 693–701. <https://doi.org/10.5194/nhess-3-693-2003>
- Hapke, C., Plant, N., 2010. Predicting coastal cliff erosion using a Bayesian probabilistic model. *Mar. Geol.* 278, 140–149. <https://doi.org/10.1016/j.margeo.2010.10.001>
- Harris, C., Stephens, M., others, 1988. A combined corner and edge detector, in: Alvey Vision Conference. pp. 10–5244.
- Hastie, T., Tibshirani, R., Friedman, J., Hastie, T., Tibshirani, R., Friedman, J., 2009. Unsupervised learning. *Elem. Stat. Learn. Data mining, inference, Predict.* 485–585.
- He, L., Coggan, J., Francioni, M., Eyre, M., 2021. Maximizing Impacts of Remote Sensing Surveys in Slope Stability—A Novel Method to Incorporate Discontinuities into Machine Learning Landslide Prediction. *ISPRS Int. J. Geo-Information* 10. <https://doi.org/10.3390/ijgi10040232>
- He, L., Coggan, J., Stead, D., Francioni, M., Eyre, M., 2022. Modelling discontinuity control on the development of Hell’s Mouth landslide. *Landslides* 19, 277–295. <https://doi.org/10.1007/s10346-021-01813-3>
- Heritage, G.L., Large, A.R.G., 2009. *Laser Scanning for the Environmental Sciences*. Wiley-Blackwell, London.
- Hills, E.S., 2012. *Elements of structural geology*. Springer Science & Business Media.
- Himmelstoss, E.A.; Henderson, R.E.; Kratzmann, M.G.; Farris, A.S., 2018. Digital Shoreline Analysis System (DSAS) Version 5.0 User Guide. *U.S. Geol. Surv. Open-File Rep., 2018-1179*.
- Hoek, E., 2007. *Practical Rock Engineering*. The development of rock engineering. <https://www.rocscience.com/learning/hoek-s-corner>

- Hoek, E., Bray, J.D., 1981. Rock slope engineering. CRC press.
- Hoek, E., Brown, E.T., 2019. The Hoek–Brown failure criterion and GSI – 2018 edition. *J. Rock Mech. Geotech. Eng.* 11, 445–463. <https://doi.org/10.1016/j.jrmge.2018.08.001>
- Hoek, E., Brown, E.T., 1997. Practical estimates of rock mass strength. *Int. J. rock Mech. Min. Sci.* 34, 1165–1186.
- Hoek, E., Carranza-Torres, C., Corkum, B., others, 2002. Hoek-Brown failure criterion-2002 edition. *Proc. NARMS-Tac* 1, 267–273.
- Hoek, E., Guevara, R., 2009. Overcoming squeezing in the Yacambú-Quibor tunnel, Venezuela. *Rock Mech. Rock Eng.* 42, 389–418.
- Hoek, E., Marinos, P., 2007. A brief history of the development of the Hoek-Brown failure criterion. *Soils and Rocks* 30, 85–92.
- Hoek, E., Marinos, P., 2000. Predicting tunnel squeezing problems in weak heterogeneous rock masses. *Tunnels Tunn. Int.* 32, 45–51.
- Hoek, E., Marinos, P., Benissi, M., 1998. Applicability of the geological strength index (GSI) classification for very weak and sheared rock masses. The case of the Athens Schist Formation. *Bull. Eng. Geol. Environ.* 57, 151–160. <https://doi.org/10.1007/s100640050031>
- Hoek, E., Marinos, P.G., Marinos, V.P., 2005. Characterisation and engineering properties of tectonically undisturbed but lithologically varied sedimentary rock masses. *Int. J. Rock Mech. Min. Sci.* 42, 277–285. <https://doi.org/10.1016/j.ijrmms.2004.09.015>
- Horikawa, K., Sunamura, T., 1970. A study on erosion of coastal cliffs and of submarine bedrocks. *Coast. Eng. Japan* 13, 127–139.
- Horikawa, K., Sunamura, T., 1967. A study on erosion of coastal cliffs by using aerial photographs. *Coast. Eng. Japan* 10, 67–83.
- Hudson, J.A., Harrison, J.P., 2000. *Engineering rock mechanics: an introduction to the principles*. Elsevier.
- Humair, F., Pedrazzini, A., Epard, J.-L., Froese, C.R., Jaboyedoff, M., 2013. Structural characterization of Turtle Mountain anticline (Alberta, Canada) and impact on rock slope failure. *Tectonophysics* 605, 133–148.
- Hungr, O., Evans, S.G., 2004. The occurrence and classification of massive rock slope failure. *Felsbau* 22, 16–23.
- Hungr, O., Leroueil, S., Picarelli, L., 2014. The Varnes classification of landslide types, an update. *Landslides* 11, 167–194. <https://doi.org/10.1007/s10346-013-0436-y>
- Hursta, M.D., Rood, D.H., Ellis, M.A., Anderson, R.S., Dornbusch, U., 2016. Recent acceleration in coastal cliff retreat rates on the south coast of Great Britain. *Proc. Natl. Acad. Sci. U. S. A.* 113, 13336–13341. <https://doi.org/10.1073/pnas.1613044113>
- Iaccarino, S.M., Bertini, A., Di Stefano, A., Ferraro, L., Gennari, R., Grossi, F., Lirer, F., Manzi, V., Menichetti, E., Lucchi, M.R., Taviani, M., Sturiale, G., Angeletti, L., 2008. The Trave section (Monte dei

Corvi, Ancona, Central Italy): An integrated paleontological study of the Messinian deposits. *Stratigraphy* 5, 281–306.

Ingensand, H., 2006. Metrological aspects in terrestrial laser-scanning technology, in: *Proceedings of the 3rd IAG/12th FIG Symposium*, Baden, Austria.

Jaboyedoff, M., Oppikofer, T., Abellán, A., Derron, M.-H., Loye, A., Metzger, R., Pedrazzini, A., 2012a. Use of LIDAR in landslide investigations: a review. *Nat. hazards* 61, 5–28.

Jaboyedoff, M., Oppikofer, T., Abellán, A., Derron, M.H., Loye, A., Metzger, R., Pedrazzini, A., 2012b. Use of LIDAR in landslide investigations: A review. *Nat. Hazards* 61, 5–28.
<https://doi.org/10.1007/s11069-010-9634-2>

James, M.R., Robson, S., 2014. Mitigating systematic error in topographic models derived from UAV and ground-based image networks. *Earth Surf. Process. Landforms* 39, 1413–1420.

James, M.R., Robson, S., 2012. Straightforward reconstruction of 3D surfaces and topography with a camera: Accuracy and geoscience application. *J. Geophys. Res. Earth Surf.* 117.

Janbu, N., 1973. Slope stability computations *Embankment Dam Engineering Casagrande Memorial Volume*.

Jaud, M., Letortu, P., Théry, C., Grandjean, P., Costa, S., Maquaire, O., Davidson, R., Le Dantec, N., 2019. UAV survey of a coastal cliff face – Selection of the best imaging angle. *Measurement* 139, 10–20. <https://doi.org/https://doi.org/10.1016/j.measurement.2019.02.024>

Jennings, J.E., 1970. A mathematical theory for the calculation of the stability of slopes in open cast mines, in: *Planning Open Pit Mines, Proceedings, Johannesburg*. pp. 87–102.

Jing, L., 2003. A review of techniques, advances and outstanding issues in numerical modelling for rock mechanics and rock engineering. *Int. J. Rock Mech. Min. Sci.* 40, 283–353.
[https://doi.org/https://doi.org/10.1016/S1365-1609\(03\)00013-3](https://doi.org/https://doi.org/10.1016/S1365-1609(03)00013-3)

Kaelbling, L.P., Littman, M.L., Moore, A.W., 1996. Reinforcement learning: A survey. *J. Artif. Intell. Res.* 4, 237–285.

Kamerman, G.W., 1993. Laser radar. *Act. Electro-Optical Syst.* 6.

Kanyaya, J.I., Trenhaile, A.S., 2005. Tidal wetting and drying on shore platforms: an experimental assessment. *Geomorphology* 70, 129–146.

Kardani, N., Zhou, A., Nazem, M., Lin, X., 2021. Modelling of municipal solid waste gasification using an optimised ensemble soft computing model. *Fuel* 289, 119903.
<https://doi.org/https://doi.org/10.1016/j.fuel.2020.119903>

Kemeny, J., 2003. The time-dependent reduction of sliding cohesion due to rock bridges along discontinuities: A fracture mechanics approach. *Rock Mech. Rock Eng.* 36, 27–38.
<https://doi.org/10.1007/s00603-002-0032-2>

Kennedy, D.M., Milkins, J., 2015. The formation of beaches on shore platforms in microtidal environments. *Earth Surf. Process. Landforms*. <https://doi.org/10.1002/esp.3610>

- Kennedy, D.M., Paulik, R., Dickson, M.E., 2011. Subaerial weathering versus wave processes in shore platform development: Reappraising the Old Hat Island evidence. *Earth Surf. Process. Landforms*. <https://doi.org/10.1002/esp.2092>
- Kennedy, D.M., Tannock, K.L., Crozier, M.J., Rieser, U., 2007. Boulders of MIS 5 age deposited by a tsunami on the coast of Otago, New Zealand. *Sediment. Geol.* 200, 222–231.
- Kirk, R.M., 1977. Rates and forms of erosion on intertidal platforms at Kaikoura Peninsula, South Island, New Zealand. *New Zeal. J. Geol. Geophys.* 20, 571–613.
- Koenderink, J.J., Van Doorn, A.J., 1991. Affine structure from motion. *JOSA A* 8, 377–385.
- Komar, P.D., Shih, S.M., 1993. Cliff erosion along the Oregon coast: a tectonic-sea level imprint plus local controls by beach processes. *J. Coast. Res.* 9(3), 747–765. <https://doi.org/https://journals.flvc.org/jcr/article/view/79045>
- Kotsiantis, S.B., 2013. Decision trees: a recent overview. *Artif. Intell. Rev.* 39, 261–283.
- Koukouvelas, I., Nikolakopoulos, K.G., Zygouri, V., Kyriou, A., 2020. Post-seismic monitoring of cliff mass wasting using an unmanned aerial vehicle and field data at Egremni, Lefkada Island, Greece. *Geomorphology* 367, 107306. <https://doi.org/10.1016/j.geomorph.2020.107306>
- La Pointe, P.R., Hudson, J.A., 1985. Characterization and interpretation of rock mass joint patterns. *Spec. Pap. Geol. Soc. Am.*, 199, 37, 1985.
- Lague, D., Brodu, N., Leroux, J., 2013. Accurate 3D comparison of complex topography with terrestrial laser scanner: Application to the Rangitikei canyon (N-Z). *ISPRS J. Photogramm. Remote Sens.* 82, 10–26. <https://doi.org/10.1016/j.isprsjprs.2013.04.009>
- Lato, M., Kemeny, J., Harrap, R.M., Bevan, G., 2013. Rock bench: Establishing a common repository and standards for assessing rockmass characteristics using LiDAR and photogrammetry. *Comput. & Geosci.* 50, 106–114.
- Lato, M.J., Hutchinson, D.J., Gauthier, D., Edwards, T., Ondercin, M., 2015. Comparison of airborne laser scanning, terrestrial laser scanning, and terrestrial photogrammetry for mapping differential slope change in mountainous terrain. *Can. Geotech. J.* 52, 129–140.
- Li, J., Li, E., Chen, Y., Xu, L., Zhang, Y., 2010. Bundled depth-map merging for multi-view stereo, in: 2010 IEEE Computer Society Conference on Computer Vision and Pattern Recognition. pp. 2769–2776. <https://doi.org/10.1109/CVPR.2010.5540004>
- Liashchynskiy, Petro, Liashchynskiy, Pavlo, 2019. Grid search, random search, genetic algorithm: a big comparison for NAS. *arXiv Prepr. arXiv1912.06059*.
- Lichti, D.D., 2007. Error modelling, calibration and analysis of an AM–CW terrestrial laser scanner system. *ISPRS J. Photogramm. Remote Sens.* 61, 307–324.
- Lim, M., Petley, D.N., Rosser, N.J., Allison, R.J., Long, A.J., Pybus, D., 2005. Combined digital photogrammetry and time-of-flight laser scanning for monitoring cliff evolution. *Photogramm. Rec.* 20, 109–129. <https://doi.org/10.1111/j.1477-9730.2005.00315.x>
- Limber, P.W., Barnard, P.L., Vitousek, S., Erikson, L.H., 2018. A model ensemble for projecting multidecadal coastal cliff retreat during the 21st century. *J. Geophys. Res. Earth Surf.* 123, 1566–1589.

- Lin, Y.-C., Zhou, T., Wang, T., Crawford, M., Habib, A., 2021. New Orthophoto Generation Strategies from UAV and Ground Remote Sensing Platforms for High-Throughput Phenotyping. *Remote Sens.* 13. <https://doi.org/10.3390/rs13050860>
- Lisjak, A., Mahabadi, O.K., Kaifosh, P., Vietor, T., Grasselli, G., 2014. A preliminary evaluation of an enhanced FDEM code as a tool to simulate hydraulic fracturing in jointed rock masses, in: *ISRM EUROCK*. p. ISRM--EUROCK.
- Liu, G., Klette, R., Rosenhahn, B., 2006. Collinearity and coplanarity constraints for structure from motion, in: *Pacific-Rim Symposium on Image and Video Technology*. pp. 13–23.
- Loggenberg, K., Strever, A., Greyling, B., Poona, N., 2018. Modelling water stress in a Shiraz vineyard using hyperspectral imaging and machine learning. *Remote Sens.* 10, 202.
- Loh, W.-Y., 2011. Classification and regression trees. *Wiley Interdiscip. Rev. data Min. Knowl. Discov.* 1, 14–23.
- Loiotine, L., 2022. Integrated Approach to Evaluate Rock Mass Stability by Means of Remote Sensing Techniques and Conventional Geostructural and Geomechanical Surveys. PhD Thesis.
- Loiotine, L., Andriani, G.F., Jaboyedoff, M., Parise, M., Derron, M.H., 2021. Comparison of remote sensing techniques for geostructural analysis and cliff monitoring in coastal areas of high tourist attraction: The case study of Polignano a mare (southern Italy). *Remote Sens.* 13. <https://doi.org/10.3390/rs13245045>
- Lollino, P., Pagliarulo, R., Trizzino, R., Santaloia, F., Pisano, L., Zumpano, V., Perrotti, M., Fazio, N.L., 2021. Multi-scale approach to analyse the evolution of soft rock coastal cliffs and role of controlling factors: a case study in South-Eastern Italy. *Geomatics, Nat. Hazards Risk* 12, 1058–1081. <https://doi.org/10.1080/19475705.2021.1910351>
- Louppe, G., Wehenkel, L., Sutera, A., Geurts, P., 2013. Understanding variable importances in Forests of randomized trees, in: *Advances in Neural Information Processing Systems*.
- Lowe, D.G., 2004. Distinctive image features from scale-invariant keypoints. *Int. J. Comput. Vis.* 60, 91–110.
- Loye, A., Pedrazzini, A., Theule, J.I., Jaboyedoff, M., Liébault, F., Metzger, R., 2012. Influence of bedrock structures on the spatial pattern of erosional landforms in small alpine catchments. *Earth Surf. Process. Landforms* 37, 1407–1423.
- Lucieer, A., Jong, S.M. de, Turner, D., 2014. Mapping landslide displacements using Structure from Motion (SfM) and image correlation of multi-temporal UAV photography. *Prog. Phys. Geogr.* 38, 97–116.
- Lucieer, A., Jong, S.M. de, Turner, D., 2013. Mapping landslide displacements using Structure from Motion (SfM) and image correlation of multi-temporal UAV photography. *Prog. Phys. Geogr. Earth Environ.* 38, 97–116. <https://doi.org/10.1177/0309133313515293>
- Mantovani, M., Devoto, S., Forte, E., Mocnik, A., Pasuto, A., Piacentini, D., Soldati, M., 2013. A multidisciplinary approach for rock spreading and block sliding investigation in the north-western coast of Malta. *Landslides* 10, 611–622. <https://doi.org/10.1007/s10346-012-0347-3>
- Marinos, P., Hoek, E., 2018. GSI: A geologically friendly tool for rock mass strength estimation. *ISRM Int. Symp. 2000, IS 2000*.

- Marinos, P., Hoek, E., 2001. Estimating the geotechnical properties of heterogeneous rock masses such as flysch. *Bull. Eng. Geol. Environ.* 60, 85–92. <https://doi.org/10.1007/s100640000090>
- Marinos, V., Carter, T.G., 2018. Corrigendum to “Maintaining geological reality in application of GSI for design of engineering structures in Rock” [*Engineering Geology* 239 (2018) 282–297] (S0013795217310049) (10.1016/j.enggeo.2018.03.022). *Eng. Geol.* 242, 222. <https://doi.org/10.1016/j.enggeo.2018.07.003>
- Marinos, V., Marinos, P., Hoek, E., 2005. The geological strength index: Applications and limitations. *Bull. Eng. Geol. Environ.* 64, 55–65. <https://doi.org/10.1007/s10064-004-0270-5>
- Marinos, P. V, 2017. New Proposed Gsi Classification Charts for Weak or Complex Rock Masses. *Bull. Geol. Soc. Greece* 43, 1248. <https://doi.org/10.12681/bgsg.11301>
- Markland, J.T., 1972. A useful technique for estimating the stability of rock slopes when the rigid wedge slide type of failure is expected. Interdepartmental Rock Mechanics Project, Imperial College of Science and~....
- Marmoni, G.M., Martino, S., Censi, M., Menichetti, M., Piacentini, D., Scarascia Mugnozza, G., Torre, D., Troiani, F., 2023. Transition from rock mass creep to progressive failure for rockslide initiation at Mt. Conero (Italy). *Geomorphology* 437, 108750. <https://doi.org/https://doi.org/10.1016/j.geomorph.2023.108750>
- Martínez, M.L., Intralawan, A., Vázquez, G., Pérez-Maqueo, O., Sutton, P., Landgrave, R., 2007. The coasts of our world: Ecological, economic and social importance. *Ecol. Econ.* 63, 254–272. <https://doi.org/10.1016/j.ecolecon.2006.10.022>
- Martino, S., Mazzanti, P., 2014. Integrating geomechanical surveys and remote sensing for sea cliff slope stability analysis: The Mt. Pucci case study (Italy). *Nat. Hazards Earth Syst. Sci.* 14, 831–848. <https://doi.org/10.5194/nhess-14-831-2014>
- Matano, F., Pignalosa, A., Marino, E., Esposito, G., Caccavale, M., Caputo, T., Sacchi, M., Somma, R., Troise, C., De Natale, G., 2015. Laser scanning application for geostructural analysis of tuffaceous coastal cliffs: The case of Punta Epitaffio, Pozzuoli Bay, Italy. *Eur. J. Remote Sens.* 48, 615–637. <https://doi.org/10.5721/EuJRS20154834>
- Matano, F., Somma, R., Marino, E., Pignalosa, A., Esposito, G., Caputo, T., Sacchi, M., De Natale, G., 2014. Laser Scanning Applications for Monitoring Tuffaceous Coastal Cliff in the Pozzuoli Bay, Punta Epitaffio Site, Italy: preliminary results.
- Matasci, B., Carrea, D., Jaboyedoff, M., Pedrazzini, A., Stock, G.M., Oppikofer, T., 2011. Structural characterization of rockfall sources in Yosemite Valley from remote sensing data: Toward more accurate susceptibility assessment, in: *Proceedings of the 14th ISSMGE Pan-American Conference*.
- Mateos, R.M., Azañón, J.M., Roldán, F.J., Notti, D., Pérez-Peña, V., Galve, J.P., Pérez-García, J.L., Colomo, C.M., Gómez-López, J.M., Montserrat, O., Devantèry, N., Lamas-Fernández, F., Fernández-Chacón, F., 2017. The combined use of PSInSAR and UAV photogrammetry techniques for the analysis of the kinematics of a coastal landslide affecting an urban area (SE Spain). *Landslides* 14, 743–754. <https://doi.org/10.1007/s10346-016-0723-5>
- Matsui, T., San, K.-C., 1992. Finite element slope stability analysis by shear strength reduction technique. *Soils Found.* 32, 59–70.

- Mazzanti, P., Caporossi, P., Muzi, R., 2020. Sliding time master digital image correlation analyses of cubesat images for landslide monitoring: The Rattlesnake Hills landslide (USA). *Remote Sens.* 12, 592.
- McDonald, G.C., 2009. Ridge regression. *WIREs Comput. Stat.* 1, 93–100. <https://doi.org/https://doi.org/10.1002/wics.14>
- Melis, M.T., Pelo, S. Da, Erbi, I., Loche, M., Deiana, G., Demurtas, V., Meloni, M.A., Dessì, F., Funedda, A., Scaioni, M., Scaringi, G., 2020. Thermal remote sensing from UAVs: A review on methods in coastal cliffs prone to landslides. *Remote Sens.* 12, 1–29. <https://doi.org/10.3390/rs12121971>
- Miccadei, E., Mascioli, F., Ricci, F., Piacentini, T., 2019. Geomorphology of soft clastic rock coasts in the mid-western Adriatic Sea (Abruzzo, Italy). *Geomorphology* 324, 72–94. <https://doi.org/https://doi.org/10.1016/j.geomorph.2018.09.023>
- Michoud, C., Carrea, D., Costa, S., Derron, M.H., Jaboyedoff, M., Delacourt, C., Maquaire, O., Letortu, P., Davidson, R., 2015. Landslide detection and monitoring capability of boat-based mobile laser scanning along Dieppe coastal cliffs, Normandy. *Landslides* 12, 403–418. <https://doi.org/10.1007/s10346-014-0542-5>
- Mikhail, E.M., Bethel, J.S., McGlone, J.C., 2001. Introduction to modern photogrammetry. John Wiley & Sons.
- Mill, T., Ellmann, A., Uueküla, K., Joala, V., 2023. ROAD SURFACE SURVEYING USING TERRESTRIAL LASER SCANNER AND TOTAL STATION TECHNOLOGIES.
- Mizuno, K., Noguchi, H., He, G., Terachi, Y., Kamino, T., Fujinaga, T., Izumi, S., Ariki, Y., Kawaguchi, H., Yoshimoto, M., 2011. A low-power real-time SIFT descriptor generation engine for full-HDTV video recognition. *IEICE Trans.* 94–C, 448–457. <https://doi.org/10.1587/transele.E94.C.448>
- Montanari, A., Mainiero, M., Coccioni, R., Pignocchi, G., 2016. Catastrophic landslide of medieval Portonovo (Ancona, Italy). *Geol. Soc. Am. Bull.* 128, 1660–1678. <https://doi.org/10.1130/b31472.1>
- Moore, L.J., Benumof, B.T., Griggs, G.B., 1999. Coastal erosion hazards in Santa Cruz and San Diego Counties, California. *J. Coast. Res.* 121–139.
- Morgenstern, N.R. u, Price, V.E., 1965. The analysis of the stability of general slip surfaces. *Geotechnique* 15, 79–93.
- Moses, C., Robinson, D., 2011. Chalk coast dynamics: Implications for understanding rock coast evolution. *Earth-Science Rev.* <https://doi.org/10.1016/j.earscirev.2011.08.003>
- Mottershead, D.N., 1989. Rates and patterns of bedrock denudation by coastal salt spray weathering: a seven-year record. *Earth Surf. Process. Landforms* 14, 383–398.
- Mutaqin, B.W., 2017. Shoreline changes analysis in kuwaru coastal area, yogyakarta, Indonesia: An application of the digital shoreline analysis system (DSAS). *Int. J. Sustain. Dev. Plan.* 12, 1203–1214.
- Nassar, K., Mahmud, W.E., Fath, H., Masria, A., Nadaoka, K., Negm, A., 2019. Shoreline change detection using DSAS technique: Case of North Sinai coast, Egypt. *Mar. Georesources & Geotechnol.* 37, 81–95.
- Naylor, L.A., Stephenson, W.J., 2010. On the role of discontinuities in mediating shore platform erosion. *Geomorphology* 114, 89–100. <https://doi.org/10.1016/j.geomorph.2008.12.024>

- Naylor, L.A., Stephenson, W.J., Trenhaile, A.S., 2010. Rock coast geomorphology: Recent advances and future research directions. *Geomorphology* 114, 3–11.
<https://doi.org/10.1016/j.geomorph.2009.02.004>
- Noormets, R., Felton, E.A., Crook, K.A.W., 2002. Sedimentology of rocky shorelines: 2: Shoreline megaclasts on the north shore of Oahu, Hawaii—origins and history. *Sediment. Geol.* 150, 31–45.
- Nourbakhshbeidokhti, S., Kinoshita, A.M., Chin, A., Florsheim, J.L., 2019. A Workflow to Estimate Topographic and Volumetric Changes and Errors in Channel Sedimentation after Disturbance. *Remote Sens.* 11. <https://doi.org/10.3390/rs11050586>
- Obanawa, H., Hayakawa, Y.S., 2018. Variations in volumetric erosion rates of bedrock cliffs on a small inaccessible coastal island determined using measurements by an unmanned aerial vehicle with structure-from-motion and terrestrial laser scanning. *Prog. Earth Planet. Sci.* 5, 33.
<https://doi.org/10.1186/s40645-018-0191-8>
- Ogawa, H., Dickson, M.E., Kench, P.S., 2016. Generalised observations of wave characteristics on near-horizontal shore platforms: Synthesis of six case studies from the North Island, New Zealand. *N. Z. Geog.* 72, 107–121. <https://doi.org/10.1111/nzg.12121>
- Ohnishi, Y., Nishiyama, S., Yano, T., Matsuyama, H., Amano, K., 2006. A study of the application of digital photogrammetry to slope monitoring systems. *Int. J. Rock Mech. Min. Sci.* 43, 756–766.
<https://doi.org/https://doi.org/10.1016/j.ijrmms.2005.12.002>
- Oppikofer, T., Jaboyedoff, M., Blikra, L., Derron, M.H., Metzger, R., 2009. Characterization and monitoring of the Åknes rockslide using terrestrial laser scanning. *Nat. Hazards Earth Syst. Sci.* 9, 1003–1019. <https://doi.org/10.5194/nhess-9-1003-2009>
- Orme, A.R., 1962. Abandoned and composite Seacliffs in Britain and Ireland. *Irish Geogr.* 4, 279–291.
<https://doi.org/10.1080/00750776209555554>
- Palmstrom, A., 2005. Measurements of and correlations between block size and rock quality designation (RQD). *Tunn. Undergr. Sp. Technol.* 20, 362–377.
<https://doi.org/10.1016/j.tust.2005.01.005>
- Palmstrom, A., 1996. RMI—a system for characterizing rock mass strength for use in rock engineering. *J. rock Mech. tunneling Technol.* 1, 69–108.
- Palmstrøm, A., 1996. Characterizing rock masses by the RMI for use in practical rock engineering: Part 1: The development of the Rock Mass index (RMI). *Tunn. Undergr. Sp. Technol.* 11, 175–188.
- Parsa, M., 2021. A data augmentation approach to XGboost-based mineral potential mapping: An example of carbonate-hosted ZnPb mineral systems of Western Iran. *J. Geochemical Explor.* 228, 106811. <https://doi.org/https://doi.org/10.1016/j.gexplo.2021.106811>
- Peiró, J., Sherwin, S., 2005. Finite difference, finite element and finite volume methods for partial differential equations, in: *Handbook of Materials Modeling: Methods*. Springer, pp. 2415–2446.
- Pepe, M., Costantino, D., Alfio, V., 2023. A GIS Procedure to Assess Shoreline Changes over Time Using Multi-temporal Maps: An Analysis of a Sandy Shoreline in Southern Italy over the Last 100 Years. *Geomatics Environ. Eng.* 17. <https://doi.org/10.7494/geom.2023.17.3.107>

- Pesci, A., Teza, G., Bonali, E., 2011. Terrestrial laser scanner resolution: Numerical simulations and experiments on spatial sampling optimization. *Remote Sens.* 3, 167–184.
- Petrie, G., Toth, C.K., 2018. Introduction to laser ranging, profiling, and scanning, in: *Topographic Laser Ranging and Scanning*. CRC Press, pp. 1–28.
- Piacentini, D., Troiani, F., Torre, D., Menichetti, M., 2021. Land-surface quantitative analysis to investigate the spatial distribution of gravitational landforms along rocky coasts. *Remote Sens.* 13, 1–23. <https://doi.org/10.3390/rs13245012>
- Poate, T., Masselink, G., Austin, M.J., Dickson, M., McCall, R., 2018. The Role of Bed Roughness in Wave Transformation Across Sloping Rock Shore Platforms. *J. Geophys. Res. Earth Surf.* <https://doi.org/10.1002/2017JF004277>
- Porter, N.J., Trenhaile, A.S., 2007. Short-term rock surface expansion and contraction in the intertidal zone. *Earth Surf. Process. Landforms J. Br. Geomorphol. Res. Gr.* 32, 1379–1397.
- Prémaillon, M., Dewez, T.J.B., Regard, V., Rosser, N.J., Carretier, S., Guillen, L., 2021. Conceptual model of fracture-limited sea cliff erosion: Erosion of the seaward tilted flyschs of Socoa, Basque Country, France. *Earth Surf. Process. Landforms* 46, 2690–2709. <https://doi.org/10.1002/esp.5201>
- Prémaillon, M., Regard, V., Dewez, T.J.B., Auda, Y., 2018. GlobR2C2 (Global Recession Rates of Coastal Cliffs): A global relational database to investigate coastal rocky cliff erosion rate variations. *Earth Surf. Dyn.* 6, 651–668. <https://doi.org/10.5194/esurf-6-651-2018>
- Price, N.J., 2016. *Fault and joint development: in brittle and semi-brittle rock*. Elsevier.
- Priest, S.D., 1993. *Discontinuity analysis for rock engineering*. Springer Science & Business Media.
- Priest, S.D., Hudson, J.A., 1981. Estimation of discontinuity spacing and trace length using scanline surveys, in: *International Journal of Rock Mechanics and Mining Sciences & Geomechanics Abstracts*. pp. 183–197.
- Priest, S.D., Hudson, J.A., 1976. Discontinuity spacings in rock, in: *International Journal of Rock Mechanics and Mining Sciences & Geomechanics Abstracts*. pp. 135–148.
- Pritchard, H.D., Vaughan, D.G., 2007. Widespread acceleration of tidewater glaciers on the Antarctic Peninsula. *J. Geophys. Res. Earth Surf.* 112.
- Quinlan, J.R., 1993. CHAPTER 2 - Constructing Decision Trees, in: QUINLAN, J.R.B.T.-C.. (Ed.), . Morgan Kaufmann, San Francisco (CA), pp. 17–26. <https://doi.org/https://doi.org/10.1016/B978-0-08-050058-4.50007-3>
- Quinn, J.D., Rosser, N.J., Murphy, W., Lawrence, J.A., 2010. Identifying the behavioural characteristics of clay cliffs using intensive monitoring and geotechnical numerical modelling. *Geomorphology* 120, 107–122. <https://doi.org/https://doi.org/10.1016/j.geomorph.2010.03.004>
- Rau, J.-Y., Chen, N.-Y., Chen, L.-C., others, 2002. True orthophoto generation of built-up areas using multi-view images. *Photogramm. Eng. Remote Sensing* 68, 581–588.
- Rebala, G., Ravi, A., Churiwala, S., 2019. *An introduction to machine learning*. Springer.
- Redweik, P., Matildes, R., Marques, F., Santos, L., 2009. Photogrammetric methods for monitoring cliffs with low retreat rate. *J. Coast. Res.* 1577–1581.

- Remondino, F., El-Hakim, S., 2006. Image-based 3D modelling: a review. *Photogramm. Rec.* 21, 269–291.
- Robinson, A.H.W., 1980. Erosion and accretion along part of the Suffolk coast of East Anglia, England. *Mar. Geol.* [https://doi.org/10.1016/0025-3227\(80\)90014-6](https://doi.org/10.1016/0025-3227(80)90014-6)
- Robinson, L.A., 1977a. Marine erosive processes at the cliff foot. *Mar. Geol.* 23, 257–271.
- Robinson, L.A., 1977b. Erosive processes on the shore platform of northeast Yorkshire, England. *Mar. Geol.* 23, 339–361.
- Rogova, G., Scott, P., Lolett, C., 2002. Distributed reinforcement learning for sequential decision making, in: *Proceedings of the Fifth International Conference on Information Fusion. FUSION 2002.* (IEEE Cat. No. 02EX5997). pp. 1263–1268.
- Romana, M., Tomás, R., Serón, J.B., 2015. Slope Mass Rating (SMR) geomechanics classification: Thirty years review. 13th ISRM Int. Congr. Rock Mech. 2015-MAY, 1–10.
- Roncella, R., Re, C., Forlani, G., 2011. Performance evaluation of a structure and motion strategy in architecture and cultural heritage. *Int. Arch. Photogramm. Remote Sens. Spat. Inf. Sci.* XXXVIII-5/, 285–292. <https://doi.org/10.5194/isprsarchives-XXXVIII-5-W16-285-2011>
- Rosser, N.J., Brain, M.J., Petley, D.N., Lim, M., Norman, E.C., 2013. Coastline retreat via progressive failure of rocky coastal cliffs. *Geology* 41, 939–942. <https://doi.org/10.1130/G34371.1>
- Rosser, N.J., Petley, D.N., Lim, M., Dunning, S.A., Allison, R.J., 2005a. Terrestrial laser scanning for monitoring the process of hard rock coastal cliff erosion. *Q. J. Eng. Geol. Hydrogeol.* 38, 363–375. <https://doi.org/10.1144/1470-9236/05-008>
- Rosser, N.J., Petley, D.N., Lim, M., Dunning, S.A., Allison, R.J., 2005b. Terrestrial laser scanning for monitoring the process of hard rock coastal cliff erosion. *Q. J. Eng. Geol. Hydrogeol.* <https://doi.org/10.1144/1470-9236/05-008>
- Ruder, S., 2016. An overview of gradient descent optimization algorithms 1–14.
- Sagi, O., Rokach, L., 2018. Ensemble learning: A survey. *Wiley Interdiscip. Rev. Data Min. Knowl. Discov.* 8, e1249.
- Sarma, S.K., 1973. Stability analysis of embankments and slopes. *Geotechnique* 23, 423–433.
- Scheffers, A., Kelletat, D., 2006. Tsunami and paleo-tsunami research: where are we now and where do we go?, in: *Tsunamis, Hurricanes and Neotectonics as Driving Mechanisms in Coastal Evolution (Proceedings of the Bonaire Field Symposium, March 2-6, 2006. A Contribution to IGCP 495).* pp. 1–5.
- Scheffers, A., Kelletat, D., 2005. Tsunami relics on the coastal landscape west of Lisbon, Portugal. *Sci. Tsunami Hazards* 23, 3–16.
- Scheidegger, A.E., 2012. *Theoretical geomorphology.* Springer Science & Business Media.
- Schneider, J., Sadler, P., 1976. Biological and inorganic factors in the destruction of limestone coasts.
- Schowengerdt, R.A., 2006. *Remote sensing: models and methods for image processing.* elsevier.

- Seymour, A.C., Ridge, J.T., Rodriguez, A.B., Newton, E., Dale, J., Johnston, D.W., 2018. Deploying fixed wing Unoccupied Aerial Systems (UAS) for coastal morphology assessment and management. *J. Coast. Res.* 34, 704–717.
- Shashua, A., 1994. Projective structure from uncalibrated images: Structure from motion and recognition. *IEEE Trans. Pattern Anal. Mach. Intell.* 16, 778–790.
- Shen, J., Karakus, M., 2014. Three-dimensional numerical analysis for rock slope stability using shear strength reduction method. *Can. Geotech. J.* 51, 164–172.
- Shepard, F.P., Kuhn, G.G., 1983. History of sea arches and remnant stacks of La Jolla, California, and their bearing on similar features elsewhere. *Mar. Geol.* 51, 139–161.
- Small, C., Nicholls, R.J., 2003. A global analysis of human settlement in coastal zones. *J. Coast. Res.* 19, 584–599.
- Smith, G.S., 1995. Digital orthophotography and GIS, in: *Proceedings of the 1995 Esri User Conference*. pp. 22–26.
- Smith, J.V., 2016. Interaction of Strength and Stress in High, Steep Rock Slopes. *J. Geogr. Geol.* 8, 14. <https://doi.org/10.5539/jgg.v8n1p14>
- Snaveley, N., Seitz, S.M., Szeliski, R., 2008. Modeling the world from internet photo collections. *Int. J. Comput. Vis.* 80, 189–210.
- Spencer, E., 1967. A method of analysis of the stability of embankments assuming parallel inter-slice forces. *Geotechnique* 17, 11–26.
- Spencer, T., 1988a. Coastal biogeomorphology, in: *Biogeomorphology*. pp. 255–318.
- Spencer, T., 1988b. Limestone coastal morphology: the biological contribution. *Prog. Phys. Geogr.* 12, 66–101.
- Spencer, T., Viles, H., 2002. Bioconstruction, bioerosion and disturbance on tropical coasts: coral reefs and rocky limestone shores. *Geomorphology* 48, 23–50.
- Spetsakis, M., Aloimonos, J.Y., 1991. A multi-frame approach to visual motion perception. *Int. J. Comput. Vis.* 6, 245–255.
- Spreafico, M.C., Cervi, F., Francioni, M., Stead, D., Borgatti, L., 2017. An investigation into the development of toppling at the edge of fractured rock plateaux using a numerical modelling approach. *Geomorphology* 288, 83–98.
- Stead, D., Coggan, J., 2012. Numerical modeling of rock-slope instability, in: Stead, D., Clague, J.J. (Eds.), *Landslides: Types, Mechanisms and Modeling*. Cambridge University Press, Cambridge, pp. 144–158. <https://doi.org/DOI: 10.1017/CBO9780511740367.014>
- Stead, D., Eberhardt, E., Coggan, J.S., 2006. Developments in the characterization of complex rock slope deformation and failure using numerical modelling techniques. *Eng. Geol.* 83, 217–235.
- Stead, D., Wolter, A., 2015. A critical review of rock slope failure mechanisms: The importance of structural geology. *J. Struct. Geol.* 74, 1–23. <https://doi.org/10.1016/j.jsg.2015.02.002>

- Stephenson, W.J., Kirk, R.M., 2001. Surface swelling of coastal bedrock on inter-tidal shore platforms, Kaikoura Peninsula, South Island, New Zealand. *Geomorphology* 41, 5–21.
- Stock, G.M., Bawden, G.W., Green, J.K., Hanson, E., Downing, G., Collins, B.D., Bond, S., Leslar, M., 2011. High-resolution three-dimensional imaging and analysis of rock falls in Yosemite Valley, California. *Geosphere* 7, 573–581.
- Stockdon, H.F., Holman, R.A., Howd, P.A., Sallenger, A.H., 2006. Empirical parameterization of setup, swash, and runup. *Coast. Eng.* 53, 573–588. <https://doi.org/10.1016/j.coastaleng.2005.12.005>
- Stone, J., Lambeck, K., Fifield, L.K., Evans, J.M. t, Cresswell, R.G., 1996. A lateglacial age for the main rock platform, western Scotland. *Geology* 24, 707–710.
- Strecha, C., Bronstein, A., Bronstein, M., Fua, P., 2011. LDAHash: Improved matching with smaller descriptors. *IEEE Trans. Pattern Anal. Mach. Intell.* 34, 66–78.
- Styles, T.D., Coggan, J.S., Pine, R.J., 2011. Back analysis of the Joss Bay Chalk Cliff Failure using numerical modelling. *Eng. Geol.* 120, 81–90. <https://doi.org/https://doi.org/10.1016/j.enggeo.2011.04.004>
- Sunamura, T., 2015. Rocky coast processes: With special reference to the recession of soft rock cliffs. *Proc. Japan Acad. Ser. B Phys. Biol. Sci.* 91, 481–500. <https://doi.org/10.2183/pjab.91.481>
- Sunamura T., 1992. *Geomorphology of rocky coasts, Coastal morphology and research*. J. Wiley, Chichester ; New York.
- Sunamura, T., 1991. The elevation of shore platforms: a laboratory approach to the unsolved problem. *J. Geol.* <https://doi.org/10.1086/629537>
- Sunamura, T., 1982. A Predictive Model for Wave-Induced Cliff Erosion, with Application to Pacific Coasts of Japan. *J. Geol.* 90, 167–178.
- Sunamura, T., 1978a. A model of the development of continental shelves having erosional origin. *Geol. Soc. Am. Bull.* 89, 504–510.
- Sunamura, T., 1978b. A mathematical model of submarine platform development. *J. Int. Assoc. Math. Geol.* 10, 53–58.
- Sunamura, T., 1977. A relationship between wave-induced cliff erosion and erosive force of waves. *J. Geol.* 85, 613–618.
- Sunamura, T., 1973. Coastal cliff erosion due to waves-field investigations and laboratory experiments. *J. Fac. Eng. Univ. Tokyo* 32, 1–86.
- Swantesson, J., Gómez-Pujol, L., Cruslock, E.M., Fornós, J.J., Balaguer, P., 2006. Processes and patterns of erosion and downwearing on micro-tidal rock coasts in Sweden and the western Mediterranean.
- Swantesson, J.O.H., Moses, C.A., Berg, G.E., Jansson, K.M., 2006. Methods for measuring shore platform micro erosion: a comparison of the micro-erosion meter and laser scanner. *Zeitschrift fur Geomorphol. Suppl.* 144, 1–17.

- Swirad, Z.M., Young, A.P., 2021. Automating coastal cliff erosion measurements from large-area LiDAR datasets in California, USA. *Geomorphology* 389, 107799. <https://doi.org/10.1016/j.geomorph.2021.107799>
- Szeliski, R., Kang, S.B., 1994. Recovering 3D shape and motion from image streams using nonlinear least squares. *J. Vis. Commun. Image Represent.* 5, 10–28.
- Talavera, L., Benavente, J., Del Río, L., 2021. UAS Identify and Monitor Unusual Small-Scale Rhythmic Features in the Bay of Cádiz (Spain). *Remote Sens.* 13. <https://doi.org/10.3390/rs13061188>
- Tan, K., Cheng, X., 2017. Specular Reflection Effects Elimination in Terrestrial Laser Scanning Intensity Data Using Phong Model. *Remote Sens.* 9. <https://doi.org/10.3390/rs9080853>
- Tang, C., 1997. Numerical simulation of progressive rock failure and associated seismicity. *Int. J. Rock Mech. Min. Sci.* 34, 249–261.
- Tang, S., others, 2011. Applications of rock failure process analysis (RFPA) method. *J. rock Mech. Geotech. Eng.* 3, 352–372.
- Taylor, J.R., Thompson, W., 1982. *An introduction to error analysis: the study of uncertainties in physical measurements.* Springer.
- Thieler, E.R., Himmelstoss, E.A., Zichichi, J.L., Ergul, A., 2009. The Digital Shoreline Analysis System (DSAS) Version 4.0 - An ArcGIS extension for calculating shoreline change, Open-File Report. Reston, VA. <https://doi.org/10.3133/ofr20081278>
- Tibshirani, R., 1996. Regression shrinkage and selection via the lasso. *J. R. Stat. Soc. Ser. B Stat. Methodol.* 58, 267–288.
- Tin Kam Ho, 1995. Random Decision Forests Tin Kam Ho Perceptron training. *Proc. 3rd Int. Conf. Doc. Anal. Recognit.* 278–282.
- Trenhaile, A.S., 2019. Hard-rock coastal modelling: Past practice and future prospects in a changing world. *J. Mar. Sci. Eng.* 7. <https://doi.org/10.3390/jmse7020034>
- Trenhaile, A.S., 2012. *Cliffs and Rock Coasts, Treatise on Estuarine and Coastal Science.* Elsevier Inc. <https://doi.org/10.1016/B978-0-12-374711-2.00309-0>
- Trenhaile, Alan S., 2010. The effect of Holocene changes in relative sea level on the morphology of rocky coasts. *Geomorphology* 114, 30–41. <https://doi.org/10.1016/j.geomorph.2009.02.003>
- Trenhaile, Alan S., 2010. The effect of Holocene changes in relative sea level on the morphology of rocky coasts. *Geomorphology* 114, 30–41.
- Trenhaile, A.S., 2009. Modeling the erosion of cohesive clay coasts. *Coast. Eng.* 56, 59–72.
- Trenhaile, A.S., 2005. Modelling the effect of waves, weathering and beach development on shore platform development. *Earth Surf. Process. Landforms J. Br. Geomorphol. Res. Gr.* 30, 613–634.
- Trenhaile, A.S., 2003. Modeling shore platforms: present status and future developments, in: *Elsevier Oceanography Series.* Elsevier, pp. 393–409.
- Trenhaile, Alan S., 2001. Modeling the effect of weathering on the evolution and morphology of shore platforms. *J. Coast. Res.* 398–406.

- Trenhaile, A.S., 2001. Modelling the Quaternary evolution of shore platforms and erosional continental shelves. *Earth Surf. Process. Landforms J. Br. Geomorphol. Res. Gr.* 26, 1103–1128.
- Trenhaile, A.S., 2000. Modeling the development of wave-cut shore platforms. *Mar. Geol.* 166, 163–178.
- Trenhaile, A.S., 1999. The width of shore platforms in Britain, Canada, and Japan. *J. Coast. Res.* 355–364.
- Trenhaile, A.S., 1997. *Coastal dynamics and landforms*. Oxford University Press on Demand.
- Trenhaile, A.S., 1987. *The Geomorphology of Rock Coasts*. Oxford University Press.
- Trenhaile, A.S., Mercan, D.W., 1984. Frost weathering and the saturation of coastal rocks. *Earth Surf. Process. Landforms* 9, 321–331.
- Trenhaile, A.S., Pepper, D.A., Trenhaile, R.W., Dalimonte, M., 1998. Stacks and notches at Hopewell Rocks, New Brunswick, Canada. *Earth Surf. Process. Landforms J. Br. Geomorphol. Gr.* 23, 975–988.
- Trenhaile, A.S., Porter, N.J., 2020. Géographie physique et Quaternaire Shore Platform Processes in Eastern Canada 60.
- Trenhaile, A.S., Porter, N.J., Kanyaya, J.I., 2006. Shore platform processes in eastern Canada. *Geogr. Phys. Quat.* <https://doi.org/10.7202/016362ar>
- Triggs, B., McLauchlan, P.F., Hartley, R.I., Fitzgibbon, A.W., 2000. Bundle Adjustment --- A Modern Synthesis, in: Triggs, B., Zisserman, A., Szeliski, R. (Eds.), *Vision Algorithms: Theory and Practice*. Springer Berlin Heidelberg, Berlin, Heidelberg, pp. 298–372.
- Troiani, F., Martino, S., Marmoni, G.M., Menichetti, M., Torre, D., Iacobucci, G., Piacentini, D., 2020. Integrated field surveying and land surface quantitative analysis to assess landslide proneness in the conero promontory rocky coast (Italy). *Appl. Sci.* <https://doi.org/10.3390/app10144793>
- Trudgill, S.T., 1987. Bioerosion of intertidal limestone, Co. Clare, Eire—3: Zonation, process and form. *Mar. Geol.* 74, 111–121.
- Tsamardinos, I., Greasidou, E., Borboudakis, G., 2018. Bootstrapping the out-of-sample predictions for efficient and accurate cross-validation. *Mach. Learn.* 107, 1895–1922.
- Tsujimoto, H., 1987. Dynamic condition for shore platform initiation. *Sci. Rept., Inst. Geosci., Univ. Tsukuba, Sec. 8*, 45–93.
- Turner, D., Lucieer, A., Watson, C., 2012. An Automated Technique for Generating Georectified Mosaics from Ultra-High Resolution Unmanned Aerial Vehicle (UAV) Imagery, Based on Structure from Motion (SfM) Point Clouds. *Remote Sens.* 4, 1392–1410. <https://doi.org/10.3390/rs4051392>
- Turner, F.J., Bartrum, J.A., 1928. *The Geology of the Takapuna-Silverdale District, Waitemata County, Auckland*.
- Turner, I.L., Harley, M.D., Drummond, C.D., 2016. UAVs for coastal surveying. *Coast. Eng.* 114, 19–24. <https://doi.org/https://doi.org/10.1016/j.coastaleng.2016.03.011>

- Tursi, M.F., Anfuso, G., Matano, F., Mattei, G., Aucelli, P.P.C., 2023. A Methodological Tool to Assess Erosion Susceptibility of High Coastal Sectors: Case Studies from Campania Region (Southern Italy). *Water (Switzerland)* 15. <https://doi.org/10.3390/w15010121>
- Tziavou, O., Pytharouli, S., Souter, J., 2018. Unmanned Aerial Vehicle (UAV) based mapping in engineering geological surveys: Considerations for optimum results. *Eng. Geol.* 232, 12–21.
- Ulusay, R., 2014. Rock characterization testing and monitoring. ISRM suggested methods., Rock characterization testing and monitoring. ISRM suggested methods. [https://doi.org/10.1016/0148-9062\(81\)90524-6](https://doi.org/10.1016/0148-9062(81)90524-6)
- Vanneschi, C., Eyre, M., Francioni, M., Coggan, J., 2017. The Use of Remote Sensing Techniques for Monitoring and Characterization of Slope Instability, in: *Procedia Engineering*. <https://doi.org/10.1016/j.proeng.2017.05.166>
- Villaescusa, E., 1992. A review and analysis of rock discontinuity mapping methods, in: *Proc. 6th ANZ Conf. on Geomechanics*. pp. 274–279.
- Viridis, S.G.P., Oggiano, G., Disperati, L., 2012. A geomatics approach to multitemporal shoreline analysis in western mediterranean: The case of platamona-maritza beach (Northwest Sardinia, Italy). *J. Coast. Res.* 28, 624–640. <https://doi.org/10.2112/JCOASTRES-D-11-00078.1>
- Voegtle, T., Schwab, I., Landes, T., 2008. Influences of different materials on the measurements of a terrestrial laser scanner (TLS), in: *Proc. of the XXI Congress, The International Society for Photogrammetry and Remote Sensing, ISPRS2008*. pp. 1061–1066.
- Walkden, M., Dickson, M., 2008. Equilibrium erosion of soft rock shores with a shallow or absent beach under increased sea level rise. *Mar. Geol.* 251, 75–84.
- Warrick, J.A., Ritchie, A.C., Adelman, G., Adelman, K., Limber, P.W., 2017. New Techniques to Measure Cliff Change from Historical Oblique Aerial Photographs and Structure-from-Motion Photogrammetry. *J. Coast. Res.* 33, 39–55. <https://doi.org/10.2112/JCOASTRES-D-16-00095.1>
- Wawrzynek, P.A., Ingraffea, A.R., 1987. Interactive finite element analysis of fracture processes: an integrated approach. *Theor. Appl. Fract. Mech.* 8, 137–150.
- Wehr, A., Lohr, U., 1999. Airborne laser scanning—an introduction and overview. *ISPRS J. Photogramm. Remote Sens.* 54, 68–82.
- Westoby, M.J., Brasington, J., Glasser, N.F., Hambrey, M.J., Reynolds, J.M., 2012. “Structure-from-Motion” photogrammetry: A low-cost, effective tool for geoscience applications. *Geomorphology* 179, 300–314. <https://doi.org/10.1016/j.geomorph.2012.08.021>
- Westoby, M.J., Lim, M., Hogg, M., Pound, M.J., Dunlop, L., Woodward, J., 2018. Cost-effective erosion monitoring of coastal cliffs. *Coast. Eng.* 138, 152–164.
- Wheaton, J.M., Brasington, J., Darby, S.E., Sear, D.A., 2010. Accounting for uncertainty in DEMs from repeat topographic surveys: Improved sediment budgets. *Earth Surf. Process. Landforms* 35, 136–156. <https://doi.org/10.1002/esp.1886>
- Wiesel, J., 1985. Digital image processing for orthophoto generation. *Photogrammetria* 40, 69–76.

- Williams, A., Pranzini, E., 2018. Rock Coasts, in: Encyclopedia of Coastal science (Ed.).
https://doi.org/10.1007/978-3-319-12127-7_315-1
- Williams, R.B.G., Swantesson, J., Robinson, D.A., 2000. Measuring rates of downwearing and mapping microtopography:: The use of micro-erosion meters and laser scanners in rock weathering studies. *Zeitschrift für Geomorphol. NF Suppl. Band 120*. 51-66.
- Williams, R.D., 2012. DEMs of Difference. *Geomorphol. Tech.* 2, 1–17.
- Windsor, C.R., 1997. Rock reinforcement systems. *Int. J. rock Mech. Min. Sci.* 34, 919–951.
- Wolters, G., Müller, G., 2008. Effect of cliff shape on internal stresses and rock slope stability. *J. Coast. Res.* 24, 43–50. <https://doi.org/10.2112/05-0569.1>
- Woodroffe, C.D., 2002. Coasts: form, process and evolution. Cambridge University Press.
- Wyllie, D.C., 2017. Rock slope engineering: civil applications. CRC Press.
- Xu, N., Tang, C., Li, H., Dai, F., Ma, K., Shao, J., Wu, J., 2012. Excavation-induced microseismicity: microseismic monitoring and numerical simulation. *J. Zhejiang Univ. Sci. A* 13, 445–460.
- Xu, N.W., Tang, C.A., Li, L.C., Zhou, Z., Sha, C., Liang, Z.Z., Yang, J.Y., 2011. Microseismic monitoring and stability analysis of the left bank slope in Jinping first stage hydropower station in southwestern China. *Int. J. Rock Mech. Min. Sci.* 48, 950–963.
- Yilmaz, O., Karakus, F., 2013. Stereo and kinect fusion for continuous 3D reconstruction and visual odometry. pp. 115–118. <https://doi.org/10.1109/ICECCO.2013.6718242>
- Young, A.P., 2018. Decadal-scale coastal cliff retreat in southern and central California. *Geomorphology* 300, 164–175. <https://doi.org/10.1016/j.geomorph.2017.10.010>
- Young, Adam P, Carilli, J.E., 2019. Global distribution of coastal cliffs. *Earth Surf. Process. Landforms* 44, 1309–1316. <https://doi.org/https://doi.org/10.1002/esp.4574>
- Young, Adam P, Carilli, J.E., 2019. Global distribution of coastal cliffs. *Earth Surf. Process. Landforms* 44, 1309–1316. <https://doi.org/10.1002/esp.4574>
- Young, A.P., Guza, R.T., Matsumoto, H., Merrifield, M.A., O’Reilly, W.C., Swirad, Z.M., 2021. Three years of weekly observations of coastal cliff erosion by waves and rainfall. *Geomorphology* 375. <https://doi.org/10.1016/j.geomorph.2020.107545>
- Young, R.W., Bryant, E.A., 1993. Coastal rock platforms and ramps of Pleistocene and Tertiary age in southern New South Wales, Australia. *Zeitschrift für Geomorphol.* 257–272.
- Zeng, T., Liang, Y., Dai, Q., Tian, J., Chen, J., Lei, B., Yang, Z., Cai, Z., 2022. Application of machine learning algorithms to screen potential biomarkers under cadmium exposure based on human urine metabolic profiles. *Chinese Chem. Lett.* 33, 5184–5188.
- Zhang, H.Q., Zhao, Z.Y., Tang, C.A., Song, L., 2006. Numerical study of shear behavior of intermittent rock joints with different geometrical parameters. *Int. J. Rock Mech. Min. Sci.* 43, 802–816. <https://doi.org/10.1016/j.ijrmms.2005.12.006>
- Zhang, L., 2016. Engineering properties of rocks. Butterworth-Heinemann.

Zhang, X., Han, L., HAN, L., Zhu, L., 2020. How Well Do Deep Learning-Based Methods for Land Cover Classification and Object Detection Perform on High Resolution Remote Sensing Imagery? *Remote Sens.* 12, 417. <https://doi.org/10.3390/rs12030417>

Zhao, K., Bonini, M., Debernardi, D., Janutolo, M., Barla, G., Chen, G., 2015. Computational modelling of the mechanised excavation of deep tunnels in weak rock. *Comput. Geotech.* 66, 158–171.

Zien, A., Krämer, N., Sonnenburg, S., Rätsch, G., 2009. The feature importance ranking measure, in: *Machine Learning and Knowledge Discovery in Databases: European Conference, ECML PKDD 2009, Bled, Slovenia, September 7-11, 2009, Proceedings, Part II* 20. pp. 694–709.

APPENDIX

APPENDIX 1: PARAMETERS EXTRACTED (Data starts from transect 1 to 310)

Cliff height (m)	Cliff slope (°)	Aspect (°)	UCS (MPa)	GSI	Cliff top retreat (m)	Beach and talus width (m)	Cliff base slope (°)	Boulders at cliff base	Beach retreat (GIZC)	Angle between shoreline and Bora (°)	Angle between shoreline and Scirocco (°)	Vegetation at cliff top
12	44	20	35	50	-6.71	25	6	1	-1	89	1	1
15	51	20	35	50	-4.32	11	13	1	-1	89	1	0
16	58	20	35	50	-4.27	18	9	1	-1	89	1	0
21	80	20	35	50	-7.50	15	11	1	-1	89	1	0
16	45	20	35	50	-3.98	8	7	1	-1	89	1	0
13	59	20	35	50	-2.90	16	5	1	-1	89	1	0
24	70	20	35	50	-8.31	9	12	1	-1	89	1	1
25	73	20	35	50	-7.60	8	10	1	-1	89	1	1
16	56	20	35	50	-5.36	7	8	0	-1	89	1	0
15	53	20	35	50	-4.55	9	9	0	-1	89	1	0
9	48	20	35	50	-4.68	9	9	0	-1	89	1	0
11	42	20	35	50	-4.21	8	14	0	-1	89	1	0
11	46	20	35	50	-4.25	8	10	0	-1	89	1	0
14	63	20	35	50	-6.18	10	11	0	-1	89	1	0
18	59	20	35	50	-6.64	7	12	0	-1	89	1	0
23	57	20	35	50	-7.10	5	11	0	-1	89	1	0
26	62	20	35	50	-4.73	5	11	0	-1	89	1	0
25	56	20	35	50	-8.56	3	18	0	-1	89	1	0
22	57	20	35	50	-8.08	4	20	0	-1	89	1	0
20	69	30	35	50	-6.55	8	14	0	0.58	89	1	0
17	60	30	35	50	-5.51	8	11	0	0.58	89	1	0
17	60	30	35	50	-3.11	6	14	0	0.58	89	1	1
21	59	30	35	50	-3.20	3	18	0	0.58	89	1	1
34	57	30	35	50	-4.74	3	18	0	0.58	89	1	1
47	49	30	35	50	-5.02	4	26	1	0.58	89	1	1
61	53	30	35	50	-3.10	10	22	1	0.58	89	1	1
55	50	30	35	50	-9.62	6	18	1	0.58	89	1	1
45	54	30	35	50	-4.38	8	11	1	0.58	89	1	1
28	44	30	35	50	-6.08	10	11	1	0.58	89	1	1
18	42	30	35	50	-3.40	6	14	1	0.58	89	1	1
27	57	30	35	50	-6.55	5	11	1	0.17	89	1	1
20	52	30	35	50	-4.47	7	15	0	0.17	89	1	1
12	57	30	35	50	-12.13	7	8	0	0.17	89	1	0
13	49	30	35	50	-12.53	6	14	0	0.17	89	1	0
14	42	30	35	50	-11.55	4	14	0	0.17	89	1	0
14	34	30	35	50	-17.07	4	14	0	0.17	89	1	0
16	36	30	35	50	-20.37	5	17	0	0.17	89	1	0
19	45	30	35	50	-14.89	2	26	1	0.17	89	1	0

“COMBINED TECHNIQUES STUDY FOR THE IDENTIFICATION OF MAIN DRIVES IN COASTAL CLIFF PROCESSES BETWEEN PORTONOVO AND TRAVE (ANCONA, ITALY)” PhD Thesis FULLIN NICOLA

20	50	30	35	50	-24.22	5	11	1	0.17	89	1	0
18	67	30	35	50	-12.31	5	17	1	0.17	89	1	1
14	62	30	35	50	-14.99	3	18	1	0.17	89	1	1
21	60	30	35	50	-10.88	7	12	1	0.17	89	1	1
25	65	30	35	50	-16.69	10	31	1	0.17	84	5	1
28	66	30	35	50	-11.27	4	14	1	0.17	84	5	1
24	68	30	35	50	-12.88	6	18	1	0.17	84	5	1
46	65	30	35	50	-19.80	8	14	1	0.17	84	5	1
30	58	30	35	50	-18.12	6	18	1	0.17	84	5	1
32	52	30	35	50	-15.40	4	11	1	0.17	84	5	1
32	60	30	35	50	-18.79	7	16	1	0.17	84	5	1
32	60	30	35	50	-19.99	7	16	1	0.17	84	5	0
32	53	30	35	50	-19.09	3	18	1	0.45	84	5	0
32	54	30	35	50	-20.96	6	18	1	0.45	84	5	0
28	62	30	35	50	-16.30	6	18	1	0.45	84	5	0
32	59	30	35	50	-21.31	7	8	1	0.45	84	5	0
32	56	30	35	50	-25.27	8	14	1	0.45	84	5	0
29	58	30	35	50	-10.34	9	12	1	0.45	84	5	0
28	52	30	35	50	-4.10	8	14	1	0.45	84	5	0
7	70	30	35	50	-6.04	7	11	1	0.45	84	5	1
10	62	30	35	50	-3.97	5	17	1	0.45	84	5	1
11	51	30	35	50	-4.01	0	0	1	0.45	84	5	1
20	54	30	35	50	-24.03	3	18	1	0.45	84	5	1
33	50	30	35	50	-26.83	9	18	1	0.45	84	5	1
41	58	30	35	50	-22.77	7	8	1	0.45	84	5	0
30	49	30	35	50	-21.90	5	11	1	0.45	84	5	0
30	52	30	35	50	-22.68	9	12	1	0.45	84	5	0
23	56	30	35	50	-15.43	7	16	1	0.45	84	5	0
12	60	30	35	50	-4.24	2	26	1	0.45	84	5	0
15	49	30	35	50	-5.10	0	0	1	-3.08	84	5	0
21	60	30	35	50	-10.38	7	12	1	-3.08	84	5	1
29	53	30	35	50	-20.45	7	15	1	-3.08	84	5	0
28	46	30	35	50	-17.71	5	11	1	-3.08	84	5	0
20	62	30	35	50	-10.42	6	14	1	-3.08	84	5	0
10	56	30	5	0	-7.83	4	14	1	-3.08	84	5	0
8	55	30	5	0	-7.80	4	11	1	-3.08	84	5	0
8	54	30	5	0	-15.73	5	11	1	-3.08	84	5	0
8	50	30	5	0	-15.07	7	8	1	-3.08	84	5	0
8	52	30	5	0	-11.88	10	8	1	-3.08	84	5	0
8	61	30	5	0	-10.99	14	3	0	-3.08	84	5	0
9	56	30	5	0	-10.59	14	6	0	-3.08	84	5	0
9	52	30	5	0	-13.21	14	6	0	-3.08	84	5	0
7	49	30	5	0	-12.71	11	6	0	-3.08	84	5	0
8	45	30	5	0	-9.55	12	5	0	-3.08	84	5	0
8	59	30	5	0	-11.66	15	6	0	-3.08	84	5	0

“COMBINED TECHNIQUES STUDY FOR THE IDENTIFICATION OF MAIN DRIVES IN COASTAL CLIFF PROCESSES BETWEEN PORTONOVO AND TRAVE (ANCONA, ITALY)” PhD Thesis FULLIN NICOLA

6	41	30	5	0	-10.36	7	2	0	-12.1	84	5	0
7	50	30	5	0	-9.48	18	3	0	-12.1	84	5	0
8	60	30	5	0	-8.91	18	3	0	-12.1	84	5	0
11	68	30	5	0	-7.88	13	4	0	-12.1	84	5	0
11	70	30	5	0	-7.41	15	5	0	-12.1	84	5	0
13	60	30	5	0	-9.50	8	7	0	-12.1	84	5	0
15	70	30	5	0	-10.43	17	5	0	-12.1	84	5	0
12	68	30	5	0	-8.99	12	7	0	-12.1	84	5	0
10	52	30	5	0	-8.74	11	5	0	-12.1	84	5	0
16	58	30	5	0	-14.58	20	6	0	-12.1	84	5	1
20	77	30	5	0	-11.09	22	7	0	-12.1	84	5	1
18	70	30	5	0	-9.95	20	6	0	-12.1	84	5	0
13	61	30	5	0	-11.60	19	6	0	-12.1	84	5	0
12	60	30	5	0	-9.85	21	4	0	-12.1	69	20	0
13	66	30	5	0	-6.31	17	5	0	-12.1	69	20	0
14	70	30	5	0	-10.95	17	6	0	-9.34	69	20	0
14	67	30	5	0	-10.96	20	6	0	-9.34	69	20	0
14	64	30	5	0	-6.51	20	4	0	-9.34	69	20	0
11	58	30	5	0	-3.73	22	4	0	-9.34	69	20	0
11	58	30	5	0	-10.09	22	4	0	-9.34	69	20	0
14	63	30	5	0	-9.09	23	5	0	-9.34	69	20	0
13	59	30	5	0	-6.15	22	3	0	-9.34	69	20	0
11	60	30	5	0	-4.44	23	3	0	-9.34	69	20	1
8	63	30	5	0	0.27	21	5	0	-9.34	69	20	0
5	40	30	5	0	1.19	20	5	0	-9.34	69	20	0
5	41	30	5	0	2.80	22	3	0	-9.34	69	20	0
4	32	30	5	0	2.34	26	3	0	-9.34	69	20	0
4	32	30	5	0	2.65	22	3	0	-6.21	69	20	0
4	32	30	5	0	1.89	27	3	0	-6.21	69	20	0
3	20	30	5	0	1.92	26	3	0	-6.21	69	20	0
3	17	30	5	0	1.33	26	2	0	-6.21	69	20	0
4	26	30	5	0	2.28	25	3	0	-6.21	69	20	0
5	35	40	5	0	2.42	24	3	0	-6.21	69	20	0
7	42	40	5	0	2.31	27	3	0	-6.21	69	20	0
5	36	40	5	0	1.46	26	2	0	-6.21	69	20	0
6	42	40	5	0	1.37	27	3	0	-6.21	69	20	0
5	35	40	5	0	1.04	27	3	0	-6.21	69	20	0
4	41	40	5	0	-0.88	24	3	0	-6.21	69	20	0
4	27	40	5	0	-0.61	27	3	0	-6.21	69	20	0
3	30	40	5	0	-0.36	27	3	0	-6.21	69	20	0
2.5	11	40	5	0	0.14	19	3	0	-6.21	69	20	0
3	22	40	5	0	-0.05	28	3	0	-6.21	69	20	0
5	41	40	5	0	0.53	25	3	0	-6.21	69	20	0
5	35	40	5	0	1.68	21	4	0	-6.21	69	20	0
5	35	40	5	0	0.78	20	4	0	-6.21	69	20	0

“COMBINED TECHNIQUES STUDY FOR THE IDENTIFICATION OF MAIN DRIVES IN COASTAL CLIFF PROCESSES BETWEEN PORTONOVO AND TRAVE (ANCONA, ITALY)” PhD Thesis FULLIN NICOLA

7	43	40	5	0	1.30	17	5	0	-6.21	69	20	0
3	30	40	5	0	0.89	20	4	0	-6.21	69	20	0
5	40	40	5	0	1.13	22	4	0	-6.21	69	20	0
5	41	40	5	0	-0.04	16	5	0	-6.21	69	20	0
6	42	40	5	0	0.64	17	5	0	-6.21	69	20	0
4	17	40	5	0	1.57	13	5	0	-6.21	69	20	0
4	23	40	5	0	2.38	12	5	0	-6.21	69	20	0
8	51	40	5	0	2.13	14	6	0	-6.21	69	20	0
8	61	40	5	0	2.75	19	7	0	-6.21	69	20	0
7	40	40	5	0	2.23	19	6	0	-6.21	69	20	0
6	35	40	5	0	2.25	18	5	0	-6.21	69	20	1
5	30	40	5	0	1.46	16	5	0	-9.21	69	20	0
5	45	40	5	0	2.13	17	7	0	-9.21	69	20	0
8	55	40	5	0	-0.19	18	7	0	-9.21	57	32	0
8	48	40	5	0	1.46	21	6	0	-9.21	57	32	0
6	35	40	5	0	2.81	21	5	0	-9.21	57	32	0
5	37	40	5	0	2.38	17	6	0	-9.21	57	32	0
5	37	40	5	0	2.62	16	7	0	-9.21	57	32	0
5	41	40	5	0	3.76	14	6	0	-9.21	57	32	0
6	33	40	5	0	0.23	10	8	0	-9.21	57	32	0
7	38	40	5	0	-1.17	11	8	0	-9.21	57	32	0
9	41	40	5	0	-1.12	13	8	0	-9.21	57	32	0
10	56	40	5	0	-1.68	20	6	0	-6.8	57	32	0
10	47	40	5	0	-0.44	17	8	0	-6.8	57	32	0
10	62	40	5	0	-0.91	21	7	0	-6.8	57	32	0
12	65	40	5	0	-1.49	22	5	0	-6.8	57	32	1
7	48	40	5	0	0.05	20	7	0	-6.8	57	32	0
7	42	40	5	0	2.62	17	7	0	-6.8	57	32	0
7	40	40	5	0	0.60	17	7	0	-6.8	57	32	0
8	43	40	5	0	0.25	19	7	0	-6.8	57	32	0
8	43	40	5	0	0.29	20	7	0	-6.8	57	32	0
9	47	40	5	0	1.95	19	7	0	-6.8	57	32	0
8	45	40	5	0	2.01	20	6	0	-6.8	57	32	0
8	48	40	5	0	2.56	16	8	0	-6.8	57	32	0
9	45	40	5	0	1.56	17	7	0	-6.8	57	32	0
8	54	40	5	0	-1.39	16	8	0	-6.8	57	32	0
10	47	40	5	0	-0.31	15	9	0	-6.8	57	32	0
13	37	50	5	0	-1.17	17	8	0	-6.8	57	32	0
13	39	50	5	0	-2.89	15	9	0	-4.21	57	32	0
12	56	50	5	0	-4.90	17	10	0	-4.21	57	32	0
11	63	50	5	0	-7.24	16	11	0	-4.21	57	32	0
11	55	50	5	0	-5.35	16	9	0	-4.21	57	32	0
12	73	50	5	0	-8.34	20	10	0	-4.21	57	32	0
12	42	50	5	0	-9.12	13	9	0	-4.21	57	32	0
11	45	50	5	0	-5.51	16	7	0	-4.21	57	32	0

“COMBINED TECHNIQUES STUDY FOR THE IDENTIFICATION OF MAIN DRIVES IN COASTAL CLIFF PROCESSES BETWEEN PORTONOVO AND TRAVE (ANCONA, ITALY)” PhD Thesis FULLIN NICOLA

9	48	50	5	0	-5.59	21	9	0	-4.21	57	32	0
9	54	50	5	0	-4.46	18	6	0	-4.21	57	32	0
9	52	50	5	0	-3.59	21	7	0	-4.21	57	32	0
8	37	50	5	0	4.68	16	7	0	-4.21	57	32	0
8	51	50	5	0	5.38	21	7	0	-4.21	57	32	0
5	30	50	5	0	5.10	18	5	0	-4.21	57	32	0
5	35	50	5	0	7.45	14	6	0	-4.21	57	32	0
7	39	50	5	0	0.19	21	6	0	-4.21	57	32	0
11	58	50	5	0	-4.19	27	6	0	-4.21	57	32	0
10	54	50	5	0	-6.68	25	7	0	-4.21	57	32	0
6	52	50	5	0	-5.24	23	5	0	-4.21	57	32	0
7	56	50	5	0	-1.67	22	6	0	-4.21	57	32	0
8	56	50	1	0	1.09	17	7	0	-2.73	57	32	0
5	41	50	1	0	1.78	14	6	0	-2.73	57	32	0
8	50	50	1	0	2.81	15	7	0	-2.73	57	32	0
8	50	50	1	0	2.45	14	8	0	-2.73	57	32	0
6	45	50	1	0	5.46	14	6	0	-2.73	57	32	0
5	39	50	1	0	5.76	16	6	0	-2.73	48	41	0
7	48	50	1	0	1.40	12	7	0	-2.73	48	41	0
7	46	50	1	0	-2.28	13	7	0	-2.73	48	41	0
5	43	50	1	0	-0.90	11	6	0	-2.73	48	41	0
5	35	50	1	0	-2.45	11	8	0	-2.73	48	41	0
5	32	50	1	0	-2.55	10	7	0	-2.73	48	41	0
4	31	50	1	0	-0.91	13	5	0	-2.73	48	41	0
5	40	50	1	0	-0.96	13	7	0	-2.73	48	41	0
5	37	50	1	0	0.23	14	6	0	-2.73	48	41	0
5	33	50	1	0	-0.34	14	5	0	-1.71	48	41	0
5	28	50	1	0	-1.94	19	5	0	-1.71	48	41	0
5	37	50	1	0	-2.55	18	6	0	-1.71	48	41	0
5	36	50	1	0	-2.30	17	7	0	-1.71	48	41	0
6	46	50	1	0	-3.28	15	6	0	-1.71	48	41	0
8	38	50	1	0	-10.86	14	6	0	-1.71	48	41	0
16	75	50	1	0	-15.14	24	7	0	-1.71	48	41	0
17	74	60	1	0	-17.59	21	8	0	-1.71	48	41	0
9	49	60	1	0	-16.59	19	6	0	-1.71	48	41	0
12	58	60	1	0	-16.69	20	7	0	-1.71	48	41	0
11	52	60	1	0	-17.34	18	6	0	-1.71	48	41	0
19	63	60	1	0	-14.19	21	8	0	-1.71	48	41	0
24	53	60	1	0	-11.30	23	7	0	-1.71	48	41	1
25	49	60	1	0	-18.32	23	7	0	-1.71	48	41	0
31	46	60	1	0	-19.95	21	5	0	-0.86	48	41	0
25	48	60	1	0	-7.32	22	8	0	-0.86	48	41	0
14	53	60	30	45	-1.78	18	6	0	-0.86	48	41	0
11	52	60	30	45	-0.36	14	8	0	-0.86	48	41	1
9	54	60	30	45	1.64	15	7	0	-0.86	48	41	0

“COMBINED TECHNIQUES STUDY FOR THE IDENTIFICATION OF MAIN DRIVES IN COASTAL CLIFF PROCESSES BETWEEN PORTONOVO AND TRAVE (ANCONA, ITALY)” PhD Thesis FULLIN NICOLA

12	51	60	30	45	0.03	14	8	0	-0.86	48	41	0
12	50	60	30	45	0.93	15	9	0	-0.86	48	41	0
10	51	60	30	45	1.09	20	7	0	-0.86	48	41	1
20	50	60	30	45	-3.89	19	8	0	-0.86	48	41	0
21	46	60	30	45	-5.62	20	7	0	-0.86	48	41	0
14	47	60	30	45	1.43	14	6	0	-0.86	48	41	0
16	54	60	30	45	-1.70	18	8	0	-0.86	48	41	1
19	63	60	30	45	-4.49	16	10	0	-0.86	48	41	0
25	59	60	30	45	-7.18	19	9	0	-0.86	48	41	0
29	52	60	30	45	-15.08	21	8	0	-0.86	48	41	0
36	51	60	25	35	-23.80	17	10	0	-0.86	48	41	0
28	59	70	25	35	-14.51	19	9	0	-0.86	33	56	0
31	52	70	25	35	-7.74	22	10	0	-0.86	33	56	0
44	54	70	25	35	-1.78	23	10	0	-0.86	33	56	0
40	50	70	25	35	-4.02	22	10	0	-0.86	33	56	0
32	65	70	25	35	-2.83	23	10	0	-3.63	33	56	0
31	71	70	25	35	-1.50	19	12	0	-3.63	33	56	0
32	64	70	25	35	-2.14	20	9	0	-3.63	33	56	0
29	58	70	25	35	-3.34	17	7	0	-3.63	33	56	0
25	72	70	25	35	-4.50	20	11	0	-3.63	33	56	0
23	77	70	25	35	-11.53	20	14	0	-3.63	48	56	0
27	80	70	25	35	-8.44	17	12	0	-3.63	33	56	0
30	79	70	25	35	-7.73	23	23	1	-3.63	33	56	0
32	77	70	25	35	-8.84	16	21	1	-3.63	33	56	0
37	72	70	25	35	-17.58	25	19	1	-3.63	33	56	0
45	65	70	25	35	-26.59	22	22	0	-3.63	33	56	0
37	73	70	25	35	-15.11	16	11	0	-3.63	33	56	1
30	70	70	25	35	-11.06	15	8	0	-3.63	33	56	0
25	68	70	25	35	-11.62	16	11	0	-3.63	33	56	0
24	71	70	25	35	-9.36	15	11	0	-3.63	40	49	0
22	75	70	25	35	-11.63	15	11	1	-3.63	40	49	0
25	73	70	25	35	-7.67	17	19	0	-3.63	40	49	0
34	72	70	25	35	-6.31	18	9	0	-3.63	40	49	0
26	54	70	25	35	-4.89	14	16	0	-3.63	40	49	0
36	59	70	25	35	-20.45	13	15	0	4.59	40	49	0
49	54	70	25	35	-22.73	11	10	1	4.59	40	49	0
52	54	70	25	35	-33.24	31	38	1	4.59	40	49	0
58	53	70	25	35	-45.54	34	30	1	4.59	40	49	0
60	55	70	25	35	-36.33	35	34	1	4.59	40	49	0
63	57	70	25	35	-29.15	22	32	1	4.59	40	49	0
54	60	70	25	35	-19.40	36	36	1	4.59	40	49	0
50	60	70	25	35	-12.85	34	37	1	4.59	40	49	0
55	51	70	25	35	-17.82	15	8	1	4.59	40	49	0
54	70	70	25	35	-13.41	30	40	1	4.59	40	49	0
54	72	60	25	35	-10.89	33	35	1	4.59	40	49	0

“COMBINED TECHNIQUES STUDY FOR THE IDENTIFICATION OF MAIN DRIVES IN COASTAL CLIFF PROCESSES BETWEEN PORTONOVO AND TRAVE (ANCONA, ITALY)” PhD Thesis FULLIN NICOLA

75	57	60	25	35	-22.44	40	31	1	4.59	40	49	0
68	58	60	25	35	-15.81	30	36	0	4.59	40	49	0
66	59	60	20	25	-8.56	32	34	0	4.59	40	49	0
78	58	60	20	25	-13.68	30	36	0	4.59	40	49	0
78	53	60	20	25	-11.51	30	45	0	4.59	40	49	0
76	53	60	20	25	-15.57	8	27	0	4.59	40	49	0
87	54	60	20	25	-28.31	11	20	0	4.59	40	49	0
100	52	60	20	25	-42.26	11	10	0	4.59	40	49	0
90	51	60	20	25	-43.69	12	18	0	4.59	40	49	0
100	52	60	20	25	-53.28	14	16	0	4.59	40	49	0
105	49	60	20	25	-46.10	19	26	0	2.39	21	68	0
85	50	60	20	25	-36.13	14	16	0	2.39	21	68	0
54	57	90	20	25	-9.06	13	32	0	2.39	21	68	0
58	60	90	25	35	-10.66	11	28	0	2.39	21	68	0
71	57	90	25	35	-14.47	15	33	0	2.39	21	68	0
75	59	90	25	35	-17.75	17	35	0	2.39	21	68	1
82	60	90	25	35	-22.56	15	34	0	2.39	21	68	1
102	54	90	25	35	-36.88	5	22	0	2.39	21	68	1
105	55	90	25	35	-33.35	16	32	0	2.39	21	68	1
110	55	90	25	35	-31.17	16	32	0	2.39	21	68	1
125	53	90	25	35	-36.50	14	30	0	2.39	21	68	1
117	53	90	25	35	-28.05	12	18	0	2.39	21	68	0
105	52	90	25	35	-19.40	13	13	0	2.39	21	68	0
100	51	90	25	35	-11.37	12	22	0	2.39	21	68	0
92	50	90	25	35	-3.72	11	42	0	2.39	21	68	0
86	51	100	25	35	-0.67	10	11	0	2.39	21	68	0
82	54	100	30	45	9.49	12	9	0	2.39	21	68	0
80	54	100	30	45	9.88	10	11	0	2.39	21	68	0
74	55	100	30	45	9.76	12	14	0	2.39	21	68	0
64	68	100	30	45	12.00	12	11	0	2.39	21	68	0
67	66	100	30	45	10.81	12	18	0	2.39	21	68	0
64	67	100	30	45	-0.92	13	15	0	2.39	21	68	0
60	72	100	30	45	3.69	12	18	0	2.39	2	89	0
52	78	100	30	45	6.14	14	16	0	2.39	2	89	0
52	78	100	30	45	-0.78	14	15	0	2.39	2	89	0
48	80	100	30	45	-12.44	14	16	0	2.39	2	89	0
46	78	100	30	45	-16.29	14	8	0	2.39	2	89	0
45	79	100	30	45	-17.66	15	11	0	2.39	2	89	0
41	76	110	30	45	-14.43	14	16	0	2.39	2	89	0
37	73	110	30	45	-10.47	20	14	0	2.39	2	89	0
33	65	110	30	45	-6.47	11	15	0	2.39	2	89	0
28	66	110	30	45	-4.68	8	11	0	2.39	2	89	0
24	62	110	30	45	-3.49	7	8	0	2.39	2	89	0
15	48	110	30	45	-7.26	10	9	0	2.39	2	89	0
10	42	110	30	45	-9.28	16	3	0	2.39	2	89	0

“COMBINED TECHNIQUES STUDY FOR THE IDENTIFICATION OF MAIN DRIVES IN COASTAL CLIFF PROCESSES BETWEEN PORTONOVO AND TRAVE (ANCONA, ITALY)” PhD Thesis FULLIN NICOLA

5	40	110	30	45	-8.20	23	2		2.39	2	89	0
4	42	110	30	45	-12.22	25	1	0	2.39	2	89	0

APPENDIX 2: MACHINE LEARNING CODE

```
import sys
from sklearn.ensemble import RandomForestClassifier, GradientBoostingClassifier
from sklearn.model_selection import cross_val_score, GridSearchCV, RandomizedSearchCV, KFold, StratifiedKFold
import numpy as np
from sklearn.impute import SimpleImputer
from skopt import BayesSearchCV
from sklearn.metrics import classification_report, confusion_matrix, ConfusionMatrixDisplay
import pandas as pd
import matplotlib.pyplot as plt
from sklearn.model_selection import train_test_split, KFold, cross_val_score
import pickle
import time
from imblearn.over_sampling import SMOTE
import matplotlib.pyplot as plt
import argparse
import tqdm

class CoastalAnalysis:
    def __init__(self, data_path, output_path, oversamp, hpo, test_size, target):
        self.data_path = data_path
        self.output_path = output_path
        self.oversample = oversamp
        self.hpo = hpo
        self.test_size = test_size
        self.target = target

# Utility functions -----
def preprocessing(self, df, feature_to_drop, strategy_missing_values, missing_values):
    features = df
    try:
        features = features.drop(columns=feature_to_drop)
        features = features.drop(columns=self.target)
    except Exception as e:
        print(e)
    target = df[self.target]
    target = target.fillna(0)

    if strategy_missing_values == "zero":
        features = features.fillna(0)
        # imp = SimpleImputer(missing_values=missing_values, strategy='constant', fill_value=0)
        # features = imp.fit_transform(features)
    elif strategy_missing_values == "mean":
        imp = SimpleImputer(missing_values=missing_values, strategy='mean')
        features = imp.fit_transform(features)
    elif strategy_missing_values == "median":
        imp = SimpleImputer(missing_values=missing_values, strategy='median')
        features = imp.fit_transform(features)
    elif strategy_missing_values == "nan":
        features = features.fillna(missing_values)

    return features, target

def hyperparameter_optimization(self, pipeline, parameters, X_train, y_train, X_test, y_test, filename, n_iter=None):
    start = time.time()

    if self.hpo == 'grid_search':
```

```
grid_obj = GridSearchCV(estimator=pipeline,
                        param_grid=parameters,
                        refit=True,
                        #cv=cv,
                        return_train_score=False,
                        scoring='accuracy',
                        verbose=0
                        )

grid_obj.fit(X_train, y_train, )

elif self.hpo == 'random_search':
    grid_obj = RandomizedSearchCV(estimator=pipeline,
                                  param_distributions=parameters,
                                  n_iter=n_iter,
                                  #cv=cv,
                                  refit=True,
                                  scoring='accuracy',
                                  return_train_score=False,
                                  verbose=0
                                  )
    grid_obj.fit(X_train, y_train, )

elif self.hpo == 'bayes_search':
    grid_obj = BayesSearchCV(
        estimator=pipeline,
        search_spaces=parameters,
        scoring='accuracy',
        # cv=cv,
        n_iter=n_iter,
        verbose=0
    )
    grid_obj.fit(X_train, y_train, )
else:
    print('enter search method')
    return

estimator = grid_obj.best_estimator_

print("##### Results")
print("Score best parameters: ", grid_obj.best_score_)
print("Best parameters: ", grid_obj.best_params_)
# print("Cross-validation Score Accuracy: ", cvs.mean())
print("Test Score: ", estimator.score(X_test, y_test))
print(classification_report(
    y_test, estimator.predict(X_test), target_names=["0", "1"]))

print("Time elapsed: ", time.time() - start)
cm = confusion_matrix(y_test, estimator.predict(X_test))
disp = ConfusionMatrixDisplay(cm, display_labels=["0", "1"])
disp.plot()
plt.savefig(filename)

results = [grid_obj.best_score_, estimator.score(
    X_test, y_test), time.time() - start] # ,result.shape[0]]
return results, estimator

def print_decision_rules(self, rf, features_names):
    f = open("decision_path_forest_exp_v3.txt", "w")
```

```

for tree_idx, est in enumerate(rf.estimators_):
    tree = est.tree_
    assert tree.value.shape[1] == 1 # no support for multi-output

    f.write('-----/nTREE: {} \n'.format(tree_idx))

    iterator = enumerate(zip(
        tree.children_left, tree.children_right, tree.feature, tree.threshold, tree.value))
    for node_idx, data in iterator:
        left, right, feature, th, value = data

        # left: index of left child (if any)
        # right: index of right child (if any)
        # feature: index of the feature to check
        # th: the threshold to compare against
        # value: values associated with classes

        # for classifier, value is 0 except the index of the class to return
        class_idx = np.argmax(value[0])

        if left == -1 and right == -1:
            f.write('{} LEAF: return class={} \n'.format(
                node_idx, class_idx))
        else:
            # f.write('{} NODE: if feature[{}] < {} then next={} else next={} \n'.format(node_idx, feature, th, left,
right))
            f.write('{} NODE: if {} < {} then next={} else next={} \n'.format(
                node_idx, features_names[feature], th, left, right))
    f.close()

def plot_feature_importances(self, clf, feature_names, filename):
    features_imp = []
    plt.figure(figsize=(150, 100))
    importances = clf.feature_importances_
    importances = importances[:30]
    indices = np.argsort(importances)
    plt.title('Feature Importances', fontsize=90)
    plt.barh(range(len(indices)),
        importances[indices], color='b', align='center')
    plt.yticks(range(len(indices)), [feature_names[i]
        for i in indices], fontsize=70, ma='left')
    plt.xlabel('Relative Importance (MDI)', fontsize=80)
    plt.xticks(importances[indices], fontsize=70, rotation=45)
    plt.savefig(filename)

    for i in indices:
        if importances[i] != 0:
            features_imp.append(feature_names[i])

    return features_imp
# -----

# Dataset -----
def dataset_preparation(self, feature_to_drop):
    data = pd.read_excel(self.data_path)
    missing_values = [" "]
    label = []

```

```
X, y = self.preprocessing(data, feature_to_drop=feature_to_drop, strategy_missing_values="zero",
missing_values=missing_values)
```

```
features = list(X.columns)
```

```
for i in y:
```

```
    if i < 0:
```

```
        label.append(0)
```

```
    else:
```

```
        label.append(1)
```

```
if self.oversample:
```

```
    oversample = SMOTE()
```

```
    X, label = oversample.fit_resample(X, label)
```

```
X_train, X_test, y_train, y_test = train_test_split(X, label, test_size=self.test_size)
```

```
return X_train, X_test, y_train, y_test, features
```

```
# -----
```

```
# Machine Learning Models -----
```

```
def RandomForest(self, feature_to_drop, model_name="RF"):
```

```
    saved_model_name = self.output_path + model_name + ".pickle"
```

```
    rf_grid = {
```

```
        'criterion': ["gini", "entropy"],
```

```
        'max_depth': [2, 5, 7, 9, 11, None],
```

```
        'max_features': ["log2", "sqrt"],
```

```
        'n_estimators': [100, 150, 200],
```

```
        'min_samples_leaf': [1, 2],
```

```
        'min_samples_split': [2, 5],
```

```
    }
```

```
X_train, X_test, y_train, y_test, features = self.dataset_preparation(
    feature_to_drop)
```

```
path_cm = self.output_path + "CM_rf.png"
```

```
clf = RandomForestClassifier()
```

```
res, est = self.hyperparameter_optimization(
```

```
    clf, rf_grid, X_train, y_train, X_test, y_test, path_cm)
```

```
with open(saved_model_name, 'wb') as handle:
```

```
    pickle.dump(est, handle)
```

```
path_fi = self.output_path + "FI_rf.png"
```

```
f_i = self.plot_feature_importances(est, features, path_fi)
```

```
def XGBoost(self, feature_to_drop, model_name="XGBoost"):
```

```
    saved_model_name = self.output_path + model_name + ".pickle"
```

```
    xgb_grid = {
```

```
        "learning_rate": [0.1, 0.2, 0.3, 0.05, 0.4],
```

```
        "max_depth": [3, 4, 5, 6, 7, 8, 9],
```

```
        "n_estimators": [50, 100, 130, 150]
```

```
    }
```

```
X_train, y_train, X_test, y_test, features = self.dataset_preparation(feature_to_drop)
```

```
path_cm = self.output_path + "CM_xg.png"
```

```
clf = GradientBoostingClassifier()
```

```
res, est = self.hyperparameter_optimization(
```

```
    clf, xgb_grid, X_train, y_train, X_test, y_test, path_cm)
```

```
with open(saved_model_name, 'wb') as handle:  
    pickle.dump(est, handle)
```

```
path_fi = self.output_path + "FI_xg.png"  
f_i = self.plot_feature_importances(  
    est, features, path_fi)
```

```
if __name__ == "__main__":  
    parser = argparse.ArgumentParser()  
    parser.add_argument("d", type=str, help="Dataset path")  
    parser.add_argument("out", type=str, help="Output path")  
    parser.add_argument("aug", type=bool, help="Oversample the dataset: True | False")  
    parser.add_argument("tsize", type=float, help="Size of the test set")  
    parser.add_argument("hpo", type=str, help="Type of hyper-parameter optimization. Choice between: 'grid_search' |  
'random_search' | 'bayes_search'")  
    parser.add_argument("t", type=str, help="Target feature")  
    parser.add_argument("m", type=str, help="Model: RF for random forest or XG for XGBoost")  
  
    args = parser.parse_args()  
  
    ca = CoastalAnalysis(args.d, args.out, args.aug, args.hpo, args.tsize, args.t)  
    #feature_to_drop = ['transetto', 'Hs (m)', 'Q-SLOPE']  
    feature_to_drop = []  
    if args.m == "RF":  
        ca.RandomForest(feature_to_drop)  
    elif args.m == "XG":  
        ca.RandomForest(feature_to_drop)  
    else:  
        print("model not found")
```

APPENDIX 3: LEM RESULTS

General Settings

Units of Measurement:	Metric Units
Time Units:	days
Permeability Units:	meters/second
Data Output:	Standard
Failure Direction:	Left to Right

Analysis Option

Slices Type	Vertical
Analysis Methods Used	GLE/Morgenstern-Price with interslice force function (Half Sine)
Number of slices:	50
Tolerance:	0.005
Maximum number of iterations:	75
Check malpha < 0.2:	Yes
Check tensile effective normal stresses in the first:	25%
Create Interslice boundaries at intersections with water tables and piezos:	Yes
Minimum lambda (Spencer, GLE, Sarma):	-0.1
Maximum lambda (Spencer, GLE, Sarma):	6
Initial trial value of FS:	3
Maximum slice base angle [deg]:	80
Steffensen Iteration:	Yes

Groundwater Analysis

Groundwater Method:	Water Surfaces
Pore Fluid Unit Weight [kN/m ³]:	9.81
Use negative pore pressure cutoff:	Yes
Maximum negative pore pressure [kPa]:	0
Advanced Groundwater Method:	None
Random Numbers	
All Open Scenarios	
Pseudo-random Seed:	10116
Random Number Generation Method:	Park and Miller v.3

Surface Options

Surface Type:	Circular
Search Method:	Auto Refine Search
Divisions along slope:	20
Circles per division:	10
Number of iterations:	10
Divisions to use in next iteration:	50%
Composite Surfaces:	Disabled
Minimum Elevation:	Not Defined
Minimum Depth:	Not Defined
Minimum Area:	Not Defined
Minimum Weight:	Not Defined

Seismic Loading

Advanced seismic analysis:	No
Staged pseudostatic analysis:	No

Materials

Argille Azzurre Trave

Strength Type	Generalized Hoek-Brown
Unit Weight [kN/m ³]	24
Unconfined Compressive Strength (intact) [kPa]	30000
GSI	45
mi	7
Disturbance	0
Water Surface	Assigned per scenario
Ru Value	0

Formazione a Colombacci

Strength Type	Generalized Hoek-Brown
Unit Weight [kN/m ³]	24
Unconfined Compressive Strength (intact) [kPa]	25000
GSI	35
mi	7
Disturbance	0
Water Surface	Assigned per scenario
Ru Value	0

Orizzonte del Trave

Strength Type	Generalized Hoek-Brown
Unit Weight [kN/m ³]	25
Unconfined Compressive Strength (intact) [kPa]	50000
GSI	50
mi	17
Disturbance	0
Water Surface	Assigned per scenario
Ru Value	0

Argille Azzurre Mezzavalle Trave

Strength Type	Generalized Hoek-Brown
Unit Weight [kN/m ³]	24
Unconfined Compressive Strength (intact) [kPa]	25000
GSI	35
mi	7
Disturbance	0
Water Surface	Assigned per scenario
Ru Value	0

Fault

Strength Type	Generalized Hoek-Brown
Unit Weight [kN/m ³]	20
Unconfined Compressive Strength (intact) [kPa]	20000
GSI	25
mi	4
Disturbance	0.6
Water Surface	Assigned per scenario
Ru Value	0

Global Minimums

Section 1

Method:	gle/morgenstern-price
FS	2.039940
Center:	164.817, 49.652
Radius:	52.504
Left Slip Surface Endpoint:	113.637, 37.935
Right Slip Surface Endpoint:	137.505, 4.811
Resisting Moment:	485193 kN-m
Driving Moment:	237846 kN-m
Resisting Horizontal Force:	5824.27 kN
Driving Horizontal Force:	2855.11 kN
Total Slice Area:	249.786 m ²
Surface Horizontal Width:	23.8682 m
Surface Average Height:	10.4653 m

Section 2

Method:	gle/morgenstern-price
FS	1.865810
Center:	163.449, 184.185
Radius:	186.745
Left Slip Surface Endpoint:	-17.680, 138.733
Right Slip Surface Endpoint:	130.423, 0.383
Resisting Moment:	2.33083e+07 kN-m
Driving Moment:	1.24923e+07 kN-m
Resisting Horizontal Force:	96290.5 kN
Driving Horizontal Force:	51607.9 kN
Total Slice Area:	4699.94 m ²
Surface Horizontal Width:	148.104 m
Surface Average Height:	31.7341 m

Section 3

Method:	gle/morgenstern-price
FS	1.529450
Center:	122.779, 137.909
Radius:	150.476
Left Slip Surface Endpoint:	-26.878, 122.232
Right Slip Surface Endpoint:	183.080, 0.044
Resisting Moment:	1.85897e+07 kN-m
Driving Moment:	1.21545e+07 kN-m
Resisting Horizontal Force:	93014.6 kN
Driving Horizontal Force:	60815.8 kN
Total Slice Area:	6863.47 m ²
Surface Horizontal Width:	209.958 m
Surface Average Height:	32.6897 m

Section 4

Method:	gle/morgenstern-price
FS	1.120510
Center:	78.492, 71.418
Radius:	57.680
Left Slip Surface Endpoint:	21.516, 62.435
Right Slip Surface Endpoint:	69.116, 14.506
Resisting Moment:	521780 kN-m
Driving Moment:	465665 kN-m
Resisting Horizontal Force:	6486.34 kN
Driving Horizontal Force:	5788.76 kN
Total Slice Area:	613.896 m ²
Surface Horizontal Width:	47.6006 m
Surface Average Height:	12.8968 m

Section 5

Method:	gle/morgenstern-price
FS	1.213030
Center:	47.828, 87.199
Radius:	54.697
Left Slip Surface Endpoint:	-5.221, 73.872
Right Slip Surface Endpoint:	38.245, 33.347
Resisting Moment:	382995 kN-m
Driving Moment:	315734 kN-m
Resisting Horizontal Force:	5265.95 kN
Driving Horizontal Force:	4341.15 kN
Total Slice Area:	469.543 m ²
Surface Horizontal Width:	43.4661 m
Surface Average Height:	10.8025 m

Section 6

Method:	gle/morgenstern-price
FS	0.911701
Center:	79.237, 115.222
Radius:	52.287
Left Slip Surface Endpoint:	28.427, 102.880
Right Slip Surface Endpoint:	48.957, 72.595
Resisting Moment:	121515 kN-m
Driving Moment:	133284 kN-m
Resisting Horizontal Force:	1404.03 kN
Driving Horizontal Force:	1540.02 kN
Total Slice Area:	161.739 m ²
Surface Horizontal Width:	20.5296 m
Surface Average Height:	7.87831 m

Section 7

Method:	gle/morgenstern-price
FS	1.144810
Center:	48.017, 116.083
Radius:	111.682
Left Slip Surface Endpoint:	-61.973, 96.719
Right Slip Surface Endpoint:	47.746, 4.401
Resisting Moment:	5.86048e+06 kN-m
Driving Moment:	5.11915e+06 kN-m
Resisting Horizontal Force:	38297.2 kN
Driving Horizontal Force:	33452.8 kN
Total Slice Area:	3579.63 m2
Surface Horizontal Width:	109.719 m
Surface Average Height:	32.6254 m

Section 8

Method:	gle/morgenstern-price
FS	0.985903
Center:	118.635, 101.728
Radius:	103.879
Left Slip Surface Endpoint:	25.203, 56.329
Right Slip Surface Endpoint:	39.540, 34.388
Resisting Moment:	120685 kN-m
Driving Moment:	122411 kN-m
Resisting Horizontal Force:	649.801 kN
Driving Horizontal Force:	659.093 kN
Total Slice Area:	71.3441 m2
Surface Horizontal Width:	14.3374 m
Surface Average Height:	4.9761 m

Section 9

Method:	gle/morgenstern-price
FS	2.262740
Center:	110.489, 71.762
Radius:	89.512
Left Slip Surface Endpoint:	24.694, 46.234
Right Slip Surface Endpoint:	52.494, 3.579
Resisting Moment:	1.74286e+06 kN-m
Driving Moment:	770242 kN-m
Resisting Horizontal Force:	11158.7 kN
Driving Horizontal Force:	4931.49 kN
Total Slice Area:	446.207 m ²
Surface Horizontal Width:	27.7992 m
Surface Average Height:	16.0511 m

Section 10

Method:	gle/morgenstern-price
FS	4.370590
Center:	69.945, 40.945
Radius:	39.213
Left Slip Surface Endpoint:	33.042, 27.684
Right Slip Surface Endpoint:	62.505, 2.445
Resisting Moment:	599059 kN-m
Driving Moment:	137066 kN-m
Resisting Horizontal Force:	11762.9 kN
Driving Horizontal Force:	2691.38 kN
Total Slice Area:	250.371 m ²
Surface Horizontal Width:	29.4632 m
Surface Average Height:	8.49774 m

Global Minimum Support Data

No Supports Present